

**The Plasma Water Reactor: A Geometric Approach to Scaling Electric Discharges
for Water Treatment**

by

Selman Mujovic

A dissertation submitted in partial fulfillment
of the requirements for the degree of
Doctor of Philosophy
(Nuclear Engineering and Radiological Sciences)
in the University of Michigan
2019

Doctoral Committee:

Professor John E. Foster, Chair
Dr. Isaiah M. Blankson, NASA
Professor Glen T. Daigger
Professor Mark J. Kushner
Professor Annalisa Manera

Selman Mujovic

mujovics@umich.edu

ORCID: [0000-0002-3269-3548](https://orcid.org/0000-0002-3269-3548)

© Selman Mujovic 2019

Acknowledgements

I would like to thank:

- Professor John Foster
- National Science Foundation
 - PFI: AIR-TT 1700848
 - I-Corps 1550469
 - CBET 1336375
- Michigan Institute for Plasma Science and Engineering
- University of Michigan Center for Entrepreneurship
- Dr. Isaiah Blankson, Prof. Glen Daigger, Prof. Mark Kushner, and Prof. Annalisa Manera
- Kent Pruss, Victor Rosenberg, and Tom Yavaraski
- Current and former colleagues in the Plasma Science and Technology Lab
- Amanda Lietz of the Computational Plasma Science and Engineering Group
- Entire NERS staff, faculty, and research scientists
- Teachers, educators, mentors, and classmates throughout my life
- Family
- Friends

Without you, this would not be possible. Thank you.

Preface

The work herein discusses advanced water treatment in the context of engineering the plasma-water interface as an alternative technology. Chapter 1 provides the water perspective with background into the need for advanced treatment technologies, their benefits and limitations, and how they are applied and assessed in water reuse. Chapter 2 scrutinizes the interaction of plasma with water as an alternative advanced treatment technology; existing embodiments exhibit improved contaminant destruction and energy efficiency yet, they are limited in throughput, or effective flow rate. Chapter 3 explores physical and chemical design criteria needed to geometrically enhance the plasma-water interface with close-packed lattices of water jets—named the Plasma Water Reactor (PWR). Chapter 4 demonstrates the experimental setup and results of PWR prototypes; particularly, distilled and single-contaminant-spiked-distilled water matrices were used in parametric and kinetic studies to optimize power deposition and radical chemistry. Chapter 5 summarizes PWR assessment, ensuing work, and anticipated applications.

Table of Contents

Acknowledgements	ii
Preface	iii
List of Figures	v
List of Tables	vi
List of Abbreviations	vii
List of Physical Constants	x
List of Symbols	xi
Abstract	xiv
Chapter 1 The Water World	1
1.1 The Water Cycle	1
1.1.1 Contamination	2
1.1.2 Contaminants of Emerging Concern	4
1,4-dioxane and PFASs	7
1.2 Advanced Treatment Technologies	9
1.2.1 Filtration	10
Reverse Osmosis	11
Membrane Bioreactor	12
Moving Bed Biofilm Reactor	12
Granular Activated Carbon	12
1.2.2 Disinfection	13
Chlorination	13
Advanced Oxidation Processes	13
Ultraviolet Light	14

	Hydrogen Peroxide	15
	Ozone	16
	Byproducts	18
1.3	Water Reuse	19
1.3.1	Framework	20
1.3.2	Reuse Treatment Trains	22
1.4	Metrics of Success in Water Reuse	23
1.4.1	Compliance	25
1.4.2	Log-Reduction	27
1.4.3	Electrical Efficiency Per Order	28
1.4.4	Cost of Water	30
	Triple Bottom Line	32
1.5	Requirements for Future Technologies	33
Chapter 2	Plasma's Place in the Water World	34
2.1	The Plasma-Water Interface	34
2.1.1	Kinetics	39
	Dose	40
	Radical Transport	43
2.1.2	Energy Transport	45
2.2	Discharge Type	46
2.3	Existing Plasma Water Treatment Systems	49
2.3.1	Best-Suited Applications	54
2.4	Throughput	56
2.4.1	Design Considerations	56
2.4.2	Multiple Plasma Jets	58
2.4.3	Multiple Ignited Bubbles	60
2.4.4	Multiple Water Jets	64
Chapter 3	Blueprint to Scale the Plasma-Water Interface	65
3.1	Packed Bed of Dielectric	66
3.1.1	Packed Bed of Water	67
3.2	Showerhead Design	68
3.2.1	Stream Size	69
3.2.2	Stream Stability	70
	Hydrodynamic Limits	71
	Electrohydrodynamic Criterion	72
3.2.3	Additional Features	73
3.3	Close-Packed Lattice of Water Jets	75
3.3.1	Plasma Generation	75
3.3.2	Electron Production	78
	Townsend Criterion	79
	Raether-Meek Criterion	80
3.3.3	Simulated Kinetics in GlobalKin	82

3.4	Model Based on Design Criteria	85
Chapter 4	The Plasma Water Reactor	94
4.1	PWR Prototypes	94
4.2	Experimental Setup	99
4.2.1	Circuit Configurations	99
4.2.2	Standard PWR	105
4.2.3	Upgraded PWR	107
4.3	Pulser Parametric Study	115
4.3.1	Fluid and Discharge Effects	118
4.3.2	ROS Dose	122
4.3.3	Variation of Hydrogen Peroxide-to-Ozone Dose	128
4.4	Indicator Compounds	130
4.5	Parametric Study of 1,4-dioxane Kinetics	133
4.5.1	Order of Reaction Rate	142
4.6	Real-Time ROS Dose	144
4.7	Validating Kinetics	164
4.7.1	CECs in the PWR and Existing AOPs	166
Chapter 5	Plasma's Forthcoming Role in Resource Recovery	169
5.1	Assessing the PWR's Efficacy	169
5.1.1	Effectiveness	170
5.1.2	Efficiency	171
5.1.3	Scalability	171
5.1.4	Versatility	172
5.1.5	Customization	172
5.2	Future Investigations	173
5.3	Prospects for the Future	176
Appendix A	Chemicals and Reactions of Interest	179
A.1	Mentioned Species	179
A.2	Highlighted Reactions	189

List of Figures

Figure 1.1	CEC pathways in the water cycle and associated solids (Petrović, Gonzalez, and Barceló, 2003).	7
Figure 1.2	Survey of 1,4-dioxane and PFOA in U.S. public water supplies using UCMR3 data.	8
Figure 1.3	Common MFRO- and GAC-based treatment trains for potable reuse (Schimmoller, Kealy, and Foster, 2015).	23
Figure 1.4	AOP power requirements for MTBE removal at various flow rates and log-reductions (Kommineni et al., 2008b).	29
Figure 1.5	E_{EO} values for different published AOPs sorted by median value (Miklos et al., 2018).	30
Figure 1.6	AOP amortized cost, daily cost, capital cost, and annual O&M cost for MTBE removal at various flow rates and log-reductions (Kommineni et al., 2008b).	31
Figure 2.1	Plasma-induced physical and chemical processes in liquid water (Foster et al., 2018).	37
Figure 2.2	Different direct discharges in plasma water treatment (Sommers, 2013).	47
Figure 2.3	Different indirect discharges in plasma water treatment (Sommers, 2013).	48
Figure 2.4	Examples of existing atmospheric plasma- $H_2O_{(l)}$ reactors.	50
Figure 2.5	High throughput configuration using multiple atmospheric plasma jets (Foster et al., 2018).	59
Figure 2.6	Submerged bubble discharge structure and development from electrode initiation to bubble-encapsulated streamer (Mujovic, Groele, and Foster, 2015a).	61
Figure 2.7	Formative time delay in multi-pulsed bubble (Mujovic, Groele, and Foster, 2015b).	62
Figure 2.8	Bubble reactor employing plasma formation and propagation in acoustically excited bubbles (Sommers, 2013).	63

Figure 3.1	Two-dimensional PBDBDs with quartz and zirconia packing media (Engeling et al., 2018).	86
Figure 3.2	Idea behind the PBDBD water design used to enhance the plasma-water contact area.	87
Figure 3.3	Water jet breakup curve and image of post-breakup droplets (McCarthy and Molloy, 1974).	87
Figure 3.4	SolidWorks models of square and hexagonal close-packed water jet lattices.	88
Figure 3.5	Ansys Maxwell \vec{E} simulations of square and hexagonal close-packed water jet lattices (Fig. 3.4). Legend ranges from 10 kV/cm (blue) to 320 kV/cm (red).	89
Figure 3.6	Multiplication factor calculated in cross section slices of square and hexagonal close-packed water jet lattices using Ansys Maxwell \vec{E} simulations. Legend ranges from 10 kV/cm (blue) to 320 kV/cm (red).	90
Figure 3.7	Reactive oxygen and nitrogen species produced in hexagonal close-packed water jet lattice simulated in GlobalKin. One trial was performed with the standard number of jets ($N_j = 18$) and the other had twice as many jets. Water flow and pulsed power structure were identical.	91
Figure 3.8	Solidworks model of PWR used in experimental investigations.	92
Figure 3.9	Ansys Maxwell \vec{E} simulation at midplane of hexagonal-packed water jet configuration shown in Figure 3.8 with 20 kV applied. The colored regions indicate $ \vec{E} > 30$ kV/cm.	93
Figure 4.1	Early PWR prototypes capable of gas injection with coaxial electrode configurations. Blue symbol indicates water flow.	96
Figure 4.2	Compact, high-throughput ($F = 15$ GPM) PWR with $d_j = 3.2$ mm. Blue symbol indicates water flow.	97
Figure 4.3	Compact, high-throughput PWR prototype operating in two plasma discharge modes.	98
Figure 4.4	Sketch of actual subscale PWR system (Courtesy of Stephen Barnard).	100
Figure 4.5	Grounded PWR circuit configuration.	101
Figure 4.6	Floating circuit setup used to assess the floating NSP operating parameter space.	102
Figure 4.7	Images of upgraded front panel and DAQ system.	104
Figure 4.8	Process flow and circuit diagram for the PWR.	105
Figure 4.9	Schematic of upgraded PWR. The 80-20 framing around the system has a one inch-by-one inch cross section and can be used as a dimension reference.	109
Figure 4.10	Images of the upgraded (real-time) PWR and a side-by-side comparison with the standard PWR.	110

Figure 4.11	Process instrument and circuit diagram for the PWR with real-time diagnostics.	113
Figure 4.12	Modified process flow and circuit diagram for the PWR where a peristaltic pump is added to send water to the H ₂ O ₂ and O ₃ sensors.	117
Figure 4.13	The ideal and actual water jet structure in the subscale PWR represented by the model and image, respectively.	119
Figure 4.14	For same pulser parameters, different PWR plasma discharge modes and their associated currents.	121
Figure 4.15	Typical power profile during long ($t > 5$ min) experiments.	123
Figure 4.16	Deposited power for ROS (H ₂ O ₂ /O ₃) dose and ΔpH in the PWR closed loop configuration (Fig. 4.8) for DI water, $V_{sys} = 0.5$ L, and $t_t = 5$ min. The left and right sides have f_p (kHz) and V_p (kV) in the legend, respectively.	125
Figure 4.17	ROS (H ₂ O ₂ /O ₃) dose and ΔpH in the PWR closed loop configuration (Fig. 4.8) for DI water, $V_{sys} = 0.5$ L, and $t_t = 5$ min. The left and right sides have f_p (kHz) and V_p (kV) in the legend, respectively.	126
Figure 4.18	ROS (H ₂ O ₂ /O ₃) dose as a function of power and pH in the PWR closed loop configuration (Fig. 4.8) for DI water ($V_{sys} = 0.5$ L) and $t_t = 5$ min.	129
Figure 4.19	Decomposition of MB, MTBE, and 1,4-dioxane in the closed loop ($V_{sys} = 0.5$ L) PWR at $V_p = 15$ kV, $f_p = 5$ kHz, and $t_p = 40$ ns.	132
Figure 4.20	Power characteristics of various pulsing techniques during PWR treatment of 1,4-dioxane batches ($c_i = 50$ ppm). The legend is given in coordinates of (V_p, f_p, t_p) with units (kV, kHz, ns) and all plots have the same legend.	135
Figure 4.21	1,4-dioxane kinetics of various pulsing techniques during PWR batch treatment ($c_i = 50$ ppm). The legend is given in coordinates of (V_p, f_p, t_p) with units (kV, kHz, ns) and all plots have the same legend.	137
Figure 4.22	Derived parameters for 1,4-dioxane kinetics of various pulsing settings during PWR batch treatment ($c_i = 50$ ppm). The legend is given in coordinates of (V_p, f_p, t_p) with units (kV, kHz, ns) and all plots have the same legend.	139
Figure 4.23	1,4-dioxane kinetics of various pulsing techniques in terms of energy density during PWR treatment of spiked-DI water batches ($c_i = 50$ ppm). The legend is given in coordinates of (V_p, f_p, t_p) with units (kV, kHz, ns).	140
Figure 4.24	Contaminant and byproduct effects in PWR 1,4-dioxane kinetics.	142
Figure 4.25	1,4-dioxane reaction rates as a function of different pulser parameters in (V_p [kV], f_p [kHz], t_p [ns]) coordinates.	143

Figure 4.26	Pulser power operating space for different peak voltage and pulse width in the closed loop PWR (Figs. 4.4 and 4.12) for DI water matrix.	148
Figure 4.27	Pulser parameter power space in the closed loop PWR (Figs. 4.4 and 4.12) for DI water matrix.	149
Figure 4.28	Pulser parameter power profile in the closed loop PWR (Figs. 4.4 and 4.12) for DI water matrix.	150
Figure 4.29	H ₂ O ₂ produced in the closed loop PWR (Figs. 4.4 and 4.12) for DI water matrix.	151
Figure 4.30	O ₃ produced in the closed loop PWR (Figs. 4.4 and 4.12) for DI water matrix.	152
Figure 4.31	H ₂ O ₂ /O ₃ ratio (mol/mol) in the closed loop PWR (Figs. 4.4 and 4.12) for DI water matrix.	153
Figure 4.32	H ₂ O ₂ produced as a function of energy density ($\frac{P_D \cdot t_t}{V_{sys}}$) in the closed loop PWR (Figs. 4.4 and 4.12) for DI water matrix.	154
Figure 4.33	O ₃ produced as a function of energy density ($\frac{P_D \cdot t_t}{V_{sys}}$) in the closed loop PWR (Figs. 4.4 and 4.12) for DI water matrix.	155
Figure 4.34	H ₂ O ₂ /O ₃ ratio (mol/mol) as a function of energy density ($\frac{P_D \cdot t_t}{V_{sys}}$) in the closed loop PWR (Figs. 4.4 and 4.12) for DI water matrix.	156
Figure 4.35	H ₂ O ₂ produced as a function of energy density ($\frac{P_D \cdot t_t}{V_{sys}} \leq 1 \text{ kW h/m}^3$) in the closed loop PWR (Figs. 4.4 and 4.12) for DI water matrix.	157
Figure 4.36	O ₃ produced as a function of energy density ($\frac{P_D \cdot t_t}{V_{sys}} \leq 1 \text{ kW h/m}^3$) in the closed loop PWR (Figs. 4.4 and 4.12) for DI water matrix.	158
Figure 4.37	H ₂ O ₂ /O ₃ ratio (mol/mol) as a function of energy density ($\frac{P_D \cdot t_t}{V_{sys}} \leq 1 \text{ kW h/m}^3$) in the closed loop PWR (Figs. 4.4 and 4.12) for DI water matrix.	159
Figure 4.38	H ₂ O ₂ /O ₃ dose as a function of energy density ($\frac{P_D \cdot t_t}{V_{sys}}$) in the closed loop PWR (Figs. 4.4 and 4.12) for DI water matrix.	160
Figure 4.39	H ₂ O ₂ /O ₃ dose as a function of time in the closed loop PWR (Figs. 4.4 and 4.12) for DI water matrix.	161
Figure 4.40	H ₂ O ₂ in pulser operating space for different peak voltage and pulse width in the closed loop PWR (Figs. 4.4 and 4.12) for DI water matrix.	162
Figure 4.41	O ₃ in pulser operating space for different peak voltage and pulse width in the closed loop PWR (Figs. 4.4 and 4.12) for DI water matrix.	163
Figure 5.1	Post-treated tap water particulate from induced oxidation and electrocoagulation.	170
Figure 5.2	Optical emission spectrum of upgraded PWR in DI water at (20 kV, 4 kHz, 40 ns).	175

Figure A.1 Decomposition pathways of MTBE and its transformation products (Acero et al., 2001; Mitani et al., 2002). 191

List of Tables

Table 2.1	Relevant ROS reaction rate coefficients at standard temperature and pressure (DeMore, 1973; Weinstein and Bielski, 1979; Simonaitis and Heicklen, 1982; Buxton et al., 1988; Suh and Mohseni, 2004; Lietz and Kushner, 2016; Fischbacher, Lutze, and Schmidt, 2018). The coefficients are second-order in units of $\text{cm}^3 \text{s}^{-1}$ unless stated otherwise.	36
Table 2.2	Comparison of different AOP technologies including plasma (Even-Ezra et al., 2009; Salveson et al., 2009; Malik, 2010; Foster et al., 2013; Stratton et al., 2017).	53
Table 4.1	Equipment list for the standard PWR subscale system (Fig. 4.8). Materials listed are wetted surfaces unless specified otherwise.	106
Table 4.2	Equipment description or operating conditions for items in Table 4.1.	108
Table 4.3	Equipment list for the upgraded PWR subscale system (Fig. 4.11). Items not shown can be found in Table 4.1.	114
Table 4.4	Equipment description or operating conditions for the upgraded PWR system (Fig. 4.11). Items and their descriptions not shown can be found in Tables 4.1 and 4.2, respectively.	116

Table 4.5	AOP parameters for MTBE destruction using reaction rate coefficients in Table A.2. Assuming pseudo first-order kinetics (Eqn. 2.2), hydroxyl production rate is expressed as $\zeta \frac{P}{V}$ where ζ is a system-dependent constant, P is power, V is volume, and scavenger S includes dissolved organic carbon, bicarbonate (HCO_3^-), and carbonate (CO_3^{2-}) except for the last three cases; the scavenger capacity for the third- and second-to-last cases were calculated based on byproducts and benzene, respectively (Elovitz and Gunten, 1999; Acero et al., 2001; Bolton et al., 2001; Mitani et al., 2002). The final case is the PWR where the scavenger capacity was approximated using nitrate ($k_{\text{HO}\cdot, \text{NO}_3^-} \langle [\text{NO}_3^-] \rangle$) and $\langle [\cdot\text{OH}] \rangle$ was estimated using 1,4-dioxane as an indicator compound at the same power.	167
Table 4.6	AOP parameters derived from effective CEC reaction rates using the PWR based on reaction rate coefficients in Table A.2. Scavenger capacity was estimated as $k_{\text{HO}\cdot, \text{NO}_3^-} \langle [\cdot\text{OH}] \rangle$. For MTBE and MB, $\langle [\cdot\text{OH}] \rangle$ was estimated using 1,4-dioxane as an indicator compound at the same power. For MB, the hydroxyl production rate is calculated assuming $k_{\cdot\text{OH}, \text{MB}} = 2 \times 10^{-10} \text{ cm}^3 \text{ s}^{-1}$	168
Table A.1	Species discussed throughout the thesis.	179
Table A.2	List of ozone (O_3) and hydroxyl ($\cdot\text{OH}$) reaction rate coefficients for 1,4-dioxane, MTBE, and their known transformation products at 25 °C calculated using different $[\text{H}_2\text{O}_2]$ and $[\text{O}_3]$. O_3 and $\cdot\text{OH}$ coefficients for MMP and HiBA were estimated based on averaging their respective values obtained for structurally similar TMA and iBA (Buxton et al., 1988; Adams, Scanian, and Secrist, 1994; Acero et al., 2001; Mitani et al., 2002; Butkovskaya et al., 2004; Suh and Mohseni, 2004).	190

List of Abbreviations

AI	Analog Input
AO	Analog Output
AOP	Advanced Oxidation Process
ATW	Advanced Treated Water
AWWA	American Water Works Association
atm	Atmospheric Pressure (101.3 kPa)
BAC	Biologically Activated Carbon
BOD	Biochemical Oxygen Demand
CEC	Contaminant of Emerging Concern
COD	Chemical Oxygen Demand
CFU	Colony-Forming Unit
CT	Concentration-Time
DAQ	Data Acquisition
DBD	Dielectric Barrier Discharge
DBP	Disinfection Byproduct
DI	Distilled
DO	Dissolved Oxygen
DPD	N,N-diethyl-p-phenylenediamine
DPR	Direct Potable Reuse
ECPR	Enhanced Contact Plasma Reactor
EP	Equipotential
EPA	U.S. Environmental Protection Agency
EMI	Electromagnetic Interference
FID	Flame Ionization Detector
GAC	Granular Activated Carbon
GC	Gas Chromatography
GND	Electrical Ground
GPM	Gallons Per Minute (gal/min)
HAA	Haloacetic acid
HDC	Hydrodynamic Cavitation
HiBA	Hydroxyisobutyraldehyde
HPLC	High-Performance LC

HS	Headspace Analyzer
HV	High Voltage
HVP	High Voltage Probe
iBA	Isobutyraldehyde
IC	Ion Chromatography
IC	Inorganic Carbon
ICPMS	Inductively Coupled Plasma-MS
IPR	Indirect Potable Reuse
I-V	Current-Voltage
LC	Liquid Chromatography
LPUV	Low-Pressure UV
LV	Low Voltage
MB	Methylene Blue
MBR	Membrane Bioreactor
MBBR	Moving Bed Biofilm Reactor
MCL	Maximum Contaminant Level
MF	Microfiltration
MMP	2-Methoxy-2-Methyl Propionaldehyde
MPUV	Medium Pressure UV
MS	Mass Spectrometry
MTBE	Methyl Tert-Butyl Ether
MVP	Minimum Viable Product
MWCO	Molecular Weight Cut-Off
NSP	Nanosecond Pulser
NWRI	National Water Research Institute
NACWA	National Association of Clean Water Agencies
NDMA	N-Nitroso-dimethylamine
NF	Nanofiltration
NOM	Natural Organic Matter
NPDES	National Pollutant Discharge Elimination System
NPOC	Non-Purgeable Organic Carbon
ODR	Ocean Discharge Reuse
O&M	Operation & Maintenance
OES	Optical Emission Spectroscopy
PBDBD	Packed Bed DBD
PFAS	Per- or Polyfluoroalkyl Substance
PFBA	Perfluorobutanoic acid
PFBS	Perfluorobutanesulfonic acid
PFOA	Perfluorooctanoic acid
PFOS	Perfluorooctanesulfonic acid
PMMA	Poly(methyl methacrylate)
ppb	part-per-billion
PPCP	Pharmaceuticals and Personal Care Product

ppm	part-per-million
ppt	part-per-trillion
PVC	Polyvinyl Chloride
PWR	Plasma Water Reactor
Redox	Reduction-Oxidation
RO	Reverse Osmosis
ROS	Reactive Oxygen Species
SPICE	Simulation Program with Integrated Circuit Emphasis
SPM	Spectrophotometer
TBA	Tert-Butyl Alcohol
TBF	Tert-Butyl Formate
TC	Total Carbon
1,1,1-TCA	1,1,1-Trichloroethane
TCE	Trichloroethylene
TDS	Total Dissolved Solids
THM	Trihalomethane
TMA	Trimethylacetaldehyde
TOC	Total Organic Carbon
UCMR	Unregulated Contaminant Monitoring Rule
UF	Ultrafiltration
UV	Ultraviolet [light]
VOC	Volatile Organic Contaminant
WEF	Water Environment Federation (WEF)
WRRF	WaterReuse Research Foundation
WHO	World Health Organization
ZLD	Zero Liquid Discharge
316SS	Grade-316 Stainless Steel

List of Physical Constants

Avogadro Constant	$N_A = 6.022 \times 10^{23} \text{ mol}^{-1}$
Boltzmann Constant	$k_b = 8.617 \times 10^{-5} \text{ eV K}^{-1}$
Elementary Charge	$e = 1.602 \times 10^{-19} \text{ C (J eV}^{-1}\text{)}$
Planck Constant	$h = 6.626 \times 10^{-34} \text{ J s}$
Speed of Light	$c_0 = 2.997 \times 10^8 \text{ m s}^{-1}$
Electric Constant	$\epsilon_0 = 8.854 \times 10^{-12} \text{ F m}^{-1}$

List of Symbols

A	Atomic, or Molecular, Weight	g/mol
A_0	Arrhenius Coefficient	cm ³ /s
c	Concentration ($[c] = \#/cm^3$)	ppm, ppb, or ppt
$\frac{\partial c}{\partial t}$	Reaction Rate	$\#/cm^3/s$
d_i	Molecule Size	Å
d_j	Water Jet Diameter	mm
D	Diffusion Coefficient	cm ² /s
\vec{E}	Electric Field	kV/cm
E_{act}	Activation Energy	eV or K
E_{EM}	Electric Energy per Mass	kW h/g
E_{EO}	Electric Energy per Order	kW h/m ³
F	Flow Rate	gal/min (GPM)
f	Fraction of Light Absorbed	#
f_p	Pulser Frequency	kHz
H	UV Fluence	mW/cm ²
H^{cc}	Henry's Law Constant	#
I	Current	A
I_0	Photon Flux	$\#/cm^2/s$
\vec{j}	Current Density	A/cm ²
T_e	Electron Temperature	eV
T_i	Ion Temperature	eV
k	Reaction Rate Coefficient	2 nd order: cm ³ /s
ℓ	Path Length	cm
L	Characteristic Breakdown Path Along \vec{E} Line	mm
M	Electron Multiplication Factor	#
m_e	Electron Mass	kg
m_i	Ion Mass	kg
n	Arrhenius Exponent	#
n_e	Electron Density	$\#/cm^3$
N	Species Number Density ($c \propto N$)	$\#/cm^3$
N_j	Number of Water Jets	#
P	Power	W

p	Pressure	psi
Re	Reynolds Number	#
R_{ct}	Ratio of hydroxyl/ozone = $\frac{\int[\bullet\text{OH}]dt}{\int[\text{O}_3]dt}$	mol/mol
r_p	Packing Ratio ($\frac{d_j}{d_j+s_j}$)	#
s_j	Interstitial Jet Spacing	mm
t_b	Jet Breakup Time	ms
t_{HR}	Hydraulic Retention Time (= F/V_{sys})	h
t_p	Pulser Pulse Width	ns
t_r	Pulse Rise Time	ns
t_t	Duration of Plasma Treatment	h
T	Heavy Particle (Neutral or Ion) Temperature	K
T_ℓ	Liquid Temperature	°C
UVT	UV Transmittance	%
V_{ECO}	Electrochemical Oxidation Potential	eV
V_p	Pulser Voltage	kV
V_{sys}	System, or Working, Volume	L
v_j	Jet Velocity	cm/s
α	Ionization Swarm Parameter	mm^{-1}
δ_0	Initial Amplitude	μm
δ_R	Penetration Depth of Radical R	μm
$\Delta\varepsilon$	Net Energy Change per Reaction	eV
ε	Molar Attenuation Coefficient	$\text{M}^{-1}\text{cm}^{-1}$
η	Attachment Swarm Parameter	mm^{-1}
γ	Secondary Electron Emission Yield	$\gamma \in (0, 1]$
γ_0	Surface Tension	mN/m
λ	Photon wavelength	nm
λ_d	(∞) Axisymmetrical Disturbance Wavelength	nm
μ	Liquid Dynamic Viscosity	m^2/s
Φ	Quantum Yield	#
ρ	Liquid Mass Density	g/cm^3
σ	Electric Conductivity	$\mu\text{S}/\text{cm}$
τ_r	Time Constant or Lifetime of Reactant r	min
ν_m	Momentum Transfer Collision Frequency	s^{-1}
app	Applied	
i	Initial, Input, or Index	
C	Contaminant	
D	Dissipated or Deposited	
eff	Effective	
f	Final	
m	Measured	
max	Maximum	
min	Minimum	

R Radical
S Scavenger or Specie

Abstract

Advanced oxidation processes (AOPs) are established disinfection methods that can remove contaminants of emerging concern (CECs) by producing hydroxyl radicals and other reactive oxygen species (ROS) in situ. Production of hydrogen peroxide (H_2O_2), ozone (O_3), and ultraviolet (UV) light in traditional AOPs can significantly contribute to the cost of water due to required consumables and associated infrastructure.

Plasma interacting with liquid water can generate additional transient ROS in solution while eliminating consumables and conversion efficiencies. Subsequently, in principle, plasma-based AOPs should be considerably cheaper and more effective than conventional AOPs. Although the plasma-water interface can facilitate vital kinetics through various pathways, approaches to date fail to scale-up to practical flow rates due to limited oxidant transport. In this work, the Plasma Water Reactor (PWR) is proposed as a scalable high-throughput system that advantageously uses flowing water to enhance plasma formation and propagation. The PWR utilizes a close-packed lattice of water jets to mimic packed bed dielectric barrier discharges where water streams serve as the dielectric media.

To sustain and maximize the plasma-water interface, the PWR design criteria incorporate jet stability and structure by considering fluid and electrohydrodynamic effects. Assuming steady jets, simulations for a hexagonal lattice with cylindrical electrodes indicated excellent plasma-water contact area with $> 82\%$ of the PWR achieving the

breakdown electric field in atmospheric air ($|\vec{E}_{br}| > 30 \text{ kV/cm}$). Computations also suggested that changes in power density result in varied oxidant production, though this needs to be further verified.

The PWR was assessed in pure or single-CEC-spiked distilled water matrices. Parametric kinetic studies using pulsed power were performed by measuring power and species concentrations while varying the pulse voltage, width, and repetition frequency. In exclusively distilled water, H_2O_2 and O_3 were measured for various combinations of pulser parameters. Though the pulser was power-limited, the PWR produced relevant oxidant concentrations and variations in $\frac{[\text{H}_2\text{O}_2]}{[\text{O}_3]}$ based on chemical probe measurements. For a given set of pulser parameters that corresponded to high oxidant dose, methylene blue, methyl tert-butyl ether, and 1,4-dioxane were decomposed. These indicator compounds demonstrated effective flow rates on the order of 0.1–0.75 gal/min for 90% removal. Since 1,4-dioxane exhibited the slowest destruction, the PWR was optimized using this compound. In addition to 1,4-dioxane, two transformation products, formate and acetate, and a plasma byproduct, nitrate, were measured. For three different pulser configurations, 1,4-dioxane kinetics were analyzed and the PWR achieved at least 0.5-log reduction, which implied sufficient oxidation. 1,4-dioxane decay displayed different order of reaction rates and real-time oxidant measurements confirmed $\frac{[\text{H}_2\text{O}_2]}{[\text{O}_3]}$ ratios spanned several orders of magnitude. Thus, the PWR demonstrated the ability to vary kinetics. In the future, pilot studies must be performed to assess the PWR's efficacy for custom water matrices.

Chapter 1

The Water World

Climate change, population growth, overdevelopment, and pollution excessively stress our freshwater quantity and quality.

1.1 The Water Cycle

Approximately 2.5% of Earth's water is freshwater; of that, 30.1% is groundwater, 0.37% is surface and other freshwater, and the remainder is stored in ice such as glaciers, ice caps, and permafrost (Shiklomanov, 1993). Climate change contributes to the rapid loss of most of Earth's freshwater as this ice melts into seawater with rising temperatures. Warming temperatures also significantly fluctuate precipitation patterns. Unprecedented drought has pushed provinces to the brink of depletion with Cape Town being the world's first major metropolis to declare 'Day Zero'.¹ More than half of Earth's 37 largest aquifers are receding and a third of them are under severe distress (Richey et al., 2015). Additionally, Earth's population is projected to grow to eight

¹Day Zero was postponed several times then canceled but, water restrictions are still in effect for Capetonians. During my graduate studies, the closest Day Zero approached was within a month in the autumn of 2017.

billion around 2020 thus, intensifying the strain on our limited freshwater supplies. This stress is further exacerbated since developing nations, which will see the greatest population growth, will also have limited resources to address scarcity and pollution.

The positive feedback loop of demand and unchecked consumption has led to strained supplies and unintended implications. Accounting for \$2.5B of California's agricultural value (in 2013 dollars), San Joaquin Valley is agriculturally and technologically rich, ranking among the U.S.'s most productive counties (CDFA, 2013). However, this central valley is home to the largest human alteration of the Earth's surface due to subsidence from excessive groundwater extraction. By the 1970s, aquifer overdraft caused more than half the valley to sink > 1 ft with some areas reaching 30 ft, eroded ecosystems and other geographical features, increased flood risk, and damaged public and private infrastructure, equivalent to a conservative cost of \$1.3B (in 2013 dollars) during 1955–1972 (Borchers et al., 2014). This estimate does not consider socio-economic threats to food and energy security since unsustainable freshwater sources are detrimental to water-intensive human activities, such as farming and electricity generation.

1.1.1 Contamination

Another form of water misuse that imperils water quality is pollution. While extreme scarcity will affect nearly two billion people within the next decade, the World Health Organization (WHO) estimates that one-half of the developing world suffers from one or more of six waterborne diseases (diarrhea, ascariasis, dracunculiasis, hookworm, schistosomiasis, and trachoma) caused by lack of sanitation (Programme, 2015). Further compounding the contamination issue, about 80% of global wastewater—over 95% in some developing nations—is released into the environment without prior treatment (Programme, 2017). Though its more likely to affect the developing world,

poor water quality indiscriminately strikes. For example, *Cryptosporidium parvum* was not identified as a human pathogen until the late 1970s yet, in 1993, more than 400,000 residents of Milwaukee, WI fell ill, 54 of which died (Kenzie et al., 1994).

Pathogen loading is harmful to human health and is often associated with nutrient loading, which is currently the most prevalent global water challenge. Global nitrate trends indicate increasing concentrations in developing countries, particularly Asia. Point and diffuse wastewater sources, such as agricultural runoff, can lead to excess nutrients in the environment and initiate eutrophication. The subsequent harmful algal blooms that form from the abundant nitrogen and phosphorus result in hypoxic zones that kill fish and send ripples through ecosystems. Commonly found in surface water, some species of cyanobacteria, specifically blue-green algae, produce toxins such as hepatotoxins, neurotoxins, and skin irritants. For microcystin-LR, the most common congener of microcystin, a type of hepatotoxin, the WHO adopted an advisory limit of 1 µg/L, or 1 part-per-billion (ppb), in drinking water (WHO, 2003). Diagnosing, measuring, and monitoring microcystin-LR can be difficult tasks on their own and this example is simply one microcosm within the water cycle. Thus, contamination and its complex cascading effects must be mitigated at all costs.

When did water contamination gain widespread attention? Some credit Ohio's Cuyahoga River famously catching fire, albeit for the 13th time, as the catalyst that launched the U.S. environmental movement (Adler, 2002). The 1969 fire catapulted to the national stage due to a *Time Magazine* article. This watershed moment illustrated the consequences of a century of unchecked industrialization. The environmental campaign grew and resulted in key directives and legislation, such as the National Environmental Policy Act (1969), the ratified Reorganization Plan No. 3 (1970), which established the Environmental Protection Agency (EPA), the Clean Water Act (1972), the Great Lakes Water Quality Agreement (1972), the Safe Drinking Water Act (1974),

the Toxic Substances Control Act (1976), and the Superfund Act (1980). Although these statutes enabled better accountability and pollution research, the impact of industrialization on the water-energy-food nexus still needs to be better understood.

The industrial footprint extends beyond the above examples of agriculture and includes oil and gas, food and beverage, semiconductor, biotech, mining, and textile. Though some implement environmental initiatives due to customer and regulatory influences, traditional and emerging industries continue to unsustainably consume water and produce wastewater at alarming rates. For instance, in hydraulic fracturing, or fracking, the ratio of water used (down-hole) to water returned (to environment) can be infinite since produced water can be deep well injected, implying that this water will never return to the water cycle; these disposal wells may induce earthquakes and are disproportionately located in minority-majority and high-poverty areas (Johnston, Werder, and Sebastian, 2016). While industries are increasingly pursuing sustainable stewardship, pollution remains the biggest threat to our water supplies.

1.1.2 Contaminants of Emerging Concern

Poor water management has led to unsustainable consumption, along with the introduction of pollutants into potable water supplies. There are many different contaminant classifications including chemical, biosusceptibility, toxicity, and origin. For anthropogenic compounds, there are over 100,000 chemicals registered for commercial use in the U.S. with global chemical production growing 3% annually and doubling every 24 years (Klosterhaus et al., 2013). Many of these compounds are not regularly monitored. For example, sucralose, an artificial sweetener and good wastewater indicator due to its prevalence, and vitellogenin, a vertebrate biomarker for environmental estrogens, can be found in Washington's Puget Sound, the third largest estuary in

the U.S. (Miller-Schulze et al., 2014). Active ingredients in pharmaceuticals and personal care products (PPCPs), such as analgesic, antibiotic, antiseptic, lipid-regulating, and endocrine-disrupting compounds, are ubiquitous in aquatic biomes at low parts-per-trillion (ppt, or ng/L) due to perpetual life-cycle and multigenerational exposure (Daughton and Ternes, 1999). As a result, PPCPs and their bioactive metabolites can be found in single species to entire ecosystems and can induce subcellular, cellular, organismal, and ecological effects (Prichard and Granek, 2016). Indeed, PPCPs remain pervasive in aquatic, aerial, and terrestrial food chains at small concentrations, raising concern regarding antimicrobial resistance, a global threat to public health. PPCPs and their ecological risks can slowly accumulate to irreversible change that would have otherwise been attributed to nature. Furthermore, microplastics, some of which are from PPCPs, span various ecosystems and their respective food chains due to trophic and ontogenic transfer (Setälä et al., 2018; Al-Jaibachi, Cuthbert, and Callaghan, 2018). Microplastics can reach and affect remote habitats, such as the pristine French Pyrenees, through atmospheric transport and travel distances of up to 95 km (Allen et al., 2019). Similar to the Cuyahoga River fire, plastic microbeads gained national attention, leading to cosmetic companies voluntarily phasing them out until the Microbead-Free Waters Act (2015) was authorized.

However, momentum like this is uncommon in regulatory agencies. In the first nationwide study by the U.S. Geological Survey, PPCPs and other organic wastewater contaminants, including pesticides, plasticizers, and polycyclic aromatic hydrocarbons, were discovered in > 75% of the 139 susceptible streams evaluated, with a median of seven pollutants detected, though this is likely an underestimate; while single compounds were measured at low ppt levels, total concentration—frequently exceeding 1 ppb—and number of pollutants exhibited a Spearman’s rank correlation

coefficient of 0.94 and a p-value < 0.001 (Kolpin et al., 2002), where the Spearman's coefficient measures the strength and direction of association between two ranked variables and the p-value determines whether or not to reject a null hypothesis; a small p-value (≤ 0.05) indicates sufficient evidence against the null hypothesis. This implies that these compounds should be assessed for individual and collective toxicity since contamination likely involves multiple constituents.

Hazardous, mass-produced compounds that perpetuate in worldwide water supplies and eventually require regulation are identified as contaminants of emerging concern (CECs). For instance, trichloroethylene (TCE) is a popular metal degreaser and known teratogen²; atrazine is a commonly used herbicide and suspected reprotoxin; methyl tert-butyl ether (MTBE) is a gasoline additive³ that induces neuro- and respiratory toxicity; 1,4-dioxane is a common industrial solvent and probable carcinogen; and perfluorooctanoic acid (PFOA), an extensively studied per- or polyfluoroalkyl substance (PFAS), is a global surfactant and suspected mutagen. These CECs and other species mentioned in this thesis are listed in Table A.1 with their respective formula and structure.

Some liquid and solid pathways for CECs are illustrated in Figure 1.1. CECs can perpetuate through mechanisms such as contamination, direct releases, infiltration, and leaching. When water or wastewater treatment plants do not address CECs with sufficient centralized treatment, these CEC pathways demonstrate the inherent circular nature of the water cycle and how CECs can accumulate over time. Overall, conventional water treatment systems are inadequately adapting to the presence of CECs and new classes of micropollutants, such as PPCPs and PFASs.

²At one point, over 60% of superfund sites on the EPA's National Priorities List were contaminated with TCE

³MTBE was prevalent throughout California due to groundwater contamination from leaky underground storage tanks. Santa Monica, the first to shut off its faucets, successfully sued major oil & gas companies for a \$423M settlement.

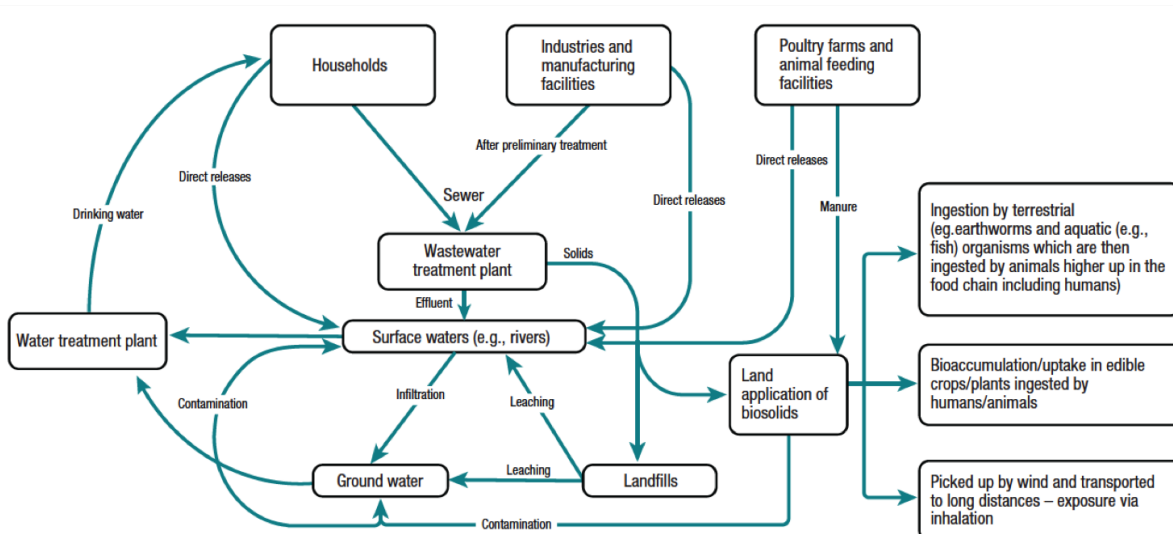


FIGURE 1.1: CEC pathways in the water cycle and associated solids (Petrović, Gonzalez, and Barceló, 2003).

1,4-dioxane and PFASs

Unexpected trends for 1,4-dioxane were evident in the EPA’s Unregulated Contaminant Monitoring Rule (UCMR) 3 data including: 1,4-dioxane is detected slightly more often (factor of 1.25, $p < 0.0001$) in groundwater than in surface water, which is likely to be more diluted ($p < 0.0001$); it is more common in large treatment systems relative to small systems (factor of 2.18, $p < 0.0001$); and it is highly correlated with the detection of chlorinated compounds, particularly 1,1-dichloroethane (odds ratio of 47, $p < 0.0001$) and 1,1,1-trichloroethane (1,1,1-TCA), manifesting its use as a stabilizer for chlorinated solvents (Adamson et al., 2017). Due to its high mobility and miscibility in water, 1,4-dioxane can spread faster and further downgradient than the associated chlorinated solvent. As illustrated in Figure 1.2a, 1,4-dioxane is detected above the EPA health advisory limit of 0.35 ppb at many U.S. sites⁴.

⁴Ann Arbor, one of these sites, is seeking EPA superfund status. Michigan’s regulatory body, the Michigan Department of Environmental Quality, lowered the 1,4-dioxane limit from 85 ppb to 7.2 ppb in 2016 even though the plume was discovered in the 1980s.

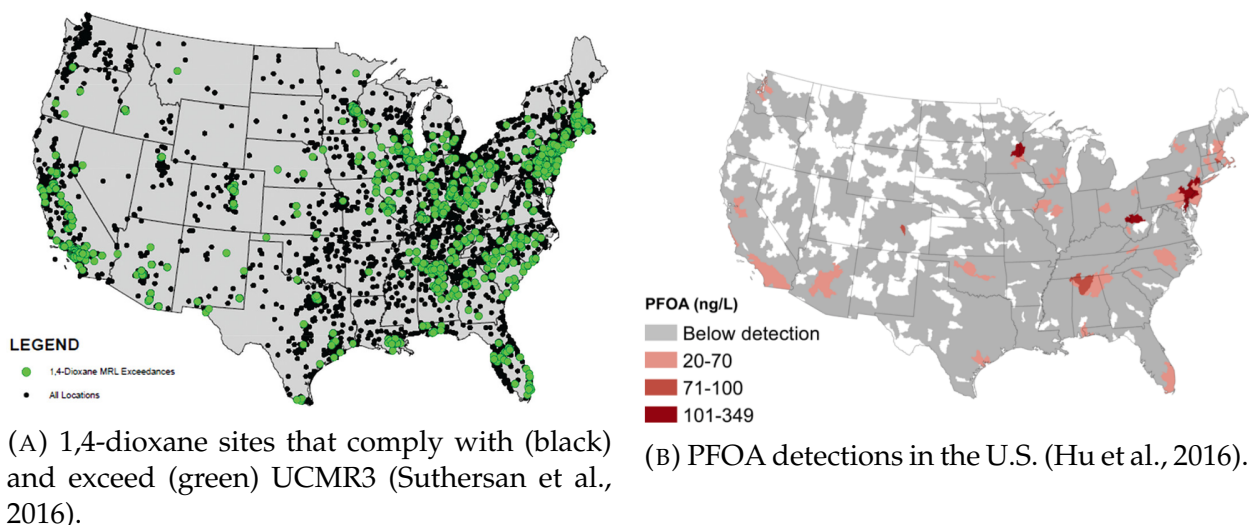


FIGURE 1.2: Survey of 1,4-dioxane and PFOA in U.S. public water supplies using UCMR3 data.

While states permit a wide range of guideline levels for 1,4-dioxane (0.25 ppb in New Hampshire to 77 ppb in Alaska), the limits of detection and quantification begin to overlap as these response, notification, and reporting levels have decreased over time, as indicated in the EPA's six-year reviews authorized by the Safe Drinking Water Act (EPA OW, 2016). Even prominent environmental and regulatory states like California have notification levels slightly higher than the one-in-a-million cancer risk level suggested by the EPA (1 ppb vs. 0.35 ppb), further demonstrating the difficulty in surveilling 1,4-dioxane at trace concentrations.

On the other hand, PFOA is not as pervasive as 1,4-dioxane, as shown in Figure 1.2b. Yet, PFOA is nearly ubiquitous in our blood streams due to bioaccumulation (Olsen et al., 2008). In fact, PFOA and perfluorooctanesulfonic acid (PFOS), a rife stain repellent and another long-chain PFAS, are found at average blood plasma concentrations of 3.4 $\mu\text{g}/\text{L}$ and 14.5 $\mu\text{g}/\text{L}$, respectively, while both have an EPA provisional health advisory limit of 0.07 $\mu\text{g}/\text{L}$. The ubiquity of PFOA and PFOS implies that while pervasiveness is important, environmental pathways and associated toxicity must always be considered, which are typically poorly understood. After extensive toxicity

assessments, chemical companies began to phaseout PFOA and PFOS production and replaced them with GenX chemicals and perfluorobutanesulfonic acid (PFBS), respectively. GenX byproducts⁵ (2,3,3,3-tetrafluoro-2-(heptafluoropropoxy)propanoic acid and heptafluoropropyl 1,2,2,2-tetrafluoroethyl ether), perfluorobutanoic acid (PFBA), PFBS, and other short-chain PFASs appear to have lower bioconcentration factors and biotransformation half-lives than PFOA and PFOS but, their persistent, bioaccumulative, and toxic properties, such as biomagnification, remain uncertain (Gebbink, Assel-donk, and Leeuwen, 2017; Newton et al., 2017).

Overall, 1,4-dioxane and legacy PFASs are prominent CECs and demonstrate decreasing trends in concentration and detection frequency over time. However, these and other anthropogenic compounds must be considered individually and collectively among other constituents in relevant water matrices. As these toxicokinetic studies are performed, some water supply systems may need improved treatment techniques (Glassmeyer et al., 2016). Thus, the inability to swiftly identify and accurately assess CECs prior to entering the environment requires **robust treatment technologies**.

1.2 Advanced Treatment Technologies

Water treatment technologies can be divided into categories based on the mechanism of removal and type. Physical, chemical, and biological methods include filtration and sedimentation, precipitation and oxidation, and catalytic microorganisms, respectively. Initial centralized wastewater treatment focused on preserving aquatic life by minimizing eutrophication through the management of nutrients (N, P) and

⁵The suspected mutagens were under scrutiny starting in 2017 in North Carolina's Cape Fear River, Wilmington's drinking water source, leading to a lawsuit against fluorochemical-producing Chemours, a DuPont spin-off. Meanwhile, in Wilmington, record-breaking 24 in rain from Hurricane Florence caused 35 casualties—with climate change the culprit—and initial indemnity worth \$13M. How did the floods further exacerbate the pollution problem? In NC, GenX has an initial health goal of 140 ppt for drinking water.

other water quality parameters, such as dissolved oxygen (DO). The environment provides many wastewater mitigation methods like sand filters and microbes. Common biochemical operations, such as bioflocculation, activated sludge, and anaerobic digestion, are among early wastewater operations that can cost-effectively recover resources while preserving the environment (Grady Jr. et al., 2011). These operations are used in technologies that have slowly evolved in the past century due to their robustness and established effectiveness. In fact, standard wastewater treatment plants are still equipped with settling, aeration, and contact tanks. Some of these technologies are coupled to other operations to further enhance multipurpose mechanisms and resource recovery, resulting in complete treatment trains.

Most modern facilities use some combination of macroscopic and microscopic treatment (filtration and disinfection) although other simple techniques, like air stripping, can economically remove CECs, such as MTBE and halogenated organics (Stocking et al., 2008). Current advanced water treatment trains include microfiltration/reverse osmosis (MFRO), packed bed bioreactors, ion-exchange membranes, membrane bioreactors (MBRs), moving bed biofilm reactors (MBBRs), granular activated carbon (GAC), and advanced oxidation processes (AOPs).

1.2.1 Filtration

Membrane filtration is a predominantly physical process and is usually classified by its pore size and molecular weight cut-off (MWCO). Common classes are microfiltration (MF, pore size $\geq \approx 0.1 \mu\text{m}$), ultrafiltration (UF, pore size $\approx 0.1 \mu\text{m}$ –10 nm), nanofiltration (NF, ≈ 1 –10 nm), and reverse osmosis (RO) (Greenlee et al., 2009). MF removes most microorganisms and suspended particles, and is usually used in series with UF, NF, or RO. UF (MWCO ≈ 2000 –500 000 g/mol) removes large proteins, viruses, and colloids whereas NF (≈ 250 –2000 g/mol) removes dissolved organics and divalent

ions. For better efficiency and higher quality effluent, dual membranes using either MF or UF with RO are typically used (del Pino and Durham, 1999).

Reverse Osmosis

RO uses a semipermeable membrane similar to filtration but, RO transport is defined by absorption, diffusion, and desorption. Consequently, though RO can effectively remove monovalent ions in desalination, certain CECs can diffuse into the bulk permeate and still persist at trace concentrations. All things considered, desalination roughly costs $\$1/\text{m}^3$ ($\$3.80/\text{kgal}$) for seawater and $\$0.60/\text{m}^3$ ($\$2.25/\text{kgal}$) for brackish water (Zhou and Tol, 2005).

Inherently, RO is energy intensive and produces concentrate as reject water. Primary energy use is pump power, which is directly related to feed pressure and flow rate, and can be improved by recovering energy from the pressurized concentrate stream (Wilf and Klinko, 2001). Energy efficiency can be optimized by RO recovery, which is defined as the ratio of permeate flow rate to feed flow rate (permeate plus concentrate). RO recovery is a function of influent water quality, such as alkalinity, liquid temperature (T_ℓ) and total dissolved solids (TDS), and concentrate disposal options. Brine disposal costs $\$0.21$ – $\$2.10/\text{kgal}$ and can be performed by deep-well injection, land application, evaporation ponds, crystallizers, and pipeline to ocean, sewer, or other dilutable discharges (Raucher and Tchobanoglous, 2014). Filtration techniques have fixed maintenance costs since membranes must be disposed of and replaced due to the fouling propensity of water. However, in some cases, such as MBRs, MBBRs, and GAC, the microorganisms are favorable.

Membrane Bioreactor

MBRs combine activated sludge with filtration. MBRs can operate at higher mixed liquor suspended solids than settling-based bioreactors, require less energy than MFRO systems, and have small-footprint retrofits, making them very attractive alternatives to conventional wastewater technology (Judd and Judd, 2006). Due to coarse bubbling and tangential flow, aerated cross-flow in submerged MBRs provides optimal energy efficiency and mitigates fouling (Le-Clech, Chen, and Fane, 2006). Though backwashing also reduces filter cake and extends filter lifetime, an MBR alternative that enables condensed, continuous biological treatment is the MBBR.

Moving Bed Biofilm Reactor

MBBRs are filter-free, very compact, and very efficient bioreactors. MBBRs minimize treatment plant footprint by maintaining biofilm on packing media with high surface area-to-volume ratio. The lack of backwashing and biomass recycling enables non-cloggable, continuous operation and low maintenance (Ødegaard, Rusten, and Westrum, 1994). MBBRs provide effective nutrient removal but, its main value of biodegradability cannot address CECs. While MBRs can remove CECs to some extent (Radjenović, Petrović, and Barceló, 2008), another cost-effective biophysical solution is GAC.

Granular Activated Carbon

GAC is a simple, stable, and easily applied technology that is well-established for bulk and trace organic removal. GAC enhances size exclusion and biomass similar to MBRs but, GAC transport is primarily controlled by adsorption. Organics, like MTBE and other CECs, such as short- and long-chain PFASs (McNamara et al., 2018), can be removed with enough GAC and contact time. However, GAC efficiency is significantly

influenced by influent water quality, particularly the presence of natural organic matter (NOM) and other synthetic organic compounds (Creek and Davidson, 2008). Though NOM can result in fouling, GAC has the intrinsic ability to be encourage the colonization of microorganisms similar to MBBRs, making it biologically activated carbon (BAC) (Weber Jr., Pirbazari, and Melson, 1978). Nonetheless, GAC encourages microbial growth, results in desorbed bacteria (Leilei, Wei, and Tao, 2008), and must precede a process that inactivates potential pathogens.

1.2.2 Disinfection

The final stage of the water treatment train is disinfection. Disinfection is responsible for the neutralization of microorganisms and must ensure effluent compliance. By damaging a pathogen's genomes and structure, physical or chemical processes can denature proteins, rendering the pathogen inactive.

Chlorination

Free chlorine (Cl), chlorine dioxide (ClO_2), and hypochlorite (ClO^-) are very cost effective, provide residual doses, and have modest electrochemical oxidation potentials (V_{ECO}), which is defined as the potential of a species' affinity for electrons. However, chlorination is ineffective for many CECs, including 1,4-dioxane, PFASs, and Cryptosporidium. Additionally, chlorination can produce hazardous disinfection byproducts (DBPs), such as trihalomethanes (THMs) and haloacetic acids (HAAs).

Advanced Oxidation Processes

AOPs destroy trace organics by producing reactive oxygen species (ROS), such as hydroxyl radicals ($\bullet\text{OH}$), in situ. Due to their high V_{ECO} , ROS reduce most CEC concentrations ($c = \text{mg/L}$ or part-per-million (ppm); $[c] = \text{mM}$ or $\#/\text{cm}^3$) below mandatory

limits and can mineralize organics into CO₂, H₂O, and inorganic salts. Taking into consideration their diffusivity (D) or transmittance (UVT), rate constants (k) and reaction rates ($\frac{\partial c}{\partial t} = f(k)$) with target compounds, and cost (\$/kgal), the most effective AOPs usually use combinations of ultraviolet (UV) radiation, hydrogen peroxide (H₂O₂), or ozone (O₃) though emerging technologies include boron-doped diamond electrodes (Carter and Farrell, 2008), hydrodynamic cavitation (HDC), photocatalytic titanium oxide (UV/TiO₂), and plasma (Gassie and Englehardt, 2017; Miklos et al., 2018). While chemical disinfectants can mineralize recalcitrant pollutants, they and their oxidative DBPs may affect the biological stability of the water.

Ultraviolet Light

UV treatment alone has desirable characteristics because it can produce ROS, directly photolyze contaminants without producing DBPs, and satisfy strict regulatory requirements. UV is created onsite with the most common operating designs involving flow-through banks of low-pressure (LPUV) or medium-pressure (MPUV) mercury (Hg) lamps. Vacuum-UV (Gonzalez et al., 2004), UV-light emitting diodes (Chen, Loeb, and Kim, 2017), polychromatic, and other configurations have also been investigated. Although some microorganisms, such as *Acanthamoeba*, can be resistant, LPUV systems produce negligible DBPs and can provide greater than one-in-a-million (6-log) inactivation for *Cryptosporidium*, *Giardia*, and many other pathogens (Hijnen, Beerendonk, and Medema, 2006). It can also photolyze certain CECs including N-nitrosodimethylamine (NDMA), a probable carcinogen, and its precursors (Sedlak and Kavanaugh, 2006). UV dose, or fluence (H), fundamentally depends on the fraction of light absorbed (f), quantum yield (Φ), molar attenuation coefficient (ϵ), photon flux (I_0), and absorbance (A) where $A = \ell \sum_i \epsilon_i c_i$ (ℓ = path length).

When coupled to other oxidants, UV and UV-produced ROS further amplify •OH

production. For example, UV enhances the effective oxidation of Cl (Fang, Fu, and Shang, 2014), ClO^- (Wang, Bolton, and Hofmann, 2012), H_2O_2 (Stefan and Bolton, 1998), O_3 (Zwiener and Frimmel, 2000), and TiO_2 (Vescovi, Coleman, and Amal, 2010). Also, different wavelengths (λ) across the germicidal UV spectrum significantly impact dose, efficiency, and compatibility. For instance, UVA ($\lambda_{max} = 350 \text{ nm}$) photocatalysis of TiO_2 is an order of magnitude more effective than UVC ($\lambda_{max} = 254 \text{ nm}$) photolysis of 3 ppm H_2O_2 (Coleman et al., 2007b). Regardless, due to UV's focus on photolysis and heavy dependence on UVT, UV-based disinfection influent must be clear (high UVT) to be efficient.

Hydrogen Peroxide

The cheap and simple anthraquinone process enables mass production of H_2O_2 (Campos-Martin, Blanco-Brieva, and Fierro, 2006). H_2O_2 is rarely used as a stand-alone technology because it is a weaker antiseptic than Cl. If UV is supplemented to longer-lived ROS, such as H_2O_2 , radicals can penetrate then excite, photolyze, or react with trace CECs in the bulk wastewater. This process ($\text{H}_2\text{O}_2 \xrightarrow{\text{UV}} 2\text{HO}^\bullet$) is a function of H_2O_2 photoproperties and UV fluence ($\sim \text{mJ}/\text{cm}^2$).

H_2O_2 is usually used in conjunction with UV to intensify reactivity, though catalysts with multiple oxidation states, such as iron (Fe), are also used (Bokare and Choi, 2014). Extensively-studied and well-established, UV/ H_2O_2 is the most commercially-implemented AOP with the first system deployed in Gloucester, Ontario in 1992 to remediate, or pump & treat, groundwater contaminated with 1,4-dioxane (Stefan, 2018). UV/ H_2O_2 can effectively destroy CECs, such as MTBE, 1,4-dioxane, other aromatic hydrocarbons, PPCPs, tertiary butyl alcohol, tertiary butyl formate, acetate, and formate (Koubek, 1975; Coleman et al., 2007a; Hofman-Caris et al., 2012; Kommineni et al., 2008a; Wols et al., 2013; Vaferi et al., 2014). Due to advances in experimental,

analytical, mathematical, computational fluid dynamic, and radiative transfer models and techniques, the photochemical kinetics of UV/H₂O₂ systems can be accurately predicted and optimized (Wols and Hofman-Caris, 2012; Bagheri and Mohseni, 2014). While UV-photolyzed H₂O₂ can be energy efficient, H₂O₂ has intrinsically poor UVC absorbance ($\epsilon(\lambda = 254 \text{ nm}) = 18.6 \text{ M}^{-1} \text{ cm}^{-1}$), resulting in low (< 10%) turnover, and if LPUV lamps are used, high H₂O₂ concentrations ($c = 5\text{--}20 \text{ ppm}$) are required (Miklos et al., 2018). However, the higher concentrations needed to achieve adequate ROS production require that residual H₂O₂ must be quenched. Furthermore, higher H₂O₂ dose increases the likelihood of self-scavenging, which affects ROS yield (Buxton et al., 1988). Thus, UV/H₂O₂ can efficiently mineralize organics but, if UV transmittance or H₂O₂ reactivity are too low, O₃ can be used.

Ozone

Ozonation (only O₃) is considered an AOP on its own since it can directly oxidize and produce various ROS, such as •OH and HO₅⁻. For example, O₃ and UV/H₂O₂ provide comparable destruction of taste and odor compounds and volatile organics (Antonopoulou et al., 2014). O₃ is an oxidant and disinfectant that is highly selective (Calderara, Jekel, and Zaror, 2002), allowing it to diffuse into the bulk, and directly or indirectly oxidize trace CECs, (Merényi et al., 2010b; Merényi et al., 2010a). Also, O₃ used prior to GAC encourages microbial growth and yields effective BAC due to ROS initiators from O₃-based AOPs. The microorganisms can reduce the loading on the GAC, assist in water treatment, and improve overall water quality.

In water, some dissociation and transformation products of O₃ are more potent oxidants (high V_{ECO}) than O₃ itself (Peleg, 1976). Though these ROS alone are limited against certain constituents such as *Cryptosporidium* (Crittenden et al., 2005), O₃ used in tandem with other AOPs can effectively augment ROS production and CEC

decomposition pathways (Kwon et al., 2012). Similar to UV-AOPs, O_3 can be complemented by catalysts, such as Co (Pines and Reckhow, 2002), and O_3 is commonly coupled to H_2O_2 , also known as the peroxone process. Peroxone is energy efficient, can cost a third of the price of UV/ H_2O_2 (Safarzadeh-Amiri, 2001), and can enhance the biodegradability of refractory organics, such as 1,4-dioxane, 1,1,1-TCA, TCE, and MTBE (Adams, Scanian, and Secrist, 1994; Mitani et al., 2002; Eberle, Ball, and Boving, 2016). For most contaminants of concern, the optimal H_2O_2/O_3 ratio (mol:mol) is 0.3–0.6 with $c_{O_3} = 1\text{--}20$ ppm (Suh and Mohseni, 2004; Miklos et al., 2018). Peroxone improves ozonation by maintaining AOP mechanisms throughout O_3 dosage whereas ozonation alone would eventually transition to a less-effective first-order reaction rate region (Fischbacher, Lutze, and Schmidt, 2018). In O_3 -based systems, R_{ct} indicates the strength of hydroxyl production relative to ozone exposure, which is defined as $R_{ct} = \frac{\int[\bullet OH]dt}{\int[O_3]dt}$. When a H_2O_2/O_3 or O_3 system begins, highly reductive compounds among dissolved NOM rapidly consume O_3 within seconds. As dissolved NOM concentrations decrease, peroxone-based ROS continue to sustain a steady R_{ct} whereas O_3 -based ROS increasingly self-scavenge AOP initiators, including HO_2^- . Consequently, slower kinetics are abruptly triggered, drastically decreasing then stabilizing R_{ct} for ozonation only.

Typical R_{ct} values for ozonation are in the range $10^{-9}\text{--}10^{-8}$ while peroxone yield is up to two orders of magnitude greater than that (Elovitz, Gunten, and Kaiser, 2000). Also, R_{ct} is contingent upon influent water quality, particularly $\bullet OH$ scavengers that can affect energy efficiency by an order of magnitude. Even though R_{ct} is much higher in peroxone, very competitive O_3 reactions limit H_2O_2 -aided AOP pathways, corresponding to $\bullet OH$ improvements up to $\approx 30\text{--}40\%$, regardless of O_3 dose (Hübner, Zucker, and Jekel, 2015). Given the relatively low V_{ECO} of H_2O_2 and the desire to move away from chemical storage and transport, an alternative to H_2O_2 is UV combined with

O₃, or photolytic ozonation. Both UV and O₃ can be produced by air plasma formation. UV/O₃ is a multi-AOP alternative that can provide thermalizable H₂O₂ and other effective ROS, such as O(¹D), O(³P), and O₂^{-•} (Sonntag, 2008; Gottschalk, Libra, and Saupe, 2010). UV/O₃ are more energy efficient than UV/H₂O₂ in terms of effective •OH yield and can surpass peroxone in photolytic water matrices (Crittenden et al., 2012). Regardless of these additional AOP mechanisms and decomposition pathways, AOPs are inadequate for some CECs, such as PFOS (Schröder and Meesters, 2005), and can produce hazardous DBPs.

Byproducts

The objective of advanced oxidation is to fully mineralize recalcitrant organics. However, transformation products and other intermediates could be more ecotoxic or pathogenic than their parent compounds (Illés et al., 2014). While ubiquitous NOM can assist in or dominate redox by regenerating ROS, NOM reactions with disinfectants can produce DBPs (Peyton and Glaze, 1988; Buffle and Gunten, 2006). For example, AOPs combined with naturally occurring halogens and NOM can produce NDMA, chlorate, and bromate (Richardson et al., 2003; Le Roux, Gallard, and Croué, 2012; Gerrity, Rosario-Ortiz, and Wert, 2018). Found worldwide, DBPs possess CEC qualifications and these DBPs include THMs, HAAs, and nitrosamines (Richardson et al., 2007). While UV can photolyze NDMA (Stefan and Bolton, 2002), peroxone can mitigate bromate (Acero et al., 2001), and most DBPs exhibit weak toxicity, unregulated DBPs must be assessed individually and collectively in relevant water matrices.

Overall, synergistic, multi-radical AOPs can efficiently inactivate and mineralize while minimizing DBP production. Although it consumes roughly 25% more energy than ozonation alone, peroxone enhances the effective oxidation of O₃ and reduces bromate formation by 70% (Katsoyiannis, Canonica, and Gunten, 2011). On the other

hand, UV/H₂O₂ uses an order of magnitude more energy than O₃ but, it provides accredited pathogen inactivation and is comparable in energy consumption for photosusceptible CECs, namely NDMA. Advanced physical, chemical, and radiative treatment techniques each have their benefits and disadvantages. Regulatory agencies must create a framework for verified AOP technologies and methods, monitored CECs and byproducts, and universal metrics of success.

1.3 Water Reuse

Water recovery, or recycling, involves repurposing treated wastewater effluent. Water reuse builds resilience and also protects the environment.

Advanced treated water (ATW) can be divided into non-potable and potable reuse. Represented by the purple pipe system, non-potable reuse directly applies ATW for irrigation, cooling, other industrial processes, and environmental remediation. ATW use in drinking water can be further classified into direct potable reuse (DPR) and indirect potable reuse (IPR). DPR injects ATW directly into either distribution systems or the influent raw water supply of drinking treatment plants. DPR has been increasingly considered to alleviate overstressed aquifers, with the world's first DPR facility deployed in Windhoek, Namibia in 1968 (Tchobanoglous et al., 2011). In addition to mitigating stressors, DPR enables environmental stewardship and the diversification of water portfolios. For example, instead of inter-basin transfer, DPR could stabilize, protect, and enhance the water supplies and ecosystems for both Southern California and San Joaquin Valley while significantly decreasing local pollution and energy required for transporting water (Schroeder et al., 2012).

On the other hand, IPR sends ATW to an environmental buffer for natural and artificial recharge via infiltration through surface spreading or dual membrane injection with wells (Asano and Cotruvo, 2004). In addition to the aquifer's innate distribution

capability, IPR may provide psychological and esthetic benefits and may be cheaper than surface water reservoirs, which is subject to evaporation and pollution including taste & odor problems from aquatic microorganisms. However, CECs, such as artificial sweeteners, can persist in soil aquifer treatment, questioning its long-term sustainability (Scheurer, Brauch, and Lange, 2009). Other forms of water reclamation include ocean discharge reuse (ODR) and zero liquid discharge (ZLD). Ocean outfalls, composed of brine diluted in stormwater or ATW, could have a substantial impact on adjacent coastal ecosystems (Occiano and Strayer, 2012) yet, if this water is recovered with ODR, it is capable of providing all municipal needs for one-fifth of California by 2020 (Raucher and Tchobanoglous, 2014). ZLD is a type of decentralized reuse that fully recycles water while making biosolids and salts suitable for disposal or recovery. Overall, these reuse methods provide various access to decentralized reclaimed water.

Water providers will consider expanding reuse initiatives depending on their current water portfolio. Excessive groundwater pumping and drought contributed to catapulting California to the forefront of water reclamation in the U.S. To protect and augment depleted aquifers, California deployed IPR for saltwater intrusion barriers in the 1950s and groundwater recharging in the 1960s (Todd, 1974). Although sustainability resolutions have proliferated since then due to concern for increasingly unreliable and unpredictable sources, IPR expansion attempts in the 1990s stagnated as public opinion⁶ waned. Thus, for water reuse to succeed, multiple disciplines must unite to develop a convincing reuse framework.

1.3.1 Framework

Though this work focuses on the technical problem of scaling plasma-based water treatment, understanding and promoting well-considered reuse policy is critical to the

⁶DPR opponents and the political climate produced a powerful phrase: toilet to tap

success of this work.

While mostly technical, water reuse framework should include regulatory considerations, sustainability strategies, and public outreach. Decision makers and taxpayers need information on source control, treatment, performance assessment, monitoring, operation and maintenance (O&M), certification, and resilience (Mosher and Minton, 2016). When compiled, these data should be applied to evaluate water portfolio, cost, reliability, energy requirements, and carbon footprint. Combined with techniques such as isotope hydrology, the data should also be used to model resource management so that communities can predict and prepare for replenishment or remediation.

Water reuse is spreading in the U.S. with seven states currently implementing policy pertaining to it (AZ, CA, CO, FL, NM, TX, and WA). Among the world's most aggressive water statutes, California's Title XXII regulations set stringent standards for many CECs and strictly define treatment techniques. AZ, NM, CO, and states exploring reuse get to learn from early adapters like CA and TX (NWRI, 2016; Mosher and Vartanian, 2018; WateReuse CO, 2018). Just as crucial, resource recovery and utilities of the future are promoted by key organizations, such as Water Environment Federation (WEF), WateReuse, National Water Research Institute (NWRI), American Water Works Association (AWWA), and National Association of Clean Water Agencies (NACWA) (NACWA, WERE, and WEF, 2013).

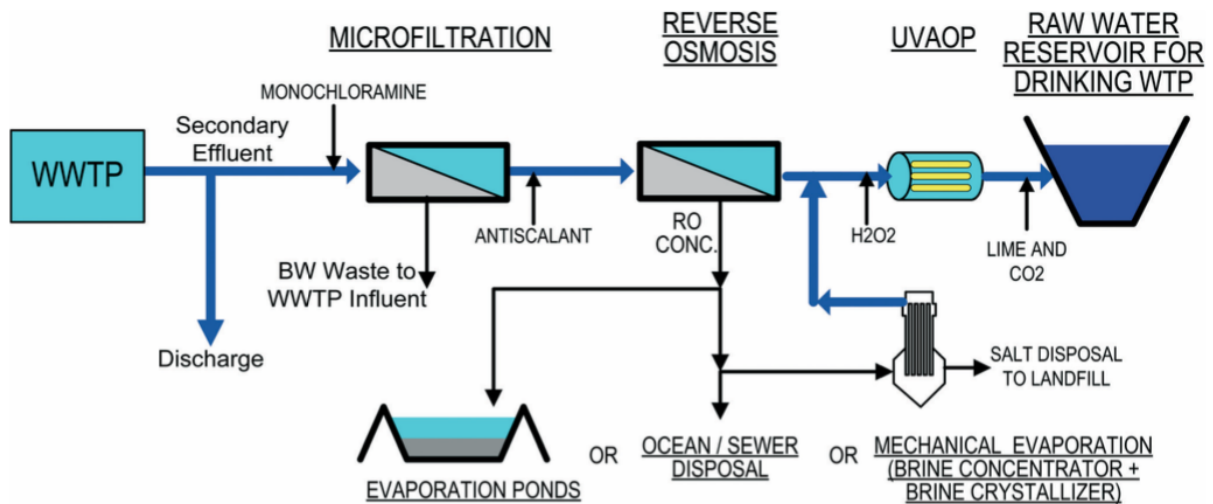
Use of existing resources (in-lieu replenishment), public outreach, and projects that relieve disadvantaged communities should be strongly encouraged. For instance, public health surveillance can assess DPR efficacy by using existing public health-related data to prevent and control disease (Soller et al., 2017). Concern for disease and privacy need to be taken seriously and communication is critical. Transparency and public awareness were key to the success of the 2017 AZ Pure Water Brew Challenge where people enjoyed and learned about beer made with recycled water. Nevertheless, the

WateReuse Research Foundation (WRRF) has a comprehensive DPR guide that discusses most of the above elements (WateReuse et al., 2015).

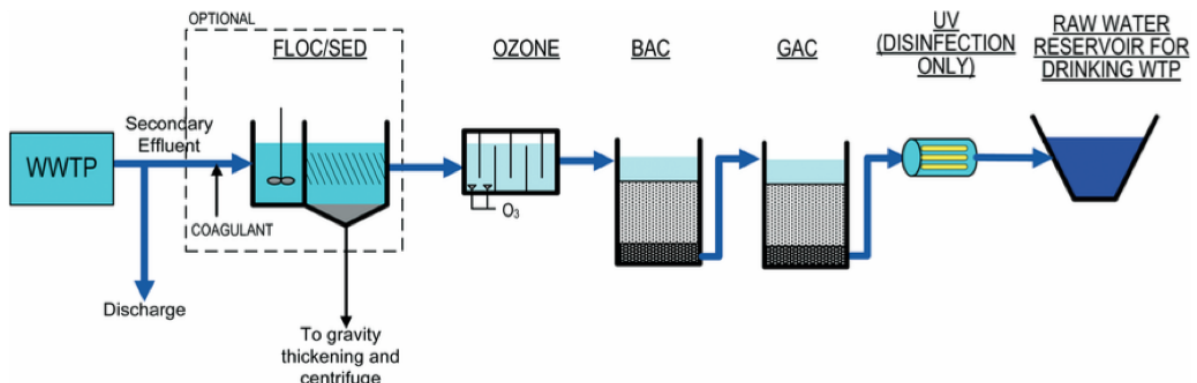
Assuming CECs continue to infiltrate water supplies and toxicity assessments remain difficult, there is an urgent public health need, especially for DPR, to actively identify and monitor CECs, such as organic and inorganic chemicals, radionuclides, microbials, precursors, and transformation products, mainly DBPs. Therefore, treatment technologies must be coupled with one another to minimize DBPs, maximize energy efficiency, and comply with regulations.

1.3.2 Reuse Treatment Trains

Each reuse application has site-specific challenges due to finances, objectives, regulations, and public acceptance. As a result, IPR and DPR treatment trains are diverse, as depicted in more than 20 facilities around the world (Gerrity et al., 2013). Though everyone has different models, the most vetted configurations have multiple barriers for various refractory toxicants and pathogens through a combination of filtration (RO or GAC) and disinfection. The dual membrane approach, illustrated in Figure 1.3a, is the gold standard in CA and the international community. MFRO has excellent performance but, it yields brine, which can be difficult and costly to dispose of. MFRO is usually coupled to UV-based AOPs to ensure trace organics and pathogens are addressed but, other AOPs are considered. On the contrary, O₃-induced GAC, as shown in Figure 1.3b, provides similar trace CEC removal and is gaining traction in the eastern U.S., particularly Virginia. Given that O₃ encourages microbial growth, the first GAC is biologically enhanced with O₃ then sent through another GAC before UV disinfection, which ensures desorbed pathogens from the GACs are inactivated. Since O₃ is ineffective against nitrosamines, BAC is a critical mitigation step.



(A) MFRO-based treatment train.



(B) GAC-based treatment train.

FIGURE 1.3: Common MFRO- and GAC-based treatment trains for potable reuse (Schimmoller, Kealy, and Foster, 2015).

RO- and GAC-based treatment trains can be implemented anywhere and provide excellent organic removal though neither can remove all CECs below detection limits. Treatment train selection is primarily based on organic removal and depends on many site-specific factors including influent water quality, effluent goals, cost, geography, type of potable reuse, and public perception. Regardless of which treatment train is picked, its effectiveness must be quantifiable.

1.4 Metrics of Success in Water Reuse

Treatment train selection for reuse is predominantly determined by influent water quality, which can be gauged with macroscopic and microscopic indicators, such as pH, T_ℓ , TDS, and contaminant concentrations. The goal of water reuse, particularly AOPs, is to ensure sufficient mineralization, which can be fundamentally expressed by $C_aH_bO_cN_d + (a + \frac{b}{4} - \frac{c}{2} - \frac{3}{4}d) O_2 \longrightarrow a CO_2 + (\frac{b}{2} - \frac{3}{2}d) H_2O + d NH_3$ where $C_aH_bO_cN_d$ can be any organic. Chemical oxygen demand (COD) indirectly quantifies the organic load by measuring the equivalent amount of oxygen (in ppm), or electrons, that can be consumed by reactions in solution. COD uses a potent oxidant like potassium dichromate ($K_2Cr_2O_7$) that reduces as pollutants are oxidized while excluding nitrification and the reductant (Cr^{3+}) is used as an indirect measurement. Similarly, biochemical oxygen demand (BOD) is the amount of DO needed by aerobic microorganisms to break down organics. BOD measures DO before and after incubation at a constant temperature and time where the EPA-recognized method calls for 5 day incubation at $T_\ell = 20^\circ C$ and is denoted BOD_5 . Useful for evaluating the effectiveness of wastewater plants, BOD is of more significance to food webs than to water quality because of aquatic life's heavy dependence on DO. Both COD and BOD are surrogate methods whereas Total Organic Carbon (TOC) directly measures the organic load. TOC uses acidification, oxidation, and detection and can be measured by either including or excluding inorganic carbon (IC), such as dissolved CO_2 and carbonic acid salts. The former, known as the TC/IC method, involves measuring the inorganic and total carbon (TC) from an acidified aliquot and subtracting the difference to get TOC. Known as the non-purgeable organic carbon (NPOC) method, the latter purges an acidified sample to eliminate the inorganic carbon then oxidizes and measures the remaining NPOC. While TOC is more useful than COD for water reuse due to its accuracy at lower concentrations ($\sim < \text{ppm}$), both TOC and COD are non-specific water quality

indicators that are subject to potential interferences.

Though macroscopic parameters can be useful, water analysis must address specific contaminants, disinfectants, biomarkers and other surrogates. Optimization of customized water treatment can be achieved by kinetic studies performed on water matrices of interest. Especially true for AOPs, kinetic studies are critical to understanding efficacy dependence on treatment pathways, influent water quality, and effluent regulatory requirements (Peyton, 1990). It is possible to elegantly capture reaction kinetics using water quality parameters, such as R_{ct} , inter-calibrated probe reaction rates, and $R_{OH,UV} = \frac{[\bullet\text{OH}]}{H}$ (Hoigné, 1997; Elovitz and Gunten, 1999; Rosenfeldt and Linden, 2007). Nonetheless, water constituents must be accurately measured yet, techniques substantially vary. For example, residual H_2O_2 must be quenched but, it can be measured using titration, spectrophotometric (absorption spectroscopy), fluorescence, and chemiluminescence methods (Brandhuber and Korshin, 2009). Thus, analytical methods must be verified and standardized.

1.4.1 Compliance

Regulations for a given toxicant define the maximum contaminant level (MCL). In order to operate with water, municipalities and industries must obtain a National Pollutant Discharge Elimination System (NPDES) permit. The first and foremost goal of these facilities is to validate that all MCLs in the NPDES permit are in compliance. Otherwise, violators are fined and documented in EPA's Enforcement and Compliance History Online (ECHO) system. If NPDES compliance is in question, contaminant concentrations must be vindicated using standard analytical methods (APHA, AWWA, and WEF, 2017).

The most common separation technique is chromatography, which can rely on adsorption, ion-exchange, partitioning, or size. Typically, a gas or liquid mobile phase

is used to extract water constituents that are sent through a specially crafted column then detected. Depending on unique chemistry and operating conditions, as analyte moves through the column, molecules adsorb and desorb until the mixture is separated by different retention times. The column effluent is sent to different detectors such as UV, reductive amperometric, electron capture, selective ion monitoring, selective thermionic, mass-spectrometric, or flame ionization detectors (FID) (Skoog, Holler, and Crouch, 2018). Gas chromatography (GC) is good for thermally stable compounds such as volatile organics (Hardy and Pollard, 1960; Guiochon and Guillemin, 1990). On the contrary, liquid chromatography (LC) or high-performance LC (HPLC) is helpful for compounds that decompose when vaporized among other things (Barceló, 1988). Instead of using an organic liquid carrier and polymer column in LC, ion chromatography (IC) separates constituents based on their affinity to the ion exchange resin using different neutralizer concentrations, such as potassium hydroxide (KOH). Chromatography of complex water matrices can be difficult since multiple compounds may separate at the same time. Therefore, GC or LC must be coupled to other techniques to further separate and analyze data.

Though FIDs are useful for the detection of organics, GC and LC are typically used with mass spectrometry (MS) to improve performance (Raina and Hall, 2008; Reemtsma, 2001). MS ionizes and deflects the column effluent in a magnetic field, which separates the species based on their charge-to-mass ratios. Usually based on electron impact, MS ionization sources vary and depend on application; for instance, inductively coupled plasma used with MS (ICPMS) is most advantageous for sensitive elemental detection (Pröfrock and Prange, 2012). Regardless, the analytical workhorse is GCMS and can detect food additives, antioxidants, fire retardants, plasticizers, industrial solvents, disinfectants, fecal sterols, polycyclic aromatic hydrocarbons, and pesticides, and endocrine disruptors Barber₂₀₁₂. To improve detection limits of GCMSs

and LCMSs, liquid or solid precolumn technologies, such as headspace (HS) analyzers (Aathithan et al., 2001), sorbents in purge & trap (Ashley et al., 1992) and solid-phase microextraction (Prosen and Zupančič-Kralj, 1999), concentrate compounds from large volumes in order to achieve lower limits. For example, purge & trap GCMS can reach a lower detection limit of 8 ppt for TCE. Furthermore, GCMS and LCMS can be used in tandem with another MS where fragments from the first MS react with inert gas in a collision cell that are then detected in the second MS (Perez et al., 2016; Kuster, Alda, and Barceló, 2006). Ease and speed of analysis, accessible range of compounds, and different degrees of matrix effects must be taken into consideration when determining the right analytical system.

1.4.2 Log-Reduction

Unlike chemical constituents, separation techniques cannot be used to assess pathogen inactivation. The simplest method is counting colony-forming units (CFUs), which estimates the number of viable pathogens in a given sample. CFU/mL is defined in wastewater for well-known pathogens, such as E. Coli. This technique, however, is subject to inconsistency and does not fully assess inactivation. Quantitative reverse transcription-polymerase chain reaction is a sensitive, powerful, and useful tool for analyzing RNA and disease-indicative patterns. This method combined with a good surrogate, such as male-specific coliphage (MS2), can correlate RNA damage and loss of viral infectivity (Freeman, Walker, and Vrana, 1999; Beck et al., 2016).

Pathogen inactivation is typically expressed in logarithmic reduction, which can be expressed as a function of concentration-time (CT) and H (Bolton and Stefan, 2002; Hijnen, Beerendonk, and Medema, 2006). A one- \log_{10} reduction corresponds to 90% inactivation, 2-log is 99%, 3-log is 99.9%, etc. In California IPR, a 12-log reduction in virus, 10-log removal in *Giardia*, and 10-log reduction in *Cryptosporidium* is required.

In DPR, a 9-log reduction for bacteria is highly recommended (WateReuse et al., 2015). For each virus, bacteria, and protozoa, facilities receive inactivation credits depending on the treatment technologies and techniques they use. For instance, the Division of Drinking Water of Californias State Water Resources Control Board allows one-log of virus removal credit for each month the purified water remains in the aquifer (Raucher and Tchobanoglous, 2014). Also, log-reduction can also be used for CECs; pursuant to Title XXII regulations, a 0.5-log reduction in 1,4-dioxane implies sufficient oxidation.

1.4.3 Electrical Efficiency Per Order

The order of reaction rate for a given constituent influences the energy efficiency of the system (Bolton et al., 2001). Zeroth-order decay of a given CEC occurs when contaminant concentration is high relative to the scavengers, resulting in a removal rate proportional to energy use. In this regime, the electric energy per mass (E_{EM}) is defined in Eq. 1.1. For a flow-through configuration, E_{EM} is a function of power (P), flow rate (F), molecular weight (A), and contaminant concentration (c). In batch mode, F is replaced with $F = \frac{V}{t}$ where V is the working volume and t is treatment time.

$$E_{EM} = \frac{P}{F \cdot A \cdot (c_i - c_f)} \xrightarrow{0^{\text{th}} \text{ order}} \frac{P}{V} \frac{1}{k_0} \quad (1.1)$$

On the other hand, in first-order decomposition, kinetics are dominated by the scavengers due to low contaminant concentrations. Subsequently, the electric energy per order (E_{EO}) is defined in Eq. 1.2 as the energy density needed for one- \log_{10} (90%) removal or, the product of the power density ($\frac{P}{V}$) and decomposition time (τ) for one- \log_{10} reduction. Similarly, E_{EM} and E_{EO} are inversely proportional to their respective effective reaction rate coefficients (k_0 and k_1), implying that these parameters should remain constant throughout their respective regions.

$$E_{EO} = \frac{P}{F \cdot \log_{10}\left(\frac{c_i}{c_f}\right)} \xrightarrow{1^{st} \text{ order}} \frac{P}{V} \frac{1}{k_1} \quad (1.2)$$

Since AOPs are usually applied for trace destruction or inactivation, CECs should experience first-order decay. As depicted in Figure 1.4, commercial AOP technologies exhibit a relatively constant E_{EO} across all effective flow rates ($F_{eff} = F \cdot \log_{10} \frac{c_i}{c_f}$). Though peroxone has the lowest E_{EO} , E_{EO} is based on direct energy use and generally does not reflect additional energy demand for chemicals or catalysts. However, auxiliary oxidants, such as H_2O_2 , can be included in E_{EO} by considering them as potential electric energy (Rosenfeldt et al., 2006).

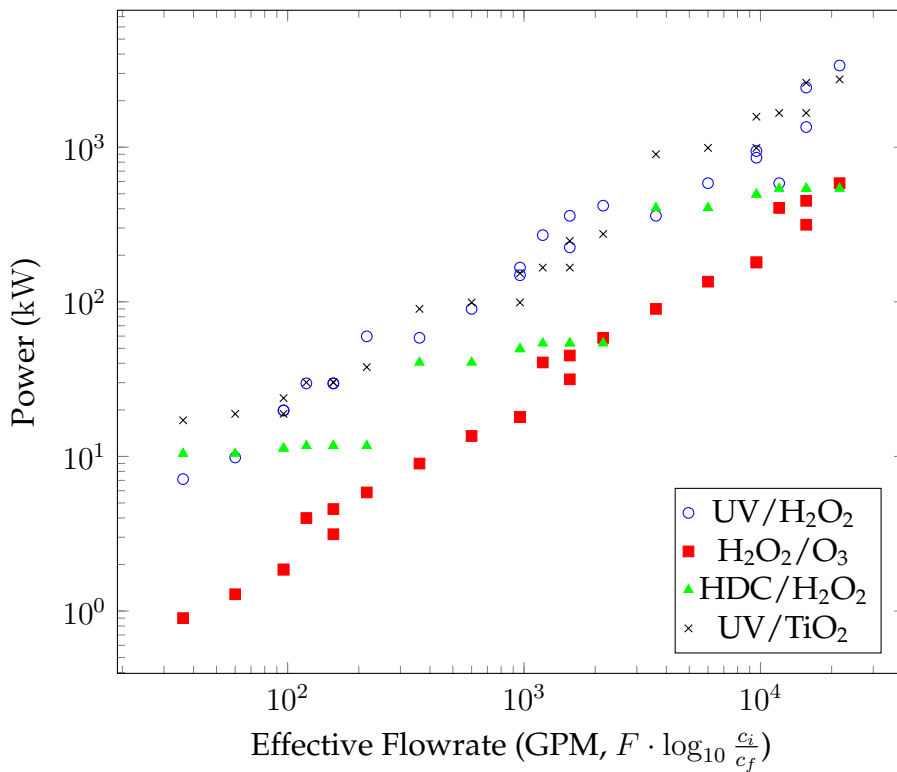


FIGURE 1.4: AOP power requirements for MTBE removal at various flow rates and log-reductions (Kommineni et al., 2008b).

These commercial technologies along with other AOPs are summarized in Figure 1.5. To avoid radical selectivity, only compounds resistant to ozonation and photolysis are shown for O₃- and UV-based AOPs. Combinations of UV, H₂O₂, and O₃ are among the lowest E_{EO} . Differences between AOPs with $E_{EO} < 1 \text{ kWh/m}^3$ are statistically insignificant, implying that various influent water matrices are likely responsible for the slight contrast (Sutherland, Adams, and Kekobad, 2004). Developing technologies, such as plasma and photo-Fenton, are not practical yet but, they provide promise and should be further investigated.

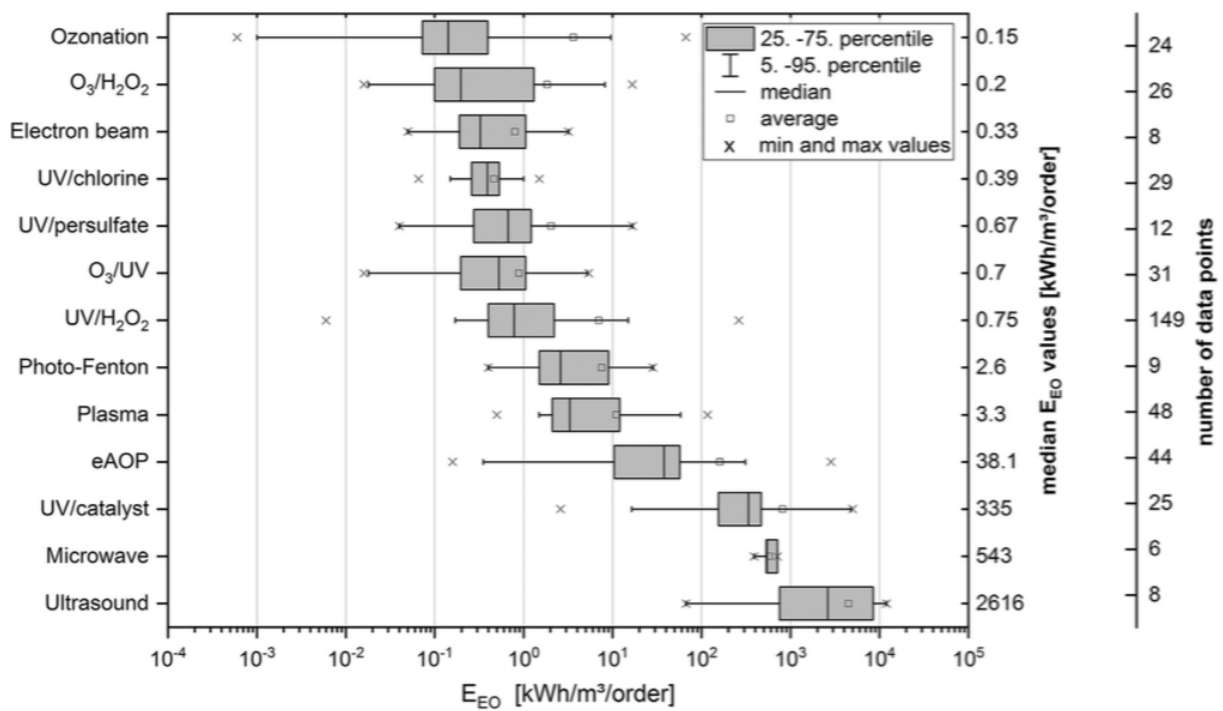


FIGURE 1.5: E_{EO} values for different published AOPs sorted by median value (Miklos et al., 2018).

1.4.4 Cost of Water

The main obstacle to AOP growth remains cost. AOPs are expensive due to required consumables and associated infrastructure. Costs for the commercial AOP technologies from Figure 1.4 are displayed in Figure 1.6. Despite peroxone having the lowest E_{EO} , it is not the cheapest. Also, please note that the data appears stepwise since the study had asked for various log-reductions at $F = 6, 60,$ and 600 gallons per minute (GPM). Nevertheless, technologies become cheaper as they scale, and once built for a given F , some AOPs are easier and cheaper to scale to different log-reductions than others. Also, the difference in amortized cost and the slope of the daily cost should provide insight into the amortization rate.

The cost to collect, treat, and dispose of or distribute water vary significantly. In 2016, neighboring agencies, Water Replenishment District of Southern California and Orange County Water District Groundwater Replenishment System, had replenishment assessments of $\$0.99/\text{kgal}$ and $\$1.23/\text{kgal}$, respectively (WRD, 2016; OCWD, 2017). The difference in cost can be explained by the recharger's size and water portfolio, which depends on basin production percentage, imported water's price, and infrastructural and geological limitations. These costs are much lower than purchasing nearby highly treated wastewater effluent ($\$2.25/\text{kgal}$) since a large portion of their water profile is imported water.

These expenses are typically passed on to homeowners, businesses, schools, retail water customers, and other community members. Since treatment facilities need to operate a business, the average price of water and wastewater in the U.S. are $\$3.38/\text{kgal}$ and $\$4.73/\text{kgal}$, respectively (DOE OEERE, 2017).

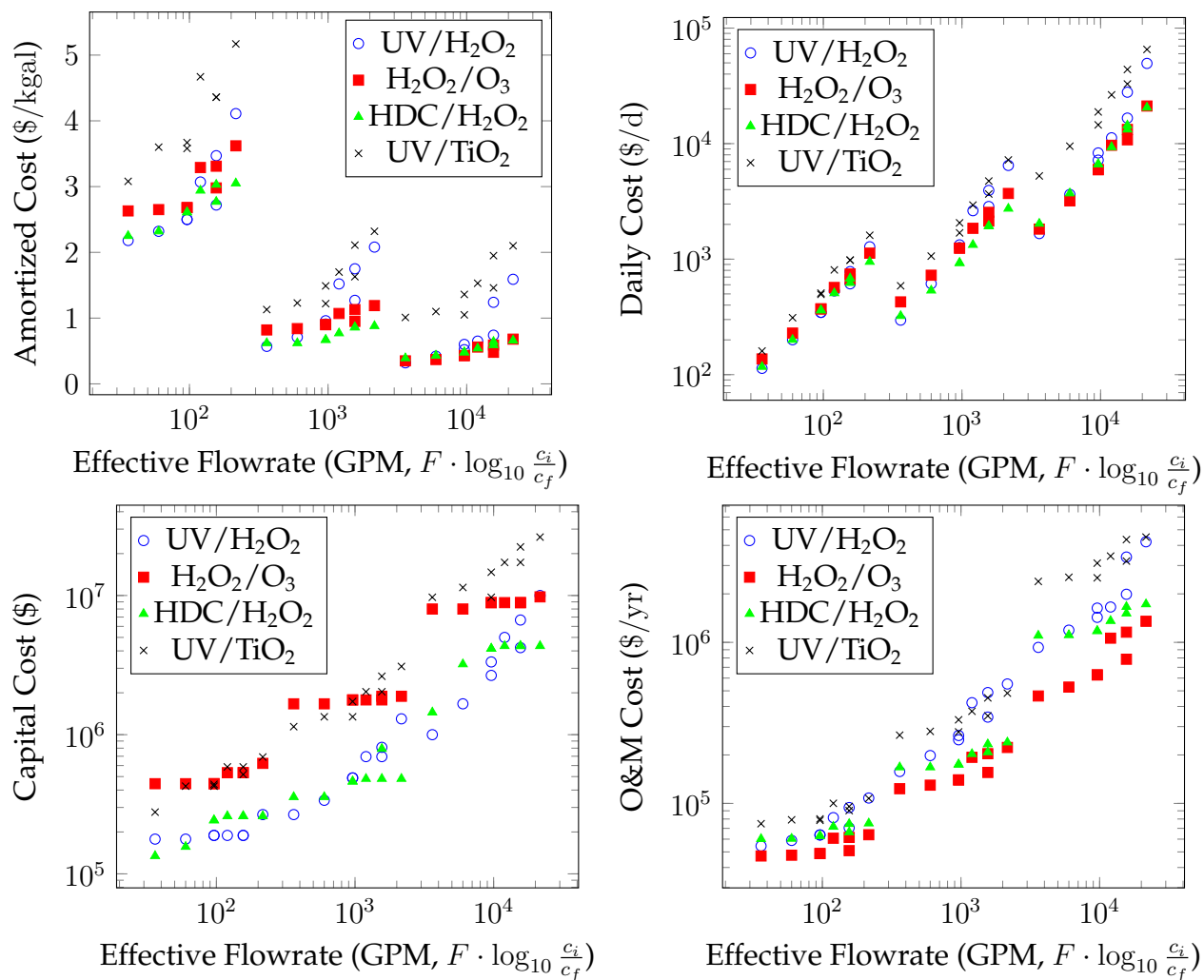


FIGURE 1.6: AOP amortized cost, daily cost, capital cost, and annual O&M cost for MTBE removal at various flow rates and log-reductions (Kommini et al., 2008b).

Triple Bottom Line

The selection and implementation of advanced treatment trains must require environmental and social elements in addition to cost. In triple bottom line accounting, financial, environmental, and social considerations help determine whether the right treatment train was selected without spending excessive funds, energy, greenhouse gas emissions, or other social costs that do not provide a return on societal investment. In DPR, the net present value for all triple bottom line costs suggests that GAC-based treatment is more valuable than all RO-based approaches (Schimmoller, Kealy, and Foster, 2015). Hence, triple bottom line methodology can provide key information to municipalities that are urgently deploying DPR systems to help cope with water shortages.

1.5 Requirements for Future Technologies

The primary barriers to water resilience are inaccurate value of water and persistent contamination. Both can be addressed by societal change but, the latter is heavily hindered by technical challenges. Advanced water treatment trains are highly site-specific and cannot easily adapt to new contaminants. As technologies evolve, they must be able to prepare for forthcoming regulations and minimize the transformation of existing infrastructure.

Given trends in industry, new technologies must be effective, efficient, scalable, versatile, and customizable. Particularly, energy efficiency must improve or remain constant with scale. Combined with figures-of-merit, kinetic studies and pilots will help determine treatment efficacy for custom water matrices. Finally, versatility will address dynamic influent water quality and enable investigations at different parts of the treatment train that help identify the most convenient application. The following

work focuses on determining whether a particular plasma-based system has any or all of these traits.

In an increasingly industrialized society, water's inherent role is more important than ever. Resource mismanagement can cascade into compounding crises and results in socioeconomic and geopolitical tensions. While true for all resources, lack of clean water threatens the security, stability, and sustainability of the world and is the greatest challenge of the 21st century.

Chapter 2

Plasma's Place in the Water World

Plasma is a quasineutral gas composed of charged, excited, and neutral species that exhibits collective behavior.

2.1 The Plasma-Water Interface

The interaction of plasma with water ($\text{H}_2\text{O}_{(l)}$) is an alternative source of AOPs. O_3 and UV are indirect plasma-based technologies where the active species are made out of solution and then, introduced into the water to be treated through fine bubbles or lamp banks, respectively. In plasma water treatment, where plasma is directly exposed to water, ROS and electrons are transported to the plasma-water interface and ultimately solvated into bulk volume (Rumbach et al., 2015). When in or in contact with liquid water, plasma induces various AOPs within the water that amplify ROS production and propagation (Kirkpatrick and Locke, 2005; Locke et al., 2006; Bruggeman and Leys, 2009; Foster et al., 2012; Foster, 2017).

In addition to the cascading and compounding AOP pathways, plasma-water interactions generate local high electric field (\vec{E}), energetic waves (UV, ultrasound, shock-waves), and many additional gas- and liquid-phase radicals, some of which are listed in Table 2.1. The energetic species incident upon the interface, such as UV, electrons, and ions, affect the internal solution through bulk $\bullet\text{OH}$ production. The plethora of physical and chemical processes initiates access to various decomposition pathways for a wide range of CECs, such as PPCPs (acetaminophen, caffeine, ibuprofen, sucralose, etc.), DBPs (NDMA, HAAs), and PFASs (PFOA, PFOS, PFBA) (Mededovic Thagard et al., 2017).

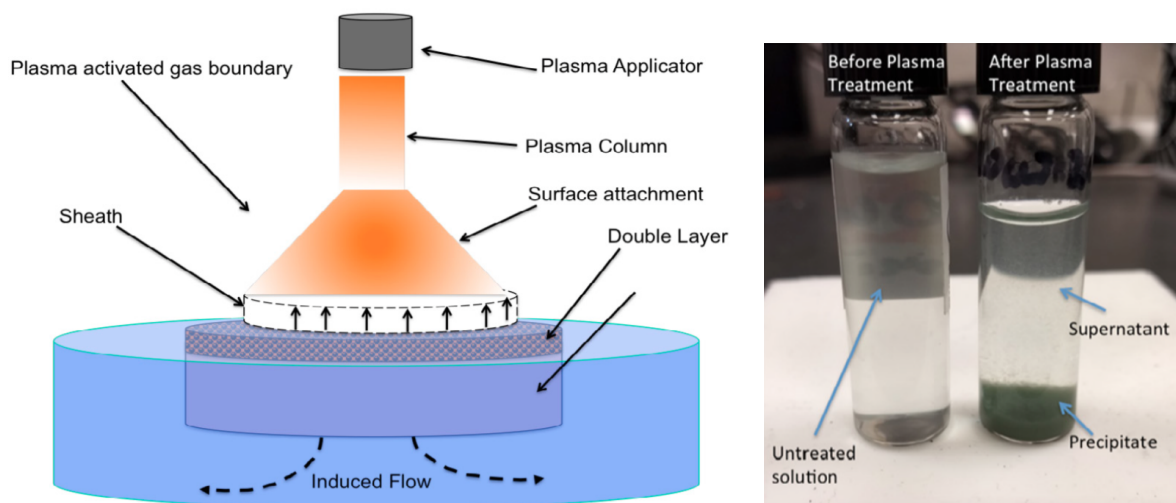
The key driver of plasma-induced reactivity in liquid water is the plasma-liquid interface. Based on the transport across the contact area between the plasma and the water, the solvation rate ultimately determines the treatable throughput; thus, understanding the physics and chemistry of the plasma-liquid interface is key to optimizing plasma-based water treatment systems.

The plasma-liquid interface (depicted in Fig. 2.1a) is the thin, reactive interfacial zone formed between the gas phase plasma and the liquid water. The reactive zone is not a distinct boundary in that it includes the supersaturated water vapor layer above the liquid as well as a thin layer within the liquid where the chemistry can be driven far from equilibrium. Here, species produced in the gas phase can diffuse into solution. These species include reactive oxygen and nitrogen species, such as $\bullet\text{OH}$, H_2O_2 , $\text{O}_2^{\bullet-}$ and N_xO_y .

Reactive oxygen and nitrogen species derived from the gas phase can diffuse into the liquid and drive secondary reactions that can produce $\bullet\text{OH}$ radicals in the bulk liquid. For example, longer-lived species, such as O_3 and H_2O_2 , derived from the plasma can diffuse directly into the liquid, ultimately forming $\bullet\text{OH}$, which in turn can attack contaminants within the bulk. Recombination of $\bullet\text{OH}$ in solution provides

TABLE 2.1: Relevant ROS reaction rate coefficients at standard temperature and pressure (DeMore, 1973; Weinstein and Bielski, 1979; Simonaitis and Heicklen, 1982; Buxton et al., 1988; Suh and Mohseni, 2004; Lietz and Kushner, 2016; Fischbacher, Lutze, and Schmidt, 2018). The coefficients are second-order in units of $\text{cm}^3 \text{s}^{-1}$ unless stated otherwise.

Reaction	Reaction Rate Coefficient
$\bullet\text{OH} + \bullet\text{OH} \longrightarrow \text{H}_2\text{O}_2$	1.7×10^{-11}
$\bullet\text{OH} + \text{}^-\text{OH} \longrightarrow \text{O}^{\bullet-} + \text{H}_2\text{O}$	8×10^{-12}
$\bullet\text{OH} + \text{O}_3 \longrightarrow \text{O}_2 + \text{HO}_2\bullet$	1.8×10^{-13}
$\bullet\text{OH} + \text{H}_2\text{O}_2 \longrightarrow \text{H}_2\text{O} + \text{HO}_2\bullet$	1×10^{-13}
$\bullet\text{OH} + \text{HO}_2\bullet \longrightarrow \text{O}_2 + \text{H}_2\text{O}$	2×10^{-11}
$\bullet\text{OH} + \text{O}_2^{\bullet-} \longrightarrow \text{O}_2 + \text{HO}^-$	1.5×10^{-11}
$\bullet\text{OH} + \text{HO}_2^- \longrightarrow \text{HO}_2\bullet + \text{HO}^-$	1.5×10^{-11}
$\bullet\text{OH} + \text{O}^{\bullet-} \longrightarrow \text{HO}_2^-$	4×10^{-11}
$\text{O}_3 \longrightarrow \text{O}_2 + \text{O}^\bullet$	$3 \times 10^{-6} \text{s}^{-1}$
$\text{O}_3 + \text{HO}^- \longrightarrow \text{O}_2^{\bullet-} + \text{HO}_2\bullet$	1.16×10^{-19}
$\text{O}_3 + \text{HO}_2\bullet \longrightarrow 2 \text{O}_2 + \bullet\text{OH}$	3×10^{-15}
$\text{O}_3 + \text{O}_2^{\bullet-} \longrightarrow \text{O}_2 + \text{O}_3^{\bullet-}$	2.66×10^{-12}
$\text{O}_3 + \text{HO}_2^- \longrightarrow \text{HO}_2\bullet + \text{O}_3^{\bullet-}$	9×10^{-15}
$\text{H}_2\text{O}_2 + \text{HO}_2\bullet \longrightarrow \text{O}_2 + \text{H}_2\text{O} + \bullet\text{OH}$	8.3×10^{-22}
$\text{H}_2\text{O}_2 + \text{O}_2^{\bullet-} \longrightarrow \text{O}_2 + \text{HO}^\bullet + \text{HO}^-$	2.16×10^{-22}
$\text{H}_2\text{O}_2 + \text{H}_2\text{O} \rightleftharpoons \text{HO}_2^- + \text{H}_3\text{O}^+$	$\text{p}K_a = 11$
$\text{HO}_2\bullet + \text{HO}_2\bullet \longrightarrow \text{H}_2\text{O}_2 + \text{O}_2$	2×10^{-12}
$\text{HO}_2\bullet + \text{H}_2\text{O} \xrightleftharpoons{k=1.4 \times 10^{-17}} \text{H}_3\text{O}^+ + \text{O}_2^{\bullet-}$	$\text{p}K_a = 4.8$
$\text{HO}_2\bullet + \text{O}_2^{\bullet-} + \text{H}_2\text{O} \longrightarrow \text{O}_2 + \text{H}_2\text{O}_2 + \text{HO}^-$	$2.68 \times 10^{-34} \text{cm}^6 \text{s}^{-1}$
$\text{HO}_3\bullet + \text{H}_2\text{O} \xrightleftharpoons[k=8.6 \times 10^{-11}]{k=1.8 \times 10^{-15}} \text{H}_3\text{O}^+ + \text{O}_3^{\bullet-}$	
$\text{HO}_3\bullet \longrightarrow \bullet\text{OH} + \text{O}_2$	1.8×10^{15}
$\text{HO}_5^- \rightleftharpoons \text{O}_3 + \text{HO}_2^-$	
$\text{HO}_5^- \longrightarrow \text{HO}_2\bullet + \text{O}_3^{\bullet-}$	
$\text{HO}_5^- \longrightarrow 2 \text{}^3\text{O}_2 + \text{HO}^-$	
$\text{O}_3^{\bullet-} \xrightleftharpoons[k=5 \times 10^{-12}]{} \text{O}_2 + \text{O}^{\bullet-}$	
$\text{O}^{\bullet-} + \text{H}_2\text{O} \xrightleftharpoons[k=3 \times 10^{-15}]{} \text{HO}^\bullet + \text{HO}^-$	



(A) Physical processes prevailing at the plasma-liquid interface. (B) Plasma-driven precipitation.

FIGURE 2.1: Plasma-induced physical and chemical processes in liquid water (Foster et al., 2018).

H_2O_2 . Incident UV can also drive $\bullet\text{OH}$ production in solution via the detachment of HO^- : $\text{HO}^- \xrightarrow{\text{UV}} \text{e}^- + \text{HO}\bullet$ (Attri et al., 2015). The incident electrons solvate only to ultimately decompose water molecules on a microsecond time scale to produce HO^- .

Understanding the effectiveness of a plasma-based water treatment system requires in turn an understanding of the mass transfer rates of the various radicals produced at the interface. This knowledge allows one to assess interfacial contact time and associated power required to deliver the dose. The longer-lived species are primarily transported via four interrelated physical processes. These processes include multi-layer diffusion, electrostatic effects, plasma-induced fluid flow, and self-organization.

As illustrated in Figure 2.1a, one can divide the plasma contact interfacial regions into a number of zones each of which play a key role in transport. Optimizing oxidant transfer from each of these various regions is key to ensuring the delivery of appropriate dose to the liquid. Beyond the plasma glow, a sheath forms at the interface. This sheath regulates the flow of charged species in and out of the solution. Just beyond

the sheath, located essentially at the interface, is an electric field in solution known as the double layer. Here, in solutions with finite conductivity, a voltage drop develops in solution. The associated electric field regulates ion transport in the vicinity of the interface. This field has been shown to affect local rate constants (Joshi et al., 1995). Since the double layer field affects ion flow, it also stratifies chemistry in the interfacial region and can give rise to a pH gradient (Rumbach et al., 2015). Interestingly, the spatial extent of this region depends on water quality parameters, such as conductivity and TDS. It has been shown that the spatial extent of the double layer can greatly exceed the classical Debye-Hückel length scale. Indeed, at high electrolyte concentrations, the length scale can exceed 100 times the classical value (Smith, Lee, and Perkin, 2016). In this regard, the double layer thickness and associated chemistry, such as dose delivery, is water quality dependent.

Charge injection, particularly the sign of the net charge, and pH stratification affect water quality in at least two important ways. Net positive irradiation tends to acidify solution while net electron flux gives rise to solvated electrons and tends to produce more basic solutions (Tochikubo et al., 2014). Charge injection can also affect the oxidation state of metal ions in solution. Reduced metal ions, such as Fe(II) and Mn(II), are also $\bullet\text{OH}$ scavengers. On the other hand, HCO_3^- and CO_3^{2-} , which are $\bullet\text{OH}$ scavengers, affect pH when introduced into the system. Particulates in solution clump when surface charge is neutralized, which is pH dependent. Furthermore, plasma-driven chemical reactions can lead to precipitation and is depicted in an in-house demonstration (Fig. 2.1b). Plasma dose can therefore aid in particulate coagulation.

In short, plasma-liquid interactions are multi-faceted AOPs. Because these plasmas can be generated in ambient air, they do not require vacuum systems or consumables. The only economic driver regarding plasma-based approaches is electric power cost.

As will be discussed later, it will be shown that such systems, if realized, would likely use power levels less than that currently used in conventional AOP systems.

2.1.1 Kinetics

The chief measure of the effectiveness of any water purification method lies in its ability to degrade contaminants to concentrations below their respective MCLs. Often, the evolution of a contaminant in solution under radical attack (e.g. $\bullet\text{OH}$) can be complex, leading to the conversion of the contaminant itself into intermediates that can consume $\bullet\text{OH}$. Indeed, the chain reaction of $\bullet\text{OH}$ with these resulting remnants of the original contaminant is desired as it ultimately leads to mineralization. The rate law for such reactions can be determined experimentally. A general overall rate law capturing these physical processes has been suggested for steady state and completely mixed solution:

$$\frac{d[C]}{dt} = - \sum_i \frac{k_{r_i c} [R_i] [C]}{k_{r_i c} [R_i] [C] + \sum_j k_{r_i s_j} [R_i] [S_j]} = - \frac{\zeta \frac{P}{V} k_c [C]}{k_c [C] + \sum_j k_{s_j} [S_j]} \quad (2.1)$$

where P is the power, V is the volume, and ζ is the system dependent constant, $[R_i]$ is the i^{th} radical molar concentration, $k_{r_i c}$ is the i^{th} radical-contaminant second-order rate constant, $[C]$ is the contaminant molar concentration, $k_{r_i s_j}$ is the i^{th} radical- j^{th} scavenger second-order rate constant, and $[S_j]$ is the j^{th} scavenger molar concentration at steady state (Bolton et al., 2001). Assuming $\bullet\text{OH}$ is the dominant radical, the rate law is simplified to include k_{rc} is the $\bullet\text{OH}$ -contaminant second-order rate constant and k_{s_j} is the j^{th} $\bullet\text{OH}$ -scavenger second-order rate constant. Here, scavengers are defined as any $\bullet\text{OH}$ -consuming compound. ζ is related to the conversion of input power to reactive species that actually participate in decomposition of contaminants. For instance, in photochemical reactors, ζ is a function of the applied power, the power of useful photons emitted, the fraction of photons absorbed by the solution, and quantum yield for

radical production. If the contaminant concentration is high, the decomposition rate exhibits zeroth-order decay and is best described by E_{EM} . If the scavenger concentration is high, the rate equation is first-order and is best suited for E_{EO} . In that case, the pseudo first-order coefficient is:

$$k_{eff} = \frac{\zeta \frac{P}{V} k_c}{\sum_j k_{s_j} [S_j]} \quad (2.2)$$

Note that for E_{EO} (Eqn 1.2), the $\log \frac{c_i}{c_f}$ factor is actually the effective first-order rate coefficient multiplied by $\log e$ and t_{HR} , which is the hydraulic retention time. Nonetheless, it has been shown that the energy efficiency for the removal of a given contaminant can vary widely depending on the initial concentration, initial pH, and volume of contaminated solution (Bobkova and Rybkin, 2015). Thus, it should be kept in mind that these parameters focus on the efficiency to remove a specific compound in a particular water matrix.

Dose

While electric efficiency is a key consideration, the dose required to achieve the desired treatment is equally important, especially for inactivation. Assessing dose in plasma reactors is somewhat difficult in that contributions to decomposition are derived from many reaction pathways, including UV-driven processes. Much emphasis in plasma studies focuses on the formation of reactive species such as $\bullet\text{OH}$, O_3 , H_2O_2 , NO , NO_3^- , and OONO^- (Graves, 2012). While these processes are critical, UV light may also play a key role in contaminant decomposition because UV can directly photolyze contaminants, such as NDMA, and produce ROS similar to conventional UV-based AOPs (Sedlak and Kavanaugh, 2006). More research is required to assess plasma-driven UV photochemistry as it is known that significant percentage of discharge power goes into UV production. The actual amount of UV production varies

with discharge type (Bruggeman et al., 2016). In the case of a UV-based AOP, the dose is related to the number of key photons deposited, which can be calculated if the integrated emission is measured.

Here, the number of photons of frequency ν generated in moles per liter is: $Q = \frac{P \cdot \eta}{N_A \cdot V \cdot h \cdot \nu}$ where P is the power deposited into the UV lamp, η is the photon conversion efficiency, h is Planck's constant, and N_A is Avogadro's constant (this expression ignores transfer efficiency and absorption probability). While straightforward to assess with conventional lamps, Q is difficult to assess in a plasma reactor as it requires a reliable method to assess η . Indeed, tracking the multitude of processes in a plasma reactor is part of the issue in assessing dose.

The plasma produced in the air-water vapor mixture is a source of UV emission. Nitrogen second positive system and $\bullet\text{OH}$ emission produce UV photons that drive photolysis directly and enhance other AOP pathways, such as the UV/H₂O₂ and UV/O₃. In general, the effectiveness of the photolysis process is species and wavelength dependent. As mentioned earlier, the rate of photolysis is characterized by the quantum yield (Φ), the molar extinction coefficient (ϵ), and the fraction of photons absorbed (f), which are functions of wavelength (λ). Given that a fraction of the power deposited into the plasma is converted into UV, the spectral power distribution can be used to ascertain the number of relevant photons input into the plasma per unit time and volume: $\Gamma_{UV} = \frac{P \cdot f \cdot \lambda}{V \cdot h \cdot c}$ where c is the speed of light. The reaction rate is therefore: $r_i = -\Phi_i(\lambda) \cdot P \cdot f_i(\lambda)$.

One can then approximate the decomposition of direct photolysis via a pseudo first-order rate constant. NDMA, a potential carcinogen that can be generated during wastewater treatment or industrial processing, is now found in trace amounts in some drinking waters. This contaminant predominantly photolyzes and thus, its decomposition is describable by this approach (Lee et al., 2005). A similar reaction rate

and effective rate constant can be written for UV-activated species, such as H_2O_2 and O_3 , which can provide insight into UV dose. Key to this analysis is the determination of the spectral power distribution.

The UV contribution should be considered in the design and optimization of the plasma-based water treatment systems. For municipal water treatment trains, UV lamps are integrated through two basic configurations. The UV lamps are aligned with their axis either parallel or perpendicular to water flow (EPA OW, 2003). Microdischarges have been investigated as intense UV light sources for water purification and offer efficient mercury-free operation (Prakash et al., 2017). In principle, it is possible to assess the UV dose via absolute emission spectroscopy or the use of other actinometers, such as potassium iodide (Rahn, 1997).

It should be pointed out that plasma-based water treatment systems could produce elevated levels of H_2O_2 . The excess H_2O_2 should be quenched to make the water drinkable (Liu et al., 2003; Olmez-Hanci, Arslan-Alaton, and Dursun, 2014). Even if the UV output from the plasma itself is low, one can expose the plasma-treated effluent to a UV stage to fully utilize the oxidation capacity of the water. Such an approach would further mineralize contaminants in water since a final UV stage can augment the effectiveness of plasma-based systems. This design consideration is based on assessing a priori how effective the plasma discharge is at converting input power into UV emission, typically around 250 nm.

In traditional advanced oxidation systems, the dose required to degrade a given contaminant to the desired level is carried out using a bench scale test (Rosenfeldt et al., 2006). Conventionally, an oxidant such as O_3 is applied to water samples spiked with known concentrations of target contaminants. The concentration of the oxidants, contaminants, and scavengers in solution are measured as a function of time. The pseudo first-order rate constant for the oxidant can be determined by fitting the data.

Similarly, the effective rate constant for the contaminants can also be determined provided that the rate law, the oxidant decay rate constant, and the $\bullet\text{OH}$ production rate by the oxidant are known. This rate constant can also be determined by best fit method. In this manner, the required dose and t_{HR} can be determined. By t_{HR} , we refer to the time the water to be treated spends or resides in the reactor and is thus, the contact time. This basic approach can also be applied to plasma reactors as well, since the dose delivered by the plasma to the liquid is currently not well understood.

In this case, one can directly measure H_2O_2 and O_3 production in addition to UV fluence as a function of time, along with assessing the concentration of the contaminant as a function of time. This would allow for the determination of the rate constants in an analogous manner with conventional advanced oxidation. This approach provides insight into kinetics and provides a basis for comparison with traditional AOPs. Here, the assumption is that plasma is simply an alternative method for delivering AOPs where instead of using consumables, it is the plasma-liquid interaction that produces the O_3 , H_2O_2 , and UV.

To summarize, currently, plasma reactor research studies utilizes non-standard units to assess efficiency. Since AOP technologies have advanced to practice in the water treatment arena and use E_{EO} to assess efficiency, it is recommended that plasma reactor studies assess performance using this metric as well.

Radical Transport

Radical average lifetime, τ_r , is defined in Equation 2.3 where k_0 is the rate constant of unimolecular reaction(s), k_{rs_j} is the rate constant of the radical- j^{th} scavenger reaction, and N_S is the number of scavengers. Here, a scavenger is considered any reactant such that the target contaminant and other radicals are considered scavengers. Since many trace organics exhibit first-order decay, a similar equation can be defined for

contaminants (τ_C) where radicals are used instead of scavengers and N_R is the number of radicals.

$$\tau_r = \frac{1}{k_{eff}} = \frac{1}{k_0 + \sum_{j=1}^{N_S} k_{rs_j}[S_j]} \quad (2.3)$$

The spread in τ for various water matrices, which are defined by their influent water parameters, will provide invaluable insight into the fundamental nature of plasma-based AOPs. If $\sum_{i=1}^{N_R} \tau_i \geq t_{HR}$, the system's effluent will contain a residual dose of radical r . Residual disinfectants may be helpful in potable water distribution though some ROS may need quenching. If $\sum_{i=1}^{N_R} \tau_i \geq \tau_C$ and $t_{HR} \geq \tau_C$, ROS will reach and react with contaminants in the bulk of the water. Assuming plasmas can get potent short-lived radicals to reach the contaminant, CECs will decompose much faster. Therefore, as long as plasmas use power densities similar to competing AOPs, plasmas should demonstrate more contaminant removal and improved E_{EO} .

Though convection dominates transport, some ROS will react with CECs at the interface while others dissolve, diffuse, and react in the bulk. The typical diffusion coefficient of freely-diffusing, noncharged ROS is that of an average small molecule in water. This, with given ROS lifetimes, can yield the average penetration depth, or mean square displacement, δ , as defined in Equation 2.4 (Nonell and Flors, 2016).

$$\sqrt{\langle \delta^2 \rangle} = \sqrt{6D\tau_i} \quad (2.4)$$

Though ROS with high k (V_{ECO}) are usually short-lived, they can be found in the bulk and visa versa. For example, HO^\bullet is scavenged very close to its generation site but H_2O_2 , which produces HO^\bullet , may diffuse tens of micrometers. On the other hand, even though some ROS have lifetimes orders of magnitude greater than their counterparts (Pryor, 1986), they may be confined to the gas-liquid interface, like HO_2^\bullet (Yusupov

et al., 2014). Furthermore, long-lived charged species, such as $\text{O}_2^{-\bullet}$, may not readily cross interfaces and bilayers (Winterbourn, 2008). As a result, ROS concentrations and transport need to be separated into volume and interface components.

Radical reactivity and bulk penetration are evident in V_{ECO} , D , and H^{cc} , and will still be limited by these fundamental parameters in addition to detention at interface. For example, O_3 mass transport in both ozonation and plasma water treatment is limited by low H^{cc} yet, it can be improved by manipulating geometries, such as acoustically oscillated bubbles (Birkin, Watson, and Leighton, 2001). In general, reactive species diffusion time in liquid water is slow (Foster and Lai, 2016). In fact, ROS propagation times as inferred via 2D plasma bubble studies suggest diffusion front speeds of order 0.1 mm/s. However, it should be pointed out that if streamers contact the surface directly, transport times can increase dramatically (>10 times). The plasma-water interface can further enhance ROS uptake and AOPs in the bulk through fluid effects including plasma-induced circulation, capillary wave formation, and turbulent diffusion (Sommers et al., 2011; Shimizu et al., 2011; Rens et al., 2014; Kawasaki et al., 2015).

2.1.2 Energy Transport

Energy must be efficiently transferred from the power supply to the plasma- $\text{H}_2\text{O}(\ell)$ interface then to radicals in the bulk of the water. The former is governed by the electron energy conservation equation (Eqn. 2.5), which is a function of electron density (n_e), electron temperature ($k_b T_e$), electron mass (m_e), heavy particle number densities (N_i or c_i), heavy particle temperatures (T), heavy particle masses (m), k_i , momentum transfer collision frequency (ν_m), net energy change per reaction ($\Delta\varepsilon_i$), current density (\vec{j}), and electric field (\vec{E}). The left-hand-side of Equation 2.5 is electron power density; on the right-hand-side, the first term is Joule heating ($\vec{j} \cdot \vec{E}$); the second expression is thermal conductivity ($\nabla \cdot \kappa \nabla T_e$); and the third term includes the net (losses minus

gains) power of collisions. Included in the final expression, the energy loss due to elastic collisions corresponds to $\nu_{mi} = k_i N_i$ and $\Delta\varepsilon_i = \frac{3}{2} \left(\frac{2m_e}{m_i} \right) k_b (T_e - T_i)$. Equation 2.5 is written as such so that enthalpy is properly accounted for. For instance, exothermic reactions and high-to-low T_e heat flux ($\vec{q} = -\kappa \vec{\nabla} T_e$) contribute positively to electron power gain.

$$\frac{\partial(\frac{3}{2}n_e k_b T_e)}{\partial t} = \vec{j} \cdot \vec{E} + \nabla \cdot \kappa \nabla T_e - \sum_i k_i n_e N_i \Delta\varepsilon_i \quad (2.5)$$

Although electrons in all plasmas are governed by Equation 2.5, different geometries (Lietz and Kushner, 2018), length scales (Bruggeman and Brandenburg, 2013), and timescales (Shneider, Pekker, and Fridman, 2012) can result in various discharge types, which will have a wide range of plasma characteristics, such as breakdown voltage, polarity of the applied voltage, propagation velocities, and other phenomenological features (Kolb, Xiao, and Schoenbach, 2008). Diffusive plasma can provide the best surface attachment but, transport is slow at the interface. On the contrary, filaments are highly localized yet, microplasmas induce rapid transport of species into the solution due to Marangoni flows driven by heat and concentration gradients (Berendsen et al., 2015). As a result, a combination of diffusive and streamer discharges is preferred since ROS in the diffuse attachment can be carried into the bulk by streamer-induced fluid flows (Lai, Petrov, and Foster, 2018). Nevertheless, discharge type will ultimately control ROS production, transport, and dose, and must be carefully considered.

2.2 Discharge Type

Plasmas in water treatment are generated at atmospheric pressure (atm) and typically non-thermal (Tendero et al., 2006; Bruggeman et al., 2016). Thus, without the

need for vacuum or consumables, plasma water treatment can be a readily-available, cost-effective, and energy efficient alternative to traditional AOPs.

These plasmas can be designed in numerous ways, some of which are illustrated in Figures 2.2 and 2.3. Direct discharges (Fig. 2.2) include pulsed streamer and spark discharges. Pulsed liquid streamer discharges are often a result of vaporization and field enhancement near the electrode surface where the head of the electron avalanche has an electric field equal to the applied field. If the the electrodes are close enough, the streamer will transition to an arc. Unlike streamers, sparks are thermal discharges that can provide higher radical production at the expense of significant energy waste in heating. The breakdown electric field (\vec{E}_{br}) for direct discharges is 1 MV/cm.

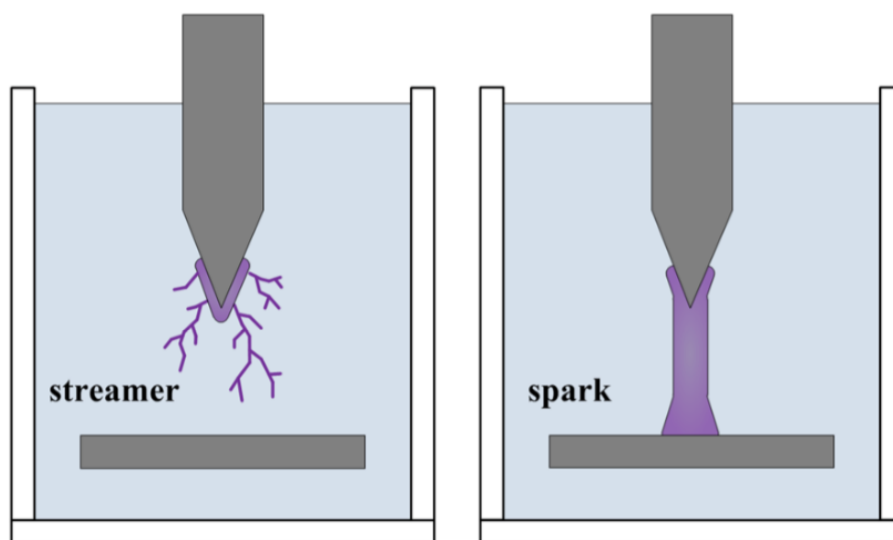


FIGURE 2.2: Different direct discharges in plasma water treatment (Somers, 2013).

On the other hand, indirect discharges (Fig. 2.3) require a much lower breakdown electric field due to plasma initiation in the gas phase. In both direct and indirect discharges, breakdown and propagation are parts of the electron avalanche phenomenon. When a high voltage is applied to a gas, electrons gain energy and initiate physical kinetics through elastic collision, excitation, ionization, and attachment processes. When

electron production exceeds electron losses, an avalanche forms. As ions are slow to move, if the avalanche builds up sufficient space charge, a self-propagating avalanche forms, also known as a streamer. For indirect atm air streamers, the Raether-Meek criterion states that the electron exponential multiplication factor, αd , must be ≈ 20 , where α is the net ionization coefficient (includes attachment losses) and d is the avalanche length (Montijn and Ebert, 2006). This corresponds to $|\vec{E}|_{min} \approx 30 \text{ kV/cm}$.

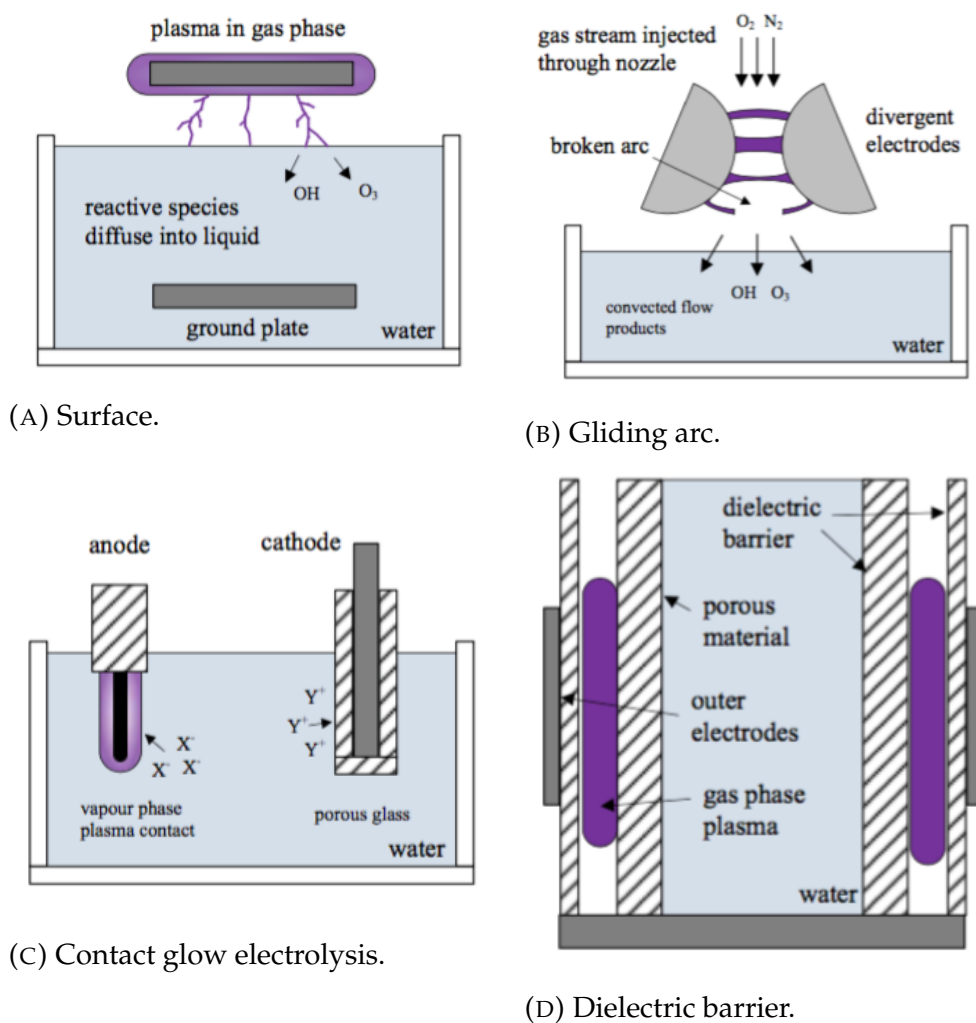


FIGURE 2.3: Different indirect discharges in plasma water treatment (Somers, 2013).

Surface discharges (Fig. 2.3a) form when an electrode is placed in close proximity to the water with the other usually submerged in water. Streamers will form above,

propagate to, and usually interact with water. During that process, gas phase radicals with diffuse into or react at the interface. Given less voltage is needed to sustain these indirect discharges, surface discharges achieve better energy efficiency (Bruggeman and Leys, 2009).

Gliding arcs (Fig. 2.3b) produce plasma in between diverging, curved electrodes that is carried towards the liquid by injected gas. Eventually, the electrode separation is too large, resulting in a streamer-like, disconnected arc that prevents excessive heating. Gliding arcs convectively transport radicals into the interface and can operate in thermal and nonthermal modes (Mutaf-Yardimci et al., 2000).

Slightly different than direct discharges, contact glow discharge electrolysis (Fig. 2.3c) extends electrolysis by applying sufficient voltage to form plasma in vapor surrounding an electrode. These configurations have demonstrated better coulombic efficiencies than standard electrolysis cells, which is suspected to be due to increased radical yield from the collision of neutrals and energetic ions accelerated through the plasma sheath (Kobayashi, Tomita, and Sanmyo, 2000).

Dielectric barrier discharges (DBDs) are composed of two electrodes partially filled with dielectric material (ex. glass) with one or both of the electrodes isolated. UV lamps can use dielectric barrier, glow, or pulsed discharges (Hofman-Caris et al., 2012) whereas O_3 is typically produced with DBDs; the DBD in Figure 2.3d is different than UV and O_3 since additional radicals are capable of making their way into the water.

In DBDs, when sufficient voltage is applied, electron avalanches initiate and propagate yet, they do not transition to arc discharges (Kogelschatz, 2003). This implies that DBDs are non-thermal, where electron temperature is much greater than the ion and neutral gas temperatures ($k_b T_e \gg k_b T_i \approx k_b T_n$). Higher electron temperature is advantageous for AOPs since radical production and overall redox are controlled by electrons.

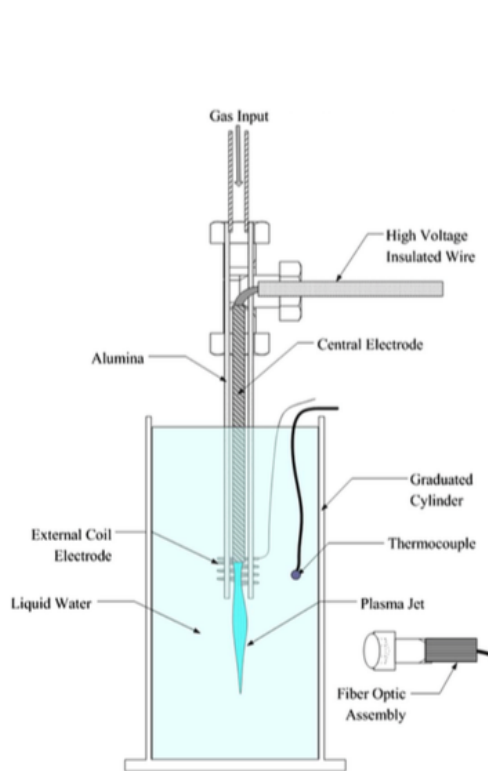
2.3 Existing Plasma Water Treatment Systems

Most plasma water treatment systems that have attempted commercialization have employed atm DBDs in their designs. DBDs further improve energy efficiency, particularly when water is the dielectric in the DBD (Foster, 2017). Various gas and power configurations can be used with DBDs to produce different ROS doses. For instance, steam instead of air can mitigate pH reduction during treatment (Gucker, Foster, and Garcia, 2015) and sinusoidal and pulsed discharges can produce electron densities two orders of magnitude apart (Neretti et al., 2017). Examples of atm DBDs with water as the dielectric are illustrated in Figure 2.4. Other commercial plasma water treatment systems include Pellucid's dense-medium plasma reactor (Manolache et al., 2001) and Symbios's plasma reactor (Johnson et al., 2016), which have demonstrated excellent and efficient inactivation.

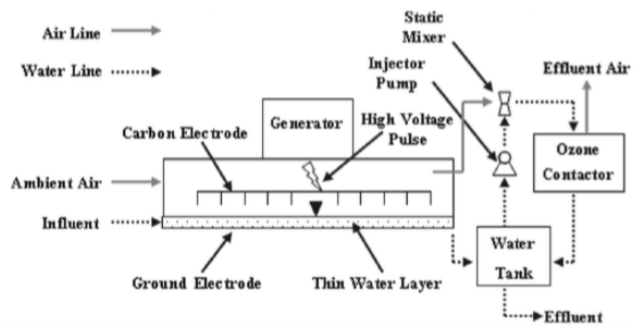
The submerged DBD plasma jet (Fig. 2.4a) is a commonly used device that can increase plasma exposure in water (Laroussi and Akan, 2007; Lu, Laroussi, and Puech, 2012; Foster et al., 2013; Reuter, Woedtke, and Weltmann, 2018). Gas is injected into a thin glass or quartz tube that houses a coaxial electrode and is surrounded by a concentric electrode. When sufficient voltage is applied, plasma forms in the tube and its radicals are carried into water. Plasma jets can operate in direct and indirect modes and can produce sufficient H_2O_2 production with a variety of gases and power supplies (Gucker, 2015).

The enhanced contact plasma reactor (ECPR) (Figure 2.4c) uses a surface discharge combined with Ar bubbling (Mededovic Thagard et al., 2017). The ECPR can remove most CECs and has exhibited the most effective rate constants for PFASs. Since PFASs cannot be destroyed by traditional AOPs, plasma provides alternative redox mechanisms, specifically the reductive properties of solvated electrons.

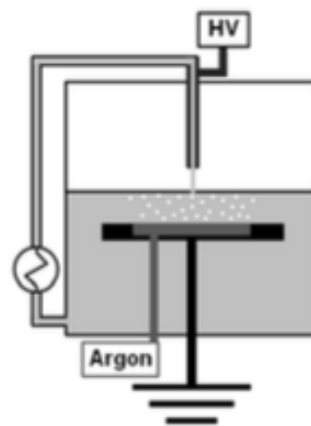
The hydro-non-thermal-plasma AOP system (Fig. 2.4b) can efficiently degrade



(A) Atm plasma jet configuration (Foster et al., 2013).



(B) Hydro-Non-Thermal-Plasma AOP System (Even-Ezra et al., 2009).



(C) Enhanced contact reactor (Mededovic Thagard et al., 2017).

FIGURE 2.4: Examples of existing atmospheric plasma- $\text{H}_2\text{O}_{(\ell)}$ reactors.

prominent CECs and has the highest flow rate found in literature at $F = 0.53 \text{ m}^3/\text{h} \approx 2.3 \text{ GPM}$ (Even-Ezra et al., 2009). The AquaPure system thins out influent water and subjects it to carbon electrode arrays of streamer discharges in ambient air. Processed water is sent to a tank and processed air is sent to an ozone contactor that is injected into the tank, further exposing water to disinfectants. Treatment levels of interest for practical applications (e.g. point-of-use or residential) start around $20 \text{ L}/\text{min}$. Higher flow rates can be generally applied to industrial water treatment applications and starting around $500 \text{ L}/\text{min}$, systems can be considered for small townships or municipalities. Consequently, the most well-known early attempt to commercialize plasma still

did not achieve practical flow rates.

Traditional AOPs use multiple technologies that each have their own inherent efficiency whereas direct plasma exposure produces all of the radicals simultaneously. Since DBDs eliminate the conversion efficiencies associated with multi-stage disinfection, DBDs have exhibited lower E_{EO} when compared to current AOPs. Other AOP metrics, such as R_{ct} , do not reflect the additional AOP pathways provided by plasmas and need to be modified. For example, the AquaPure system has a O_3 residual dose of 0.1 ppm, which is much lower than the O_3 dose in H_2O_2/O_3 and other conventional O_3 systems. This implies that comparison of oxidant doses does not necessarily correlate to contaminant log-reduction. Therefore, energy metrics, such as E_{EO} and E_{EM} , must be used to quantify the collective effectiveness of the different plasma-based AOPs.

Energy yield (G_{50}) has been used for plasma comparison and is defined as $G_{50} = 1.8 \cdot 10^6 C_0 V_0 A / (P \cdot t_{50})$ where C_0 is the initial contaminant molar concentration, V_0 is the volume in liters, A is the contaminant molecular weight, P is the power in watts, and t_{50} is the time in seconds required for 50% conversion (Malik, 2010). G_{50} has units of g h/kW and is best suited to compare energy consumption for zeroth-order reactions and batch reactors. This expression does not capture efficiency or energy requirements for flow through systems. Additionally, the metric does not consider evaporation or give any direct insight into the kinetics of the reaction.

As illustrated in Malik's work, G_{50} is a useful parameter to compare past fixed-volume plasma reactor data; however, the unit itself is not standard. Instead, in the advanced oxidation water treatment community, E_{EM} is used, which is essentially the inverse of G_{50} . Furthermore, the initial concentrations in Malik, 2010 were fairly low for most cases, suggesting that E_{EO} may be a better metric to evaluate the efficacy of these systems. As a result, these data along with other plasma-based and traditional AOPs are listed in Table 2.2.

TABLE 2.2: Comparison of different AOP technologies including plasma (Even-Ezra et al., 2009; Salveson et al., 2009; Malik, 2010; Foster et al., 2013; Stratton et al., 2017).

Technology	Contaminant	E_{EO} (kW h/m ³)
O ₃ /H ₂ O ₂	MTBE	0.1
HDC/H ₂ O ₂	MTBE	0.3
UV/TiO ₂	MTBE	0.8
UV/H ₂ O ₂	MTBE	0.7
	TCE	1.7
	NDMA	0.7
	1,4-dioxane	0.7
Pulsed air/H ₂ O _(ℓ) DBD (AquaPure)	MTBE	0.8
	TCE	1.2
	NDMA	0.5
	1,4-dioxane	2.0
Pulsed Ar/Ar-bubbled H ₂ O _(ℓ) DBD (ECPR)	PFOA	4.0
HDC	PFOA	231.5
Electrochemical (SS-Ti/RuO ₂)	PFOA	14.6
AC air-quartz DBD in H ₂ O _(ℓ) (plasma jet)	MB	41.0
Diaphragm discharge in H ₂ O _(ℓ)	MB	206.1
RF discharge in H ₂ O _(ℓ)	MB	97.5
μ -wave discharge in air bubbles in H ₂ O _(ℓ)	MB	46.5
Pulsed corona in O _{2(g)} bubbles in H ₂ O _(ℓ)	MB	28.0
Pulsed corona on H ₂ O _(ℓ) in O _{2(g)}	MB	7.2
Pulsed corona in H ₂ O _(ℓ)	MB	146.5

UV/H₂O₂, which is commonly used in tandem with MFRO, can efficiently remove 1,4-dioxane relative to the AquaPure system. On the other hand, AquaPure exhibited similar E_{EO} for MTBE and superior E_{EO} for TCE and NDMA. The lower E_{EO} values and lack of consumables have demonstrated lower O&M costs. For example, for TCE destruction, electric and chemical costs for UV/H₂O₂ and the AquaPure system are \$0.82/kgal and \$0.55/kgal, respectively (Salveson et al., 2009).

Methylene blue (MB) was used to compare different discharge types. MB is a blue dye, good redox indicator, and a medication mainly used to treat methemoglobinemia. It is also a representative pollutant for textile mill wastewater. Based on these data,

surface discharges have a much lower E_{EO} for MB relative to direct discharges. Indeed, those reactor configurations that exposed thin water layers or small water droplets to plasma were most efficient. These geometries maximize the plasma-induced dose in the liquid. It is argued that in these cases the surface area-to-volume ratio presented to the plasma is larger. Therefore, the thinner the water layer, the more complete the treatment as the liquid passes through the active plasma treatment zone.

While the Malik study points one in the direction of which geometries make the most efficient plasma water treatment systems, his assessment suggests that the most efficient geometries are also inherently low throughput—with the general focus on thin water layers or small droplets. More recently, Foster et al., 2018 and Stratton et al., 2017 developed general guidelines for plasma-water treatment system design and optimization. This study highlighted the importance of maximizing the plasma-liquid contact area and radical transport across the interface. Nonetheless, surface discharges and DBDs have limited effective flow rates due to the need for a high surface area-to-volume ratio.

2.3.1 Best-Suited Applications

Although flow rates are limited, plasmas still can be practical for water reuse applications. Peroxone is cost efficient for trace organics, such as TCE and MTBE, but inefficient for NDMA whereas visa versa is true for UV/H₂O₂. Consequently, limitations of individual AOPs requires an even more collective approach to treatment. Traditional AOPs are used in tandem with one another for synergistic effects and plasma can provide enhanced destruction while reducing energy consumption. Inherently low flow rate, high contaminant concentration streams can be a viable industrial application for plasma-based water treatment systems. For instance, although it usually makes up a small percentage of a wastewater treatment plant's influent, landfill leachate can

significantly reduce the overall UVT, requiring substantially higher power input for inactivation. Plasma can treat leachate at the source and considerably reduce the load on the wastewater treatment plant. Thus, plasma-water systems can decentralize water treatment while improving contaminant destruction and energy efficiency.

Plasma-based synergy can be further enhanced when coupled to other advanced treatment technologies. For example, O₃ used to augment MBRs or GAC can be replaced by plasmas. Specifically, the reactive oxygen and nitrogen species can amplify biological growth in MBRs and GAC. However, such a conclusion is site-specific and must be assessed through a pilot. Assuming a plasma-based system is versatile, it can easily be deployed at different parts of the treatment train to determine where it provides the best effectiveness and efficiency. Plasmas may also be able to improve brine recovery while providing inactivation credits. IPR and DPR applications are promising but, the easiest barrier to entry is in industrial water treatment. While the possibilities are endless, external market forces, especially regulations, will drive plasma-water treatment applications. Since AOPs have gained popularity due to excellent destruction and inactivation, hence regulatory compliance, plasma pilots should focus on prominent CECs, especially if traditional AOPs cannot remove them. These pilots should be picked wisely since each application will require a unique pilot due to the custom nature of water matrices.

Highlighted contaminants are always a good start for plasma-based water treatment systems. Indeed, plasma treatments have demonstrated excellent degradation of surfactant-like contaminants, such as PFASs, which, in general, are difficult to remove with conventional treatment methods, such as AOPs (Trojanowicz et al., 2018). While GAC can remove long-chain PFASs, such as PFOA and PFOS (McNamara et al., 2018), it cannot effectively remove short-chain PFASs. Plasmas can efficiently eliminate these compounds in addition to preventing the need to replace filters (Mededovic

Thagard et al., 2017). Short-chain PFASs, such as GenX, are gaining national attention and given the slow pace of the water treatment industry, these compounds should remain highlighted contaminants so long as regulations still trend along their current path. Plasma-based water treatment systems should pursue these organics in addition to other emphasized CECs.

In general, while numerous plasma reactors have demonstrated the ability to decompose a range of contaminants, the majority of these studies processed water in small batch reactor configurations. Typically, once-through configurations are desired for practical applications, particularly where throughput is fairly high.

2.4 Throughput

The chief scale-up issue regarding atmospheric pressure plasma technology is that the discharges tend to be filamentary in form. Hence, the plasma-water interface is highly restricted to the discharge contact area due to the reduced electron diffusion lengths, typically micrometers, at 1 atm. In this regard, the application of high voltage at atmospheric pressure produces discharges that are very localized and reminiscent of lightning. This very localized nature makes it difficult to integrate into large flow rate geometries. In the lab, contaminated water volumes on the order of a liter have been treated, but as mentioned earlier, treatment flows of order tens of L/min are required in practice.

2.4.1 Design Considerations

The engineering embodiment of any plasma reactor must satisfy a number of key design considerations. These include: (1) efficiency, (2) reactor lifetime, (3) process volume/throughput, (4) an understanding of the toxicity of intermediates formed, and

(5) pre- and post- treatment requirements, and (6) ancillary hardware simplicity. Efficiency metrics were commented upon earlier. It is important that the reactor is characterized in a manner that allows for direct comparison to existing treatment technologies. In plasma systems, electrodes are often in contact with liquid water. In this case, the electrode tends to degrade over time due to electrochemical-derived erosion. Such erosion has two negative effects: (1) reduced plasma production efficiency typically arising from the modification of applied electrodes (e.g. tip sharpness) and (2) introduction of electrode-derived material into the liquid, which itself is a contaminant. Gas phase ROS can also attack exposed electrodes. Engineering robust electrode designs is therefore important. Design embodiments that isolate the electrodes from the water are therefore desirable.

Process volume and throughput is a function of plasma-liquid contact area and associated reactions driven at the interface. A key objective in reactor design is to maximize the plasma-liquid contact surface area. The most straightforward approach to achieving this is to operate a multitude of sources in parallel. The relationship between delivered dose, the number of applicators, and the required input power is complex. Distance between localized plasma treatment sites can influence overall effectiveness. Discharge overlap tends to lead to synergism and thus reduces the power required to deliver a given dose. Another attribute associated with interfacial processes is the role of the local electric field and induced fluid dynamic effects. The double layer electric field can control rates of ion flow to and from the interface and can even stratify the pH locally (Rumbach et al., 2015; Rumbach, Clarke, and Go, 2017). Plasma driven fluid flows, such as Marangoni flows, can greatly affect transport of radicals from the interface into the bulk solution. These processes enhance the delivery of dose into the liquid water.

Even if a high throughput system is developed that can deliver the appropriate oxidant dose to the liquid water (O_3 , H_2O_2 , UV), the resulting solution must be free of plasma-generated hazardous byproducts, such as NO_3^- , NO_2^- , and BrO_3^- . For example, nitrate exposure puts babies at risk for methemoglobinemia, which is associated with red blood cell oxidation. High nitrate concentrations (10 ppm EPA MCL) has also been linked to cancer, thyroid disease and diabetes (Knobeloch et al., 2000). Contaminants such as these can be removed at added cost via other technologies, such as RO, electrodialysis, or bioreactors (Zhu et al., 2008). Indeed, the combination of advanced oxidation with biological remediation methods has been studied as a means to address treatment byproducts (Oller, Malato, and Sánchez-Pérez, 2011). Additionally, the intermediates left by the treatment process must also be relatively nontoxic. In general, incomplete oxidation can generate species that can be more toxic than the parent molecule. In order to assess treated water, chemical analysis and bioassays are suggested (Radjenović, Petrović, and Barceló, 2009; Rizzo, 2011; Justo et al., 2014). If the raw influent water is too heavily laden with NOM, then pretreatment such as MF may also be necessary. Each of these aspects must be considered throughout the design and test process, and repeated until optimization is achieved. This is especially true for point-of-use systems.

Finally, system simplicity is usually desired. Systems requiring low maintenance and relatively straightforward upkeep reduce the amortized cost of the system. It is also likely that first generation systems will require pulsed power and perhaps pumps to input air. Aeration is common in water treatment but, it does account for a significant fraction of a water treatment plant's electric costs (Rosso, Larson, and Stenstrom, 2008). It is desirable that pulsed power sources operate at fixed frequency and fixed applied voltage waveforms, which significantly reduce system complexity and overall cost.

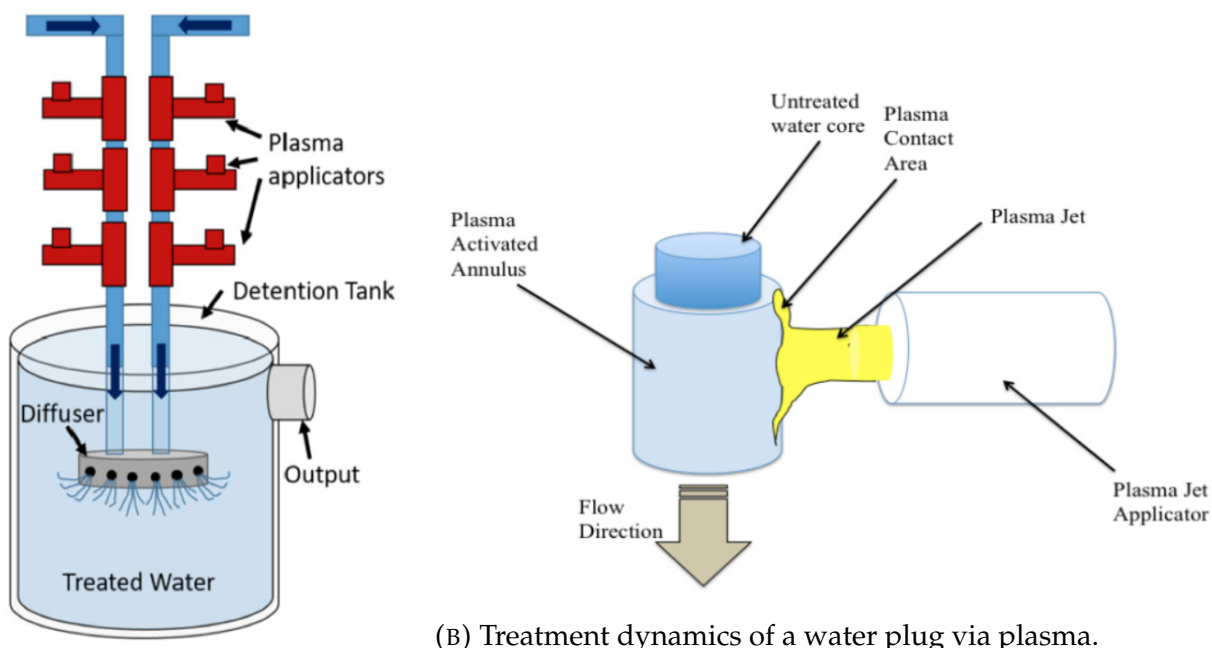
The discharge type discussed herein is of the dielectric barrier discharge (DBD) type. Here, streamers and microdischarges generate reactive oxygen and nitrogen species for treatment. These were chosen largely because they are amenable to scale-up approaches (Kunhardt, 2000). The working gas unless otherwise specified is air but, in any of the cases discussed, an inert gas can also be used. Although $O_{2(g)}$ and $H_2O_{(g)}$ produce ROS more efficiently and do not suffer from scavengers like NO_x , atm air is abundantly available and is used for point-of-use applicability in mind since it eliminates the need for consumables.

2.4.2 Multiple Plasma Jets

One potential pathway to scale-up involves using a multitude of small-scale reactors operating in parallel to provide sufficient plasma-liquid contact area.

Developed at NASA Glenn with the University of Michigan, the nanosecond-pulsed DBD plasma jet is a building block and pathway to realizing high throughput may be possible (Foster et al., 2010). This apparatus has been used to decompose a range of organic contaminants (Gucker, 2015). Figure 2.5a depicts the high throughput embodiment of this device. This approach directly treats water by forcing it to pass through the plumes of several underwater plasma jets. This delivers a characteristic dose of O_3 , $\bullet OH$, H_2O_2 , and UV to each slug of water that passes each jet, as illustrated in Figure 2.5b.

At reasonable flow rates, exposure times are not long enough to allow the plasma to treat the entire slug; rather only a thin layer is treated. The actual thickness of this annular region is dependent on diffusion and induced fluid dynamic flow effects. This dosed water, carrying the longer-lived reactive species with it, is then sent into a diffuser integrated into a contact tank. The retention tank and diffuser are sized such that the contaminants are exposed long enough to radicals and are fully treated before the



(A) Large-scale plasma jet implementation.

(B) Treatment dynamics of a water plug via plasma.

FIGURE 2.5: High throughput configuration using multiple atmospheric plasma jets (Foster et al., 2018).

water leaves the tank. This topology or architecture is scalable since one would add additional lines to accommodate higher flows. In this respect, the flow through a given line is reduced while the plasma exposure time of a given slug of water is increased. Alternatively, one can increase the number of inline plasma jet applicators per line. This would have the same effect—increasing the dose to a given slug of water.

Overall, this geometry can be thought of as a dosage approach where plasma generates reactive species and deposits them into the water as water flows through the active zone. The dosed water is then detained in the retention tank long enough for this dose to be effective. The plasma essentially replaces consumables used in conventional AOPs, thereby greatly reducing cost and enhancing effectiveness. Another operational attribute of multiple jets is the observed synergistic effects where measured decomposition times are shorter than one would expect from simple summative effects; rather, the inferred decomposition rate is nonlinear with applicator number

(Foster et al., 2013). The origin of this nonlinearity is not well understood but may be related to second-order processes associated with the overlap of plasma-activated liquid layers, which may enhance circulation and produce additional precursor species for $\bullet\text{OH}$ production. Finally, it should be pointed out that because the process water is not in physical contact with the powered electrode, electrochemical erosion is minimized. On the contrary, if not covered, the electrode can be attacked by gas phase ROS.

2.4.3 Multiple Ignited Bubbles

Plasma ignition and propagation in water is still not well understood. Similar to crack propagation in solids, a theory for direct electrical breakdown in liquids has been suggested (Lewis, 1998). In this model, the intense electric field at the electrode-liquid boundary electromechanically tears the voids in the surrounding liquid. The gas pockets are believed to be initiated by the transfer of vibrational phonon energy from the electrode to the liquid. The gas pockets are the locations of plasma formation, thereby recreating the large electric fields at the electrode surface. This process leads to the gradual crack enhancement through microbubbles in the liquid medium allowing a gaseous plasma to propagate behind it.

Streamer structure and development is imaged in Figure 2.6 by applying high voltage to an acoustically levitated bubble. Dark streamers (Fig. 2.6a) ignited in the liquid phase travel to the bubble boundary from the electrode. Then, photoionization and field enhancement due to the curved surface results in a streamer forming on the inner bubble interface (Fig. 2.6b). The streamer hugs the inner bubble interface and this surface behavior is important for radical production (Tian, 2015). Finally, the streamer propagates along the interface until it covers the entire inner bubble surface (Fig. 2.6c).

This process was on the order of the pulse width ($\sim 1 \mu\text{s}$) and shorter widths would exhibit similar structure except that partially ignited bubbles are more likely.

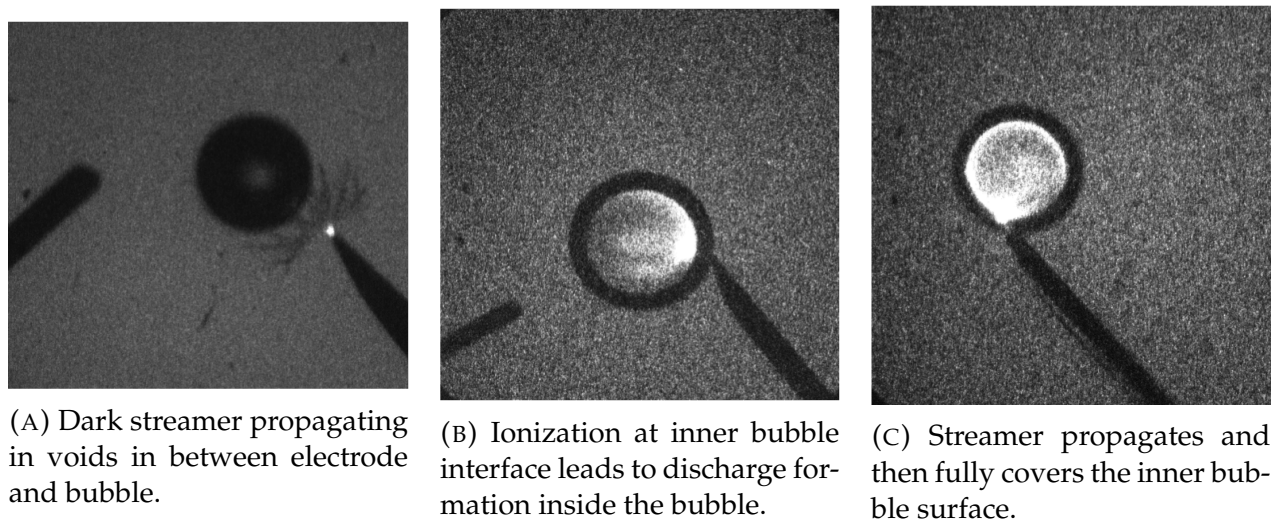
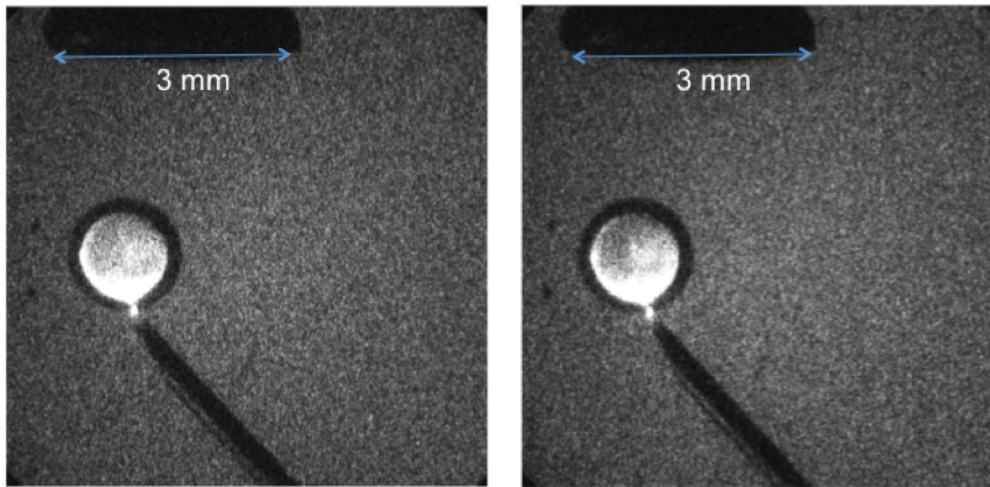


FIGURE 2.6: Submerged bubble discharge structure and development from electrode initiation to bubble-encapsulated streamer (Mujovic, Groele, and Foster, 2015a).

To ensure sufficient ROS dose is provided to the water, bubbles may need to be pulsed multiple times. If a bubble is exposed to multiple high voltage pulses, a formative time delay is evident, as depicted in Figure 2.7. There is approximately a $1.9 \mu\text{s}$ time delay between the first (Fig. 2.7a) and fifth (Fig. 2.7b) ignitions, which is more than half the time it took to ignite for the first discharge. Since collision and recombination times are faster than the period between pulses, this implies that compositional changes may change the breakdown voltage (Marković, Stamenković, and Gocić, 2007). Subsequently, optical emission spectroscopy can be used to measure transient gas species present during single and successive bubble breakdown, which will provide tremendous insight into plasma-induced kinetics.

Furthermore, excited bubbles can locally enhance the electric field at the bubble



(A) First bubble ignition with $3\ \mu\text{s}$ time delay. (B) Fifth bubble ignition with $4.9\ \mu\text{s}$ time delay.

FIGURE 2.7: Formative time delay in multi-pulsed bubble (Mujovic, Groele, and Foster, 2015b).

surface thus, fostering plasma formation and propagation along the gas-liquid interface. A simplified configuration that incorporates these features is illustrated in Figure 2.8. Injected bubbles float upward into the acoustic field and are then pulsed to form plasma in the bubble volume. After getting pulsed, bubbles will continue to diffuse ROS outward into the bulk of the water.

In conventional activated sludge, water is aerated to encourage biological growth and in ozonation, O_3 is microbubble injected through a contact tank. Instead, plasma can augment these aerated mediums with very little infrastructure modifications; electrodes can be retrofitted to an aeration or contact tank and transducers can provide capillary wave oscillations. When voltage is applied, plasma can fill the vibrationally-excited bubbles and a multiphase streamer may develop. If a bubble of radius 1 mm were deformed by capillary waves, an electric field of approximately $20\ \text{kV}/\text{cm}$ would be sufficient to satisfy the streamer criterion (Sommers, 2013). Also, if bubbles are close enough, the multiphase streamer hops between bubbles and can achieve greater plasma-water exposure, resulting in streamer branching (Babaeva and Kushner, 2008).

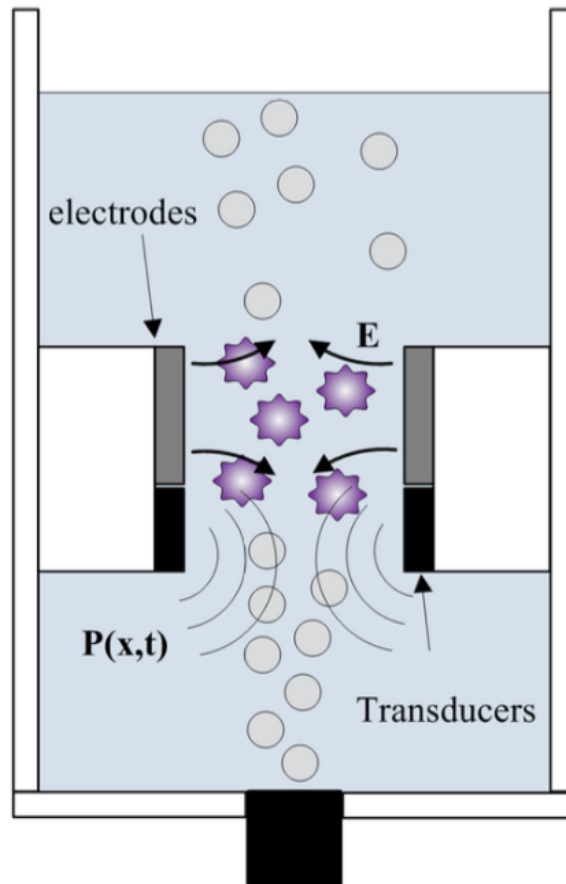


FIGURE 2.8: Bubble reactor employing plasma formation and propagation in acoustically excited bubbles (Sommers, 2013).

Nonetheless, if gas bubbles can be manipulated to promote plasma ignition and propagation in water, an alternative plasma-water treatment system may be possible.

2.4.4 Multiple Water Jets

Overall, energy must efficiently be transferred from the power supply to the radicals in the vicinity of the water. The interaction of water with plasma rapidly mineralizes contaminants by inducing advanced oxidation in addition to other chemical, physical and radiative processes, such as precipitation, shockwaves and UV. However,

the diffusion of radicals into water is a transport-limited challenge. The primary barrier to implementation of plasma-based water treatment is process volume scale-up.

Instead of enhancing the plasma-water interface through plasma formation and propagation in bubbles, the same can be done with water streams, which eliminates the need for aeration. In this work, process volume scale-up is investigated with the plasma water reactor (PWR), which uses thin water jets to maximize the plasma-water interface. Here, water serves as the dielectric media in the packed bed DBD, where closely-spaced water streams enhance plasma propagation. This system along with its design criteria is described in the following chapter.

Chapter 3

Blueprint to Scale the Plasma-Water Interface

Plasma is the ultimate redox mechanism and has the potential to replace conventional AOPs in advanced water treatment trains. The key challenge to the scale-up of plasma reactors involves optimizing the plasma-liquid contact surface area. Physical processes and associated transport taking place in this boundary layer drive reactivity. Thus, the objective is to increase radical production by maximizing this contact area. Plasmas are inherently filamentary at high pressure, which makes diffuse, uniform plasma contact with a liquid surface difficult to achieve. As a means of circumventing this issue, at the University of Michigan, we have developed the Plasma Water Reactor (PWR). In this device, the influent water is converted into a series of very thin, close-packed collimated water streams via a showerhead applicator. Water serves dual purposes, as the contaminant(s) carrier and the dielectric media. This chapter outlines the design criteria needed to enhance the plasma-water interface using a close-packed lattice of water jets.

3.1 Packed Bed of Dielectric

The PWR uses an alternative approach that may scale the plasma-water interface: packed bed dielectric barrier discharges (PBDBDs). PBDBDs occur when dielectric material, commonly oxides, ceramics, or ferroelectrics, occupy the electrode gap and is subject to voids (Chen et al., 2008). For example, Figure 3.1 demonstrates the electric field enhancement caused by close-packed dielectric disks of quartz and zirconia. As pictured in Figure 3.1a, the two-dimensional hexagonal arrays of quartz ($\epsilon/\epsilon_0 = 3.8$) and zirconia ($\epsilon/\epsilon_0 = 26.6$) are placed in a pin-to-plane electrode. When subject to 20 kV, the packing media with the higher dielectric constant, zirconia, produced more intense and localized microdischarges in the interstitial spacings of the disks, as shown in Figure 3.1b. The electric field is locally amplified at the surfaces of the water jets and the interstitial jet spaces: $E_g = E_p \cdot \frac{\epsilon_p}{\epsilon_g}$, where E_p is the electric field in the packing media, ϵ_p is the packing material dielectric constant, ϵ_g is the gas dielectric constant, and E_g is the electric field in the interstitial gas void.

Due to polarization, the close spacing and contact points of the dielectric material increase the local electric field (\vec{E}), which locally induces higher electron temperature and reaction rates (Ohsawa, Morrow, and Murphy, 2000). The enhanced electric field also amplifies the initiation of surface ionization waves at the interface between low and high permittivity matter (Van Laer and Bogaerts, 2016). At 1 atm, PBDBD behavior is highly filamentary where interstitial microdischarges produce surface ionization waves that propagate along the dielectric surface; below 1 atm, a diffuse discharge occupies the interstitial spacings, regardless of the dielectric media (Engeling et al., 2018).

Thus, porous dielectric media can improve plasma propagation and radical production at the plasma-dielectric interface. However, plasma formation and propagation in porous media is not well understood and is a function of many variables including

packing material, packing media orientation and surface morphology, packing fraction, pressure, applied voltage, and electrode finish and configuration.

3.1.1 Packed Bed of Water

Water is among liquids with the highest relative dielectric constants (ϵ/ϵ_0) and can serve as the leaky dielectric media in PBDBDs. Due to the hydrogen bonding of polarized water dimers, water has a relative dielectric constant of 80 (at 20 °C), is much higher than common polar liquids with similar dipole moments (Cabane and Vuilleumier, 2005). Furthermore, water's polar properties result in unique physical phenomena, such as solvated electron shielding and its predominant composition of voids. Since the high relative dielectric constant should correlate to more interstitial microdischarges, the distribution of bulk water into water jets increases the surface area-to-volume ratio and should improve dose, hence enabling higher effective flow rates. Using a liquid rather than a solid, the role of the dielectric in this context is similar to the role it plays in a conventional PBDBD (Chen et al., 2008).

Existing water-DBD-based reactors, depicted in the left diagram of Figure 3.2a, usually use thin, flat water sheets as the dielectric layer. Due to water's polar properties, there is a large localized electric displacement gradient at the gas-water interface that can be further enhanced if the surface is curved (Sommers et al., 2011; Babaeva et al., 2017). Existing water-DBD-based systems do not take advantage of geometry (Foster, 2017). Since PBDBDs are geometric enhancements of available media, the gas-liquid interface in a plasma-water treatment system can be manipulated to augment streamer formation and propagation (Fig. 3.2). Water jets, the simplest curved geometry, can be tightly packed to provide the electric field enhancement necessary to initiate and propagate streamers along the many multi-phase interfaces. As illustrated in

Figure 3.2b, two discharge modes can be evident: primary streamers and interstitial microdischarges.

The primary streamers travel between electrodes (HV and LV) along the surfaces of water streams. By propagating through the narrow macroscopic voids, the discharge is still indirect. Streamers form locally and attach to the water jets, and deposit charge. Sufficient charge deposition leads to the formation of surface discharges that propagate along the surface of the jet, thereby increasing plasma contact with liquid water. The surface discharges give birth to microdischarges that propagate to adjacent water jets along regions of high, localized electric fields. Indeed, local electric field enhancement from the curved geometry may encourage secondary streamers and interstitial filaments to form. Streamers may strike water jets and initiate surface ionization waves, which travel along the surface to the closest interstitial space and then propagate to the adjacent stream. This manner of propagation—microdischarge to surface discharge to microdischarge—is typical of packed bed discharge behavior (Kruszelnicki et al., 2017). Therefore, the combination of primary streamers and interstitial microdischarges should ameliorate the plasma-water contact area issue.

3.2 Showerhead Design

While multiple variants are possible, the chief design consideration is filling the interelectrode gap with densely-packed dielectric media. The dielectric medium here is the water itself in the form of rods, streams, or jets of liquid water. For plasma to successfully dose water, the PWR must meet multidisciplinary criteria and consider chemo-, electro-, photo-, physico-, and thermo-hydrodynamic effects (Anderson, 1976; Probstein, 1994).

The packing ratio (r_p) is defined in Equation 3.1, where d_j is the water jet diameter and s_j is the interstitial jet spacing. In the PWR, the dense packing of the dielectric

elements prevents line of sight between electrodes, which could otherwise lead to an arc. This implies that the PWR is close-packed, in that it has a closed-packing ratio (r_{cp}) greater than 0.866. While a tighter packing of jets is ideal for PBDBDs, streamer thickness and manufacturing limitations must be considered.

$$r_p = \frac{d_j}{d_j + s_j} \longrightarrow r_{cp} \in \left[\frac{\sqrt{3}}{2}, 1 \right] \quad (3.1)$$

While keeping the packing ratio in mind, the water jets themselves are subject to two key design constraints: stream size and stability.

3.2.1 Stream Size

Though larger diameters are preferred due to the desire for high throughput applications ($F \propto d_j^2$), the limiting factor must determine the jet diameter. In this case, it is the regulation of radicals at the plasma-water interface. From a ROS transport perspective, the water jets must be thin due to low Henry's Law constants, short penetration depths (Pryor, 1986), low diffusion speeds (Foster and Lai, 2016), and detention at the interface (Joshi et al., 1995; Winterbourn, 2008; Yusupov et al., 2014). Hence, the diameter of the water jets must be as small as practically possible.

Conveniently, the surface area-to-volume ratio of the water jets scales inversely with jet diameter. Thin jets allow for more complete uptake of plasma-produced species, especially when the primary transport phenomenon is diffusion. Per Fick's first law of diffusion (Fick, 1855), the diffusivity of species i into the jet can be approximated using the StokesEinstein relation, shown in Equation. 3.2, where D is the diffusion coefficient, d_i is the size of the molecule, μ is the liquid dynamic viscosity, and T_ℓ is the liquid temperature.

$$D_i = \frac{k_b T_\ell}{3\pi\mu d_i} \quad (3.2)$$

Subsequently, the flow speed of species i into the liquid is: $v_i = \frac{-D_i \cdot \nabla n_i}{n_i}$, where n_i is the species number density.

Thus, the dose criteria for stream size is that an effective dosage requires: $2v_i \cdot \tau \sim d_j$, where τ is the radical lifetime or plasma exposure time to a differential plug of water once-through the PWR (whichever is lesser). This approximation assumes that the reactive species are uniformly mixed into the plug and ignores convection, which dominates in this system. Regardless, the effective dose term is restrained by low diffusion speeds, short lifetimes, and detention at the interface, indicating that water streams must be thin, as mentioned earlier. Therefore, close-packed **thin** water jets can serve as the leaky dielectric media for the proposed PWR using PBDBDs.

3.2.2 Stream Stability

Jet structure is threatened by innate instabilities stemming from fluid dynamics and electrohydrodynamics.

The PWR's gas-liquid-electrode geometry uses all four common states of matter. In any case, surface chemistry regulates interfacial transport and the jet structure must be understood. The compressible Navier-Stokes equation best represents the non-equilibrium behavior of viscous fluids and is depicted in Equation 3.3, where ρ is mass density, \vec{v} is velocity, p is pressure, and \vec{g} is gravitation, or generally acceleration.

$$\frac{\partial}{\partial t} (\rho \vec{v}) + (\vec{v} \cdot \nabla) (\rho \vec{v}) = -\vec{\nabla} p + \mu \nabla^2 \vec{v} + \frac{1}{3} \mu \vec{\nabla} (\vec{\nabla} \cdot \vec{v}) + \rho \vec{g} \quad (3.3)$$

The water jets are assumed to be cylindrical throughout the reactor chamber, which is a poor approximation. Future work will attempt to better represent the water jets

by solving the Navier-Stokes equation (Eqn. 3.3). This will be expanded to include the electric field based on Maxwell's Equations and kinetics, resulting in a more accurate computational multiphysics model that can assist in geometry optimization.

For now, the showerhead design criteria will focus on maintaining continuous water streams as they flow through the reaction chamber for given electric fields.

Hydrodynamic Limits

Jet stability depends on fluid and nozzle parameters (Fig. 3.3). After water exits the showerhead, surface tension and diffusive, viscous, and inertial forces amplify surface perturbation growth and result in an instability that breaks up the jet. The characteristic jet breakup length (Z) is shown in Equation 3.4, where γ_0 is the surface tension, ρ is the liquid mass density, v_j is the jet speed ($|\vec{v}_j|$), λ_d is related to the axisymmetrical disturbance wavelength of initial amplitude δ_0 (McCarthy and Molloy, 1974). Paradoxically, cohesive forces (γ_0) promote the breakup of water jets (Eggers and Villermaux, 2008).

$$\frac{Z}{d_j} = \left(\ln \frac{d_j}{2\delta_0} \right) v_j \left(\sqrt{\frac{\rho d_j}{\gamma_0}} + \frac{3\mu}{\gamma_0} \right) \quad (3.4)$$

At length scales of on the order of Z and less, the jet is cylindrical in shape. However, beyond Z , the amplitude of the growing perturbation is on the order of the jet radius. At this point, the jet undergoes varicose breakup, as imaged in Figure 3.3a. In general, unstable modes along the surface can occur when the product of the wave number (k) and the jet radius is less than one ($k \cdot d_j < 2$).

The stability of a liquid jet exiting into a gaseous atmosphere is depicted by Figure 3.3b. The expression in Equation 3.4 roughly governs the BC region of the jet stability curve, which is the section prior to the first critical point. The other regions of the extended jet stability curve can be expressed in terms of nozzle parameters (d_j , v_j , δ_0)

and dimensionless numbers in fluid mechanics (Weber, 1931; McCarthy and Molloy, 1974).

The time to breakup can also be estimated, which is shown in Equation 3.5. In this regard, the conversion of tubular pipe flow to gravity-aligned jets represents a well-defined spatial run. As mentioned in the previous section, thinner jets are required for effective dosage. However, thinner jets result in shorter breakup times and higher definite resonance frequencies.

$$t_b \approx 1.03 \cdot \sqrt{\frac{\rho \cdot d_j^3}{\gamma_0}} \quad (3.5)$$

The quality of the jet is a function of nozzle parameters, such as interior surface smoothness, the contraction angle, the contraction ratio, and the nozzle aspect ratio (McCarthy and Molloy, 1974). Optimization of nozzle parameters and pressure head allows for jet diameters as small as a micrometer, such as those used in water jet cutters (Ng and Guannan, 2015). Also, depending on the nozzle features, Equations 3.4 and 3.5 can have slightly different constants and exponents but, its overall structure and variable dependence is similar.

Electrohydrodynamic Criterion

As demonstrated in Figure 3.1, high dielectric constants produce high localized electric fields in the interstitial voids of PBDBDs. This leads to the production of energetic electrons, which can drive gas- and liquid-phase reactions. The curvature of the jets also influences the local electric field intensity. Narrow jets are associated with higher electric field. A high surface electric field can actually distort and even destabilize the jet. In this respect, both surface tension and local electric field play key roles in jet stability. The \vec{E} -induced distortion further amplifies the local field, thereby leading to positive feedback. This instability can lead to jet disintegration. Such multiplication

effects have been observed in bubbles in water, which can actually lead to breakdown in bubbles (Babaeva et al., 2017).

In the presence of an electric field, the instability threshold of spherical water droplets occurs when Equation 3.6 is roughly satisfied, where r_d is the droplet radius in cm, E is the electric field in Gaussian units, and γ_0 is the surface tension in 1×10^{-5} N/cm (Ausman and Brook, 1967).

$$E \cdot \sqrt{\frac{r_d}{\gamma_0}} \simeq 1.51 \quad (3.6)$$

Although not strictly applicable to the cylindrical jet, this expression can be used to obtain a rough approximation of the maximum electric field that can be applied for a given jet radius. For example, if one considers $E = 30$ kV/cm for a jet of 5 mm diameter, the expression is approximately 0.37, which is stable. In that design, the safety margin is about four times the minimum breakdown electric field. Also, note that this expression does not include acoustic effects, such as shock waves, from streamer strikes.

Detailed analysis of water jet stability and its susceptibility to Raleigh-Taylor or Kelvin-Helmholtz instabilities may be executed following similar analysis methods discussed by Melcher, 1963; Holgate, Coppins, and Allen, 2018. Regardless, the water jets must spatially (Eqns. 3.4 and 3.6) and temporally (Eqn. 3.5) sustain their structure throughout their duration in the PWR.

3.2.3 Additional Features

While there are strict conditions for water jet parameters, there are some intrinsic benefits and consequences of the showerhead design. For instance, the transition of pipe flow to thin jets presents high surface area for the effusion of dissolved gases, such as volatile organic compounds (VOCs). In the PWR, VOCs move from the water into the interstitial spaces, which is akin to the process known as air stripping. The

difference here, however, is that the plasma treats VOCs after they leave the liquid state. VOCs are driven out via diffusion regulated by Henry's Law. Assuming the VOC is in equilibrium in solution and in air, H^{cc} implies that $[X_g] = H^{cc} \cdot [X_{aq}]$, where X is the solute, or VOC in this case. For non-equilibrium low concentrations, the relationship between the partial pressure of the VOC and its liquid phase concentration may be expressed: $p_x = H_x \cdot \alpha_x \cdot [X]$, where α_x is the activity of X in solution.

Air stripping is most effective for those species with higher Henry's Law constants. This technique has been utilized to remove CECs, such as TCE, MTBE, and benzene (Stocking et al., 2008). The thin water jets provide large surface area for mass transfer to the gas phase (and visa versa for radicals). In fact, the geometry is similar to the so-called thin film air-water contactor. In the case of a conventional air stripper, water flows through packing media. As water flows along the packing media surfaces, the effective mass transport surface area greatly increases. In the case of the PWR, air-stripped molecules, such as VOCs, can be mineralized in the gas phase plasma.

Synergistic effects of the showerhead nozzle also include improving discharge distribution. When water exits the showerhead, the pressure head (Δp) at the nozzle effluent reduces the local pressure around the water jets and should encourage a hybrid of diffuse and streamer discharges along the gas-water interface. The square root of Δp is proportional to v_j and ω_{res} . While the showerhead design may lead to irregular space charge, discharges will inherently navigate towards extinguished regions and reinitiate plasma propagation there, ensuring dose is uniformly and effectively applied. Furthermore, the intensified ROS dose is supplemented by higher UV yield. Since water is the dielectric in the PWR's PBDBDs (Fig. 3.2b), the UV light source—the discrete microdischarges and surface attachments—runs essentially parallel with water flow in a similar fashion to UV banks. In this respect, the PWRs packed bed geometry inherently takes advantage of UV photons produced. However, assessing

the photon flux of the PWR is left to future work. This would require photochemical kinetics coupled to computational fluid dynamics.

Overall, water jets inherently exhibit free-surface motion, hydrodynamic instability, and singularity formation promoting droplet breakup. The practical collimated streams can conveniently retrofit and augment existing water treatment trains yet, jet dynamics are sensitive to the surrounding fluid medium and the turbulent or thermal excitations.

3.3 Close-Packed Lattice of Water Jets

The PBDBD design of the PWR should increase the plasma-water interface surface area and improve energy efficiency. However, this design requires thin jets for radicals to diffuse into bulk, which lowers the effective flow rate. Furthermore, larger lattices may need higher applied voltage to achieve breakdown across more jets. This may lead to electric field-induced perturbations at interface, resulting in irregular jets and hence, irregular power distribution.

Although many variants are possible, the PWR is depicted schematically in Figure 3.4. In the interest of simplifying the number of variables, the two close-packed configurations explored were of planar (Fig. 3.4a) and cylindrical (Fig. 3.4b) geometries. The aspect ratio of the showerhead is large such that the length of the nozzle is much larger than the entrance length. This suggests that the main variables are water jet parameters: d_j , s_j , and the number of jets (N_j).

Given the number of jets on a side (n), the planar geometry uses a square close-packed design with $N_j = n^2$ whereas the cylindrical geometry uses a hexagonal close-packed design with $N_j = (\sum_{i=n}^{2n-1} i) - 2n$.

3.3.1 Plasma Generation

Application of voltage facilitates breakdown near the dielectric elements. Various DC, pulsed, and AC high voltage (HV) power supplies can be used to generate the breakdown electric field (\vec{E}_{br}). For high radical yield, the most energy efficient configurations utilize nanosecond pulses due to very high electric fields. HV pulses with ns rise times rapidly increase electron density and temperature. Since ions have electric response times on the order of microseconds, ns pulse widths ensure that the ions are considered to be immobile on these timescales and energy is predominantly given to the electrons. In the case of streamers striking the water jets, the jet should retain its structure if the pulse width is short enough. Therefore, short rise times and pulse widths maximize energy deposition and efficiency, respectively. However, the increased current density intensifies the space charge effect, leading to discharge irregularities.

It is well documented that the liquid accommodates charged species, such as electrons and ions, by solvating them thus, affecting the chemistry, charge, and associated electrolytic activity within. Indeed, depending on its influent water quality (conductivity, pH, and scavengers), water absorbs charge, typically on fast time scales; electron solvation and in solution lifetime are on the order of ps and μ s, respectively (Rumbach, Clarke, and Go, 2017). The charge accumulation within the dielectric builds to the point where it can offset the applied electric field, causing it to fall below the value necessary to drive the discharge in the interstitial space between water jets. When this occurs, the microdischarge extinguishes. The advantage of a liquid water dielectric is that it is essentially a leaky capacitor and thereby can accommodate longer and larger charge transfers before the discharge extinguishes. This is a direct consequence of the absorbed charged species, which drive reactivity in the solution. Hence, charge accumulation and reactivity induction are coupled.

Plasma forms between dielectric elements if the interstitial electric field is sufficiently high. This requirement imposes a lower limit on the applied voltage for a given geometry. The electric field in a planar geometry (Fig. 3.4a) is capacitively divided between alternating quasi-layers of water and air gaps. In cylindrical configurations (Fig. 3.4b), the situation is similar though the electric field in the cylindrical geometry varies with distance since $E = \frac{\lambda}{2\pi\epsilon_0 r}$, where r is the radius and λ is the charge per unit length.

For a simple system consisting of an air gap and a single radially symmetric ring of water jets (a reduced version of Fig. 3.4b), the total voltage across the water (the dielectric) and air gap depends on the geometric dimensions of the system. The voltage drop across the air gap is $V_{air} = \frac{\lambda}{2\pi\epsilon_0} \cdot \left[\ln \frac{c}{a} \right]$, where c is the radial distance between the central conductor surface (of radius a) and the boundary of the water layer (array of jets). For symmetry purposes, the central electrode diameter was fixed to the jet diameter in the PWR. On the other hand, the voltage drop across the water layer is $V_{water} = \frac{\lambda}{2\pi\epsilon} \cdot \left[\ln \frac{b}{c} \right]$, where ϵ is the relative permittivity ($80\epsilon_0$) and b is the radial distance between the boundary of the water layer and the concentric outer electrode.

The relations for voltage drop across the air gap and water layer suggest that there is a practical size limit to a cylindrical device. As the reactor gets larger, the number of alternating air and water layers increases, further dividing the voltage drop. One cannot simply increase the voltage since the resulting electric field significantly decreases with the natural logarithm of the ratio of the radii. If the cylindrical embodiment has similar gas and water layer thicknesses, the ratio of the radii approaches one. In effect, the natural logarithm factor gets smaller with increasing radius. Therefore, one cannot simply increase the number of layers to process more water because for a fixed voltage, breakdown will not occur in the outer layers.

Increasing voltage is not a viable solution either. Overvoltage can lead to jet destabilization in the central regions and irregular plasma distribution. The inner layer plasma may also increase local conductivity, leading to further nonuniformity in the electric field, particularly at the outer layers. This likely results in unstable and impractical operation since field requirements for outer layers in large systems would be substantial. In this respect, to avoid this issue for scale-up, one can use multiple cylindrical units in parallel.

3.3.2 Electron Production

Surface discharges greatly increase the contact area of the plasma-water surfaces while diffuse discharges maintain plasma-water attachment. Therefore, mixed modes of micro- and surface discharges are highly desirable and regulate reactive species at the plasma-water interface. Possible with a better understanding of energy and mass transport, scale-up is ultimately a matter of efficient and effective oxidant dose. Since reduction-oxidation (redox) processes are electron mechanisms and non-thermal plasmas are primarily electron-driven, electron transport will facilitate the upper limit of the system's Coulombic efficiency.

Energetic electrons drive reactivity in and out of the double layer by directly interacting with species at the plasma-water interface or producing synergistic radicals that migrate to the interface. Either way, plasma existence is contingent on a sustained energetic electron population.

There are various reactions buried within the complex plasma chemistry that contribute to net change in electron density and temperature, with some mechanisms more impactful than others. For instance, low percentages ($< 0.01\%$) of impurities can provide enough metastable states that can tremendously amplify the effective ionization coefficient via Penning ionization (Dutton and Powell, 1971).

Gain processes include detachment, and impact, photo-, dissociative, and Penning ionization whereas loss mechanisms include recombination, diffusion, and radiative, dissociative, and multi-body attachment (Locht and Schopman, 1974; Dutton, 1975). Other reactor-dependent gain mechanisms include electron capture, chemi-, charge exchange, and associative ionization. Although some reactions do not change the net number of electrons, such as deexcitation or ion dissociation, these reactions can still affect electron energy and other species. On the contrary, processes like electron-ion recombination can be neglected because the fractional ionization is very small during non-thermal breakdown. For instance, electronegative gases, such as oxygen, may experience detachment, which liberates electrons from negative ions or molecules, thus providing a gain process (Eccles, O'Neill, and Craggs, 1970). However, in 1 atm air, oxygen's strong affinity for electrons results in substantial attachment and net electron loss. Although the detachment rate is relatively insignificant compared to the attachment rate, detachment activates additional electron pathways, enhancing space charge and current growth in the conductive gas medium (Price, Lucas, and Moruzzi, 1973). Thus, all reactions should be accounted for unless confident in a given rate's insignificance.

Depending on the reaction process and properties of the target atom or molecule, the electron impact cross section (σ) is a measure of the probability of an electron colliding with a species and yielding a product. Discrete energy intervals and sharp threshold energies in $\sigma(\varepsilon)$ help identify the quantized nature of atomic and molecular energy states for a given reaction, such as rotational, vibrational, or electronic excitation.

Nevertheless, the goal is to exponentially multiply electrons and populate them in the upper energy region of the electron energy distribution function. By tailoring the concentration of energetic electrons, the induced radical yield and redox mechanisms can be optimized for custom water matrices.

Townsend Criterion

Electron swarm parameters provide a decent initial assessment into whether the discharge can form and propagate. Expressed as functions of reduced field ($\frac{|\vec{E}|}{N_g}$ where N_g is gas density), steady-state swarm parameters have been calculated for various gases for mechanisms including diffusion, detachment, drift velocity, and more (Harrison and Geballe, 1953; Naidu, Prasad, and Craggs, 1972; Lucas, Price, and Moruzzi, 1973; Dutton, 1975; Blevin, Fletcher, and Hunter, 1985). The Townsend ionization coefficient (α) and the attachment coefficient (η) are primary gain and loss mechanisms, especially for electronegative gases (Kruithof and Penning, 1937; Prasad and Craggs, 1962).

To sustain breakdown, electron gain must be greater than or equal to electron loss.

During avalanche breakdown, electrons can ionize or attach to gas molecules and ions can eject electrons from the cathode, also known as secondary electron emission. The Townsend criterion implies that $\gamma [e^M - 1] = 1$, where M is the multiplication factor and γ is the secondary electron emission coefficient. The multiplication factor can be calculated by integrating the net swarm parameters over the characteristic breakdown length (L) along an \vec{E} line. Assuming ionization is the dominant electron process in avalanches, the Townsend criterion can be expressed as Equation 3.7.

$$M = \int_0^L \left(\alpha \left(\frac{E}{N_g} \right) - \eta \left(\frac{E}{N_g} \right) \right) dx \xrightarrow{\alpha \gg \eta} \int_0^L \alpha \left(\frac{E}{N_g} \right) dx = \ln \left(\frac{1}{\gamma} + 1 \right) \quad (3.7)$$

Raether-Meek Criterion

When the critical multiplication factor ($M \approx 18-21$) is met, the avalanche will transition into a streamer—a self-sustaining discharge. This is also known as the Raether-Meek criterion, which is shown in Equation 3.8 (Meek, 1940; Loeb, 1960; Raether, 1964;

Raju, 2005; Montijn and Ebert, 2006). In humid air, the critical multiplication factor corresponds to $\vec{E}_{br} \approx 30 \text{ kV/cm}$. Thus, the voltage applied across the reactor must be sufficient to establish interstitial electric fields greater than the breakdown field.

$$M = \int_0^L \left(\alpha \left(\frac{E}{N_g} \right) - \eta \left(\frac{E}{N_g} \right) \right) dx \sim 18-21 \quad (3.8)$$

To establish the same close-packing ratio for simulation purposes, the particular configurations depicted in Figure 3.4 have a number of variables in common including $d_j = 1.59 \text{ mm}$, $s_j = 0.3 \text{ mm}$, $N_j = 36$, electrode gap volume ($a^3 = a \frac{\pi}{4} (d_{sys}^2 - d_j^2)$), and electrode gap cross section ($a^2 = \frac{\pi}{4} (d_{sys}^2 - d_j^2)$). Constant electrode gaps and water lattice parameters imply that the interstitial void volume and cross section are also constant. Given an applied voltage of 20 kV, Figure 3.5 depicts the midplane electric field for the cylindrical (Fig. 3.4b) and planar (Fig. 3.4a) geometries. As can be seen in Figures 3.5a and 3.5b, the interstitial electric fields primarily exceed the breakdown electric field of 30 kV/cm.

Indeed, the electric field exceeds the breakdown field in air for 50.13% of the planar cross section and 82.26% of the cylindrical cross section. Half of the cross section appears to be the geometric limit of square packing due to streamers only propagating along the axis perpendicular to the planar electrodes. In the cylindrical geometry, while the field drops off radially, what is apparent is the spatial extent of regions where the electric field exceeds the breakdown field. These regions extend further for inner jets in contrast to the highly localized interstitial regions parallel to a normal segment across the gap in the planar case. This observation highlights both the inherent advantage of the cylindrical geometry and demonstrates its size limitation, as discussed earlier. Alternatively, a large planar geometry with spatially uniform electric fields may be more applicable for certain water matrices.

The ionization coefficient is shown in Equation 3.9 in units of cm^{-1} .

$$\alpha \left(\frac{E}{N_g} \right) = 5 \times 10^{-16} \cdot N_g \left(1 + \frac{6 \times 10^6}{\left(\frac{E}{N_g} \right)^3} \right) e^{\frac{-1010}{\left(\frac{E}{N_g} \right)}} \quad (3.9)$$

On the other hand, the three-body and two-body attachment coefficients are displayed in Equations 3.10 and 3.11, respectively, in units of cm^{-1} .

$$\eta_{3-b} \left(\frac{E}{N_g} \right) = 1.6 \times 10^{-37} \cdot N_g^2 \left(\frac{E}{N_g} \right)^{-1.1} \quad (3.10)$$

Prior to the absolute minimum that occurs at $E_{crit} = 10 \text{ kV/cm}$, the dominant attachment mechanism is 3-body (η_{3-b}). For fields greater than E_{crit} , 2-body attachment (η_{2-b}) is the primary loss process (Babaeva, 2014).

$$\eta_{2-b} \left(\frac{E}{N_g} \right) = 4.3 \times 10^{-19} \cdot N_g \cdot e^{-1.05 \left| 5.3 - \log \left(\frac{E}{N_g} \right) \right|^3} \quad (3.11)$$

The multiplication factors in interstitial voids should match associated electric fields. Using the \vec{E} simulations in Figure 3.5, the multiplication factor in the interstitial voids is calculated using Equations 3.8, 3.9, 3.10, and 3.11. In the interstitial spaces, as demonstrated in Figure 3.6, the planar and cylindrical configurations yield uniform and nonuniform multiplication factors, respectively.

3.3.3 Simulated Kinetics in GlobalKin

GlobalKin is a zero-dimensional global kinetic model for plasma and surface chemistry. Although it does not capture spatial dependent phenomena including PBDBDs, GlobalKin can be used to approximate the complex nature of plasma-based water treatment systems. By inputting databases of plasma chemistry reaction mechanisms, ion mobilities, and electron cross sections, the code can use base modules to provide a

complete kinetic perspective of the plasma chemistry. The foundational modules include the plasma chemistry and surface chemistry modules, which can be coupled to additional modules, options, and solvers (Kushner, 2014). These include the circuit module, plug flow module, diffusion option, gas flow option, Boltzmann equation solver for electrons, and the double-precision variable-coefficient ordinary differential equation solver for rate equations. The Boltzmann solver obtains electron transport and collision rate coefficients from fundamental cross section data and can derive the electron energy distribution function. The rates solver evaluates numerical solutions of the initial-value problems for species systems of first-order ordinary differential equations. Assuming certain species and their reaction rates are negligible, an exclude file can also be submitted to remove specific species and rates, thus improving an already rapid computation time.

In addition to the gas energy equation, evaporation and oversaturation considerations, and more outlined in Lietz and Kushner, 2016, GlobalKin uses Equations 3.12, 3.13, 3.14, and 3.15 to simulate plasma chemistry given input parameters. Assuming a well-stirred reactor, the system can be treated as two separate phases (plasma and liquid water) enclosed by diffusive and adsorbing surfaces. Diffusion principally occurs at the gas-liquid interface whereas adsorption transpires at the interior reactor surfaces, such as the contact area of exposed electrodes.

$$\frac{\partial(\frac{3}{2}n_e k_b T_e)}{\partial t} = \vec{j} \cdot \vec{E} - n_e \sum_i \Delta \varepsilon_i k_i N_i - \sum_i \frac{3}{2} n_e \nu_{mi} \left(\frac{2m_e}{m_i}\right) k_b (T_e - T_i) \quad (3.12)$$

$$\begin{aligned} \frac{dn_i}{dt} = & \sum_j^{rxns} \left\{ \left(a_{ij}^{(R)} - a_{ij}^{(L)} \right) k_j \prod_l n_l^{a_{ij}^{(L)}} \right\} + \frac{1}{\tau_{flow}} \left(n_{i0} - n_i \left(1 + \frac{p - p_0}{p_0} \right) \right) \\ & + \sum_m^{materials} \left\{ -\frac{D_i n_i}{\Lambda^2} f_m \left(\frac{H^{cc} n_{i,g} - n_{i,m}}{H^{cc} n_{i,g}} \right) + \sum_k^{specs} \frac{D_k n_k}{\Lambda^2} f_m g_{ikm} \left(\frac{H^{cc} n_{k,g} - n_{k,m}}{H^{cc} n_{k,g}} \right) \right\} \end{aligned} \quad (3.13)$$

$$\frac{dn_{i,aq}}{dt} = \sum_j^{rxns} \left\{ \left(a_{ij}^{(R)} - a_{ij}^{(L)} \right) k_j \prod_l n_l^{a_{ij}^{(L)}} \right\} + \left(\frac{D_{i,g} n_i}{\Lambda} \right) \left(\frac{H^{cc} n_{i,g} - n_{i,aq}}{H^{cc} n_{i,g}} \right) \frac{A_p f_l}{V_l} \quad (3.14)$$

$$\frac{dn_{e,aq}}{dt} = \frac{D_a n_e}{\Lambda} \frac{A_p f_l}{V_l} + \sum_j^{rxns} \left\{ \left(a_{ij}^{(R)} - a_{ij}^{(L)} \right) k_j \prod_l n_l^{a_{ij}^{(L)}} \right\} \quad (3.15)$$

The terms on the right hand side of the electron energy equation (Eqn. 3.12) are due to power deposition, inelastic collisions, and elastic collisions, respectively. The terms on the right hand side of the gas species density equation (Eqn. 3.13) are net species gain/loss due to gas phase reactions, gas flow, and diffusion, respectively, where $a_{ij}^{(L)}$ and $a_{ij}^{(R)}$ are the number of molecules of species i on the left side and right side of reaction j , τ_{flow} is the average retention time of the gas in the plasma, n_{i0} is the species number density flowing in, p is the instantaneous pressure, p_0 is the desired operating pressure, f_m is the fractional area of material m , Λ is the diffusion length, and g_{ikm} is the consumed fractional flux of species k that returns as species i , which is also known as the give fraction. The neutral and charged (electron) liquid species (Eqns. 3.14 and 3.15) include the surface area of the plasma (A_p), the liquid volume (V_l), and the fraction of the area of the plasma that is in liquid contact (f_l). The liquid species density equations would include an additional loss term when the liquid is oversaturated and the major difference between these equations is that for charged species, the diffusion coefficient is the ambipolar diffusion coefficient (D_a).

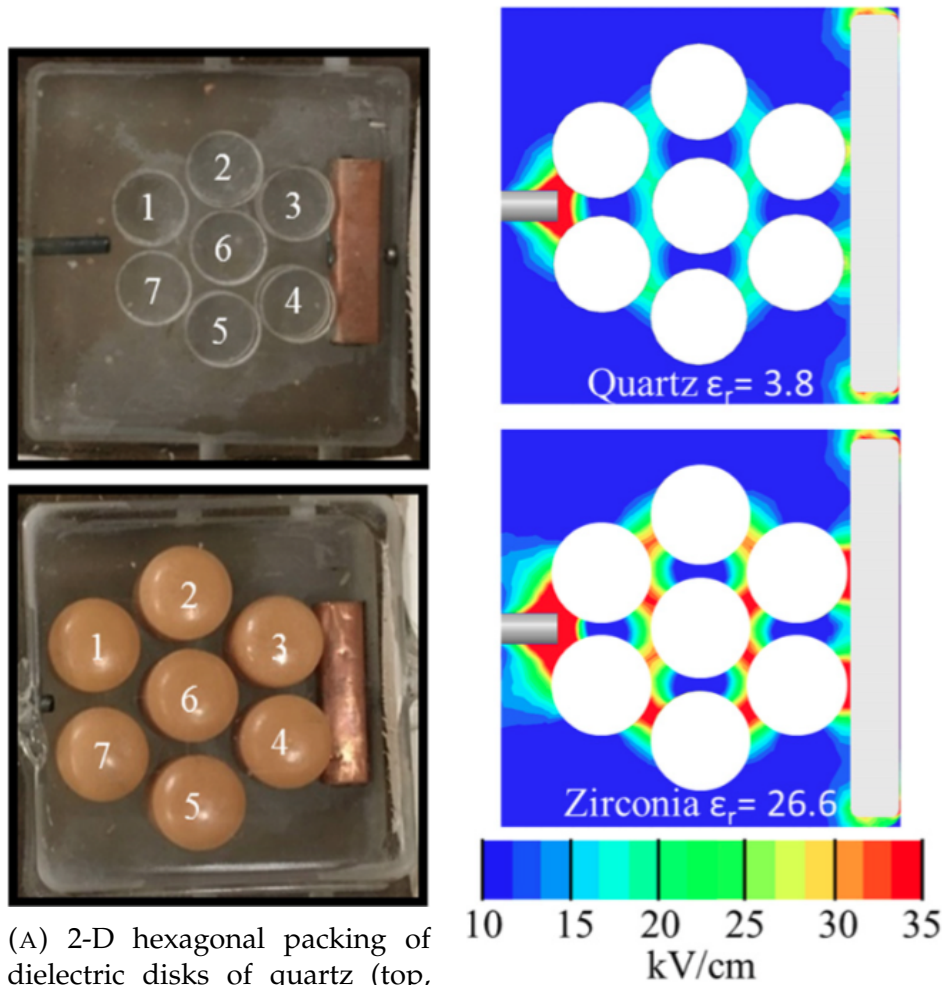
Furthermore, in GlobalKin, the photon species are actually represented as a photon density and can provide an estimate for UV dose. For an averaged homogeneous UV dose, the UV fluence can be calculated by multiplying the photon density with the maximum interstitial distance between adjacent water jets.

Using GlobalKin and the same water jet lattice as the \vec{E} simulations, ROS and reactive nitrogen species (RNS) results are shown in Figure 3.7 for the same and twice the number of water jets. In each case, the jet diameter and spacing were constant but, the volume of water doubled. In both cases, there was humid standard atm air with no gas flow, the instantaneous pulse power was 1 MW, the pulse width was 13 ns, the pulse frequency was 10 kHz, the plug speed was 10 m/s, and the treatment time was 7.6 ms. These values were based on experimental data and the desire to assess once-through ROS dose. The original water jet lattice used (Figures 3.7a and 3.7b) produced a final molar concentration for H_2O_2 and O_3 that were roughly equal ($\sim 1 \times 10^{10}/\text{cm}^3$). On the contrary, the same lattice but double the number of water jets (Figures 3.7c and 3.7d) resulted in a slightly higher O_3 concentration relative to H_2O_2 . Consequently, computations should be coupled to prototyping to roughly determine ROS and RNS concentrations for a given design. Futuremore, the rapid computation time enables a hybrid real-time analysis of simulated results based on experimental data.

3.4 Model Based on Design Criteria

Taking into consideration all of the design criteria and initial computations, the water jet lattice that is going to be used for subscale experiments in the following chapter is illustrated in Figures 3.8 and 3.9. Figure 3.8 shows that this experimental reactor utilizes the hexagonal close-packed ratio and the rod-mesh electrode configuration. As evident in Figure 3.9, throughout most of the reactor, the electric field is greater than

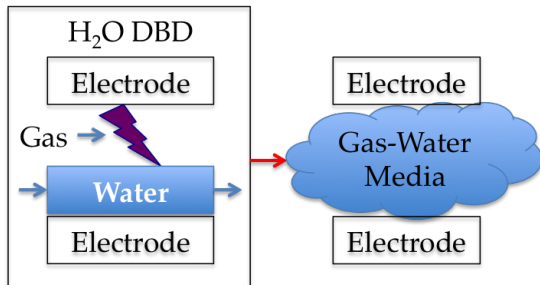
the threshold field needed for atm air breakdown. This suggests that this lattice design is favorable since streamers should form along the surface of most water jets.



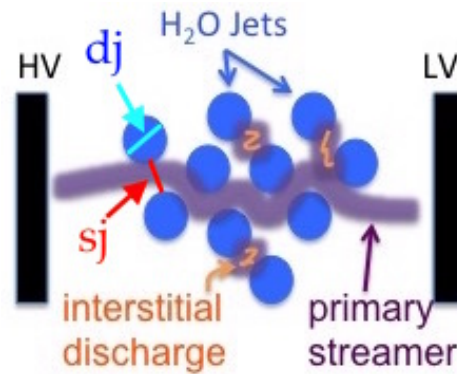
(A) 2-D hexagonal packing of dielectric disks of quartz (top, 5 mm diameter) and zirconia (bottom, 6.1 mm diameter).

(B) Calculated electric field ($V = 20$ kV) for quartz (top) and zirconia (bottom) configurations.

FIGURE 3.1: Two-dimensional PBDBDs with quartz and zirconia packing media (Engeling et al., 2018).

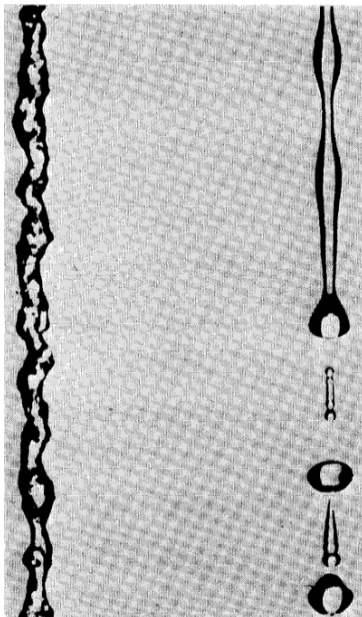


(A) Manipulating geometry to enhance plasma-water interface.

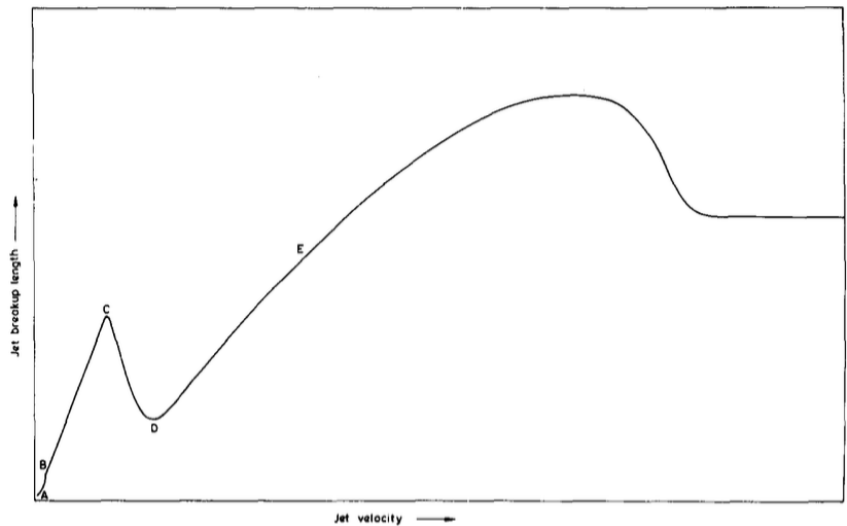


(B) Cross sectional schematic of PBDBD with water jets.

FIGURE 3.2: Idea behind the PBDBD water design used to enhance the plasma-water contact area.

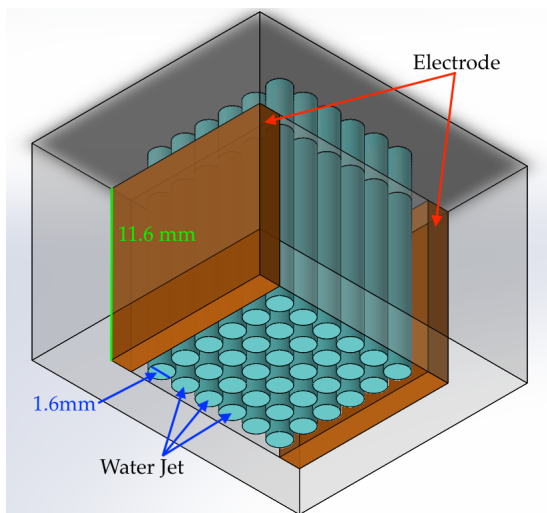


(A) Modes of jet deformation due to growth of surface disturbance.

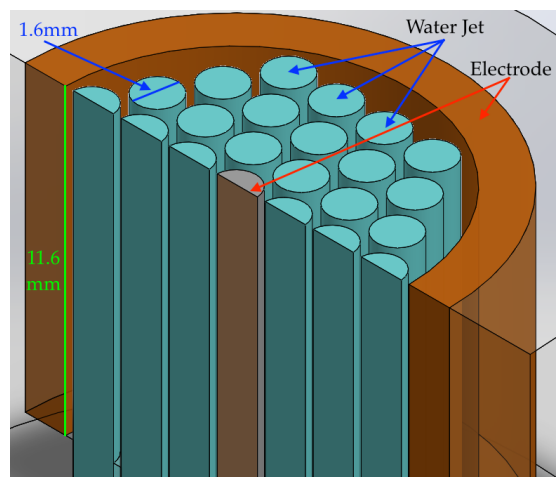


(B) Extended jet stability curve schematic of $Z = f(v_j)$. Equation 3.4 governs the BC region.

FIGURE 3.3: Water jet breakup curve and image of post-breakup droplets (McCarthy and Molloy, 1974).

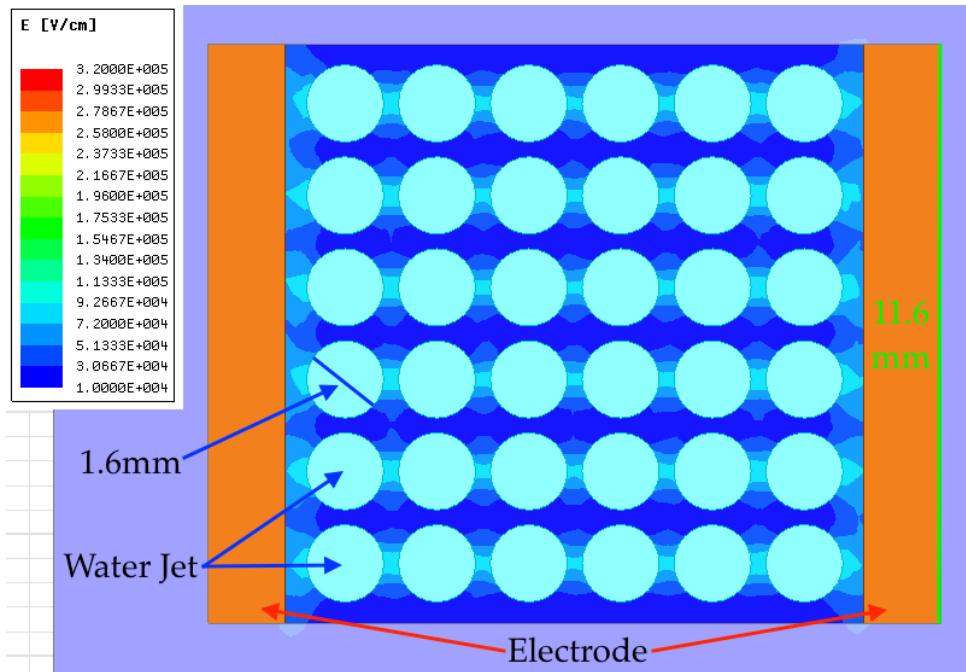


(A) Square packing of water jets with planar electrodes.

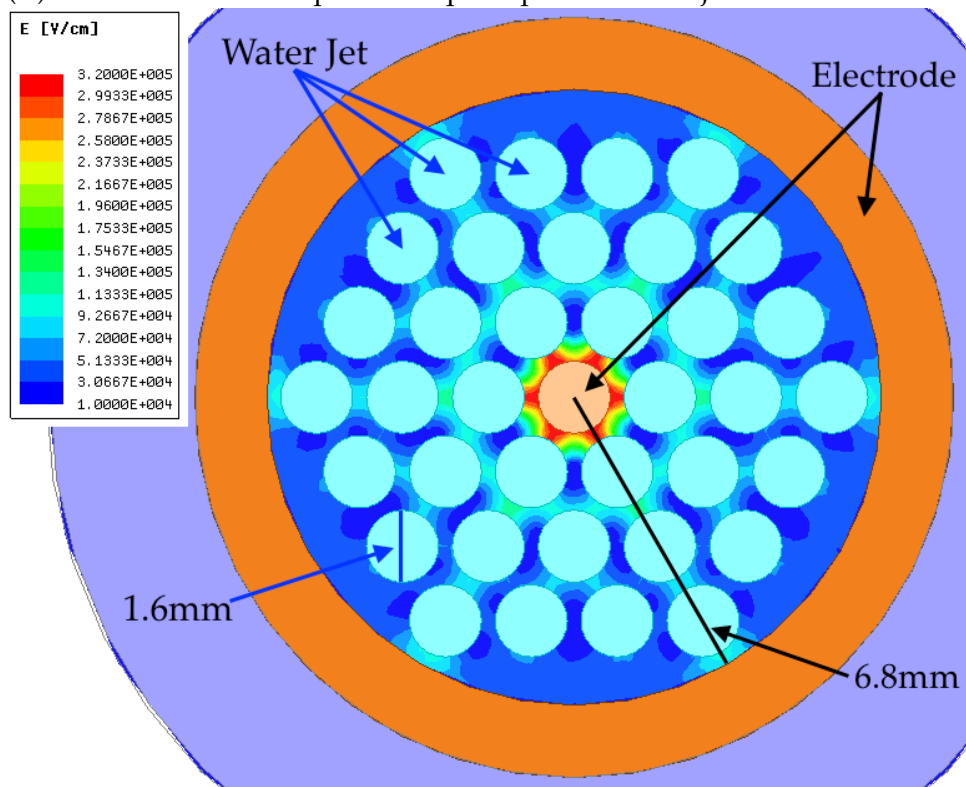


(B) Hexagonal packing of water jets with concentric electrodes.

FIGURE 3.4: SolidWorks models of square and hexagonal close-packed water jet lattices.

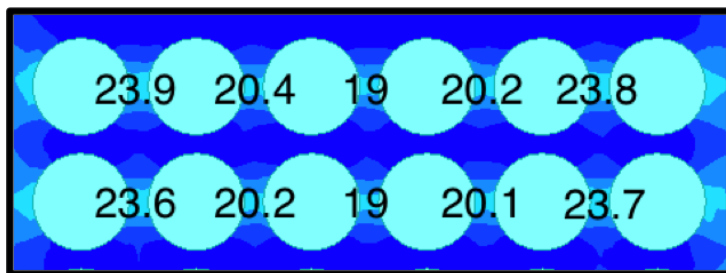


(A) \vec{E} simulation at midplane of square-packed water jets.

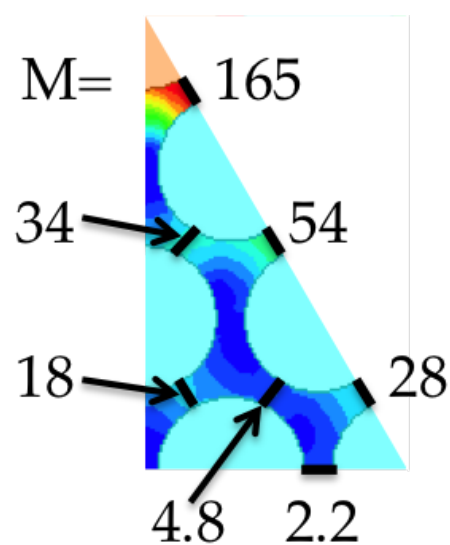


(B) \vec{E} simulation at midplane of hexagonal-packed water jets.

FIGURE 3.5: Ansys Maxwell \vec{E} simulations of square and hexagonal close-packed water jet lattices (Fig. 3.4). Legend ranges from 10 kV/cm (blue) to 320 kV/cm (red).

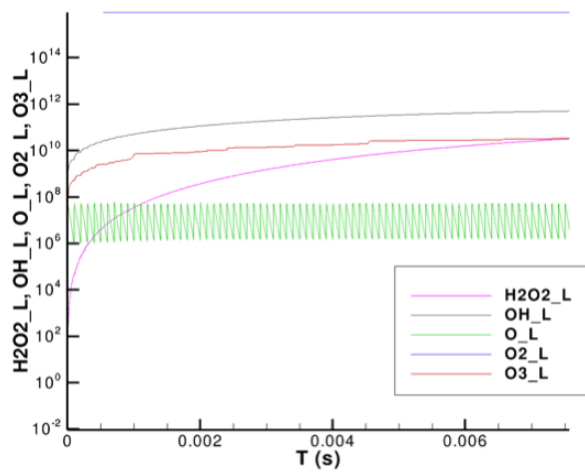


(A) M calculations for interstitial voids perpendicular to planar electrodes.

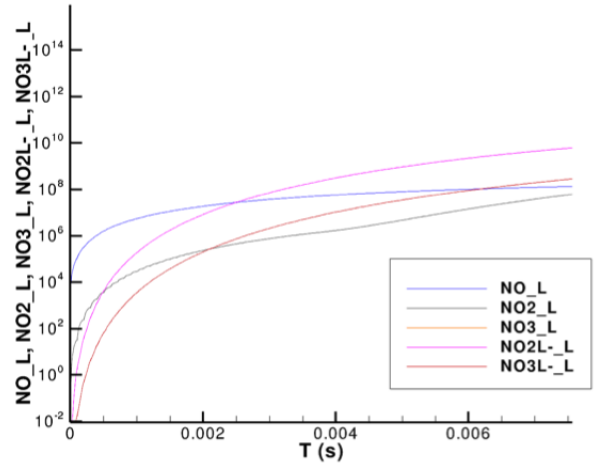


(B) M calculations for interstitial voids in between concentric electrodes.

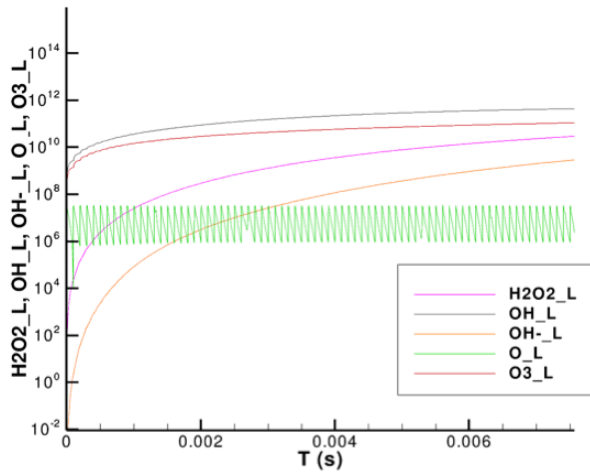
FIGURE 3.6: Multiplication factor calculated in cross section slices of square and hexagonal close-packed water jet lattices using Ansys Maxwell \vec{E} simulations. Legend ranges from 10 kV/cm (blue) to 320 kV/cm (red).



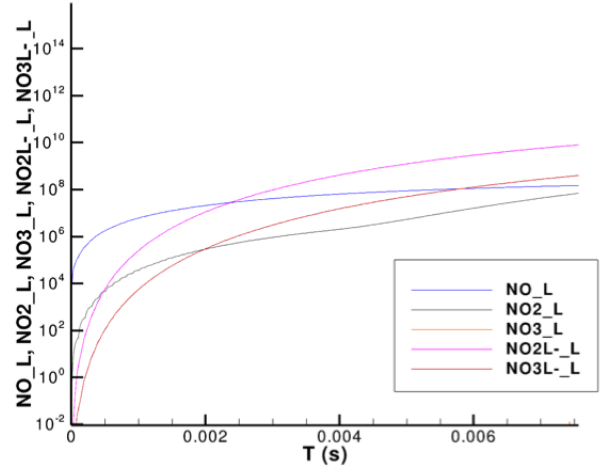
(A) ROS with standard number of jets.



(B) RNS with standard number of jets.

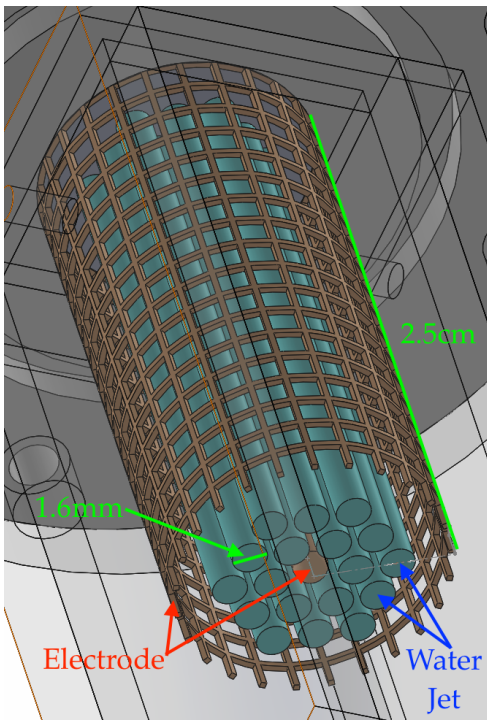


(C) ROS with twice as many jets.

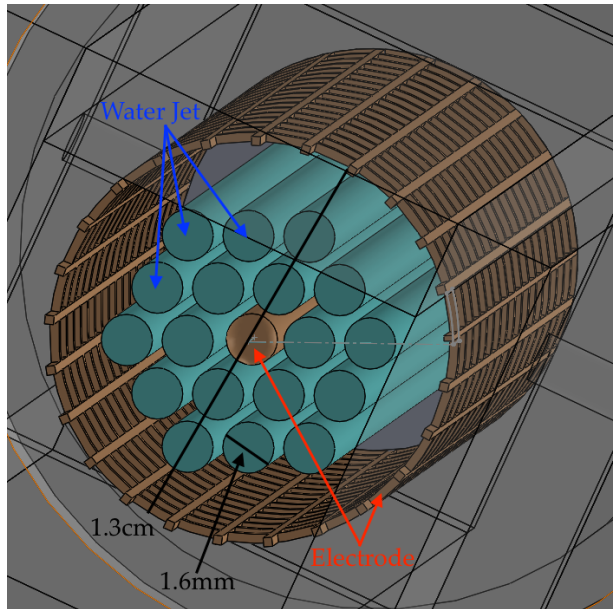


(D) RNS with twice as many jets.

FIGURE 3.7: Reactive oxygen and nitrogen species produced in hexagonal close-packed water jet lattice simulated in GlobalKin. One trial was performed with the standard number of jets ($N_j = 18$) and the other had twice as many jets. Water flow and pulsed power structure were identical.



(A) Isometric view of hexagonal-packed water jets.



(B) Bottom of isometric view.

FIGURE 3.8: Solidworks model of PWR used in experimental investigations.

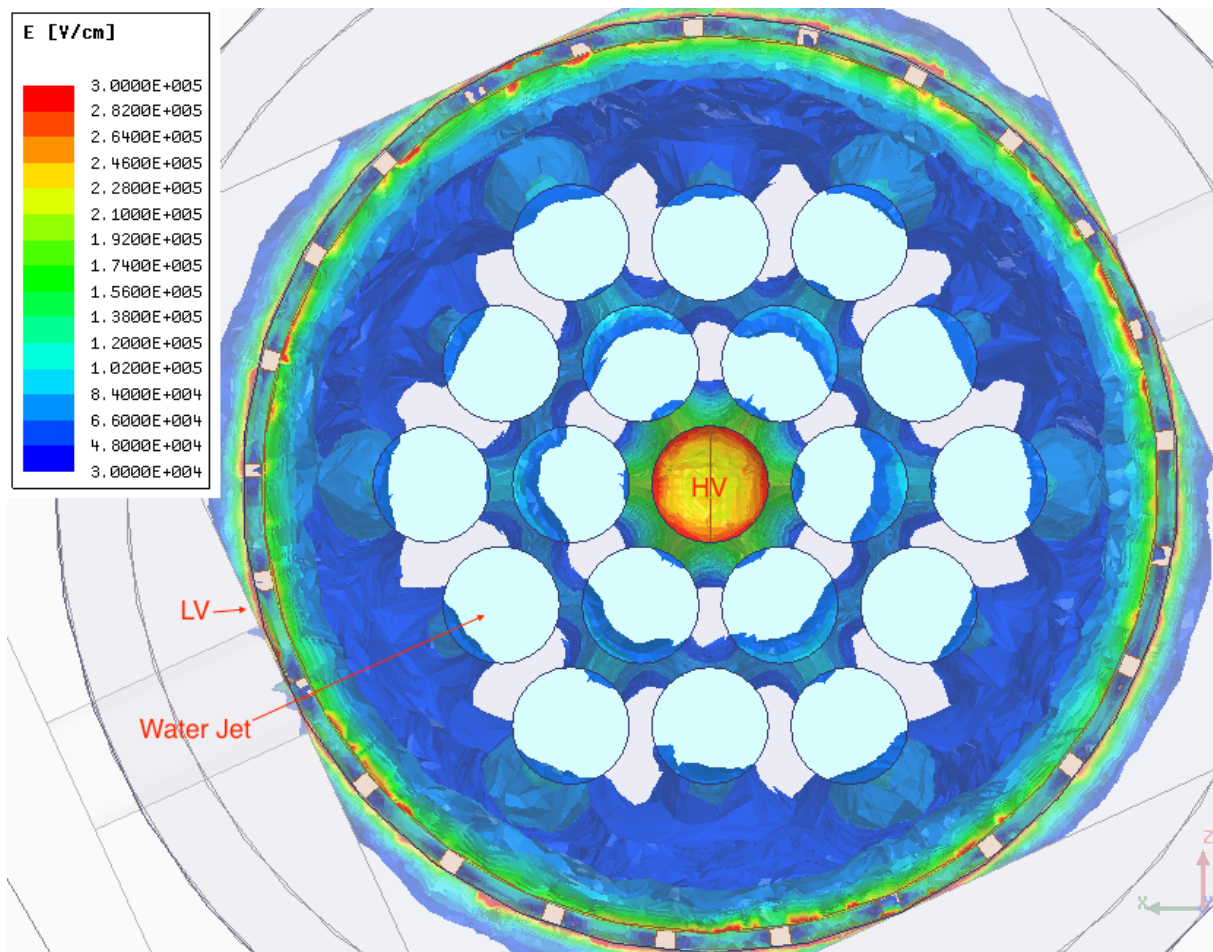


FIGURE 3.9: Ansys Maxwell \vec{E} simulation at midplane of hexagonal-packed water jet configuration shown in Figure 3.8 with 20 kV applied. The colored regions indicate $|\vec{E}| > 30 \text{ kV/cm}$.

Chapter 4

The Plasma Water Reactor

The plasma water reactor (PWR) was designed with simplicity and scalability in mind. The PWRs were made out of safe, commercially available materials, such as poly(methyl methacrylate) (PMMA), polyvinyl chloride (PVC), nylon, 316 stainless steel (316SS), and copper (Cu). PWRs are modular and their components are readily exchangeable. All PWR prototypes include a multi-water-jet nozzle, nicknamed the showerhead, and a reaction chamber housing concentric electrodes.

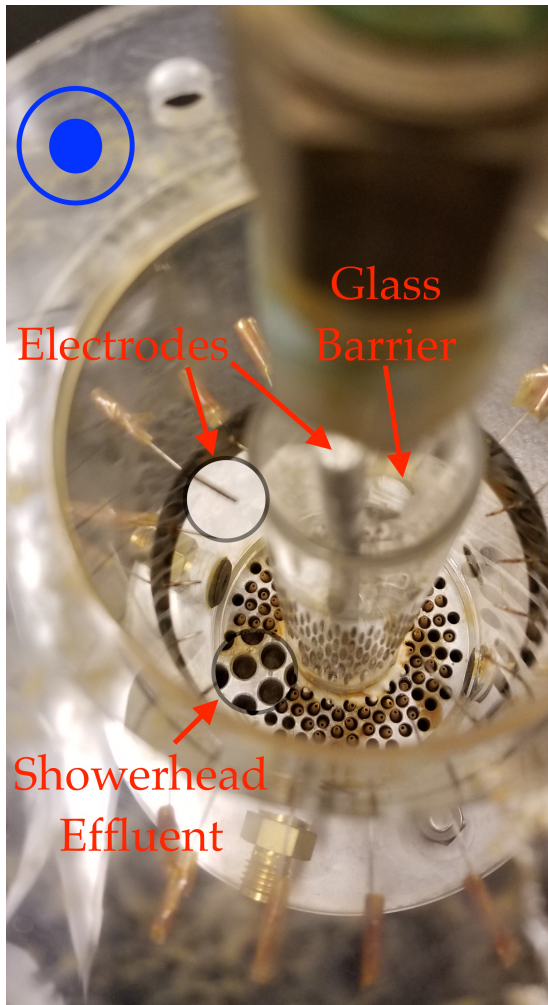
4.1 PWR Prototypes

Pictured in Figure 4.1, early PWR embodiments were capable of gas injection, water cooling, and various showerhead and electrode configurations. The showerheads usually generated water jets although sheets, droplets, and other arbitrary geometries can be used. The outer electrode was a cylindrical mesh, tube, or array of needles while the center electrode was typically a rod that could inject gas. Both electrodes could be shielded with solid dielectric, such as PMMA or alumina. Using an AC power supply

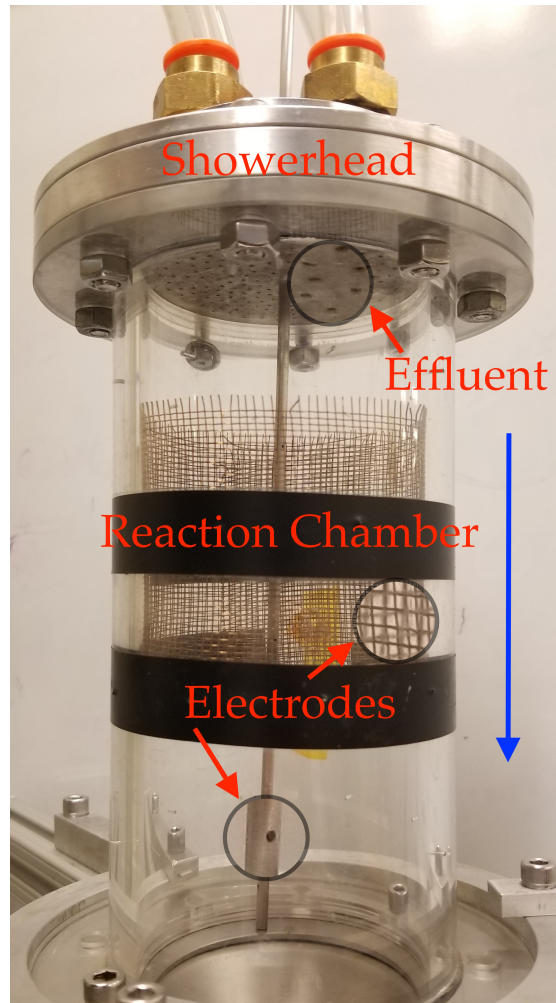
(Elgar 501SL), the needle-thread arrangement (Fig. 4.1a) experienced high voltage traveling arcs, or Jacob's ladder, whereas the mesh-rod electrodes (Fig. 4.1b) underwent a combination of streamer and arc discharges. When a high voltage nanosecond-pulsed power supply was used, streamers predominantly formed at high curvature regions of the outer electrode, either needle array or mesh. Regardless, these early prototypes could not promote breakdown or propagation near inner water jets, suggesting that these preliminary jet lattices did not adhere to the guidelines in Chapter 3.

The following generation of PWRs, shown in Figure 4.2, used a denser close-packed jet lattice ($r_p \sim 0.9$) and were modified to be more compact, modular, and versatile—capable of conveniently adapting to existing water treatment infrastructure. The high-throughput PWRs were composed of a PVC pipe adapter, a PMMA multi-water-jet nozzle, and a PMMA cylindrical reaction chamber with Cu coaxial electrodes, which can be seen in Figures 4.2a and 4.2b. The mesh and perforated rod were preferred due to the desire for gas injection and imaging purposes. This electrode arrangement also encouraged field emission and higher discharge currents, which resulted in greater electromagnetic interference (EMI) with nearby electronics. To minimize interference with fluid flow and conductivity, the center electrode was shielded prior to the nozzle and was on axis with the flow of water into the nozzle, as illustrated in the SolidWorks model in Figure 4.2c. This serviceable design enables straightforward setups for pilot studies.

Given the several gal/min (GPM) flow rates needed to make plasma water treatment a viable AOP alternative, these PWRs featured a flow rate of approximately 15 GPM. However, the large water jets used ($d_j = 3.2$ mm) and the limitations of the power supply voltage required PWRs to operate in batch mode and resulted in nonuniform discharges, similar to the ones shown in Figure 4.3. The brighter discharge (Fig. 4.3a) is arc-like. The dimmer, streamer-like discharge (Fig. 4.3b) demonstrated an

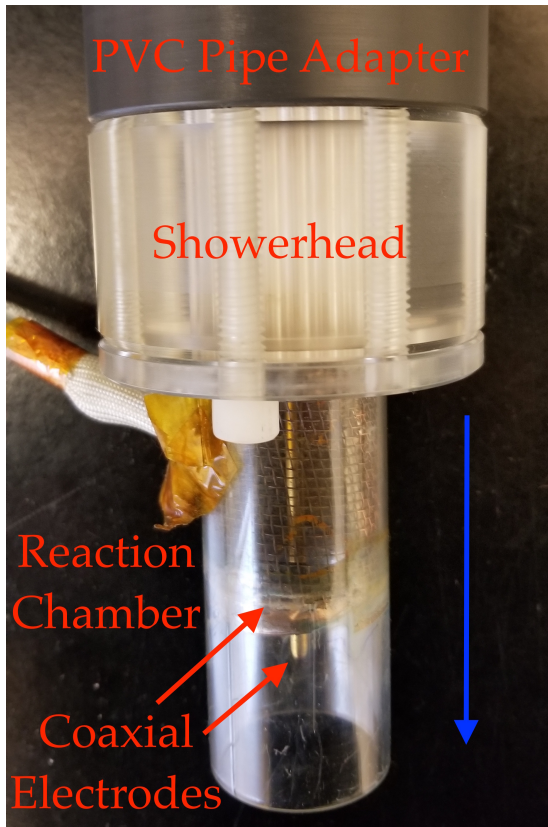


(A) Array of needles and glass-shielded screw thread.

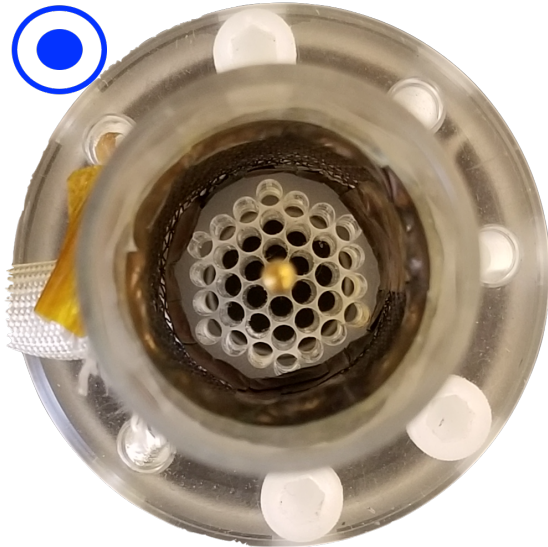


(B) Coarse mesh and perforated rod.

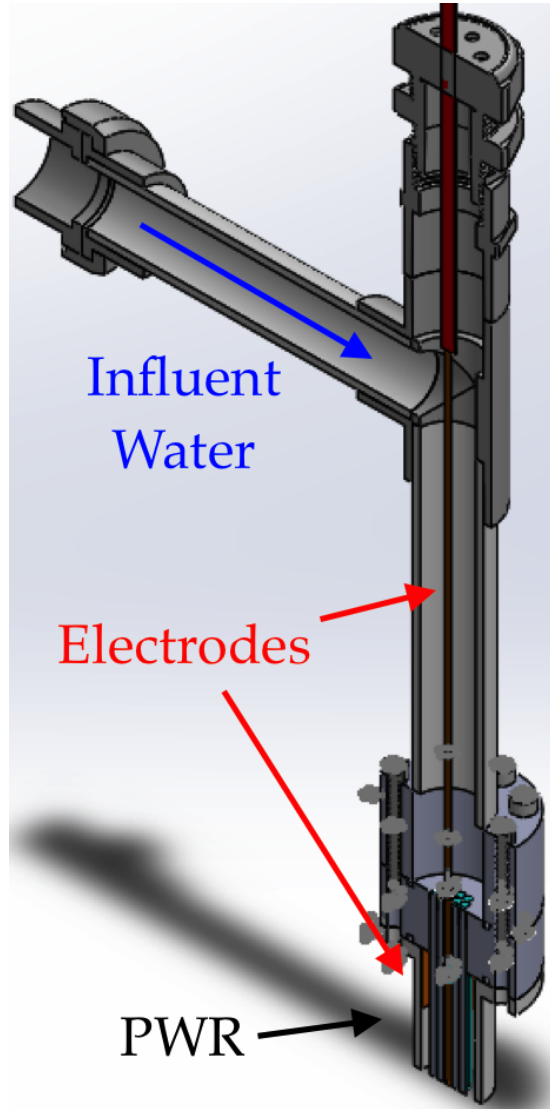
FIGURE 4.1: Early PWR prototypes capable of gas injection with coaxial electrode configurations. Blue symbol indicates water flow.



(A) PWR Side View.



(B) PWR Bottom View.



(C) PWR retrofitted to a 1 in PVC pipe.

FIGURE 4.2: Compact, high-throughput ($F = 15$ GPM) PWR with $d_j = 3.2$ mm. Blue symbol indicates water flow.

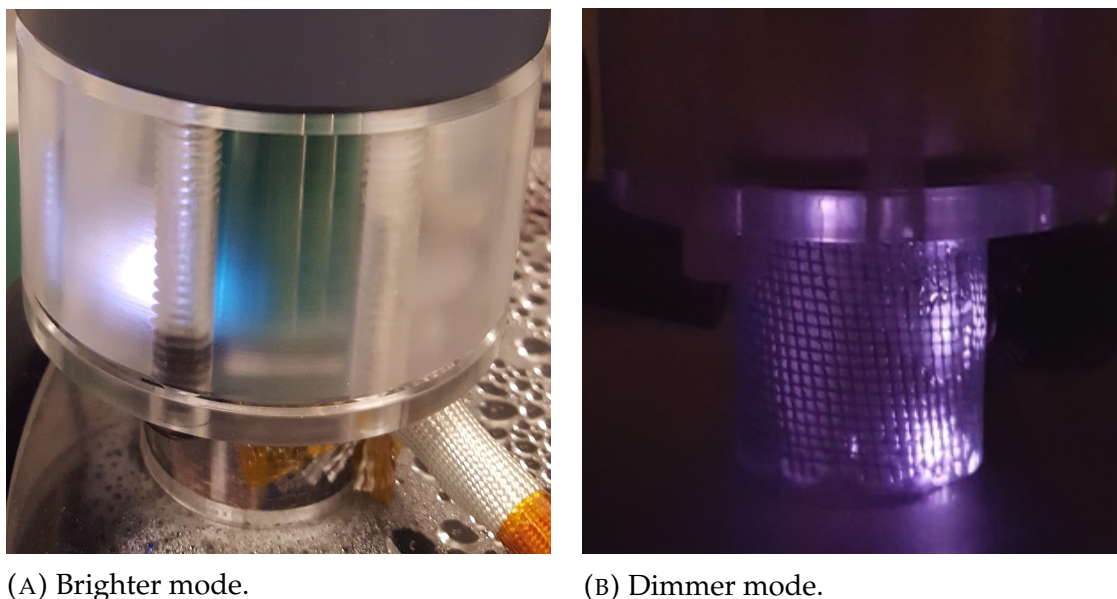


FIGURE 4.3: Compact, high-throughput PWR prototype operating in two plasma discharge modes.

initial E_{EO} of 3.8 kWh/m^3 for MB using a FID GmbH (FPG 10-10KM; peak voltage of 10 kV and pulse width of 13 ns) nanosecond pulser (NSP). While this experiment needs to be revisited with better power measurements, this E_{EO} is promising since it is among the most energy efficient plasma-based systems listed in Table 2.2.

The initial MB experiment used tap water instead of distilled (DI) water due to lab constraints and the preference to mimic typical water matrices. The tap water had an initial pH and conductivity of 8–9 and $\sim 600 \mu\text{S cm}^{-1}$. Originally suspected to be pump corrosion, particulate matter was building up in the system as the water decolorized. Regardless of discharge mode, it was ultimately deduced that minerals in the tap water electrocoagulated, though this needs to be confirmed. This is a desirable feature as it could potentially be a means to remove metal ions in addition to organic matter.

Although the early PWR prototype portrayed in Figure 4.2 demonstrated many water treatment capabilities, such as mineralization and precipitation, its effective flow rate (90% removal) was limited to several gal/h. The research priority was and still

is to better distribute plasma throughout the reactor without increasing power. Consequently, the PWR became smaller to increase power density. To maintain a high packing ratio using thinner water jets, the showerheads were made with a very high resolution 3D printer (ProJet 3500) that can provide biocompatible parts and feature detail down to 200 μm . Furthermore, while the outer electrode remained concentric with the center electrode, the reaction chamber was a square prism instead of a tube to mitigate optical distortion.

The smaller PWR, dubbed subscale, is illustrated in Figure 4.4 and is the main focus of this work.

4.2 Experimental Setup

Given the variety of PWR embodiments and water matrices that can be assessed, the experiments were intended to help determine the optimal geometric and power configurations that correspond to different favorable features, such as high energy efficiency, high throughput, and high oxidant dose.

4.2.1 Circuit Configurations

One objective is to minimize power consumption and maximize flow rate. The standard and upgraded PWR subscale systems can diagnose power real-time by recording current-voltage (I-V) waveforms while the latter is capable of additional measurements, controls, and operations. The two main configurations of power supplies are grounded and floating. When a supply is grounded, the low voltage (LV, $V_-(t)$) side is connected to ground (GND). In that case, high voltage (HV, $V_+(t)$) can be measured using a single-ended high voltage probe (HVP) attached to GND, as depicted in the circuit in

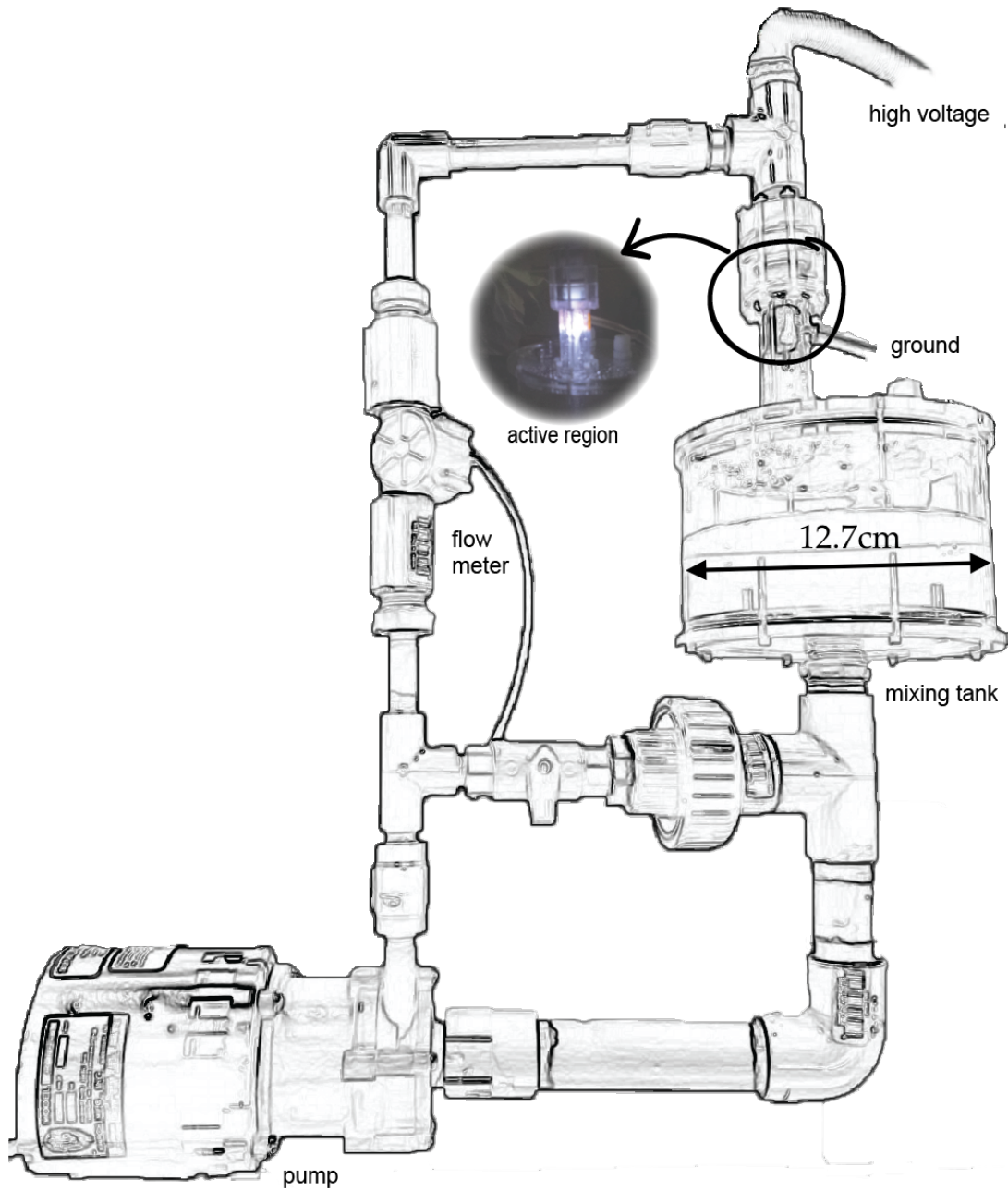


FIGURE 4.4: Sketch of actual subscale PWR system (Courtesy of Stephen Barnard).

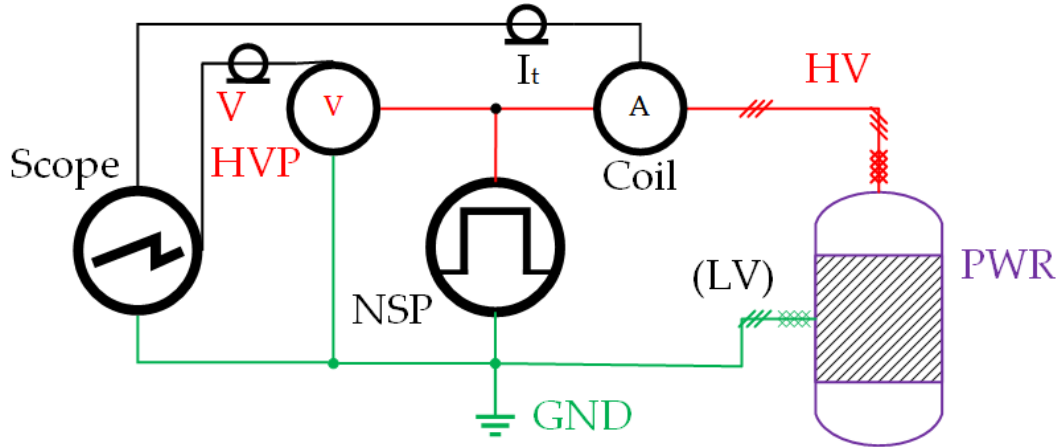


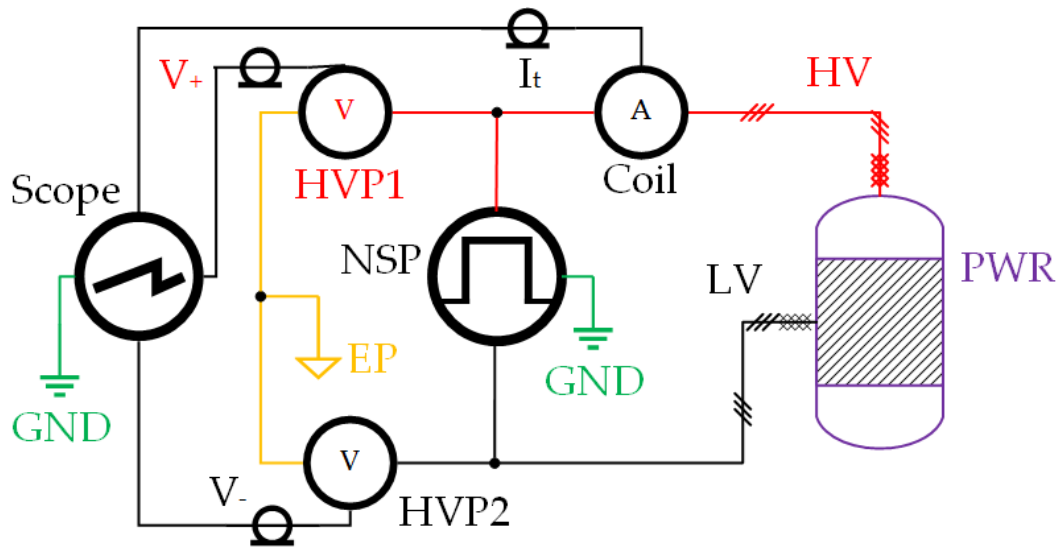
FIGURE 4.5: Grounded PWR circuit configuration.

Figure 4.5. The power in the initial MB experiment was calculated using this configuration. Though other power supplies can be applied, both PWR designs use a NSP for reasons previously discussed.

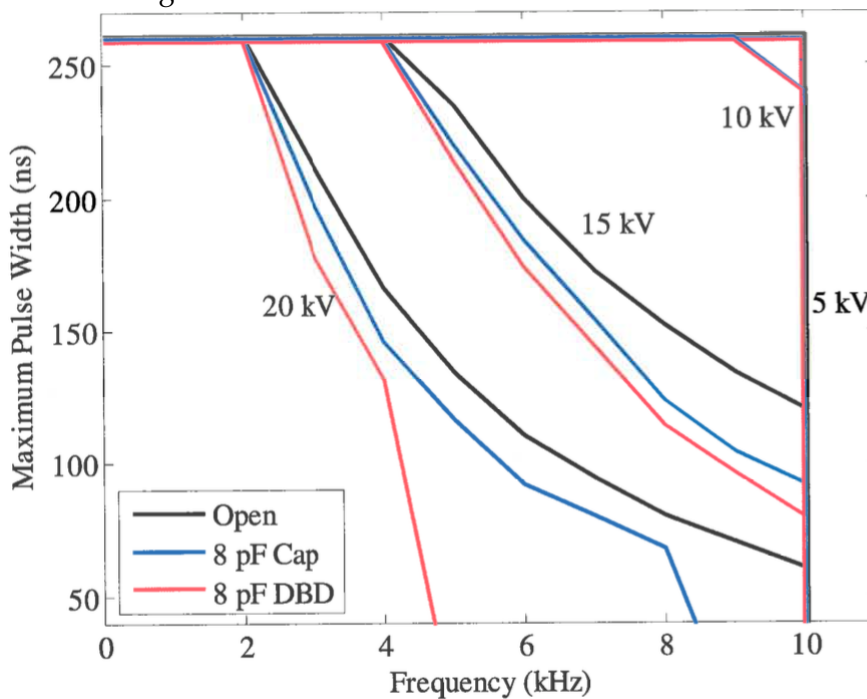
Owing to the fast rise time of NSPs, GND-based NSPs and GND power supply configurations are subject to EMI. An alternative system that mitigates EMI is a floating NSP. To diagnose a floating NSP, two single-ended HVPs can be used, as diagrammed in Figure 4.6a. The Eagle Harbor Technologies floating NSP (NSP-120-20) used for all experiments had variable pulse voltage (V_p), pulsing frequency (f_p), and pulse width (t_p). As demonstrated in Figure 4.6b, this NSP's parameter space cannot sustain V_p at higher f_p and t_p . Taking Figure 4.6 into consideration, the pulser parameters were strategically selected to assess or vary kinetics. Nonetheless, both power supply configurations use a Pearson coil in series with the load to measure current ($I_t(t)$) and the diagnostics are connected to an oscilloscope via RG-58/U (50 Ω) coaxial cables.

The data acquisition (DAQ) systems measured pulser parameters and determined the deposited power (P_D), which can be calculated using Equation 4.1.

$$P_D = f_p \int_0^{t_p} (V_+(t) - V_-(t)) I_t(t) dt \quad (4.1)$$



(A) Floating circuit configuration.

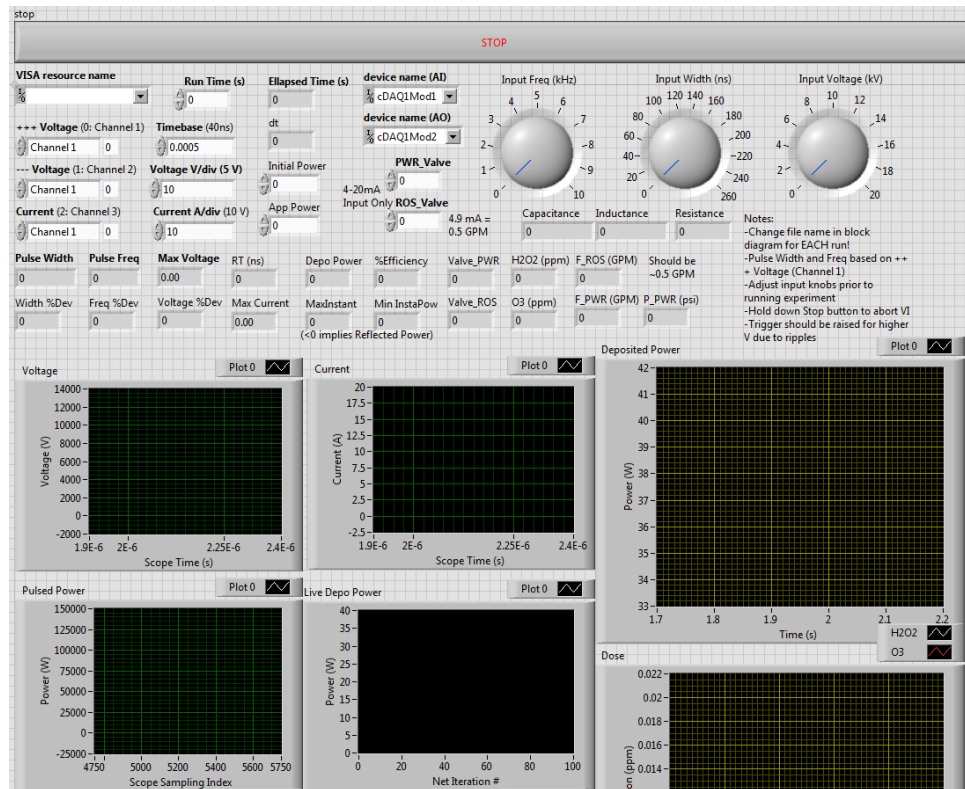


(B) Eagle Harbor Technologies NSP Parameter Space.

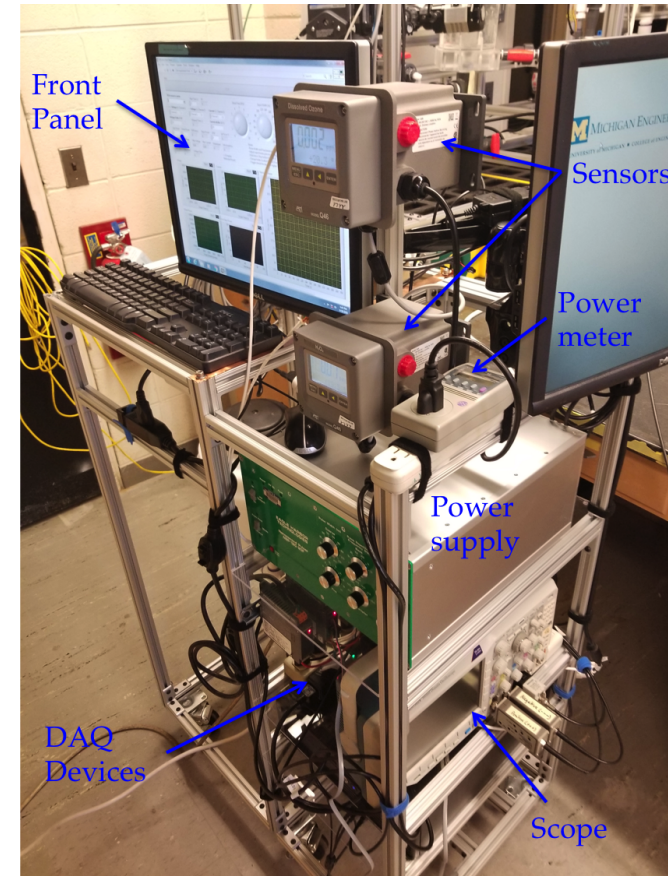
FIGURE 4.6: Floating circuit setup used to assess the floating NSP operating parameter space.

First, the PWR is prepped for the experiment and initial conditions are submitted into an in-house LabVIEW (National Instruments) code. Throughout the run, the plasma I-V traces are transferred from the oscilloscope to the computer and are analyzed, stored, and output to the screen. Since the pulsing period ($1/f_p$, $f_p < 10$ kHz) is orders of magnitude less than the pulse width ($t_p < 260$ ns), f_p and t_p cannot be measured in the same oscilloscope frame. Regardless of other pulser parameters, the NSP can consistently provide the input pulse repetition frequency throughout the length of the run and f_p is measured once at the beginning of the experiment to be safe. After f_p is found, the scope is zoomed into the region of interest and records I-V traces as quickly as possible while measuring V_p and t_p , and calculating P_D . At the end of the run, water is immediately sampled and either analyzed or stored for later.

The upgraded PWR system has a similar DAQ approach. The upgraded system controls and monitors instruments, such as valves, flow meters, and sensors, and further manipulates the I-V waveforms for analysis. In addition to calculating P_D , this DAQ system measures the pulse rise time (t_r), takes the Fourier transform of current ($I_t(t) \xrightarrow{\mathcal{F}} f(\omega)$), calculates first-order impedance, controls instruments with analog output (AO), and records sensor readings with analog input (AI). Some of these additional parameters can be seen in the human-computer interface imaged in Figure 4.7a. The DAQ system is contained within the rack pictured in Figure 4.7b.



(A) Front panel for in-house code that communicates with oscilloscope (USB) and instruments (AI/AO). The code outputs I-V waveforms, pulsed power, dissipated power, flow rates, pressure, and ROS ($\text{H}_2\text{O}_2/\text{O}_3$) dose.



(B) Upgraded DAQ rack.

FIGURE 4.7: Images of upgraded front panel and DAQ system.

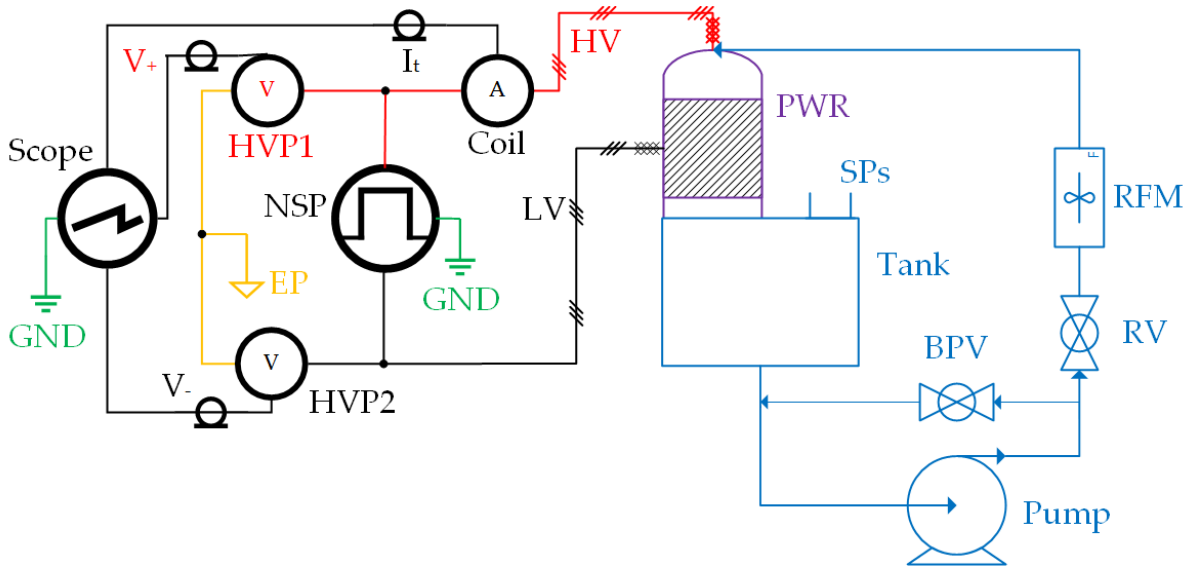


FIGURE 4.8: Process flow and circuit diagram for the PWR.

4.2.2 Standard PWR

The performance of the subscale PWR, illustrated in Figure 4.4, is assessed in a closed loop configuration. The standard PWR subscale system is depicted in the process flow and circuit diagram in Figure 4.8. Shown in the right half of Figure 4.8, batch mode consists of the PWR, a contact tank, a pump, a flow meter, and bypass and throttle valves. The left half is the floating circuit configuration diagramed in Figure 4.6a. Descriptions for all of the equipment in Figure 4.8 are listed in Tables 4.1 and 4.2. Information and settings for analytical tools are also listed in Tables 4.1 and 4.2.

TABLE 4.1: Equipment list for the standard PWR subscale system (Fig. 4.8). Materials listed are wetted surfaces unless specified otherwise.

Code	Name	Manufacturer	Model	Material
NSP	Nanosecond Pulser	Eagle Harbor Technologies	NSP-120-20	
Scope	Mixed Domain Oscilloscope	Tektronix	MDO3024	
HVP	High Voltage Probe	Tektronix	P6015A	
Coil	Current Wideband Monitor	Pearson Electronics	6585	
ICCD	ICCD Camera	Andor		
PWR	Plasma Water Reactor	Kent Pruss	v4	PMMA, 316SS, Cu
Tank	Contact Tank	Kent Pruss	v4	PMMA, nylon
Pump	Centrifugal Magnetic Drive Pump	March Pumps	AC-2CP-MD	Polypropylene
RFM	Reactor Flow Meter	Digiten	G1/2"	Nylon
RV	Reactor Valve			PVC
BPV	Bypass Valve			PVC
HS	HS Autosampler	Tekmar	7000	
GC	GC with FID	Aglient	5890 Series II	DB-624 Column
IC	Ion Chromatograph	Dionex	ICS-2100	AS11-HC Column
HPLC	HPLC with MS	Thermo Fisher		
TOC	TOC Analyzer	Shimadzu	TOC-V _{CSH}	
SPM	UV/Vis Spectrophotometer	Analytikjena	Specord 200 Plus	
PM	UV/Vis Photometer	Hanna Instruments	HI83399-01	
WM	Water Meter	Thermo Fisher	Orion Star A329	
Strip	Reagent Strips	EMD Millipore	MQuant 1100110001	
OES	Optical Emission Spectrometer	Ocean Optics		

4.2.3 Upgraded PWR

In order to create a kinetic protocol for plasma water treatment, power and water data must be amassed and mass analyzed. Furthermore, while batch mode may be adequate for bench-scale tests, pilot-scale studies will require once-through configurations. The upgraded PWR subscale system, illustrated in Figure 4.9 and pictured in Figure 4.10a, is capable of measuring partial ROS dose (only H_2O_2 and O_3) and operating in batch, semi-batch, and once-through configurations.

The upgraded and standard PWRs are imaged side-by-side in Figure 4.10b, portraying that the upgrades did not significantly increase the size of the PWR system. As can be seen in Figure 4.10, the PWR systems are compact and can be easily deployed.

Although once-through treatment is ideal, batch or semi-batch may be needed depending on power supply voltage limitations, influent water quality, and effluent water requirements. Batch is useful for custom water matrix studies whereas semi-batch allows for continuous production in manufacturing. The PWR in this system shields one or both electrodes with a dielectric barrier, such as PMMA or alumina, to mitigate arcs and EMI. Due to the proximity of sensors to the PWR, reducing EMI is critical for the DAQ system to operate properly.

The pump sends the solution from the contact tank through two streams: one to the O_3 and H_2O_2 flow cells, which house their respective sensors, and another to the PWR. Flow cell effluent is returned to the contact vessel whereas PWR effluent can be returned to the tank (batch), siphoned off (semi-batch), or fully diverted (once-through). Throughout treatment, in addition to collecting I-V traces, the upgraded system controls electric actuated valves and the peristaltic pump, and records flow rates, water pressure (p), and H_2O_2 and O_3 concentrations. These data are stored and analyzed using a modified in-house code.

TABLE 4.2: Equipment description or operating conditions for items in Table 4.1.

Code	Description or Conditions
NSP	20 ns rise time, unipolar DC 20–250 ns pulses, max of 20 kV, 10 kHz
Scope	200 MHz; USB connection used for data acquisition
HVP	Input impedance: 100 M Ω , 3 pF
Coil	1.5 ns rise time; 200 MHz, 500 A max
ICCD	ICCD camera used to image water jets without Cu mesh installed
PWR	Nozzle with concentric 316SS rod & Cu mesh electrodes
Tank	1 L reservoir that has three sample ports (SPs)
Pump	5 GPM max flow at 60 Hz
RFM	Turbine-based with flow rates of 1 L/min–30 L/min
RV	Ball valve used to control flow to reactor
BPV	Ball valve used to relieve pump pressure
HS	10 mL sample equilibrated at 80 °C for 28 min
GC	105 m \times 0.53 mm ID Column, 3 μ m-thick film N ₂ carrier (F = 5 mL/min, p = 15 psi) injected at 150 °C; FID at 200 °C Heats at 40 °C for 6 min, ramps to 175 °C at 10 °C/min
IC	250 mm \times 2 mm ID Column 20 μ L injection at 30 °C with KOH eluent (F = 0.75 mL/min) 1 mM for \sim 5 min, \sim 10 min incremental ramps to 15, 30, then 60 mM
HPLC	20 μ L injection; electrospray ionization-MS (Fragment at 150 V)
TOC	Furnace combustion at 680 °C
SPM	UV/Vis range from 320 nm–950 nm
PM	Colorimetric meter used for O _{3(aq)} , NO _{2⁻(aq)} , NO _{3⁻(aq)} , and Cu
WM	Measures pH, conductivity (TDS), DO, and select ions
Strip	Used for H ₂ O ₂ ; NO _{3⁻} strips are used as IC check
OES	Captures PWR spectra

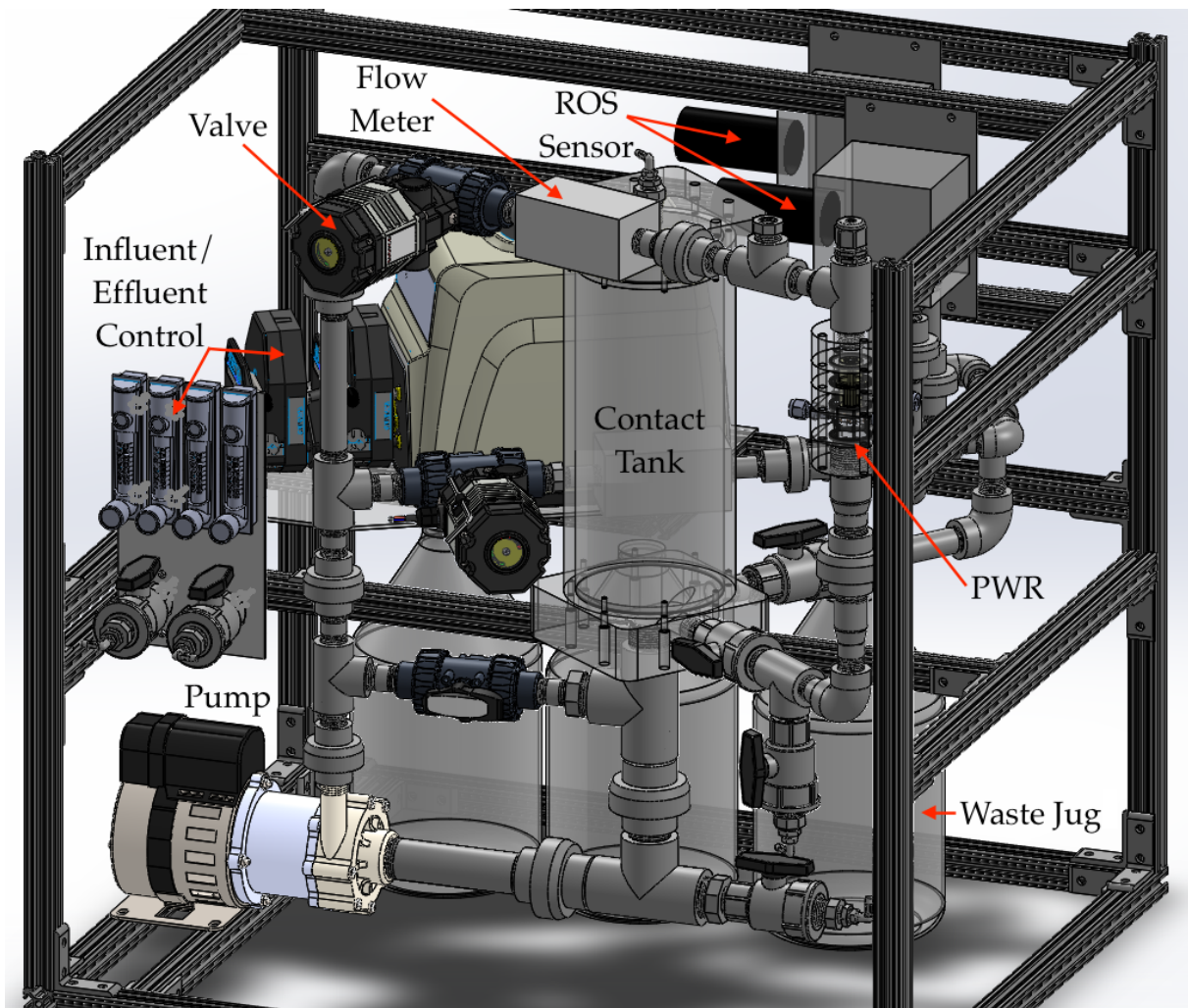
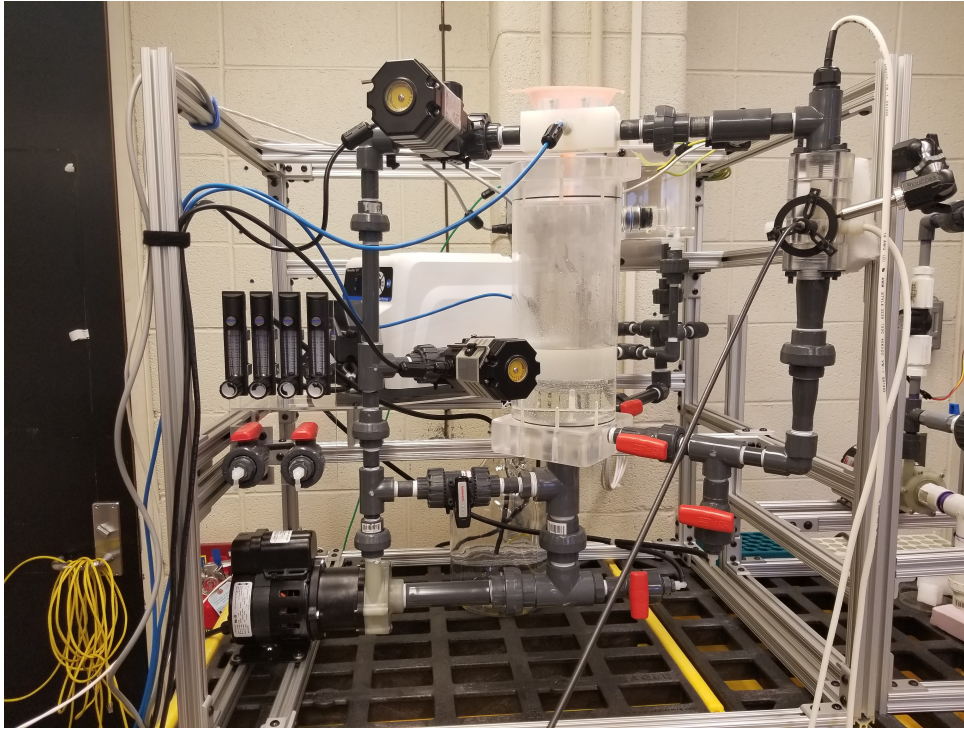
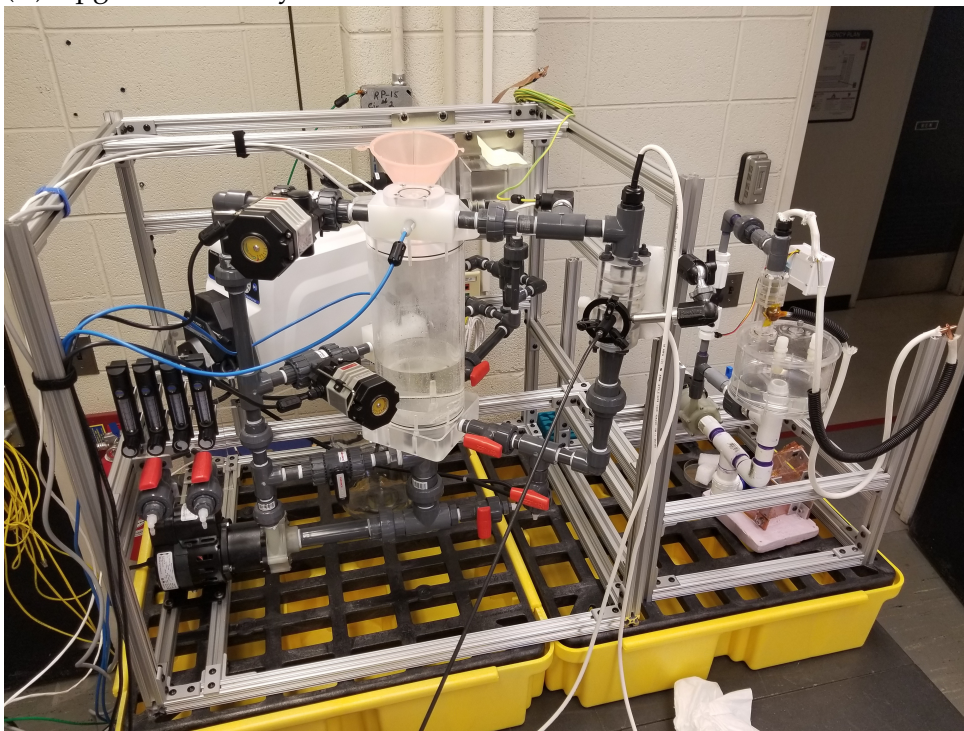


FIGURE 4.9: Schematic of upgraded PWR. The 80-20 framing around the system has a one inch-by-one inch cross section and can be used as a dimension reference.



(A) Upgraded PWR system.



(B) Upgraded PWR (left) next to standard PWR (right).

FIGURE 4.10: Images of the upgraded (real-time) PWR and a side-by-side comparison with the standard PWR.

The process, instrument, and circuit diagram of the upgraded PWR subscale system (Fig. 4.9) is illustrated in Figure 4.11, which features the original closed loop configuration (Fig. 4.8) plus DAQ equipment (top left), optional gas injection (top), and a peristaltic pump subsystem to regulate water flow in and out of the system (bottom right). Information and descriptions for all of the equipment in Figure 4.11 are listed in Tables 4.3 and 4.4, respectively.

The data are transmitted via AI/AO 4–20 mA signals, which is the de facto standard for industrial process control; 24 VDC was still needed to power the signal conditioners, the pressure transducer, and the AO module. The turbine-based flow meters are current-sinking open collectors (NPN) and need VDC to provide a pulsing frequency that is proportional to the number of rotations, or flow rate. The signal conditioners are programmed to count the pulses, incorporate the K-factor (# of pulses/gal) and bounds of the meters, and output a corresponding 4–20 mA signal. The pressure gauge outputs 4–20 mA but, it must be grounded, which may interfere with experimental results, particularly conductivity. Finally, the AO module uses the DC voltage to provide 4–20 mA for valve position and peristaltic pump speed. Not listed in Tables 4.3 and 4.4, a compact DAQ chassis (National Instruments 781157-01) is the liaison between the AO/AI modules and the computer.

Also not listed in Table 4.3, a 600 RPM variable speed motor (Cole Parmer 07528-10) drives the two peristaltic pump heads (EPH and IPH) at the same speed. This implies that one or both of the pump heads can be used to sample or prepare, and enable flow-through, respectively. In other words, the peristaltic pump can assist in semi-batch or once-through mode and rinse or drain the contact tank. Dual-channel pump heads help minimize pulsation and the peristaltic pump subsystem uses FDA-compliant viton tubing (Cole Parmer 96412-25). The rotameters are used to fine-tune

influent and effluent flow rates and backflow is controlled by the check valves (McMaster 47245K12, polypropylene body with fluoroelastomer diaphragm). High density polyethylene (HDPE) 1 gal jugs, typically used for waste disposal, are utilized for the influent, effluent, and DI water sources. Although other containers and direct water and wastewater lines can be used, these jugs sit compactly below the peristaltic pump. Jug ports were fitted with carbon filters to address any exhaust fumes as an additional safety precaution. Contaminant-based experiments were performed with the entire apparatus in the fume hood.

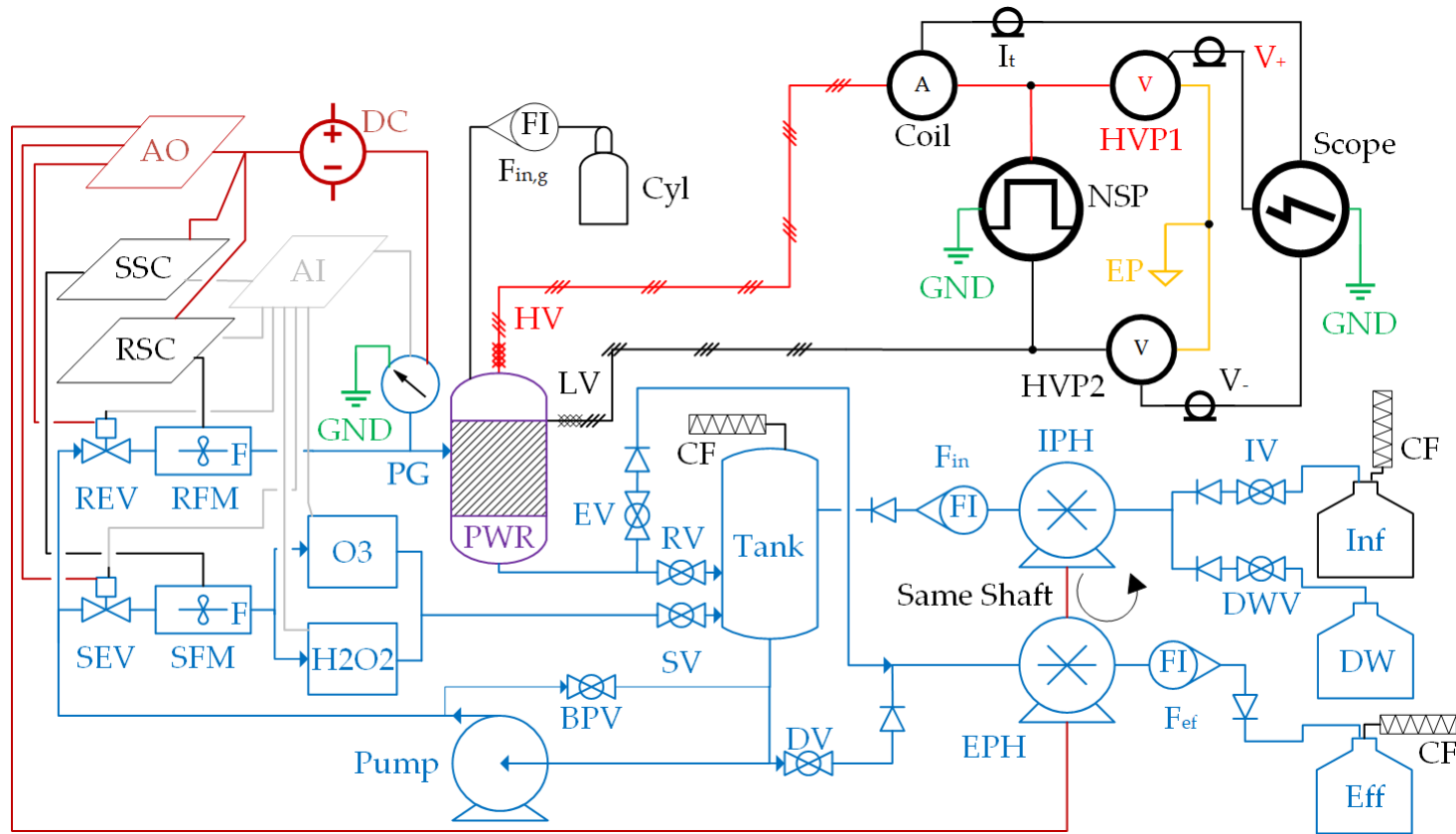


FIGURE 4.11: Process instrument and circuit diagram for the PWR with real-time diagnostics.

TABLE 4.3: Equipment list for the upgraded PWR subscale system (Fig. 4.11). Items not shown can be found in Table 4.1.

Code	Name	Manufacturer	Model	Material
AI	AI Module	National Instruments	779516-01	
AO	AO Module	National Instruments	779334-01	
DC	DC power supply	Omega	iDRN-PS-1000	
RSC/SSC	Reactor/Sensor Signal Conditioner	Omega	iDRN-FP	
PWR Tank	Plasma Water Reactor Contact Tank	Kent Pruss	v4RT	PMMA
Pump	Centrifugal Magnetic Drive Pump	March Pumps	AC-5C-MD	Polypropylene
RFM	Reactor Flow Meter	Omega	FPR302	Polypropylene
SFM	Sensor Flow Meter	Omega	FPR301	Polypropylene
REV/SEV	Reactor/Sensor Electric Valve	Valworx	566257	PVC
PG	Pressure Gauge	PressureWorx	34452	
DWV/DV	DI Water/Drain Valve	McMaster	4953K53	PVC
EV/IV	Effluent/Influent Valve	McMaster	4953K53	PVC
RV/SV	Reactor/Sensor Valve	McMaster	4953K53	PVC
BPV	Bypass Valve	Valworx	551008	PVC
H ₂ O ₂	H ₂ O ₂ Sensor/Flow Cell	Analytical Technology	Q46	PVC, 316SS, PMMA
O ₃	O ₃ Sensor/Flow Cell	Analytical Technology	Q46H/64	PVC, 316SS, PMMA
CF	Carbon Filter	Foxx Life Sciences	EZwaste	
Cyl	Gas Cylinder			Ar, others
DW/Eff/Inf	DI Water/Effluent/Influent jug	Millipore Sigma		HDPE
F_{ef}/F_{in}	Effluent/Influent Flow Meter	McMaster	5079K55	Polycarbonate
$F_{in,g}$	Influent Gas Flow Meter	McMaster	5079K65	Polycarbonate
EPH/IPH	Effluent/Influent Pump Head	Cole Parmer	77202-60	316SS

The DAQ modifications (Fig. 4.7) were reflected in an ambition to create a negative feedback loop of analysis and treatment such that the PWR is fully automated. Unfortunately, attempts to use the full upgraded system prior to finishing this thesis failed due to EMI. The desire to operate at higher power in order to demonstrate scale results in more and severe EMI. After several shielding attempts, EMI was mitigated enough to allow the collection of optical emission spectroscopy.

While all these new features are favorable and work towards a minimum viable product, EMI caused by energetic electrons can significantly interfere with DAQ and remains a persistent problem. In fact, it temporarily prevented an extensive ROS study. As EMI is further mitigated with techniques such as ferrite cores and an improved Faraday cage, the upgraded PWR subscale system can be an effective way to quickly map out the electronic parameter space of a given, custom water matrix.

As a short-term solution, the standard subscale PWR was placed several meters away and retrofitted to components of the upgraded setup to yield the system depicted in Figure 4.12. The I-V traces and $\text{H}_2\text{O}_2/\text{O}_3$ concentrations were used to determine ROS dose for various power and pulser parameters.

4.3 Pulser Parametric Study

Plasma water treatment appears to be best suited for trace organic removal. Plasma-based systems must be compared to existing work by roughly quantifying their ROS production, specifically [$\bullet\text{OH}$] and its reaction rate in solution. Traditional AOPs utilize precursors that allow for the direct determination of $\bullet\text{OH}$ production. In plasma-based systems, on the other hand, all precursors are not well quantified or understood. In this work, the contribution of the peroxone process to $\bullet\text{OH}$ production in the PWR is assessed by measuring H_2O_2 and O_3 . In an attempt to determine the roles of the lesser known species and compare the PWR to traditional AOPs, these measurements can

TABLE 4.4: Equipment description or operating conditions for the up-graded PWR system (Fig. 4.11). Items and their descriptions not shown can be found in Tables 4.1 and 4.2, respectively.

Code	Description or Conditions
Scope	Ethernet connection used for data acquisition
AI	AI from electric valves & flow meters, H ₂ O ₂ , O ₃ , and transducer
AO	AO to peristaltic pump drive, and reactor and sensor electric valves
DC	Supplies 24 VDC to signal conditions, transducer, and AO module
RSC	Conditions NPN signal from REV to 4–20 mA
SSC	Conditions NPN signal from SEV to 4–20 mA
PWR	Nozzle with concentric 316SS rod & Cu mesh electrodes Thin (1/16") PMMA in between outer most jets and Cu mesh
Tank	~1 gal vessel, PWR and sensor lines enter at bottom
Pump	17 GPM max flow at 60 Hz
RFM	Turbine-based, current sinking (NPN) with $F \in [0.1, 10]$ GPM
SFM	Turbine-based, current sinking (NPN) with $F \in [0.07, 5]$ GPM
REV	4–20 mA AI/AO Ball Valve
SEV	4–20 mA AI/AO Ball Valve
PG	Grounded transducer with 4–20 mA output
DV	Ball valve used to empty the contact tank
DWV	Ball valve for DI water that dilutes influent or rinses reactor
EV	Enables semi-batch or once-through operation and sampling
IV	Ball valve to allow contaminated water to enter the system
RV	Ball valve used to control flow to reactor
SV	Ball valve used to moderate flow from sensor flow cells
BPV	Ball valve used to relieve pump pressure
H ₂ O ₂	Polarographic membraned sensor with AO; susceptible to Cl
O ₃	Polarographic membraned sensor with AO
CF	Safely prevents exposure to off-gases
Cyl	Gas injection for changing kinetics
DW	DI Water jug for diluting or rinsing out reactor
Eff	Effluent jug for storing waste; can be a stream
F_{ef}	2–25 gal/h rotameter with knob for effluent
F_{in}	2–25 gal/h rotameter with knob for influent
$F_{in,g}$	1–11 standard ft ³ /h (scfh) rotameter with knob for influent gas
Inf	Influent jug for storing contaminated water; can be a stream
IPH	Dual-channel peristaltic pump head for influent
EPH	Dual-channel peristaltic pump head for effluent

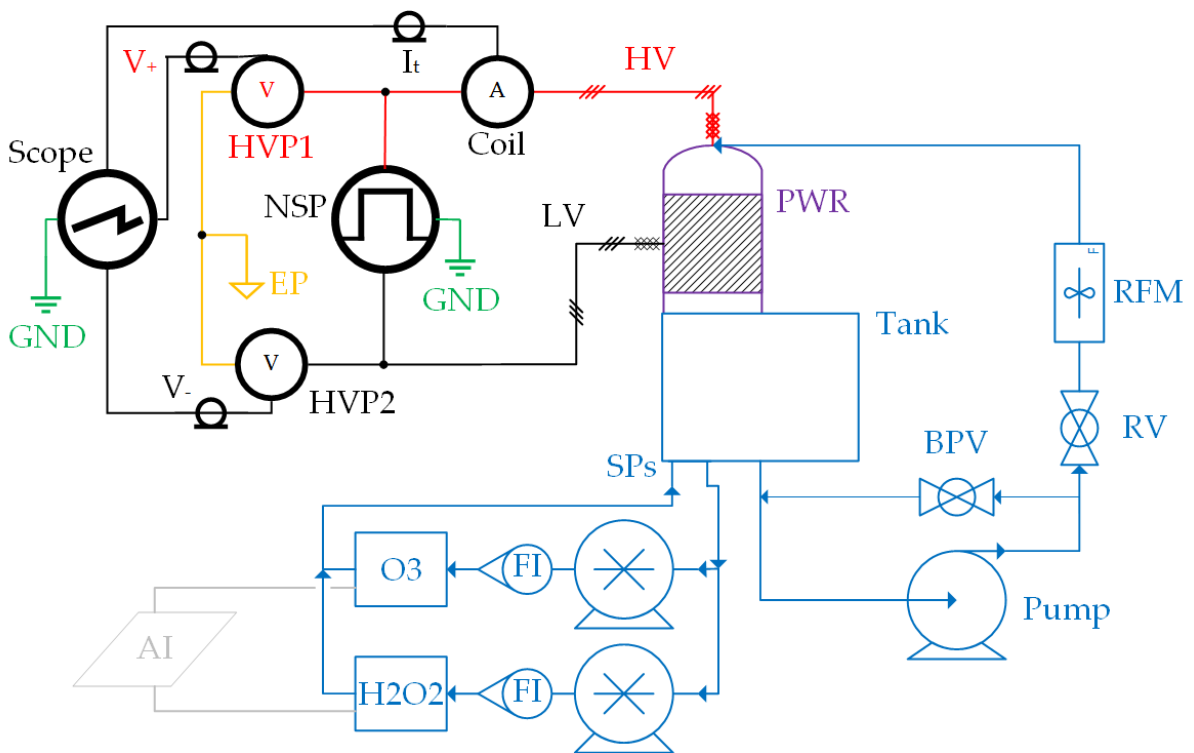


FIGURE 4.12: Modified process flow and circuit diagram for the PWR where a peristaltic pump is added to send water to the H₂O₂ and O₃ sensors.

be used in conjunction with decomposition studies of contaminants that have known $\bullet\text{OH}$ pathways and conventional AOP metrics, such as $\frac{\text{H}_2\text{O}_2}{\text{O}_3}$, $R_{ct} = \frac{[\bullet\text{OH}]}{[\text{O}_3]}$, and $R_{OH,UV} = \frac{[\bullet\text{OH}]}{H}$.

Prior to measuring ROS, V_p , f_p , and t_p were swept across the pulser parameter space to identify qualitatively and quantitatively different discharges in DI water. The DI water used in all experiments was Milli-Q Type 1 water with $\text{TOC}_i \approx 3$ ppb, $\text{pH}_i \approx 6$, and $18.2 \text{ M}\Omega \text{ cm}$ at 25°C .

4.3.1 Fluid and Discharge Effects

Jet stability issues in the early PWR prototypes (Figs. 4.1a, 4.1b, and 4.2) encouraged explorations into fluid effects early on. In order to achieve the design criteria outlined in Chapter 3, the subscale PWR needed to further decrease the spacing in the jet lattice, which is illustrated in Figure 4.13a. While this design sustained atm air breakdown ($|\vec{E}_{br}| \approx 30 \text{ kV/cm}$) throughout most of the reactor in simulations, PBDBD propagation is contingent upon jet structure. Although the water jets were simulated as cylindrical rods that maintain their shape, this is unlikely since high-throughput typically requires turbulent flow, as evident in Figure 4.13. While the subscale design had significantly improved the distribution of streamers throughout the PWR in experiments, it was difficult to determine whether discharges were taking place along the surfaces of the inner water jets.

Given that water jet perturbations are inevitable, it is critical to ensure that the jets are stable enough for long enough to enable sufficient plasma propagation and exposure. This implies that the PWR does not necessarily have to operate with laminar flow. In fact, it is favorable to operate with semi-stable turbulent flow since it enables higher flow rates and does not require a specially-machined nozzle. The Reynolds number (Re) is the ratio of inertial to viscous forces in the fluid and provides some insight into

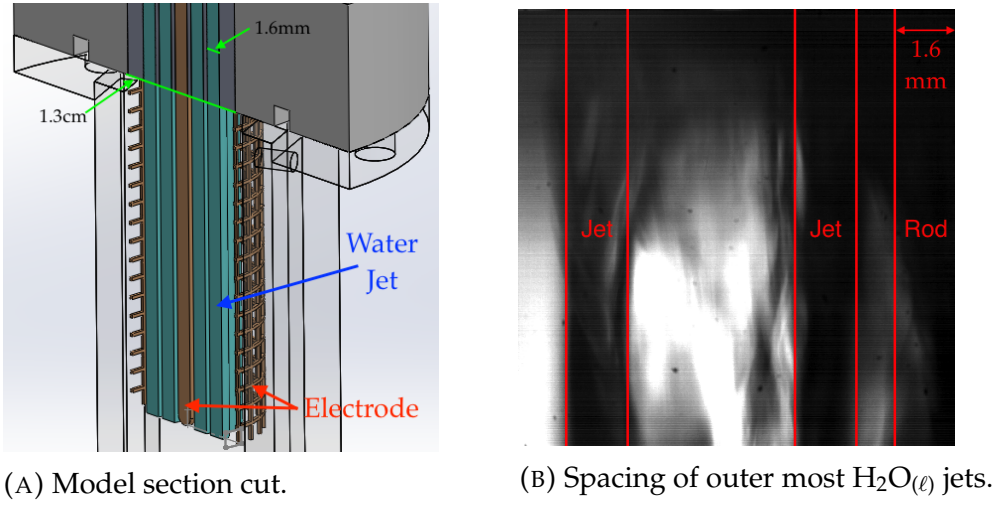


FIGURE 4.13: The ideal and actual water jet structure in the subscale PWR represented by the model and image, respectively.

the type of fluid flow. It is a function of water density (ρ), dynamic viscosity (μ), fluid velocity (v), and hydraulic diameter (D_H). For the PWR, Re can be expressed in terms of flow rate (F), jet diameter (d_j), and number of jets (N_j), as shown in Eq. 4.2. Based on the experiments performed, the average flow rate was roughly 1.2 GPM, which corresponds to $Re \sim 3800$ at standard temperature and pressure for the standard subscale PWR (Fig. 4.4). This Reynolds number suggests that the water jets are turbulent.

$$Re = \frac{\rho \cdot v \cdot D_H}{\mu} = \frac{4\rho \cdot F}{\pi \cdot \mu \cdot d_j \cdot N_j} \quad (4.2)$$

Without the outer electrode in place, water flow in the PWR was imaged with an intensified charged-coupled device (ICCD) camera. The PWR's reaction chamber, where the electrodes are housed, is a square prism and thus, the flat surface prevents optical distortion. The jets appear to be stable at the nozzle effluent and throughout the reaction chamber, as pictured in Figure 4.13b. While this can be true for water flow alone, jet stability is not guaranteed during plasma interactions. However, atm streamers are highly irregular discharges that can perturb the water jets. For this work, Re was

roughly fixed with a flow of $F \sim 4.3$ L/min. Without plasma but with flowing water, the capacitance of the system is approximately 80 pF, which was measured with a QuadTech 1730 LCR digi-bridge.

For the same Re , the plasma can experience different discharge modes depending on pulser settings. Similar to the modes seen in Figure 4.2, the modes in the subscale PWR appear to be two distinct regions. In Figure 4.14, the dimmer, streamer-like discharge (Fig. 4.14a) and its I-V are shown in the top half whereas the brighter, arc-like discharge (Fig. 4.14b) and its I-V are shown in the bottom half. At a higher voltage but same frequency, the more powerful discharge exhibits a significant secondary current spike in the latter half of the pulse prior to the fall time and a notable tertiary pulse after the fall time. The white and brighter discharges in this mode suggest high electron density. Though the lower power mode has a much less prominent local current maxima after the fall time, both modes witness ringing in the pulse tail, which indicates the oscillating impedance match of the NSP and PWR.

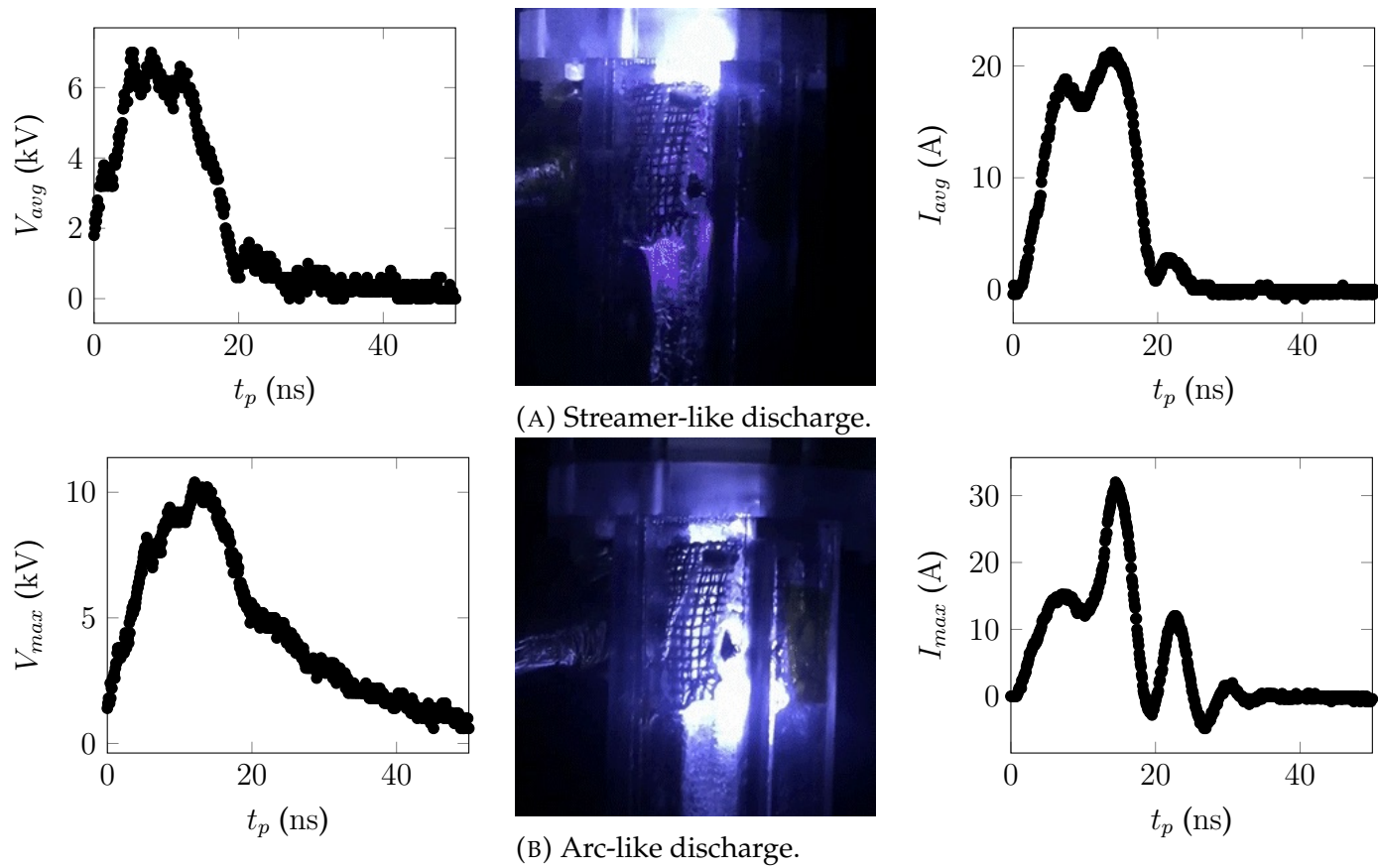


FIGURE 4.14: For same pulser parameters, different PWR plasma discharge modes and their associated currents.

Based on initial tests, when a particular set of parameters provided the brighter mode, one of the three pulser parameters were varied to see what happens to the discharge. Voltage seemed to have the largest effect on discharge mode. Interestingly, at higher power mode, as pulse width increased, the secondary current pulse would roughly start at the same time and would sustain the higher current until the pulse fall time. This indicates that once it jumps to the higher mode, the discharge will not extinguish until the pulse turns off, suggesting arc-like properties. During a given experiment, the plasma can oscillate very few or many times between the two modes, which is evident in power profiles by erratic fluctuations in the measured deposited power. Since f_p is \sim kHz and the DAQ code as written is relatively slow (\sim 0.8s time step), information about the occurrence and dynamic nature of these arc-like modes are mostly lost.

A typical deposited power profile for a lengthy experiment ($t > 5$ min) operating near the limits of the pulser parameter space is plotted in Figure 4.15. The arc-like discharges predominantly occur before the maximum and significantly deviate from the bulk of the data. Most of the data that fits on the power curve appear to correspond to streamer modes, suggesting that there are more streamer modes than arc modes but, this must be validated with faster DAQ. Though not many high power modes are seen here, fluctuations caused by the arc-like discharges can substantially oscillate above and below the bulk data, implying that there are inherent instabilities with this mode since the pulser is not properly matched, though more work needs to be done.

4.3.2 ROS Dose

Using the experimental setup illustrated in Figure 4.8, constant volumes ($V_{sys} = 0.5$ L) of DI water were exposed to plasma in the subscale PWR (Fig. 4.4) for various treatment times (t_t) and pulser parameters. The goal of this study is to determine

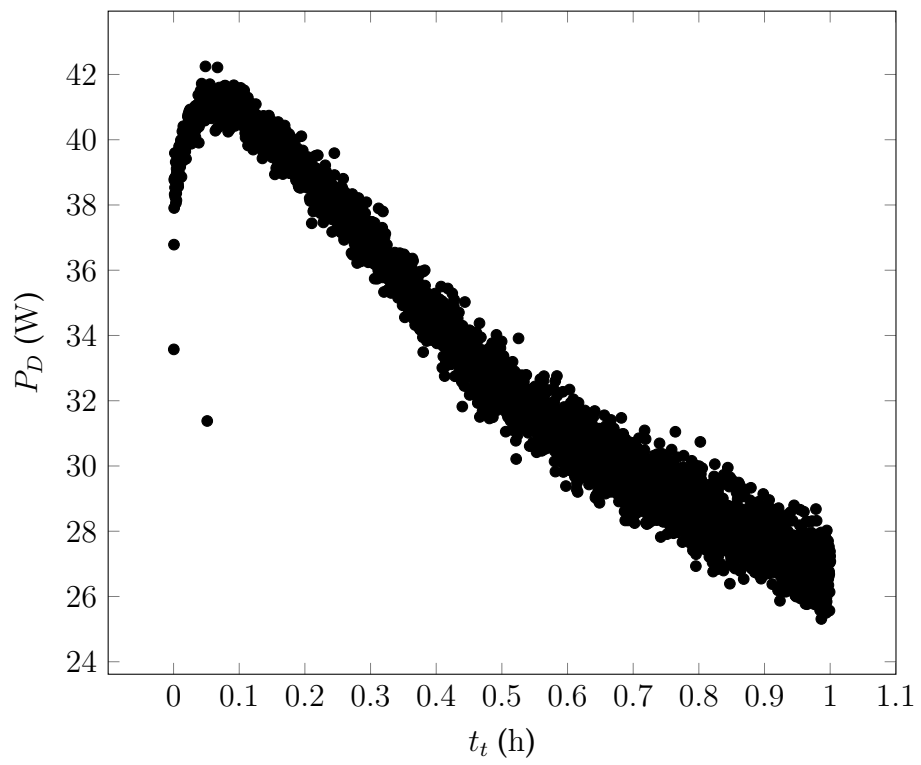


FIGURE 4.15: Typical power profile during long ($t > 5$ min) experiments.

the relationships between ROS dose, deposited power, and pulser parameters and to identify the rate-determining step, specifically if mass-limited transfer occurs for O₃. Established AOP species, such as H₂O₂, O₃, and UV, should be measured in order to provide direct comprehensive comparisons. However, it is extremely difficult to accurately measure these radicals due to many complex plasma-based AOP pathways.

Using the NSP, pulses of various width ($t_p \in [40, 80, 120]$ ns), repetition frequency ($f_p \in [1, 5, 10]$ kHz), and peak voltage ($V_p \in [10, 15, 20]$ kV) resulted in I-V characteristics and discharges similar to those in Figure 4.14. Measured pulser parameters and dissipated power were extracted from I-V waveforms using the in-house code. At the end of an experiment, a sample is tested in the photometer to measure O₃ whereas chemical test strips and a water meter were used to measure H₂O₂, pH, TDS, temperature, and DO directly in the contact tank (see Table 4.1 for equipment information). For O₃ measurements, the N,N-Diethyl-p-phenylenediamine (DPD) colorimetric method was performed at 525 nm and had an error of ± 0.02 mg/L or $\pm 3\%$ of reading at 25 °C. O₃ was immediately measured after testing to avoid desolvation. For H₂O₂ measurements, peroxidase transfers O₂²⁻ to an organic redox indicator and the strips had a quantized scale of 0.5, 2, 5, 10, and 25 mg/L. In both cases, the DPD method and the H₂O₂ reagent strips are subject to oxidation by other oxidants, such as chlorine, implying that more potent plasma-based radicals can affect these measurements. Thus, without additional analysis, using chemical probes to quantify ROS concentrations is an inadequate approach.

While the objective is to minimize power consumption and to maximize ROS dose, the ultimate intent is to tailor chemistry by understanding AOP pathways across the pulser parametric space. The dissipated power is energy transfer from the HV ns pulses to electrons, which then cascade into radicals via redox mechanisms. Subsequently, if power can be expressed in terms of pulser parameters, it may be possible to

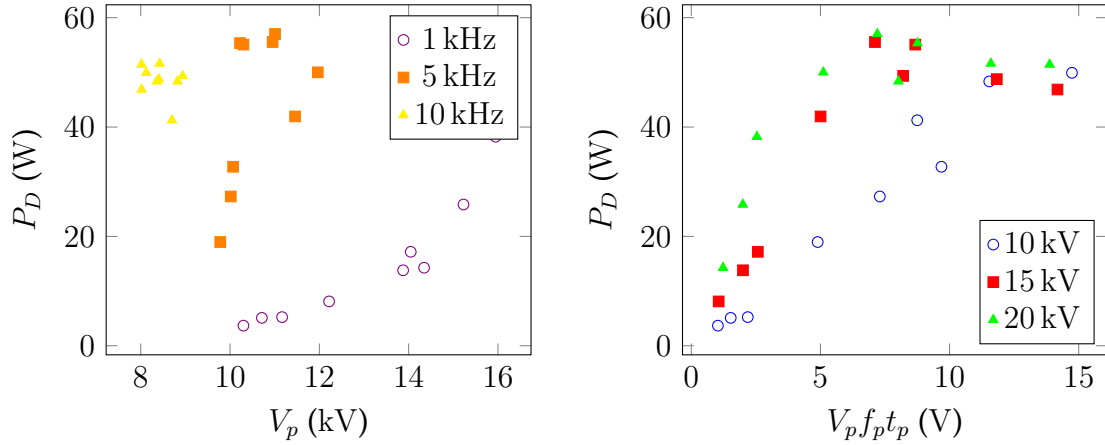


FIGURE 4.16: Deposited power for ROS ($\text{H}_2\text{O}_2/\text{O}_3$) dose and ΔpH in the PWR closed loop configuration (Fig. 4.8) for DI water, $V_{sys} = 0.5 \text{ L}$, and $t_t = 5 \text{ min}$. The left and right sides have f_p (kHz) and V_p (kV) in the legend, respectively.

simplify the system of equations.

Assuming the I-V waveforms can be portrayed as square, triangle, or trapezoidal pulsed waveforms, the dissipated power (Eq. 4.1) is proportional to V_p , f_p , t_p , and the maximum average current. This also assumes zero delay between applied voltage and current but, the shift, rise time, and fall time can be taken into consideration for a more accurate approximation. As a result, for $t_t = 5 \text{ min}$ in DI water ($V_{sys} = 0.5 \text{ L}$), power and water variables were conveyed as functions of pulser parameters, particularly V_p and $V_p f_p t_p$, in Figures 4.16 and 4.17. The results in Figures ?? and 4.17 were also plotted as functions of t_p and $f_p t_p$ but, there were no clear patterns in the data. Since V_p appears to display boundaries in the pulser operating space while $f_p t_p$ and t_p did not, this suggests that dissipated power is least and most affected by t_p and V_p , respectively.

The left column of Figures 4.16 and 4.17 shows a precise cluster of data for $f_p = 10 \text{ kHz}$, little variation in V_p for $f_p = 5 \text{ kHz}$, and a spread of V_p for $f_p = 1 \text{ kHz}$, indicating that the pulser cannot sustain the requested voltage at higher repetition frequencies. Since the power supply is made with fast switches (insulated-gate bipolar transistors), the power-limited NSP will deliver the demanded repetition frequency at the expense

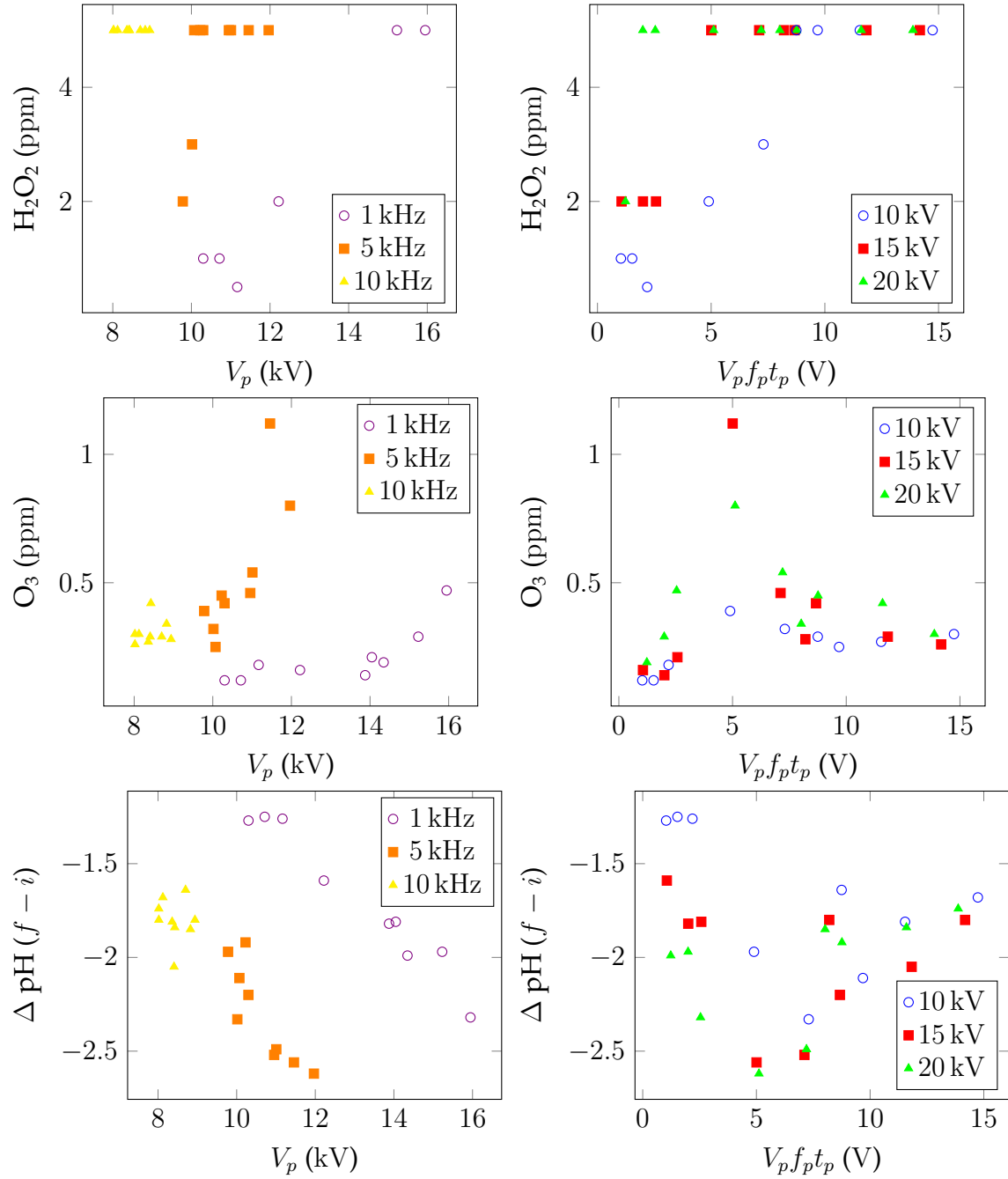


FIGURE 4.17: ROS (H₂O₂/O₃) dose and ΔpH in the PWR closed loop configuration (Fig. 4.8) for DI water, $V_{sys} = 0.5L$, and $t_t = 5$ min. The left and right sides have f_p (kHz) and V_p (kV) in the legend, respectively.

of voltage. Since the NSP can sustain f_p at the expense of V_p and t_p at the limits of its operating space, a frequency sweep is needed to better understand the role f_p plays in dose and power. For $f_p = 1$ kHz and $f_p = 5$ kHz, O_3 production increases around $V_p = 14$ kV and $V_p = 10$ kV, respectively, suggesting that O_3 production is enhanced and likely increasing with V_p and f_p . At the higher end of f_p ($= 10$ kHz), the remaining tunability in V_p disappears since the NSP's limited maximum power (120 W) is not enough. These pulser parameters appear to control P_D , O_3 , H_2O_2 , $|\Delta pH|$, and therefore vary AOPs. Exploring the higher frequency space is favorable since it is a pathway to higher throughput (and also out of the human hearing range). Thus, a higher power NSP is needed to fully drive the PWR at requested pulser parameters.

The measured maximum peak voltage was weighted with its duty cycle to yield the right side of Figure 4.17. For $V_p = 15$ kV and $V_p = 20$ kV, P_D depicts knees that roughly correspond to maximum O_3 concentrations at $V_p f_p t_p \approx 5$ V. The plateauing of P_d implies that though f_p and t_p can increase, pulsed power (the product of the V-I waveforms) will decrease to yield a constant P_D . For $V_p = 10$ kV, P_D appears capable of continuing to rise at higher $f_p t_p$. For all three frequencies, O_3 concentrations would increase to their maxima at $V_p f_p t_p \approx 5$ V then decrease and plateau. $V_p f_p t_p$ is used to simplify the input pulser parameters into one variable that appears proportional with power. Although the maximum for $V_p = 10$ kV is not as pronounced and more research needs to be carried out, the maxima suggest that the combination of pulser parameters are more insightful than P_D alone. For P_D and $V_p f_p t_p$, a relationship cannot be derived for ΔpH whereas for V_p , ΔpH appears to be in two distinct regions separated by whether or not the NSP is maintaining the load. Nevertheless, $V_p f_p t_p$ helps identify roughly at what point does the power supply start to tap out. In this ROS study ($V_{sys} = 0.5$ L and $t_t = 5$ min), the subscale PWR system yielded $V_p f_p t_p \approx 5$ V. The final study in this work, real-time power and non-chemical H_2O_2/O_3 measurements for

various t_t , f_p , and t_p , utilized this approximate location of the NSP power limitations to select combinations of f_p and t_p at maximum V_p .

Therefore, out of the three controllable pulser parameters, preliminary ROS evidence suggests that the pulser variables can be ranked from most to least influential as such: V_p , f_p , and t_p . Furthermore, these combinations of pulser parameters appeared to vary the $\text{H}_2\text{O}_2/\text{O}_3$ ratio but, the quantization of the H_2O_2 reagent strips make it difficult to validate the extent of the spread in $\text{H}_2\text{O}_2/\text{O}_3$ ratio. Though more information is needed to verify this, it is a good starting point for trying to simplify and optimize kinetics with these parameters and other well known variables.

4.3.3 Variation of Hydrogen Peroxide-to-Ozone Dose

ROS ($\text{H}_2\text{O}_2/\text{O}_3$) dose was plotted as functions of power and pH change in Figure 4.18. As expected, H_2O_2 and O_3 concentrations increased with P_D . On the other hand, while pulses drive ROS production, water quality parameters can mitigate or enhance production. The $\text{H}_2\text{O}_2/\text{O}_3$ ratio and O_3 concentration are depicted as functions of ΔpH , which is important for O_3 . Different O_3 dosages are required for different pH levels since higher pH leads to greater $\bullet\text{OH}$ production, hence O_3 consumption (Elovitz and Gunten, 1999). Since the DI water batch acidifies during treatment, O_3 production should not be mitigated, which was evident in Figure 4.18. $\text{H}_2\text{O}_2/\text{O}_3$ was also plotted but, the quantization of the H_2O_2 strips (0.5, 2, 5, 10, 25 ppm) prevented detailed analysis. The range of H_2O_2 doses suggested that $[\text{H}_2\text{O}_2]$ may be influenced by discharge mode (Fig. 4.14) but, the strips were susceptible to other oxidants and may have misrepresented $[\text{H}_2\text{O}_2]$. Regardless, this ratio was much higher than the optimal $0.5 = [\text{H}_2\text{O}_2]/[\text{O}_3]$ (Miklos et al., 2018). Lastly, the direct linear relationship ($r^2 = 0.97$) between applied power (P_{app}) and P_D suggests that P_{app} can be used in lieu of P_D for kinetic studies. Indeed, the power meter (P3 P4460) used at the wall is much

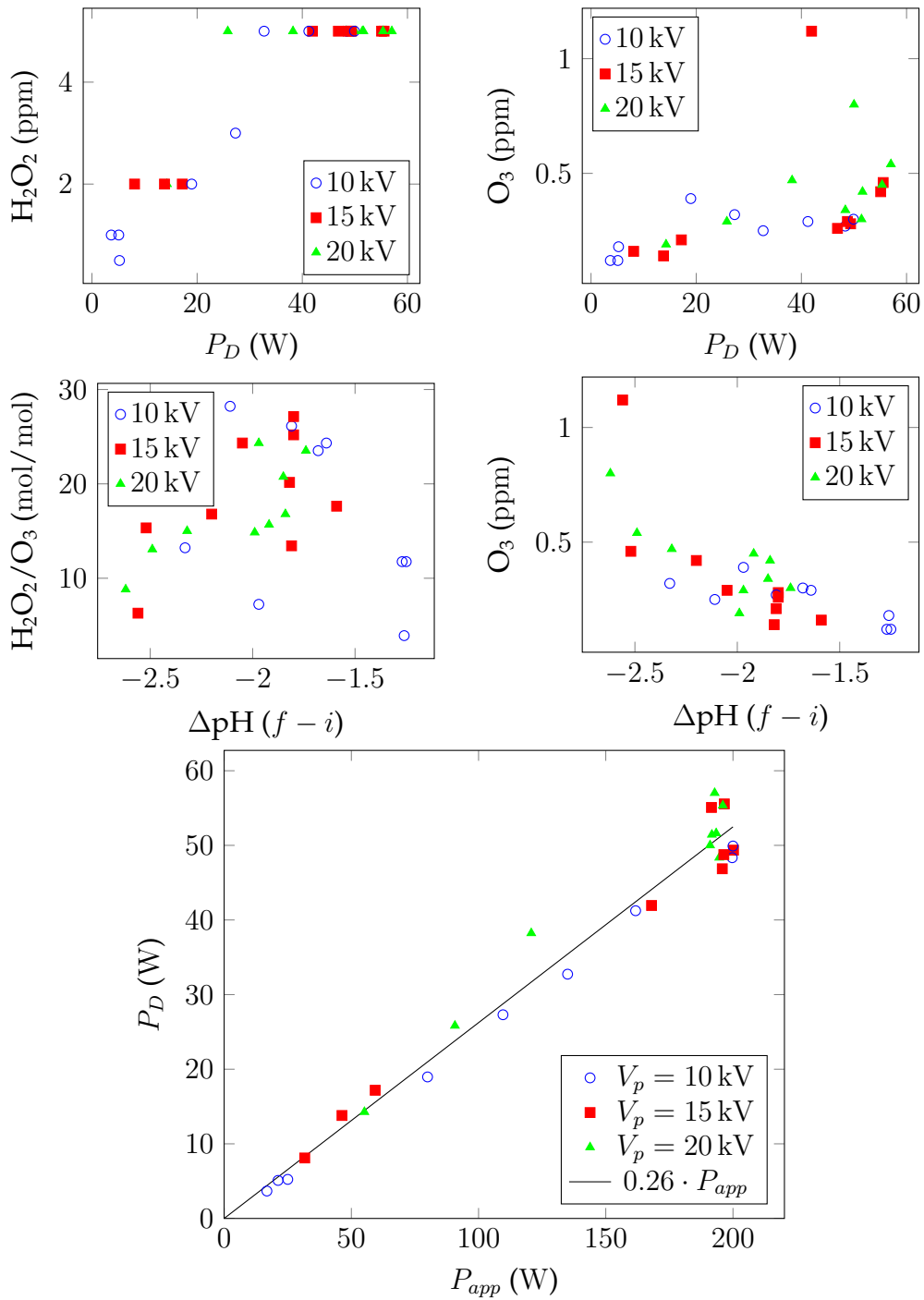


FIGURE 4.18: ROS (H_2O_2/O_3) dose as a function of power and pH in the PWR closed loop configuration (Fig. 4.8) for DI water ($V_{sys} = 0.5$ L) and $t_t = 5$ min.

more convenient and cost effective than I-V probes and a scope. Though the pulser's efficiency (26%) is poor, it can be significantly improved with better matching between the NSP and the PWR.

Based on Figure 4.18, the concentration-per-power (ROS/P_D) for H_2O_2 and O_3 are 3.7×10^{-4} ppm/J and 3.3×10^{-5} ppm/J, respectively, for $t_t = 5$ min. The same calculation was performed for $t_t = 10$ min for a few different voltages at a given repetition frequency. Though this experiment needs to be revisited, $t_t = 10$ min yielded 3.8×10^{-4} ppm/J for H_2O_2 and 1.7×10^{-5} ppm/J for O_3 , suggesting that either the NSP is power limited or O_3 is limited in mass transfer by $t_t = 5$ min.

For both treatment times, temperature (T_ℓ), conductivity, and DO were also measured. T_ℓ increases due to cyclic fluid pumping and when the control data is subtracted out, the change in T_ℓ is negligible, implying that the discharge is mostly non-thermal. Conductivity increases with time, leading to a false measurement in TDS. This must be considered when working with non-distilled water matrices. DO concentrations slightly increase then decrease and slowly plateau over treatment time. This pattern may be attributed to splashing in the contact tank and the continual consumption of oxygen for ROS production.

Nonetheless, based on the pulser parameter space when coupled to the PWR, the settings that provided the greatest ROS dose in the DI matrix will be used to assess the kinetics of indicator compounds.

4.4 Indicator Compounds

To assess the subscale PWR's ability to decompose organics, indicator compounds were spiked into DI water, one chemical at a time. Ideally, the kinetics of each single-compound-spiked batch should be explored across the pulser parameter space before

moving to multi-compound matrices. Such study should be complemented with a decomposition model to understand reaction pathways.

The first contaminant evaluated was methylene blue (CAS 61-73-4, > 95%). MB can be quantified by HPLCMS at 284.12 m/z or SPM at 609 nm (Foster et al., 2013). Using the experimental setup and procedure from the DI water ROS study (Fig. 4.8), DI water batches ($V_{sys} = 0.5$ L) were spiked with MB to an initial concentration of 50 ppm. 50 ppm was picked so that the PWR can demonstrate at least one-log reduction prior to falling below detection limits. The batches were treated using $V_p = 15$ kV, $f_p = 5$ kHz, and $t_p = 40$ ns, which was within the available operating parameter space and corresponded to the highest O₃ dosage in the previously described experiment.

Decomposition analysis by HPLCMS and SPM yielded first-order reaction rate constants of 1.62 s^{-1} ($r^2 = 0.98$) and 1.48 s^{-1} ($r^2 = 0.88$), respectively. The deviation in HPLCMS- and SPM-based concentrations suggests that absorption spectra alone is insufficient for determining species concentrations in plasma-based systems.

Using a HS-coupled GC instead, the same experiment was performed with MTBE (CAS 1634-04-4, $\geq 90\%$; methanol $\in [0.1, 1)\%$) and 1,4-dioxane (CAS 123-91-1, $\geq 90\%$) as the indicator compounds. Based on retention times of 9.63 min for MTBE and 14.52 min for 1,4-dioxane, the GC results, along with the MB HPLCMS data, are plotted in Figure 4.19. All three contaminants exhibited first-order decay with MTBE decomposing the fastest and 1,4-dioxane decomposing the slowest. Their time constants (τ) indicate that the batch needs to be cycled many times before sufficient destruction takes place. Without residual H₂O₂ and O₃ measurements, it was difficult to determine whether or not this was caused by mass transport limitations, limited NSP power, or poor PWR geometry.

Regardless, the curves in Figure 4.19 demonstrated decomposition that was on par or better than current plasma-based technologies. For MB, the PWR had $\tau = 37.3$ min,

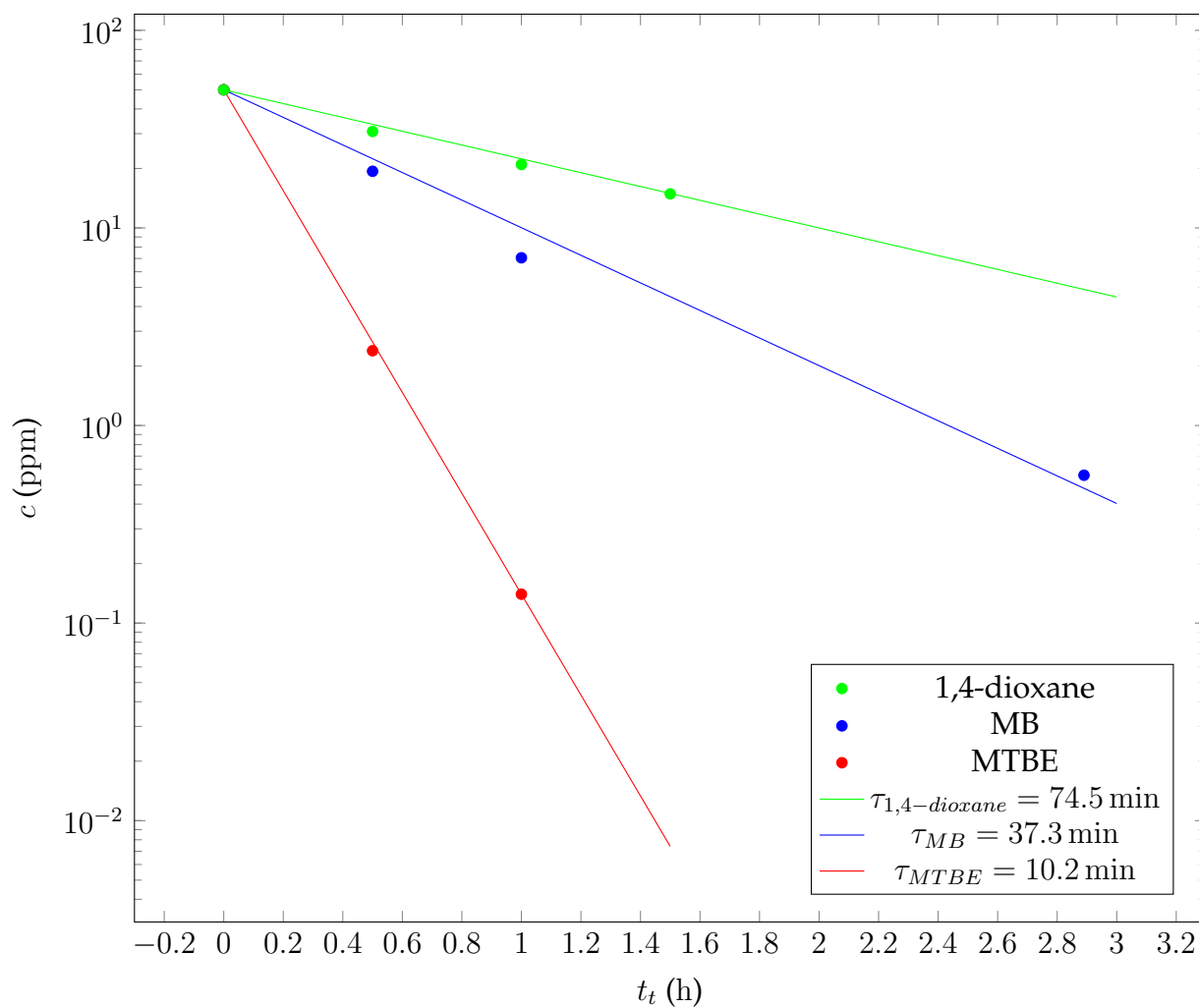


FIGURE 4.19: Decomposition of MB, MTBE, and 1,4-dioxane in the closed loop ($V_{sys} = 0.5$ L) PWR at $V_p = 15$ kV, $f_p = 5$ kHz, and $t_p = 40$ ns.

which is analogous to the atm plasma jet (Fig. 2.4a) at $\tau = 38.5$ min (Foster et al., 2013). This implies that their effective reaction rates were approximately equal. For MTBE, the PWR had an effective reaction rate that was roughly twice the effective rate in the AquaPure system (Fig. 2.4b) while consuming less energy.

Future studies should include real-time power and ROS measurements during periodic water matrix sampling. Since MTBE reacts with both $\bullet\text{OH}$ and O_3 (Mitani et al., 2002) whereas 1,4-dioxane only reacts with $\bullet\text{OH}$ (Stefan and Bolton, 1998), power and kinetic information about peroxone, MTBE, and 1,4-dioxane can be used to approximate the relative contribution of peroxone and other AOP pathways to plasma-based $\bullet\text{OH}$ production.

Given 1,4-dioxane's low effective reaction rate and its impact on public health, maximizing 1,4-dioxane destruction while maintaining energy efficiency is the objective of the following section.

4.5 Parametric Study of 1,4-dioxane Kinetics

1,4-dioxane is recalcitrant and its selectivity makes it the perfect compound for probing AOP kinetics. Pursuant to Title XXII regulations, a 0.5-log (69%) 1,4-dioxane reduction design criteria is required to demonstrate sufficient oxidation. Similar to the ROS study, a pulser parametric study is performed on DI water spiked with 1,4-dioxane. Though concentrations of interest are ~ 1 ppb for 1,4-dioxane, the initial concentration ($c_i = 50$ ppm) was picked due to the limited sensitivity of the analytical tools available at the time (the HS-coupled GC had a detection limit ≈ 1 ppm). The high concentration (ppm) parametric study started by monitoring and converting pulser variables into parameters such as P_D and conductivity, as shown in Figure 4.20. Then, the kinetics are expressed as functions of time (Fig. 4.20), energy density (Fig. 4.23), or

constituent concentrations (Fig. 4.24). Once again, the goal is to optimize kinetics using pulser parameters and predict reaction rates.

Using the previous experimental setup and procedure (Fig. 4.8), spiked DI water batches ($V_{sys} = 0.5$ L) are treated for various t_t using three different sets of pulser parameters: (20 kV, 1 kHz, 40 ns); (20 kV, 1 kHz, 120 ns); and (15 kV, 5 kHz, 40 ns). Based on the DI ROS experiments, the pulser settings are selected with a one-variable difference between each set; 20 kV would have been used in the last set but, the pulser could not sustain that voltage at 5 kHz. Throughout the following kinetic plots, the pulser parameters are expressed as a coordinate system (V_p [kV], f_p [kHz], t_p [ns]). In some cases, for clarity, legends are not included to prevent overlap with data points but, all of the 1,4-dioxane data use the same pulser coordinate legend.

Similar to Subsection 4.3.2, Figure 4.20 depicts input and derived expressions, primarily P_D , as functions of pulser parameters and time. This was performed to examine whether V_p , f_p , and t_p can ultimately vary the plasma-based peroxone pathways. Like the ROS study, dissipated power as a function of $V_p f_p t_p$ exhibits distinct discharge regions in the pulser parameter space, indicating that the plasma and its I-V characteristics are unaffected by the presence of an indicator compound in the DI water matrix. The slope of P_D and $V_p f_p t_p$ should provide a rough estimate of the average peak current; (20 kV, 1 kHz, 40 ns) data falls on the same line as (15 kV, 5 kHz, 40 ns) data, indicating similar currents. Unlike the other two cases, (20 kV, 1 kHz, 120 ns) was able to sustain initial pulser parameters, namely V_p , and dissipated power over time. Compared to the (20 kV, 1 kHz, 40 ns) case, (15 kV, 5 kHz, 40 ns) operated at higher power and experienced a greater decrease in power and peak voltage over time, which suggests that operating at the limits of the pulser parameter space can be detrimental to load coupling between the NSP and PWR. The distribution in power in the $V_p f_p t_p$ plot can also be used to interpret the degree of deviation from peak power and voltage over

time, further promoting the possibility of representing key variables, such as dose and power, in the pulser parametric space.

As illustrated in Figures 4.21 and 4.22, the three pulser configurations resulted in time-dependent kinetics. In the top left plot of Figure 4.21, the data set of (20 kV, 1 kHz, 40 ns) displayed the slowest destruction, which makes sense given that it operated at lower power relative to the other two pulser arrangements. Interestingly, though more information is needed, the higher frequency case (15 kV, 5 kHz, 40 ns) exhibited several slight slope changes, implying transitions between different reaction rate regimes. The log-reduction ($\log_{10} \frac{c_i}{c_f}$) can be calculated and is shown in the top left plot of Figure 4.22. The 0.5-log reduction line is drawn and all three cases would meet this threshold by $t_t = 2$ h.

Since the subscale PWR is a closed loop system and 1,4-dioxane is expected to exhibit first-order decay, the effective flow rate of the system, which is defined as 90% removal, can be expressed as $F_{eff} = \frac{V_{sys}}{t_t} \log_{10} \frac{c_i}{c_f}$. For first-order decay, the effective flow rate should remain constant for a given power, which is evident except for the beginning of (15 kV, 5 kHz, 40 ns). Subsequently, the slope of P_D and F_{eff} for each pulser parameter arrangement should be constant and correspond to the average E_{EO} . However, this was inconclusive due to the clustering and insufficient number of data points, per Figure 4.22. Alternatively, the E_{EO} can be calculated for each time step using Equation 1.2. This plot demonstrated that each configuration exhibited an E_{EO} that increases, stays constant, or decreases with time. This confirmed that NSP-PWR matching and water treatment are load and pulser parameter dependent.

The changing log-reduction and effective flow rate of 1,4-dioxane using (15 kV, 5 kHz, 40 ns) indicated that other prominent species form to sufficient concentrations and compete with 1,4-dioxane for $\bullet\text{OH}$, which influences the effective reaction rate of 1,4-dioxane. This makes sense since some reactive species, such as NO_3^- , have high

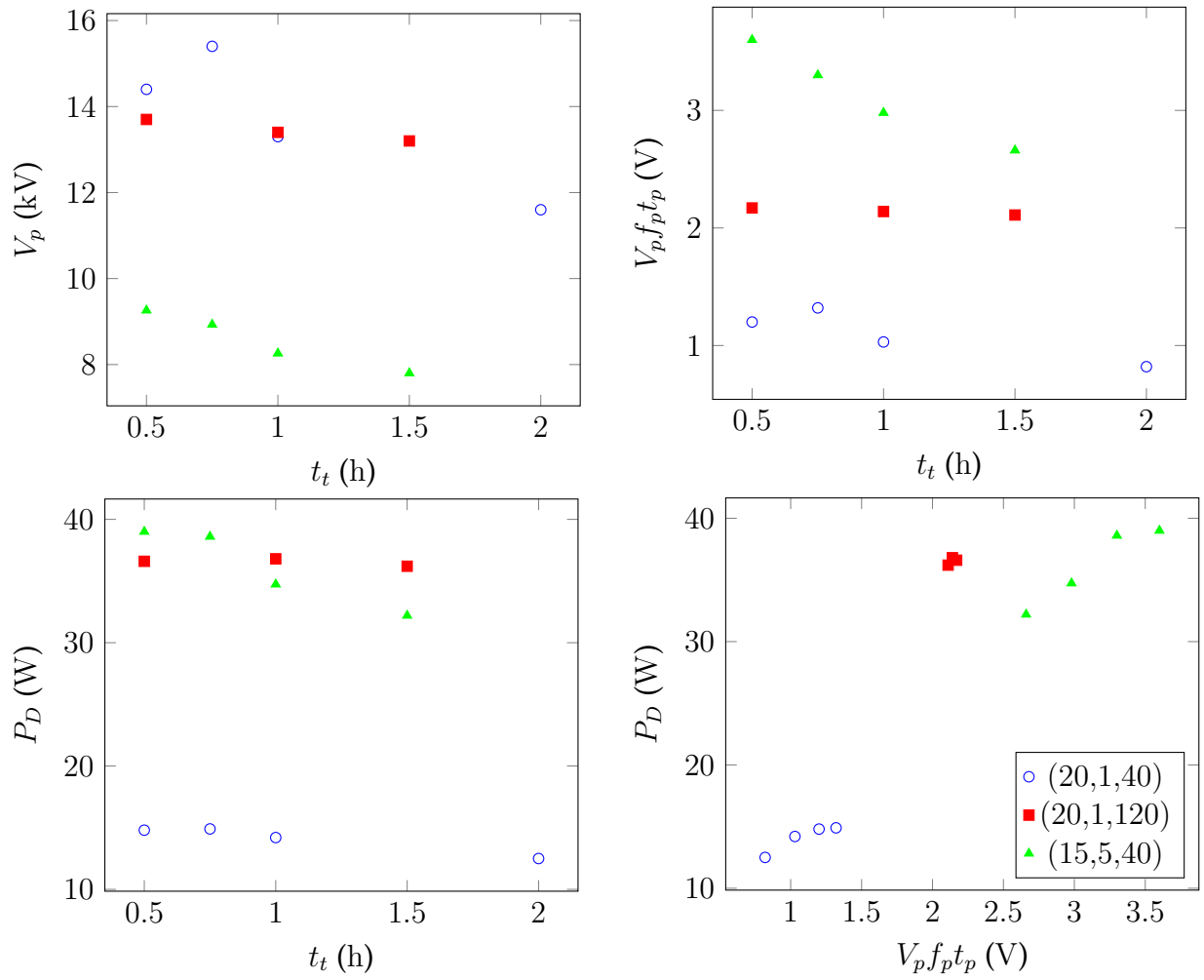


FIGURE 4.20: Power characteristics of various pulsing techniques during PWR treatment of 1,4-dioxane batches ($c_i = 50$ ppm). The legend is given in coordinates of (V_p, f_p, t_p) with units (kV, kHz, ns) and all plots have the same legend.

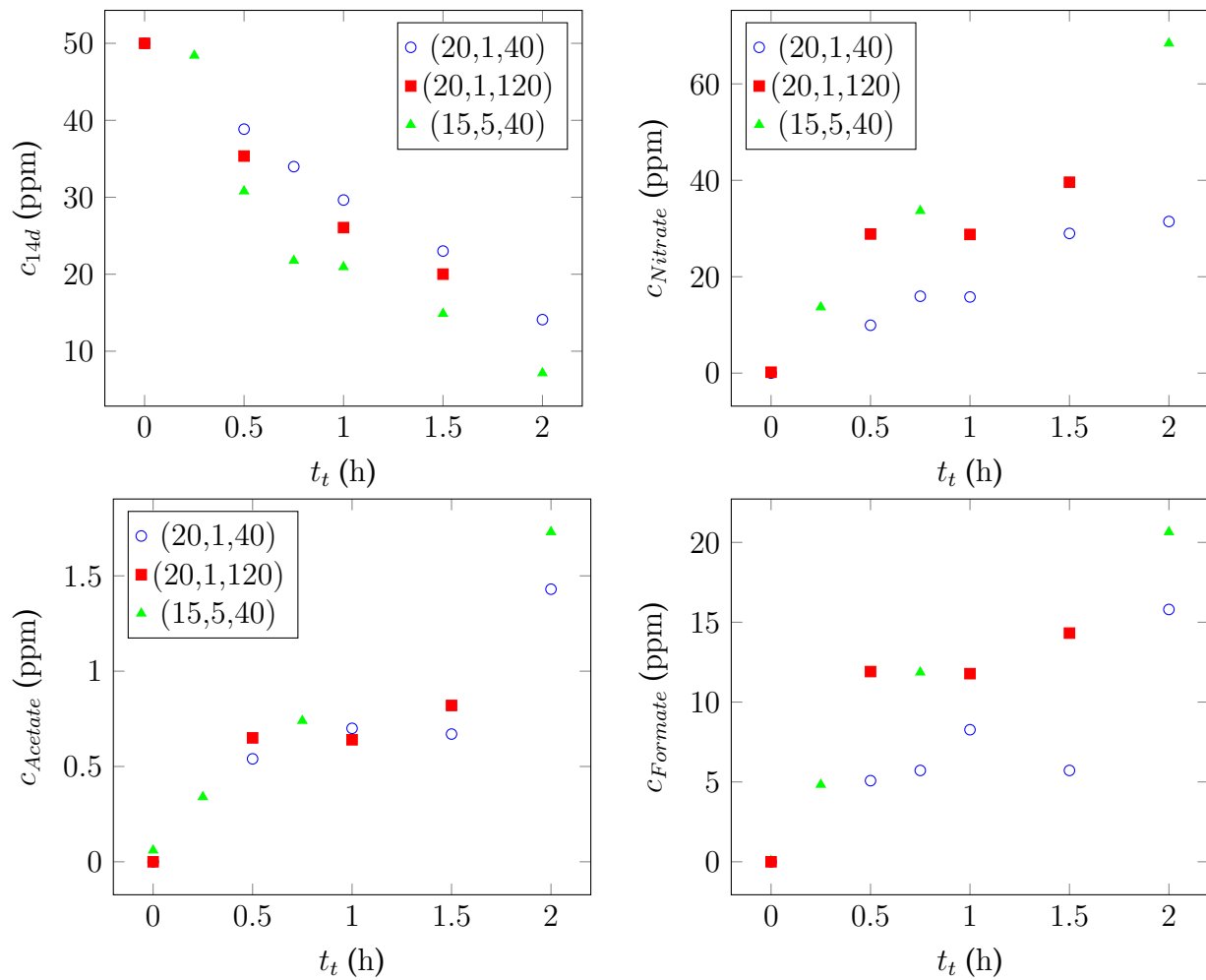


FIGURE 4.21: 1,4-dioxane kinetics of various pulsing techniques during PWR batch treatment ($c_i = 50$ ppm). The legend is given in coordinates of (V_p, f_p, t_p) with units (kV, kHz, ns) and all plots have the same legend.

radical reaction rates and can accumulate in the system, thus significantly increasing the scavenging capacity. The $\bullet\text{OH}$ -consuming species include transformation products and other constituents in the water matrix. Therefore, these species and their mechanisms must be better understood prior to investigating practical, more complex water matrices.

Formic acid and acetic acid are 1,4-dioxane intermediates (Stefan and Bolton, 1998) and nitric acid is an air plasma byproduct. Formate, acetate, and nitrate concentrations were measured with an IC (Fig. 4.21). The reaction rates of formate and acetate appear to transition to lower values around $t_t = 30$ min and then appear to return back to their original values around $t_t = 1.5$ h. Prior and during this region, 1,4-dioxane is still consuming $\bullet\text{OH}$ as evident in its decreasing concentration, resulting in formate and acetate being formed, yet the byproduct reaction rates plateau. It is unclear what species and mechanisms are responsible for this. If the experiments went longer, both formate and acetate should reach a maximum then decrease back to zero. On the other hand, nitrate appears to be directly proportional with t_t regardless of configuration, which is a consequence of air plasma. Other than the slight change in slope for (20 kV, 1 kHz, 120 ns), nitrate concentrations suggest that the overall kinetics of the system do not affect this terminal species. This will be an obstacle to PWR implementation but, parameters can be optimized to mitigate NO_x production or the PWR can be combined with nutrient recovery.

As demonstrated in Figure 4.23, energy density provides insight into decomposition capabilities and cost, which can be used to compare the PWR to traditional AOPs. While (20 kV, 1 kHz, 40 ns) exhibited the slowest 1,4-dioxane decomposition (Fig. 4.21), it is the most energy efficient, requiring half of the energy density used by the other two configurations to achieve 0.5-log reduction. When E_{EO} is plotted as a function of energy density, the relationship seen is similar to E_{EO} as a function of time, indicating

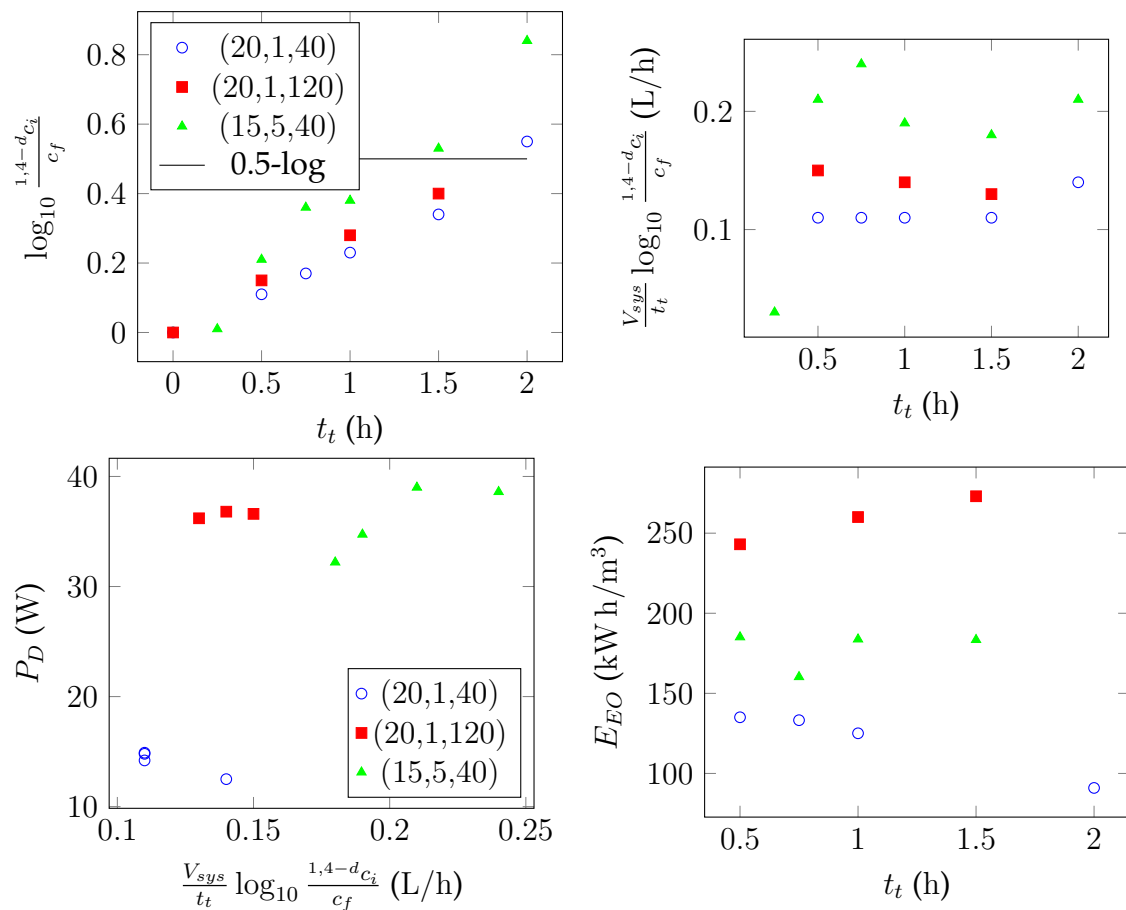


FIGURE 4.22: Derived parameters for 1,4-dioxane kinetics of various pulsing settings during PWR batch treatment ($c_i = 50$ ppm). The legend is given in coordinates of (V_p, f_p, t_p) with units (kV, kHz, ns) and all plots have the same legend.

that an increase in power density should correlate to an increase in log-reduction.

Two main patterns were revealed when represented as a function of energy density for acetate, formate, and nitrate—the only identified constituents in the water matrix that consume $\bullet\text{OH}$ outside of the target contaminant. For the shorter pulse width case (20 kV, 1 kHz, 40 ns), these $\bullet\text{OH}$ scavengers witnessed a direct relationship with energy density, suggesting that their production is zeroth-order. In this case, the reciprocal of the slope is similar to E_{EM} except that the contaminant is being produced instead of reduced. For the longer pulse width case (20 kV, 1 kHz, 120 ns), scavenger kinetics transition to a different reaction rate regime at $\approx 40 \text{ kW h/m}^3$. This transition was noticeable in the time plots of formate, acetate, and nitrate but, the E_{EM} -like relationship was unresolved. Future experiments should include different volumes to further validate the linear relationship between energy density and log-reduction.

Also, kinetics can be expressed as functions of the compound concentration in the water matrix. For instance, this can be very helpful when trying to identify at what concentration a given contaminant begins to transition to a different reaction rate regime ($k = \frac{\partial c}{\partial t} = f(c)$). Figure 4.24 displays the measured transformation products as functions of 1,4-dioxane. If these parametric plots were linear, then it can be inferred that there is a stoichiometric relationship between the parent compound and the intermediates.

In this case, although the byproducts were an order of magnitude apart in concentration, both stagnate in concentration even as 1,4-dioxane continued to decrease in concentration. Consequently, either 1,4-dioxane is successfully targeted by almost all of $\bullet\text{OH}$ or more likely, other unidentified species are consuming $\bullet\text{OH}$. Furthermore, if two matrix contaminants react with exclusive radicals, such as NDMA (UV) and 1,4-dioxane ($\bullet\text{OH}$), their parametric plot would help illustrate how plasma distributes

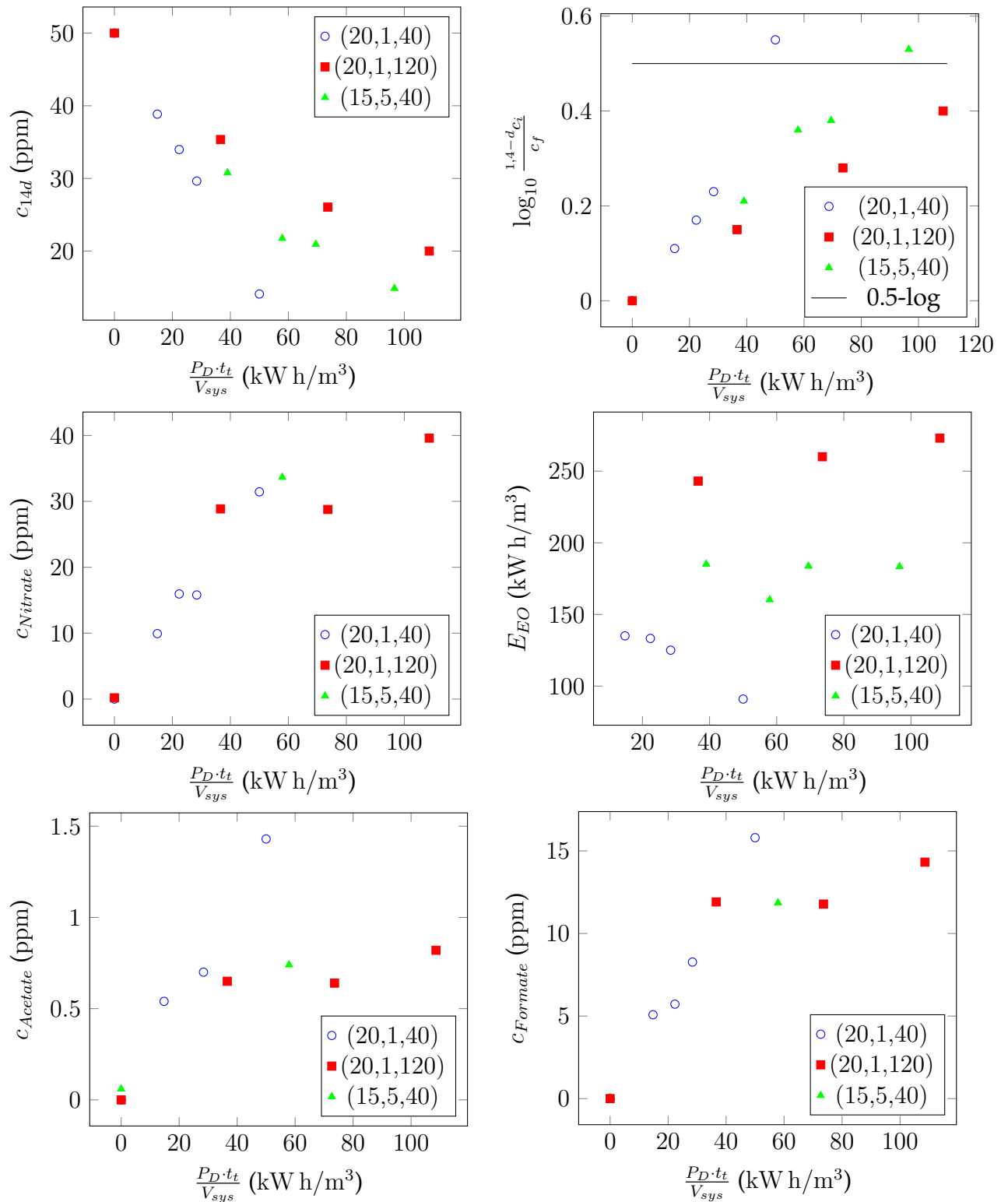


FIGURE 4.23: 1,4-dioxane kinetics of various pulsing techniques in terms of energy density during PWR treatment of spiked-DI water batches ($c_i = 50$ ppm). The legend is given in coordinates of (V_p, f_p, t_p) with units (kV, kHz, ns).

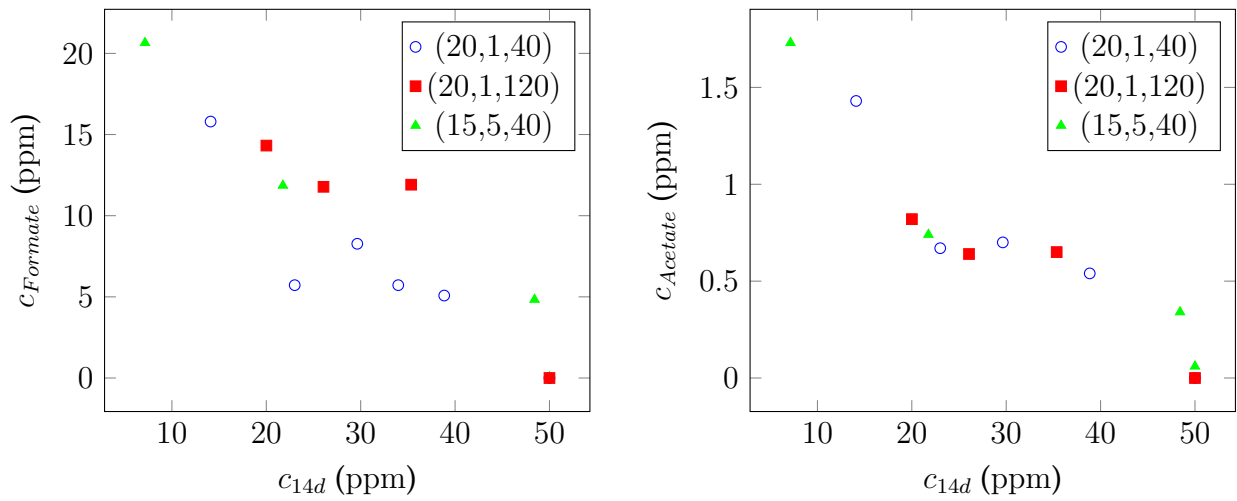


FIGURE 4.24: Contaminant and byproduct effects in PWR 1,4-dioxane kinetics.

energy into the production of the respective radicals. As more data is added, by expressing constituents in terms of other matrix constituents, the number of variables can be reduced and rough estimates of difficult-to-measure compounds can be made.

4.5.1 Order of Reaction Rate

The top left graph in Figure 4.23, which shows the relationship between 1,4-dioxane concentration and applied energy density, can be used to determine reaction rates and their respective regimes for a given pulser setup. As discussed in Subsection 1.4.3, E_{EM} (Eqn. 1.1) and E_{EO} (Eqn. 1.2) correspond to zeroth-order and first-order decay, respectively. These indices can be combined into an n -th order energy metric, E_{En} , where $\frac{\partial c}{\partial t} \propto [c]^n$.

$$E_{En} = \frac{P}{F \cdot \int_{c_f}^{c_i} \frac{dc}{c^n}} \quad (4.3)$$

Figure 4.25 reveals the different reaction rates for 1,4-dioxane. Using either a zeroth-

or first-order fit, the better fit of the two was plotted in Figure 4.25 and all three fits have $R^2 > 0.99$. While responsible for the slowest decomposition, (20 kV, 1 kHz, 40 ns) is the most energy efficient configuration due to its zeroth-order removal of 1,4-dioxane. Though not evident in the concentration space (\sim ppm) explored in these experiments, this reaction rate should transition to first-order decay at a low enough concentration. While (15 kV, 5 kHz, 40 ns) witnessed about double the effective flow rate, it needed more than twice the power of (20 kV, 1 kHz, 40 ns) to achieve F_{eff} , which places this pulser combination at moderate efficiency. The longer pulse width case (20 kV, 1 kHz, 120 ns) exhibited the worst efficiency and had similar destruction to the shorter pulse width scenario. This preliminarily suggests that the plasma exhibited a current spike narrower than the long pulse width thus, wasting high voltage.

Suggested future work for this kinetic study include probing low concentrations (\sim ppb), collecting more data, and measuring ROS dose during decomposition, which will be performed in the upgraded PWR.

4.6 Real-Time ROS Dose

As mentioned in Section 4.2, EMI prevented an extensive ROS study with the fully upgraded system. Instead, the subscale PWR (Fig. 4.4) was placed several meters away from diagnostics and was moderately shielded. Building upon the subscale configuration in Figure 4.8, this system used a peristaltic pump to flow batch water through the H_2O_2 and O_3 sensors and back into the contact tank, as illustrated in Figure 4.12. The polarographic membraned sensors measured H_2O_2 and O_3 directly, were less susceptible to interference from other oxidants, and may be better suited for plasma-based AOP analysis than certain chemical probes.

Compared to the earlier ROS study (4.3.2), this investigation used the same subscale PWR, similar flow rates at $F \sim 4.3\text{L}/\text{min}$, and longer treatment times where

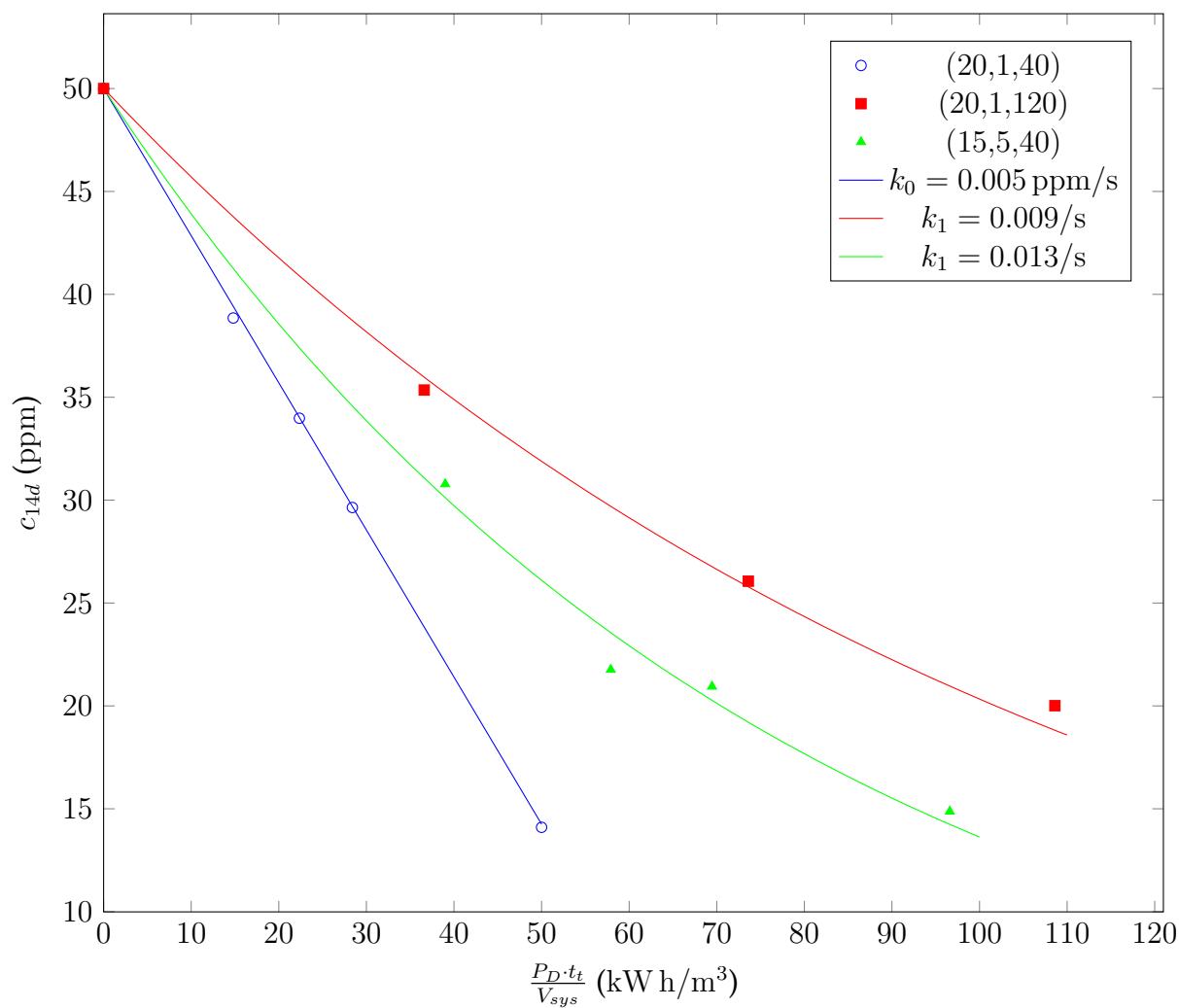


FIGURE 4.25: 1,4-dioxane reaction rates as a function of different pulser parameters in $(V_p[\text{kV}], f_p[\text{kHz}], t_p[\text{ns}])$ coordinates.

$t_t \leq 45$ min. In addition, a greater DI batch volume of $V_{sys} = 0.75$ L was required to flow sufficient water to each ROS sensor at $F \approx 10$ gal/h. Taking into consideration the desire to operate at the highest voltage, the NSP's power limitations, the NSP's ability to sustain repetition frequency, and pulse widening due to the PWR load, combinations of maximum voltage ($V_p \in [20]$ kV), an order of magnitude frequency span ($f_p \in [0.5, 0.8, 1, 5]$ kHz), and the lower end of pulse widths ($t_p \in [20, 40, 60, 80]$ ns) were used. Since V_p was fixed for these trials, the legend in the following figures is of the coordinate format (f_p, t_p) .

Similar to earlier parametric studies, the electric and water variables are plotted as functions of input and derived parameters in an attempt to simplify this dynamic system. The dissipated power is presented as a function of peak voltage and pulse width (Fig. 4.26), and pulser parameter product (Fig. 4.27). As evident in Figures 4.26 and 4.27, the colored streaks indicate a decrease in V_p and t_p during treatment, help identify operating regions for various f_p and t_p , and demonstrate if power limited. For example, regardless of t_p , the highest f_p (5 kHz) experienced the greatest loss of peak voltage and power during treatment. As peak voltages and pulse widths decreased with treatment time, some (f_p, t_p) combinations would maintain P_D , suggesting higher current.

For a given operating condition's data cluster in the pulser parameter space, the common plasma mode was streamer discharge but, infrequent power fluctuations were a sign of pseudoarcs. If they were to occur, the arc-like discharges tend to form at the beginning of an experiment ($t_t < 10$ min), which can be recognized as power outliers in Figure 4.28. The power profiles for (f_p, t_p) operating near the limits of the pulser parameter space decreased with treatment time whereas (f_p, t_p) away from the power-limited region resulted in better NSP-PWR load matching and consistent dissipated power throughout treatment. While the majority of the trials span a small dissipated

power range ($\sim 5\text{--}15\text{ W}$), the various (f_p, t_p) configurations are capable of significantly different ROS behavior over time, as depicted in Figures 4.29, 4.30, and 4.31.

Both H_2O_2 and O_3 concentrations spanned an order of magnitude and experienced various reaction rates. Dose profiles included exponential, logarithmic, linear, local maximum, and delayed production. The main differences are that the maximum H_2O_2 concentration was roughly an order of magnitude greater than the maximum O_3 concentration and for most trials, H_2O_2 (Fig. 4.29) had some direct relationship with treatment time whereas O_3 (Fig. 4.30) would quickly rise then decay. These phenomena produced a $\text{H}_2\text{O}_2/\text{O}_3$ ratio that ranges several orders of magnitude ($10^{-1}\text{--}10^3$ mole/mole) with most trials contained between $\frac{[\text{H}_2\text{O}_2]}{[\text{O}_3]} = 1\text{--}100$. The ability to significantly vary $\frac{[\text{H}_2\text{O}_2]}{[\text{O}_3]}$ is highly favorable since the PWR can be applied to a wide range of custom water matrices. For each treatment scenario, a parametric sweep similar to this investigation would be performed to determine the appropriate dose and power consumption. This parametric sweep can also be used to throttle the treatment of dynamic influent streams.

In addition to varying $\frac{[\text{H}_2\text{O}_2]}{[\text{O}_3]}$, high electrical efficiency, or low energy consumed per volume treated, is also very advantageous. For a batch, semi-batch, or flow-through system, energy density can be expressed as $\frac{P_D \cdot t_t}{V_{sys}}$, $\frac{P_D \cdot t_{HR}}{V_{sys}}$, or $\frac{P_D}{F}$, respectively. Similar to Figure 4.23, the pulser parameters and oxidants can be expressed in terms of energy density. H_2O_2 , O_3 , and $\frac{[\text{H}_2\text{O}_2]}{[\text{O}_3]}$ are shown for the entire energy density range (Figs. 4.32, 4.33, and 4.34, respectively).

For H_2O_2 (Fig. 4.32), most (f_p, t_p) exhibited direct relationships throughout treatment. Since H_2O_2 transport should not be mass-limited, plateauing or decreasing H_2O_2 concentration was likely due to ROS scavengers in the system, such as plasma-produced nitrates and nitrites. The trials with the steepest, positive linear fits provided the most energy efficient H_2O_2 yields. For O_3 (Fig. 4.33), only the high frequency cases

($f_p = 5$ kHz) displayed a direct relationship between energy density and concentration throughout treatment whereas the other configurations underwent a rapid rise in O_3 concentration at low energy density then decayed as $\frac{P_D \cdot t_t}{V_{sys}}$ increased. For parameters away from the limits of the NSP operating space, the rapid rise in O_3 concentration relative to H_2O_2 concentration implies that O_3 production is more energy efficient than H_2O_2 production at low $\frac{P_D \cdot t_t}{V_{sys}}$. Due to this phenomena, if the optimal $\frac{[H_2O_2]}{[O_3]}$ ratio of 0.5 is required, the PWR must operate at low $\frac{P_D \cdot t_t}{V_{sys}}$, as shown in Figure 4.34.

Since traditional AOPs operate and compete at high energy efficiencies, H_2O_2 (Fig. 4.35), O_3 (Fig. 4.36), and $\frac{[H_2O_2]}{[O_3]}$ (Fig. 4.37) were zoomed into such that $\frac{P_D \cdot t_t}{V_{sys}} < 1$ kWh/m³. As seen in Figure 4.35, there is a direct relationship between H_2O_2 concentration and energy consumed per volume treated. On the other hand, in Figure 4.36, some (f_p, t_p) arrangements reached a maximum O_3 concentration for low $\frac{P_D \cdot t_t}{V_{sys}}$. These ROS doses were combined to produce Figure 4.37, which demonstrates that at low $\frac{P_D \cdot t_t}{V_{sys}}$, several (f_p, t_p) configurations can provide the optimal H_2O_2/O_3 ratio for various $\frac{P_D \cdot t_t}{V_{sys}}$. Therefore, the PWR can be customizable and efficient.

In an attempt to minimize the number of variables, future goals include mapping out the kinetic and operating parametric spaces, viewing data from different perspectives, such as Figures 4.38 and 4.39, and determining if there are any relationships between input pulser parameters and ROS dose, such as Figures 4.40, and 4.41.

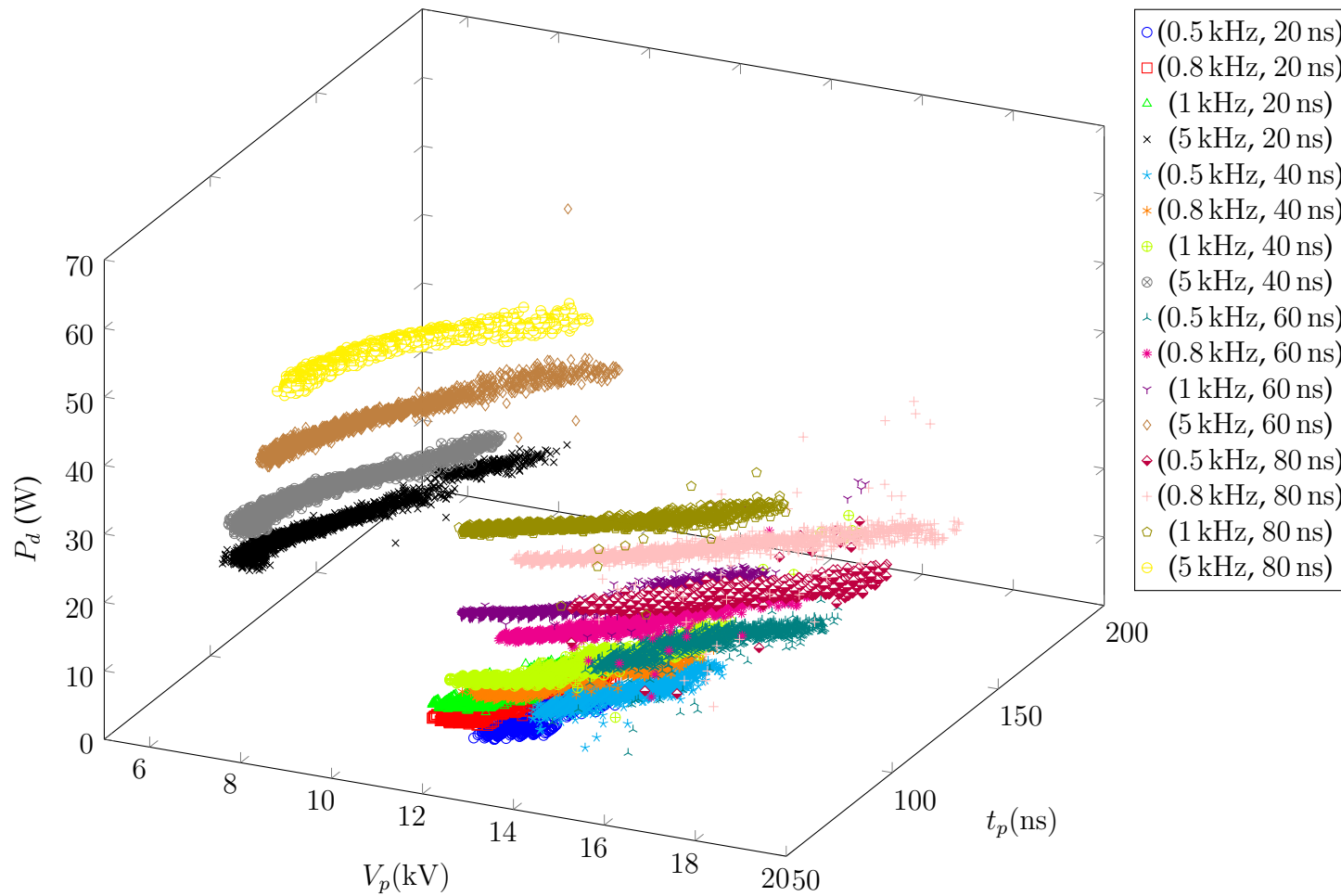


FIGURE 4.26: Pulser power operating space for different peak voltage and pulse width in the closed loop PWR (Figs. 4.4 and 4.12) for DI water matrix.

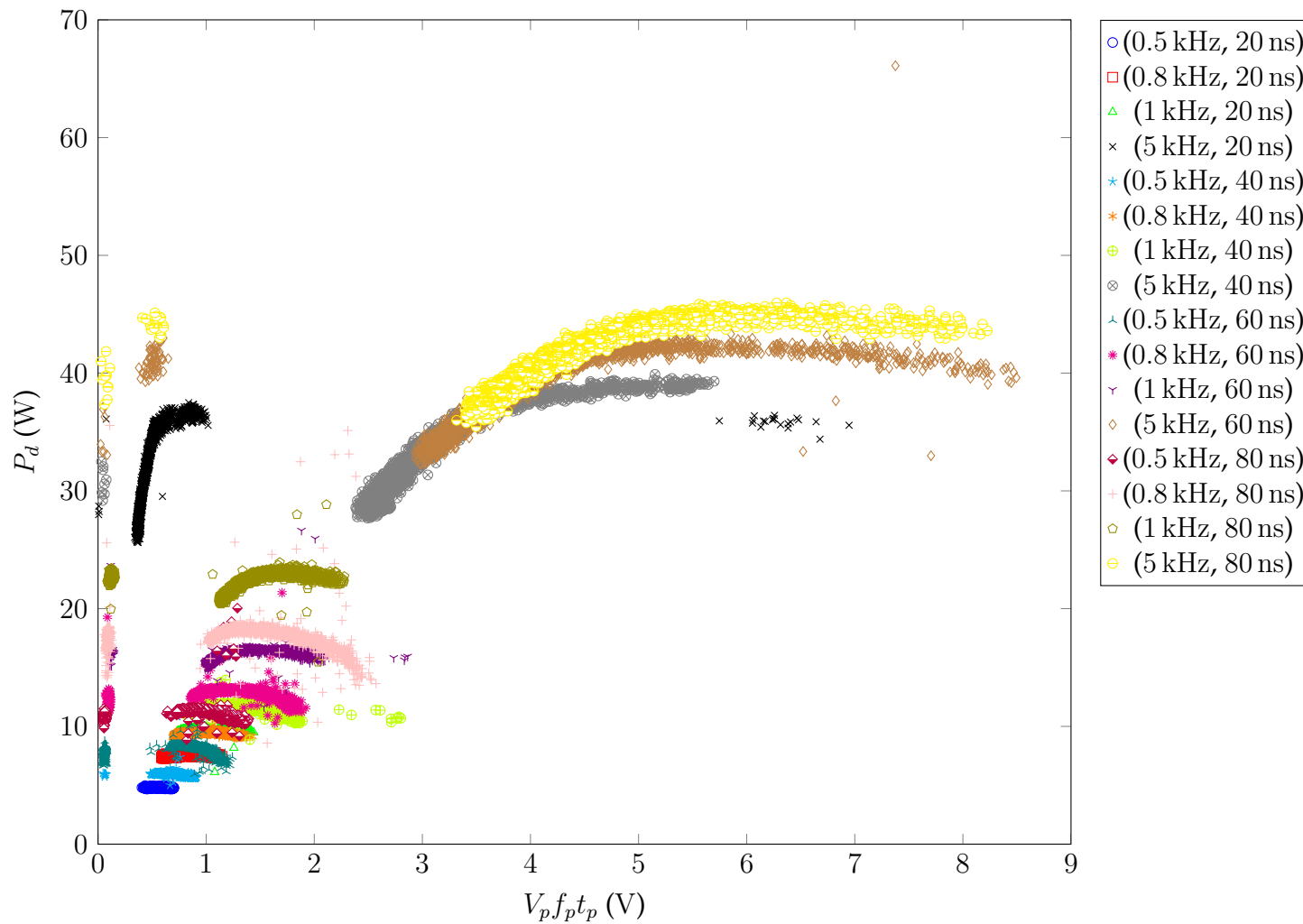


FIGURE 4.27: Pulser parameter power space in the closed loop PWR (Figs. 4.4 and 4.12) for DI water matrix.

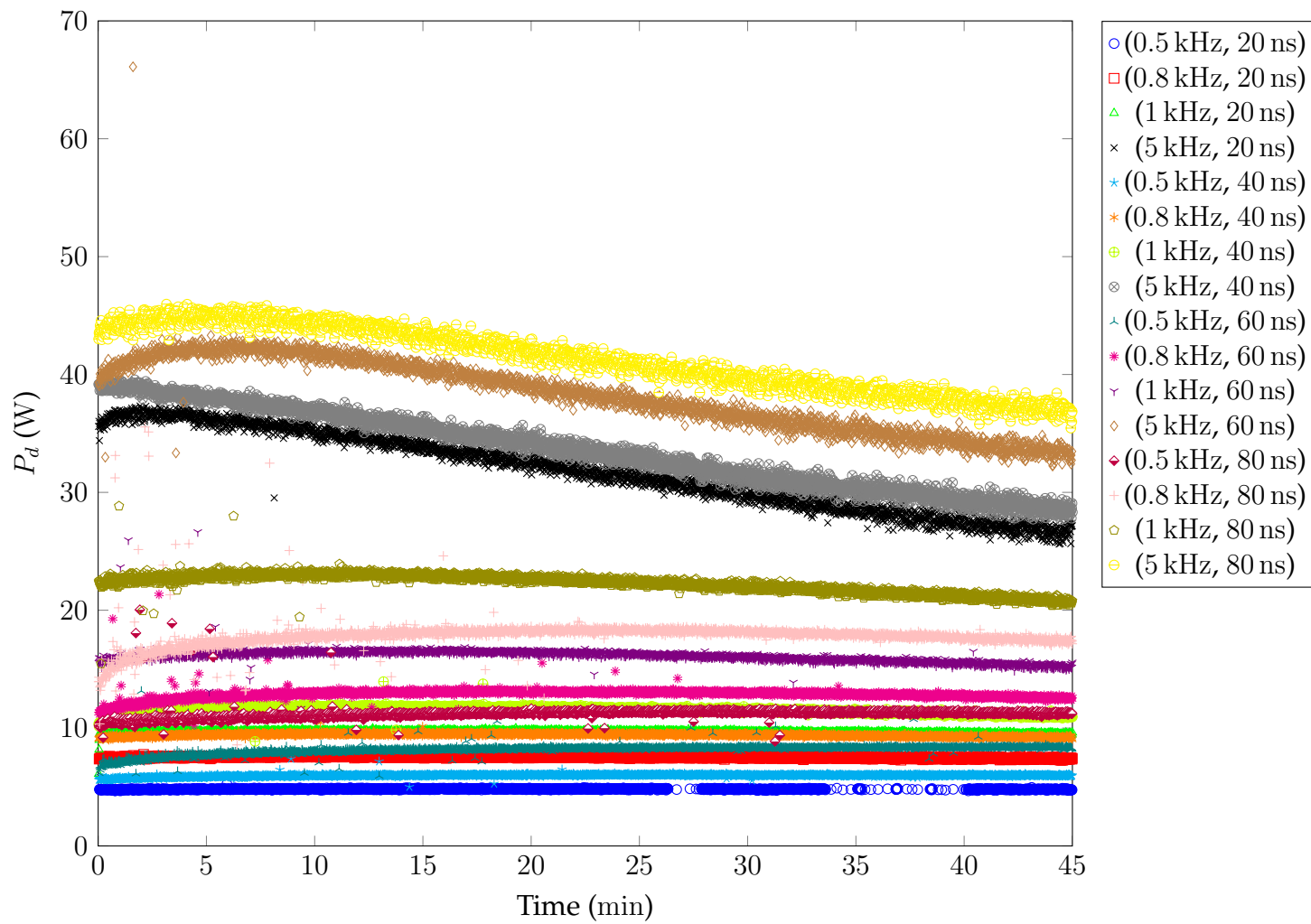


FIGURE 4.28: Pulsed parameter power profile in the closed loop PWR (Figs. 4.4 and 4.12) for DI water matrix.

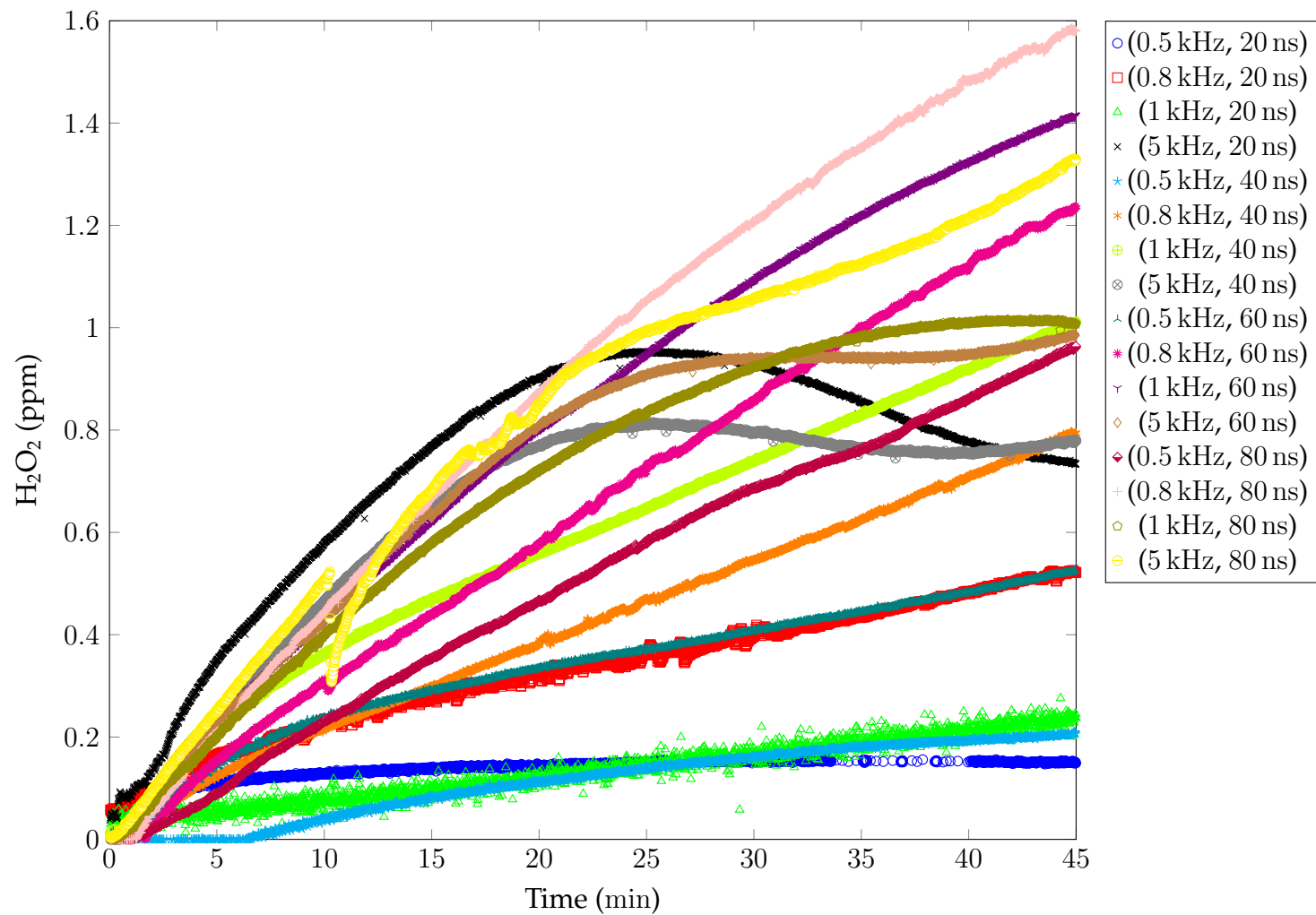


FIGURE 4.29: H_2O_2 produced in the closed loop PWR (Figs. 4.4 and 4.12) for DI water matrix.

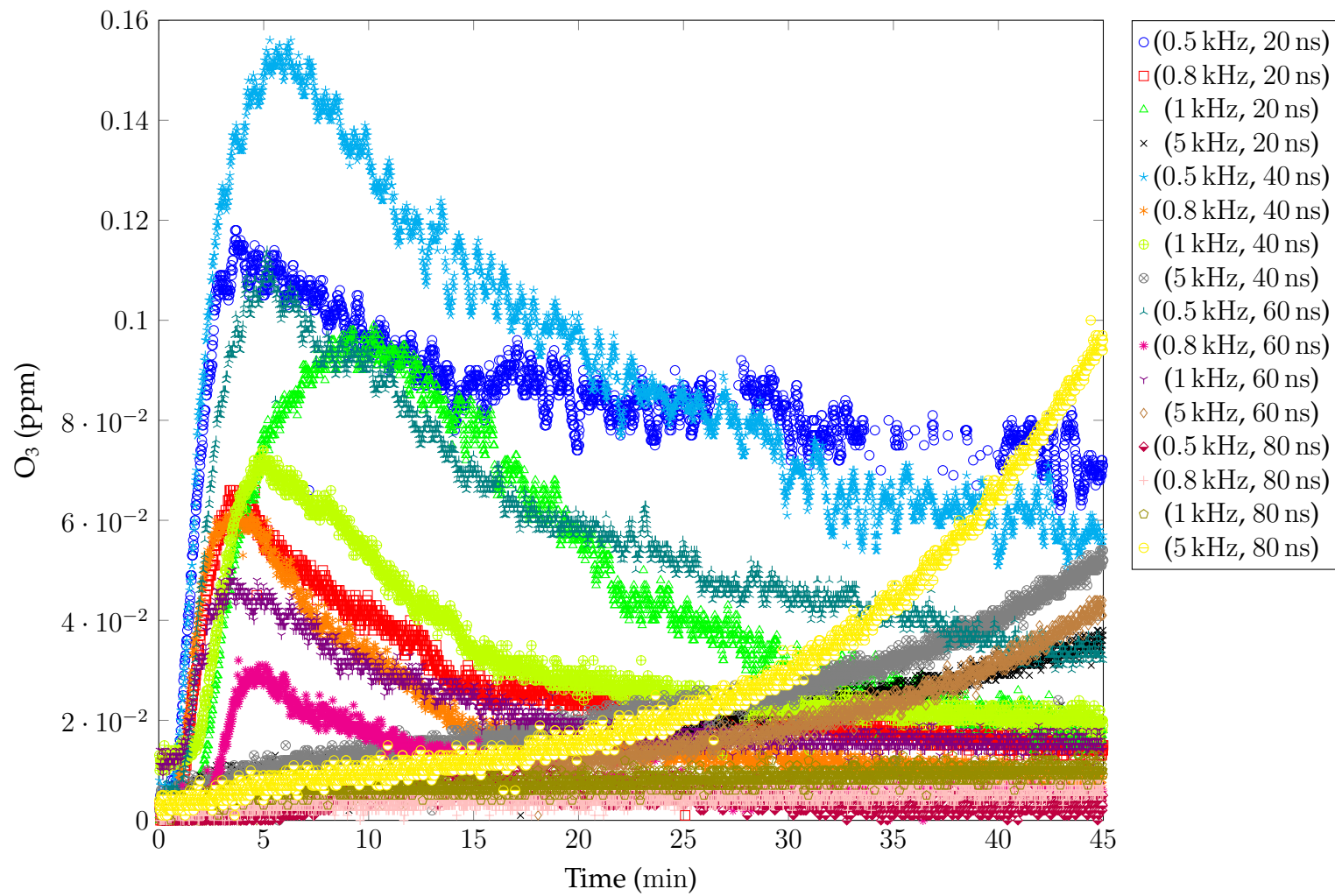


FIGURE 4.30: O₃ produced in the closed loop PWR (Figs. 4.4 and 4.12) for DI water matrix.

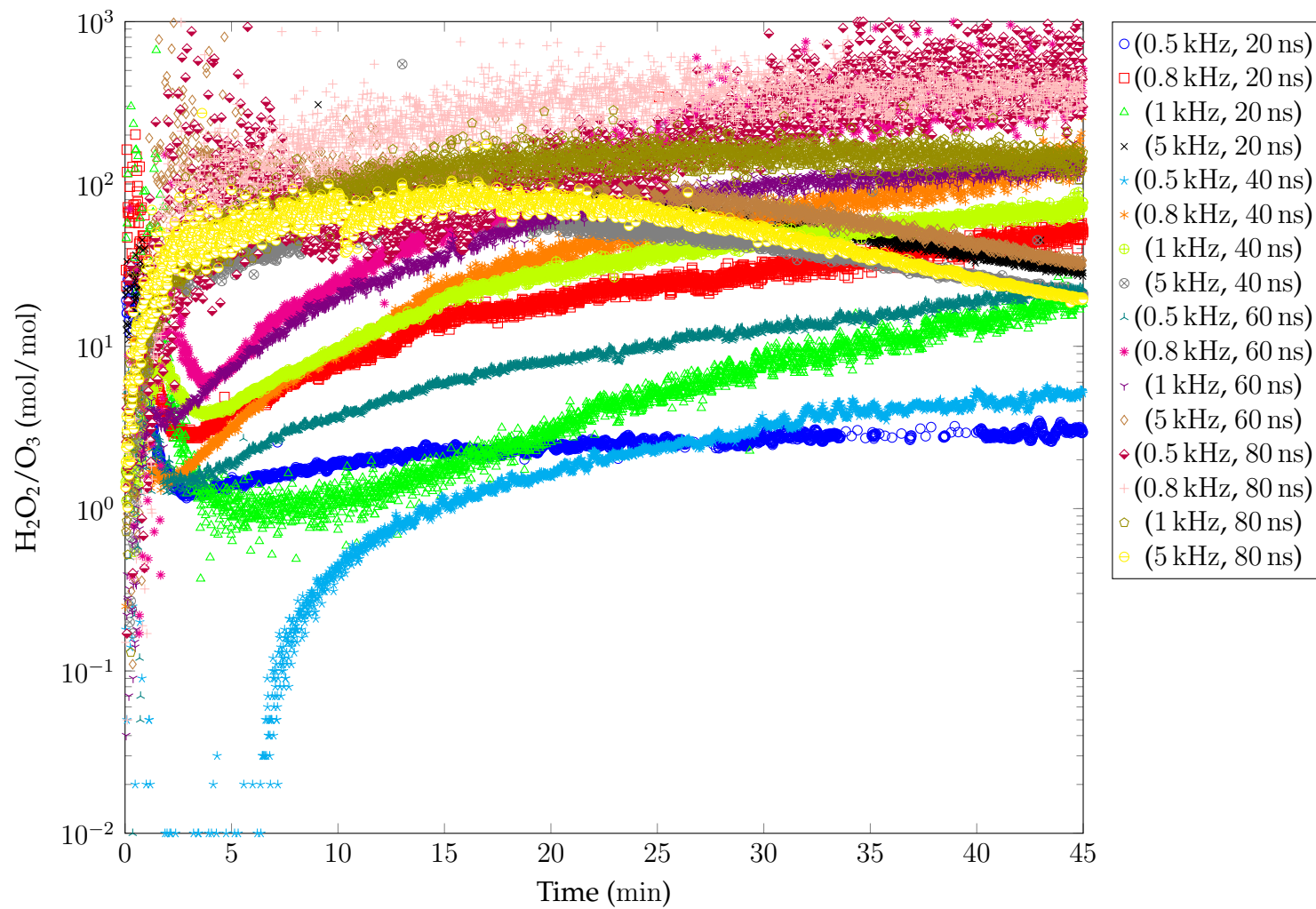


FIGURE 4.31: $\text{H}_2\text{O}_2/\text{O}_3$ ratio (mol/mol) in the closed loop PWR (Figs. 4.4 and 4.12) for DI water matrix.

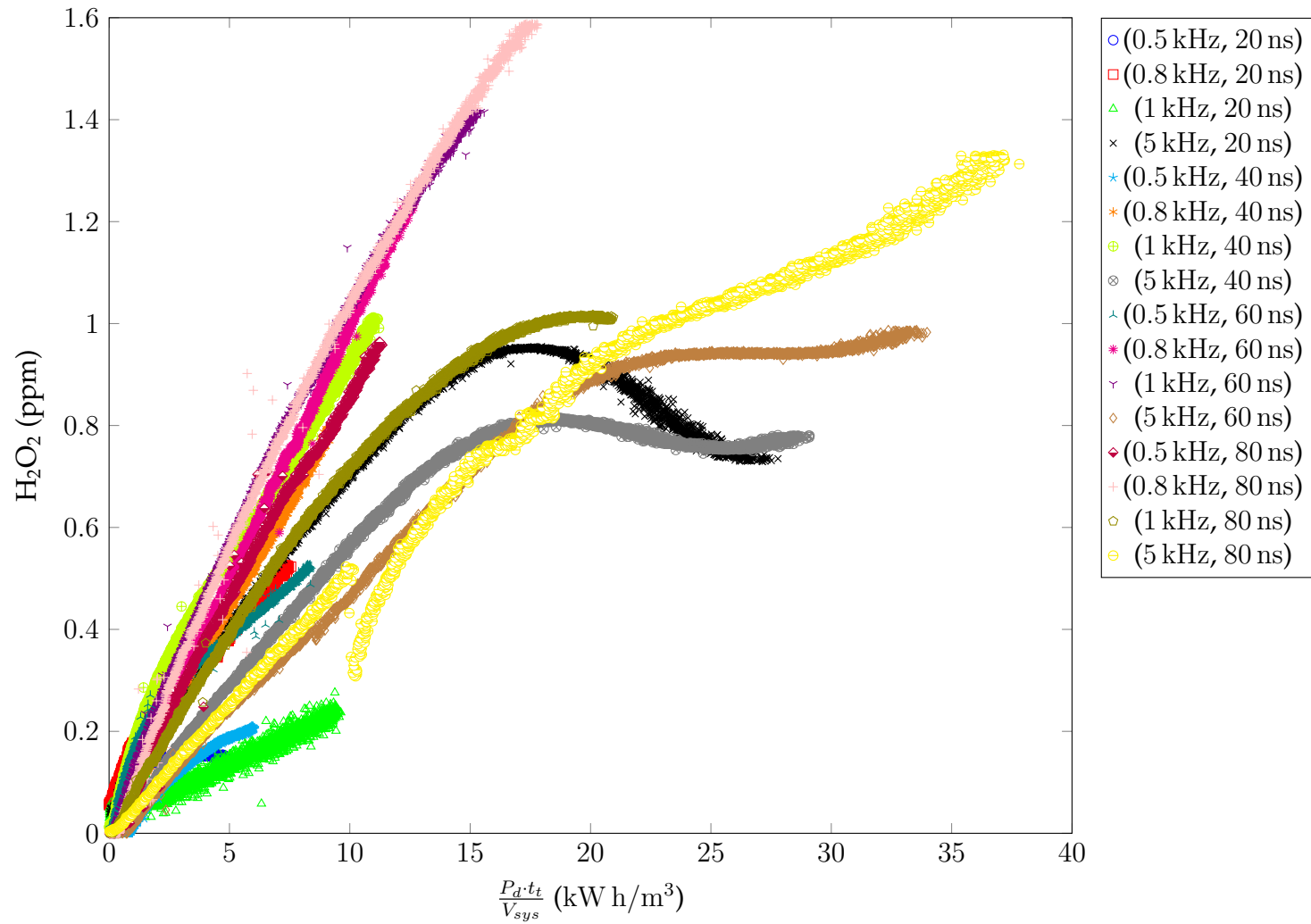


FIGURE 4.32: H_2O_2 produced as a function of energy density ($\frac{P_D \cdot t_t}{V_{sys}}$) in the closed loop PWR (Figs. 4.4 and 4.12) for DI water matrix.

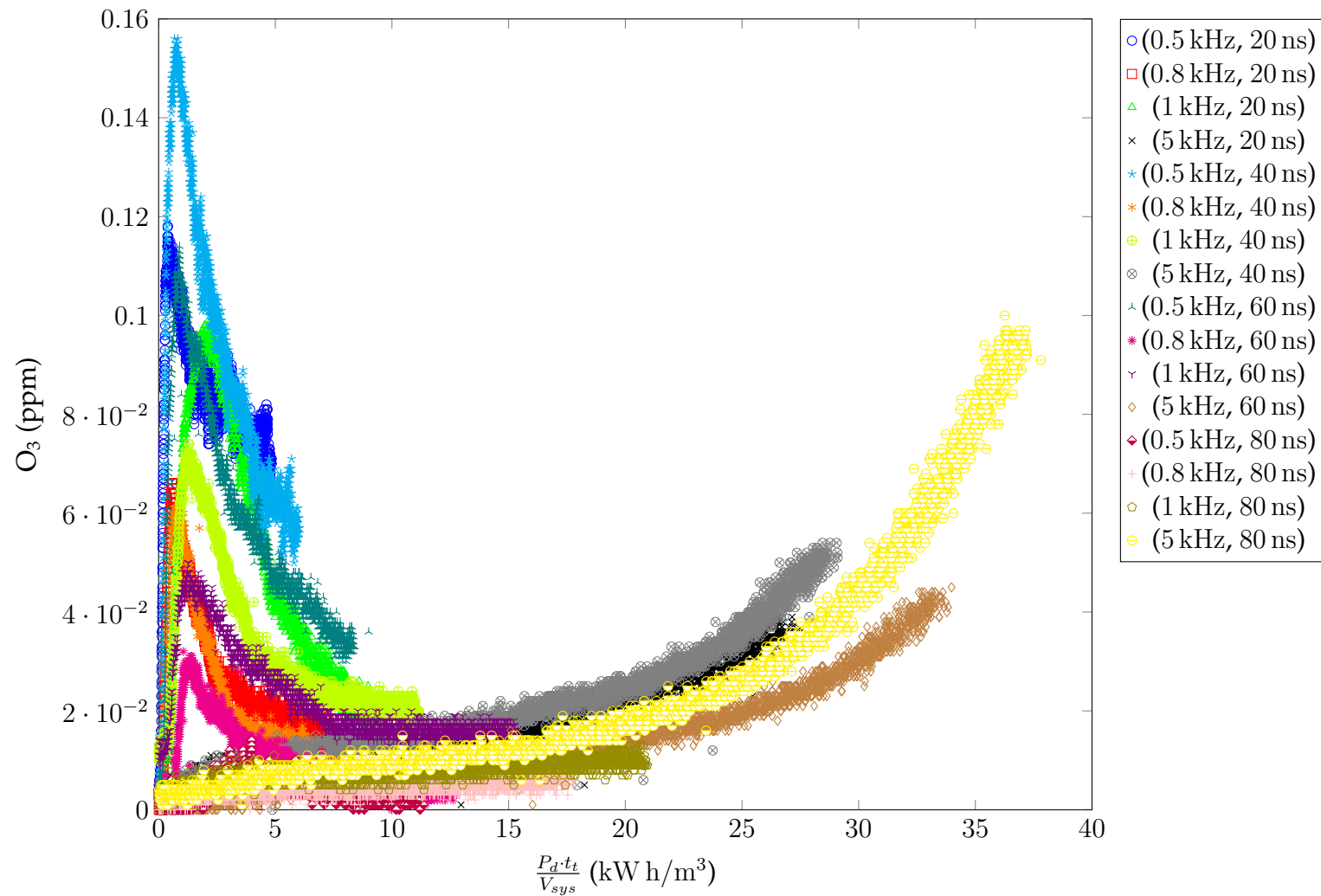


FIGURE 4.33: O_3 produced as a function of energy density ($\frac{P_d \cdot t_t}{V_{sys}}$) in the closed loop PWR (Figs. 4.4 and 4.12) for DI water matrix.

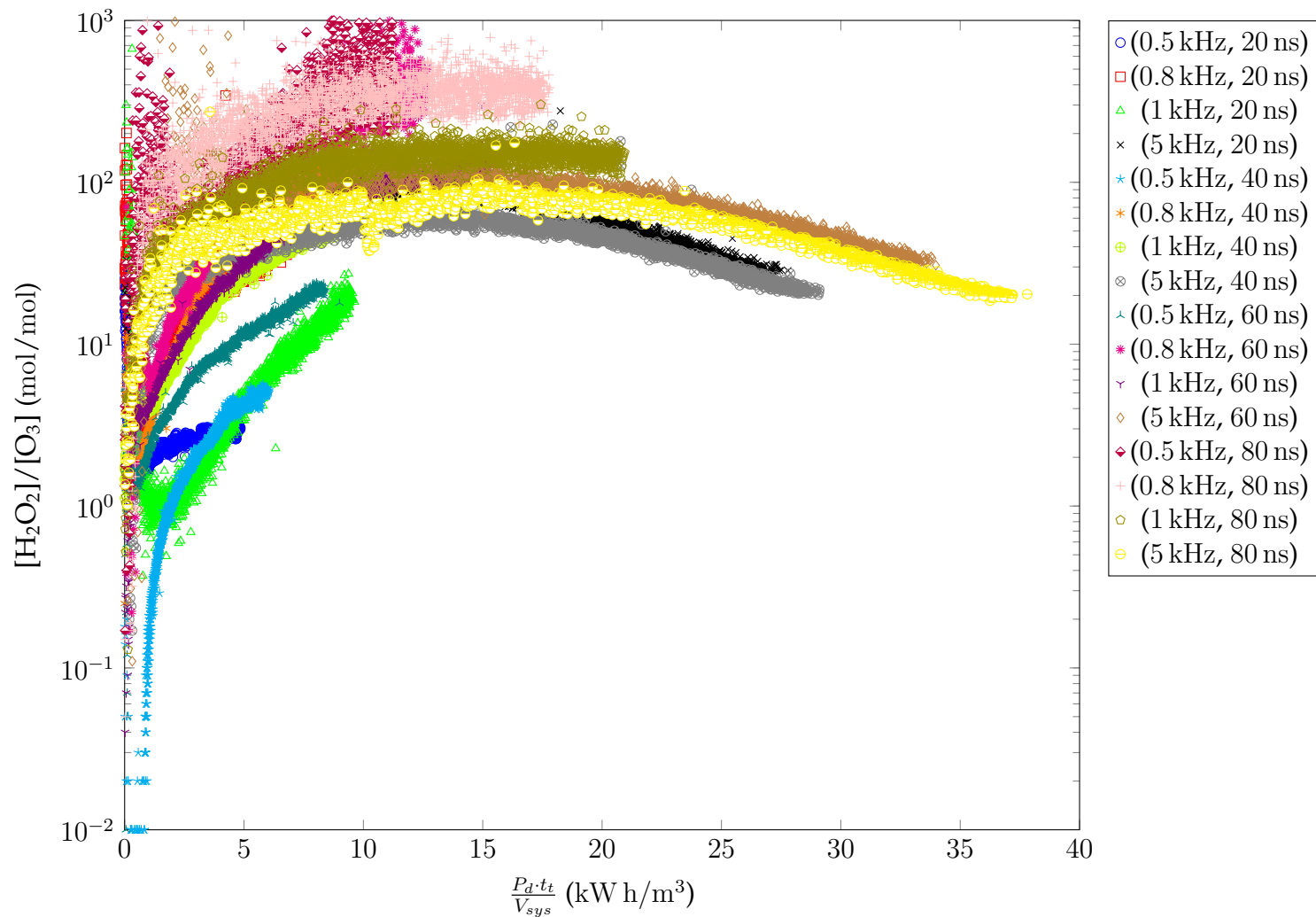


FIGURE 4.34: $\text{H}_2\text{O}_2/\text{O}_3$ ratio (mol/mol) as a function of energy density ($\frac{P_d \cdot t_t}{V_{sys}}$) in the closed loop PWR (Figs. 4.4 and 4.12) for DI water matrix.

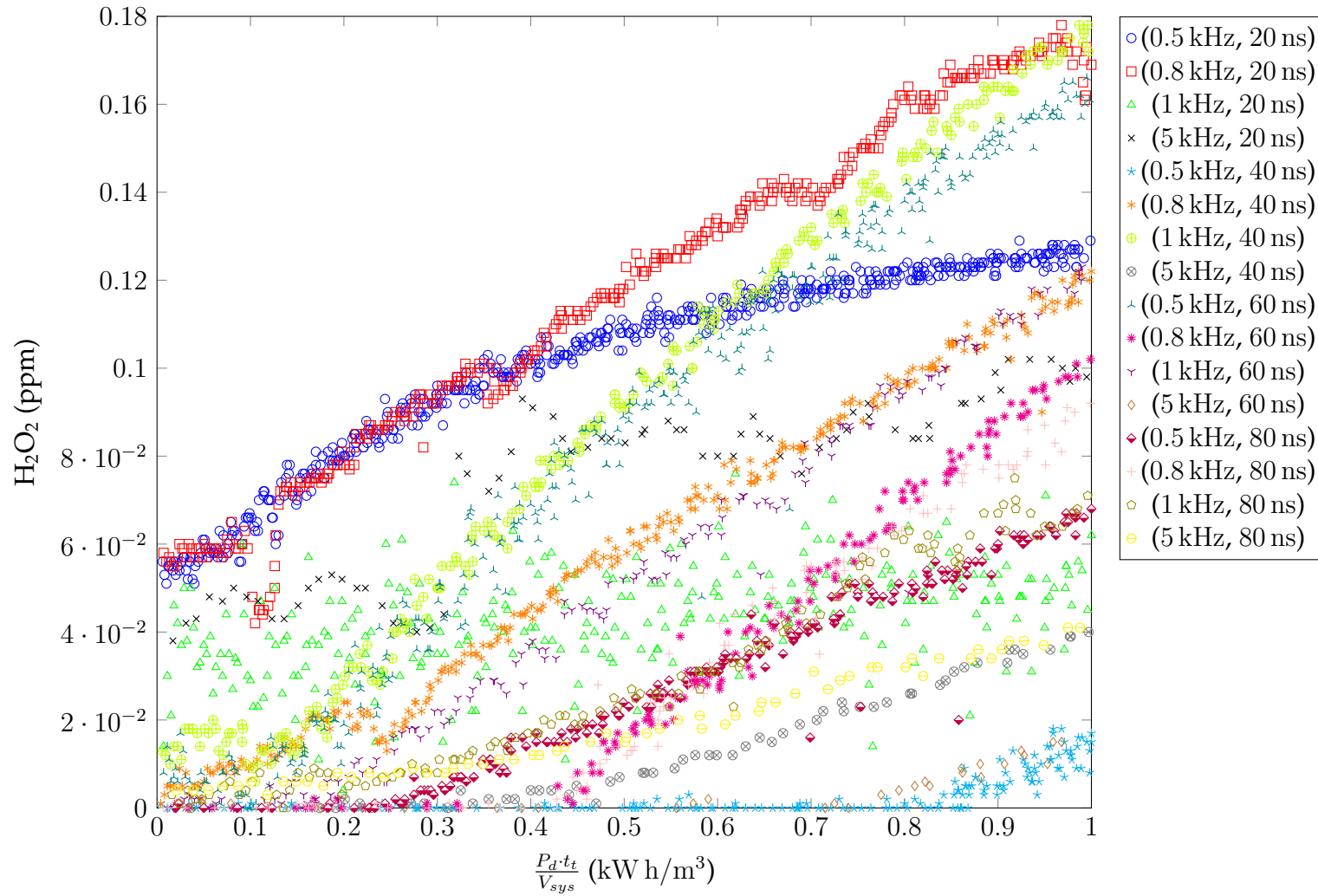


FIGURE 4.35: H_2O_2 produced as a function of energy density ($\frac{P_d \cdot t_t}{V_{sys}} \leq 1 \text{ kW h/m}^3$) in the closed loop PWR (Figs. 4.4 and 4.12) for DI water matrix.

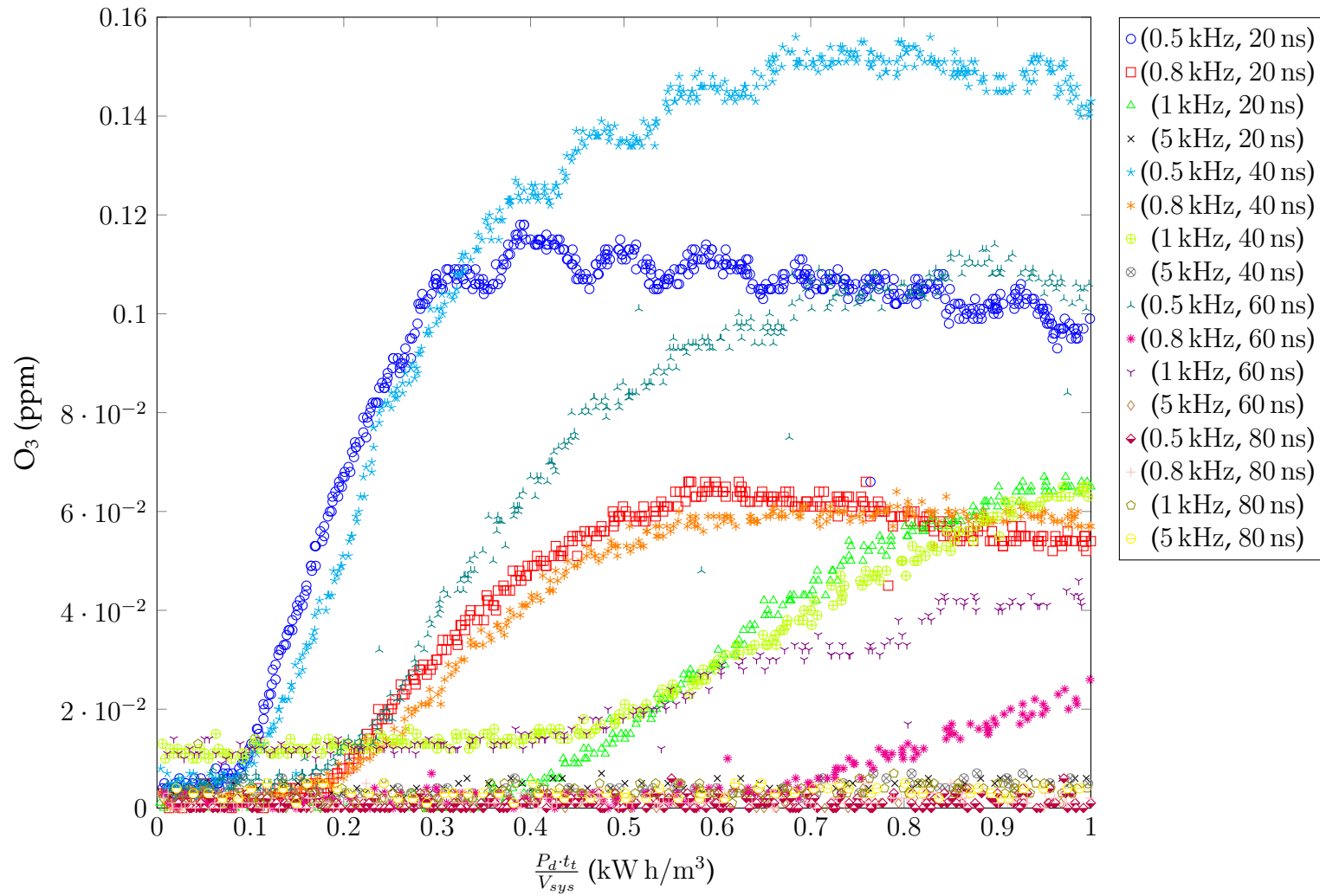


FIGURE 4.36: O_3 produced as a function of energy density ($\frac{P_a \cdot t_t}{V_{sys}} \leq 1 \text{ kW h/m}^3$) in the closed loop PWR (Figs. 4.4 and 4.12) for DI water matrix.

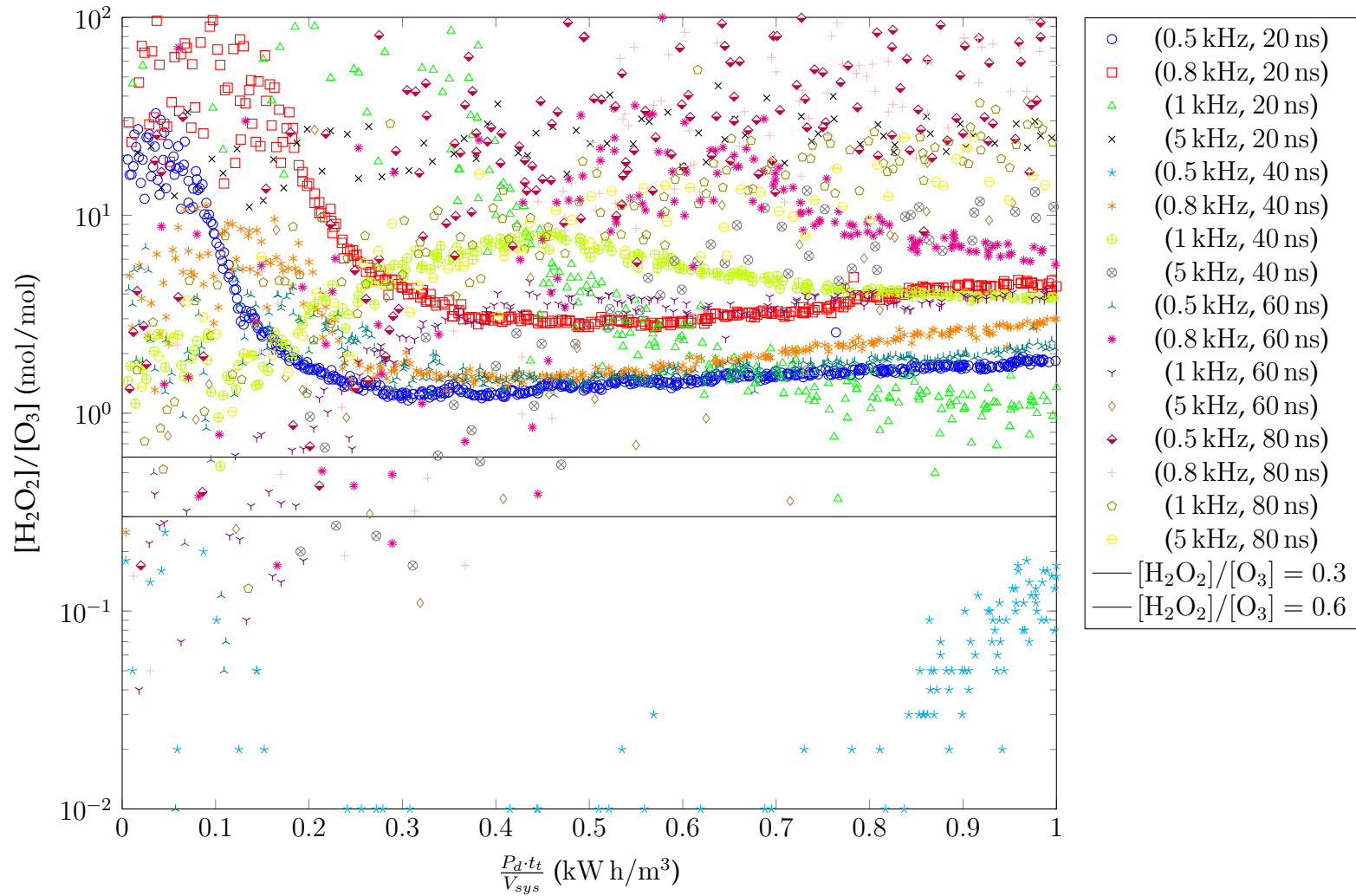


FIGURE 4.37: $\text{H}_2\text{O}_2/\text{O}_3$ ratio (mol/mol) as a function of energy density ($\frac{P_d \cdot t_t}{V_{sys}} \leq 1 \text{ kW h/m}^3$) in the closed loop PWR (Figs. 4.4 and 4.12) for DI water matrix.

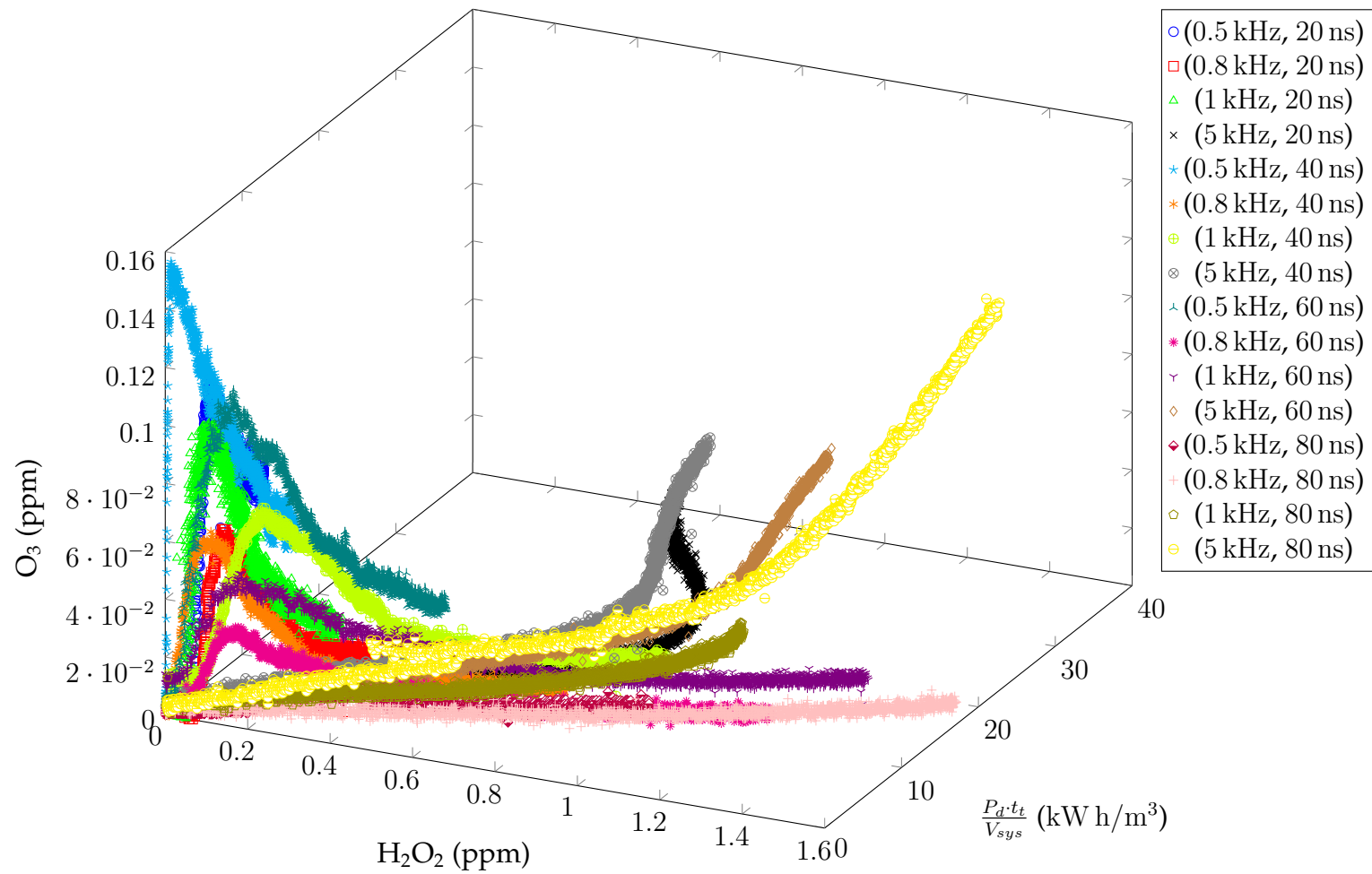


FIGURE 4.38: H_2O_2/O_3 dose as a function of energy density ($\frac{P_d \cdot t_t}{V_{sys}}$) in the closed loop PWR (Figs. 4.4 and 4.12) for DI water matrix.

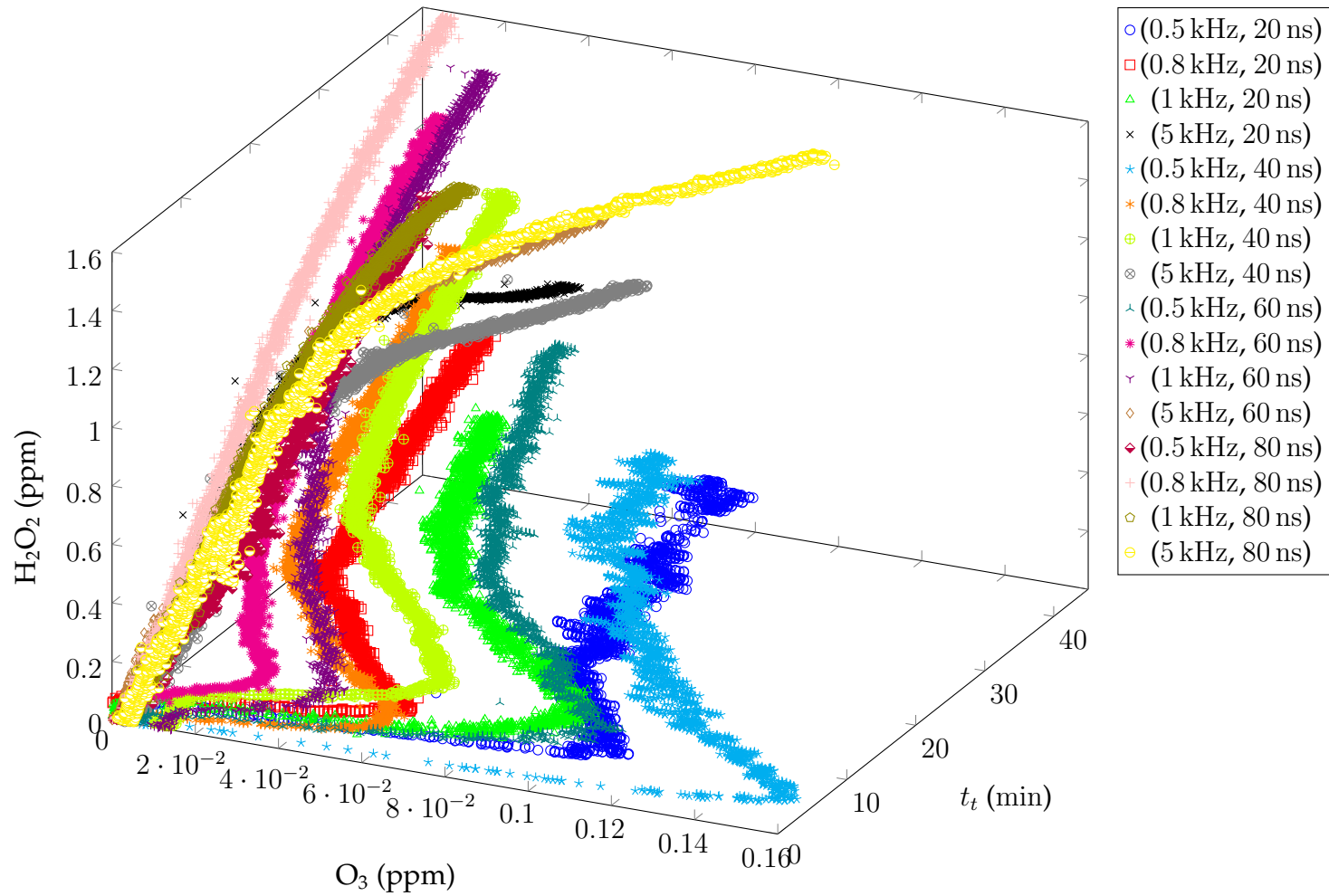


FIGURE 4.39: H_2O_2/O_3 dose as a function of time in the closed loop PWR (Figs. 4.4 and 4.12) for DI water matrix.

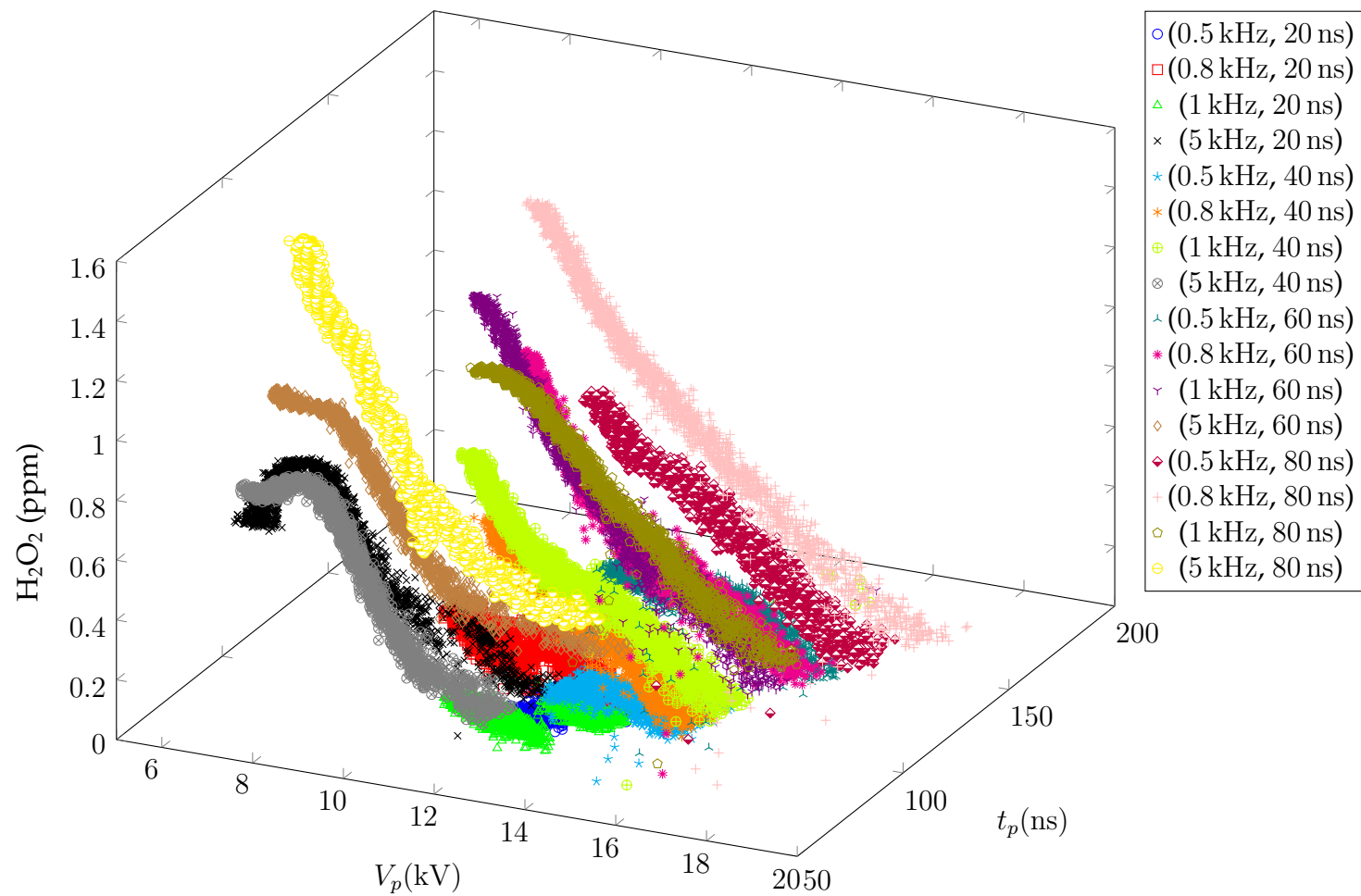


FIGURE 4.40: H_2O_2 in pulser operating space for different peak voltage and pulse width in the closed loop PWR (Figs. 4.4 and 4.12) for DI water matrix.

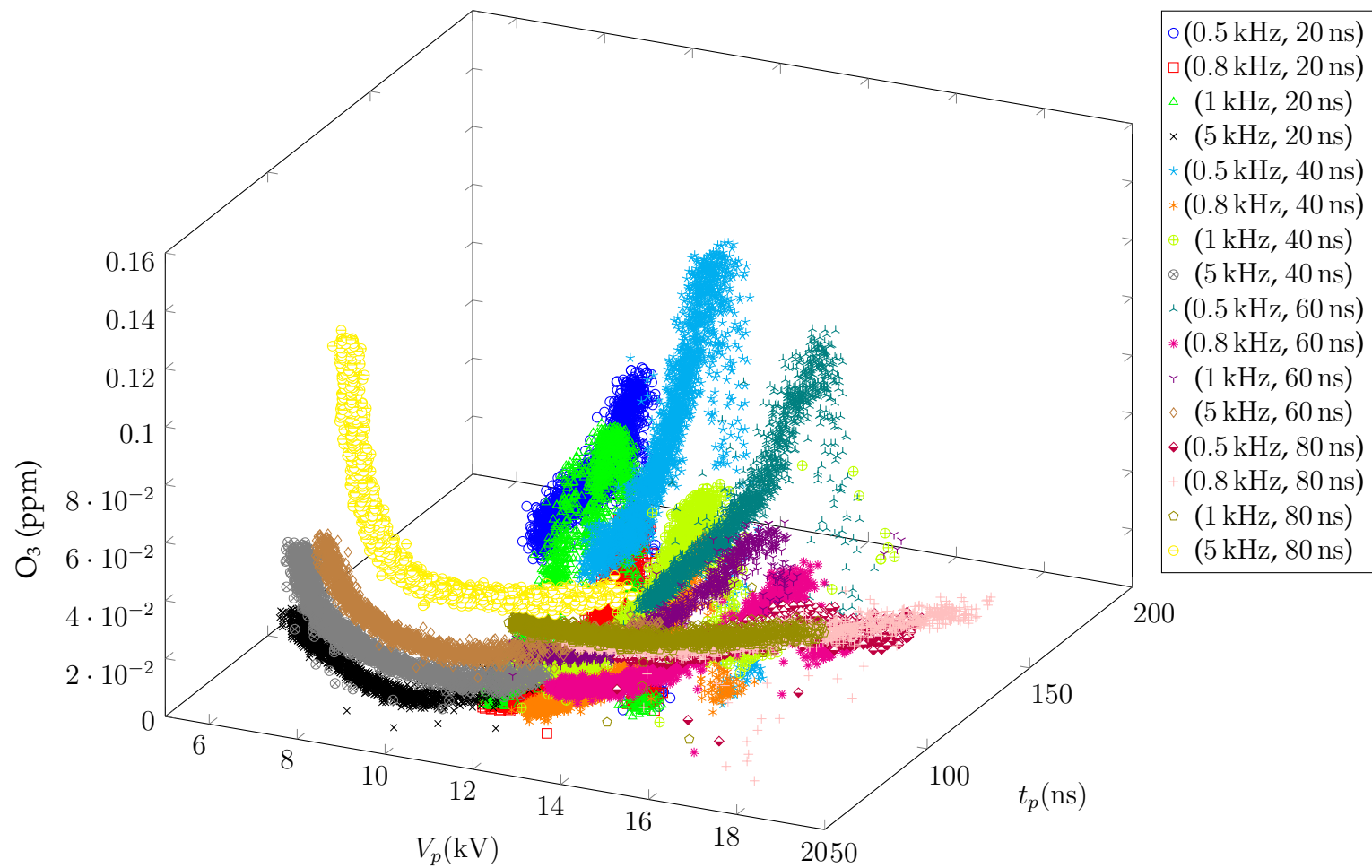


FIGURE 4.41: O_3 in pulser operating space for different peak voltage and pulse width in the closed loop PWR (Figs. 4.4 and 4.12) for DI water matrix.

4.7 Validating Kinetics

Based on the wide range in H_2O_2 and O_3 concentrations, water parameters and other species must be considered to identify rate-determining steps. For instance, the rate of ozone loss significantly increases with increasing pH due to the initiation reaction $\text{O}_3 + \text{HO}^- \longrightarrow \text{O}_2^{\bullet-} + \text{HO}_2^{\bullet}$ ($k = 1.16 \times 10^{-19} \text{ cm}^3 \text{ s}^{-1}$). Since ozonation is an AOP, kinetic models must include contributions from ROS transients. Assuming steady state ($\frac{d}{dt}[\bullet\text{OH}] = 0$), O_3 , $\bullet\text{OH}$, HO_2^{\bullet} , and $\text{O}_2^{\bullet-}$ and a few of their reactions with one another can be used to approximate the ozone reaction rate, shown in Equation 4.4 (Weiss, 1935). Reaction rate coefficients for these and other relevant ROS are listed in Table 2.1.

$$\frac{d[\text{O}_3]}{dt} = -\frac{2}{3}k_{\text{O}_3, \text{HO}^-} [\text{O}_3] [\text{HO}^-] - 2\sqrt{\frac{k_{\text{HO}_2, \text{HO}_2^{\bullet}}k_{\text{O}_3, \text{HO}^-}k_{\text{O}_3, \text{HO}_2^{\bullet}}}{k_{\text{HO}_2^{\bullet}, \bullet\text{OH}}}} [\text{O}_3]^{1.5} [\text{HO}^-]^{0.5} \quad (4.4)$$

Although Equation 4.4 incorrectly assumes $2\text{HO}_2^{\bullet} \longrightarrow \text{O}_3 + \text{H}_2\text{O}$ instead of $2\text{HO}_2^{\bullet} \longrightarrow \text{H}_2\text{O}_2 + \text{O}_2$, the order of the expression is similar. Nonetheless, H_2O_2 and its reactions can be taken into account to estimate the averaged steady-state hydroxyl concentration $\langle[\bullet\text{OH}]\rangle$, as shown in Equation 4.5.

$$\langle[\bullet\text{OH}]\rangle = \sqrt{\frac{k_{\bullet\text{OH}, \text{O}_3} + \frac{[\text{H}_2\text{O}_2]}{[\text{O}_3]}k_{\text{HO}_2^{\bullet}, \text{H}_2\text{O}_2}}{k_{\text{O}_3, \text{HO}_2^{\bullet}} + \frac{[\text{H}_2\text{O}_2]}{[\text{O}_3]}k_{\text{HO}^{\bullet}, \text{H}_2\text{O}_2}} \left[\frac{k_{\text{O}_3, \text{HO}^-}}{k_{\text{HO}_2^{\bullet}, \bullet\text{OH}}} \right] [\text{O}_3] [\text{HO}^-]} \quad (4.5)$$

As evident in Equations 4.4 and 4.5, the ozone decomposition rate and hydroxyl concentration are strongly dependent on pH. However, the negative net changes in pH in Subsection 4.3.2 suggest that like other atmospheric pressure air plasmas, the PWR produces reactive nitrogen species that acidify the solution. On long timescales, terminal acids (Ex. HNO_3) maintain the low pH, which mitigates O_3 self-scavenging, but the higher concentrations result in a higher scavenging capacity in the water matrix,

which is defined as $\sum_j k_{\text{HO}^\bullet, S} [S_j]$. The higher scavenging capacity indicates first-order kinetics and prevents ozone from reaching its saturation concentration. Since the relative solubility of the reactive nitrogen species (Ex. $H_{\text{HNO}_3}^{cc} = 4.8 \times 10^6$) is much higher than ozone (Ex. $H_{\text{O}_3}^{cc} = 0.3$) at standard temperature and pressure (Sander, 2015), diffusion is the rate-determining step for ozone. Thus, due to ozone being produced in the gas phase first, the mass transport limit can be used to approximate key plasma characteristics for given water matrices.

Since ozone is only produced by plasma and relies on solvation, the reaction rate of $\text{O}_{3\text{aq}}$ can be related to the reaction rate of $\text{O}_{3\text{g}}$. This combined with a global model that includes electron impact reactions with known reaction rate coefficients, such as $\text{e}^- + \text{O}_3 \longrightarrow \text{O}_2 + \text{O}^-$, can estimate electron density and temperature. The maximum $\frac{|\vec{E}|}{N_g}$ was approximated to be $1.3 \times 10^{-15} \text{ V cm}^{-2}$, or 130 Td. Since the pulser cannot sustain the PWR load, $\frac{|\vec{E}|}{N_g}$ roughly decreases by a factor of two throughout the experiments. This should yield electron temperatures and densities of $\sim 1\text{--}5 \text{ eV}$ and $10^{10}\text{--}10^{13} \text{ cm}^{-3}$, respectively. Computational models confirm ozone is diffusion-limited and pulser parameters can be optimized to yield different ROS dose. For instance, the peaked gas-phase concentration of O_3 suggests that the increasing amount of O^\bullet leads to more O_3 ($\text{O}^\bullet + \text{O}_2 + \text{M} \longrightarrow \text{O}_3 + \text{M}$) but, as voltage increases, the increasing amount of NO_2^\bullet consumes more O^\bullet ($\text{O}^\bullet + \text{NO}_2^\bullet + \text{M} \longrightarrow \text{NO}_3^\bullet + \text{M}$), resulting in less O_3 (Lietz and Kushner, 2016). Future work will explore ozone optimization in the pulser parametric space to confirm this maximum. It is difficult to validate this now since the voltage is not constant throughout each run, falsely implying that there is a minimum instead (Fig. 4.41).

Overall, experimental and computational models that include the relative contribution of transient radicals can better reflect kinetics.

4.7.1 CECs in the PWR and Existing AOPs

According to Equation 4.5, GlobalKin, and 1,4-dioxane experiments, $\langle[\bullet\text{OH}]\rangle$ was determined to be 10^{16} , 10^{12} , and 10^7cm^{-3} , respectively. The wide range between theory, computation, and experiment indicates that lab and pilot studies will be the most reliable in determining the PWR's effective oxidant dose in a given water matrix.

Since 1,4-dioxane is predominantly destroyed by hydroxyl radical, the effective reaction rate can yield $\langle[\bullet\text{OH}]\rangle$. Assuming that the oxidant dose was the same for MTBE as it was for 1,4-dioxane using the same water matrix and pulser parameters (Subsection 4.4), MTBE decomposition is assessed and compared to existing peroxone systems in Table 4.5. Interestingly, the observed effective reaction rate ($1.6 \times 10^{-3}\text{s}^{-1}$) is an order of magnitude greater than the sum of $\bullet\text{OH}$ and O_3 reaction rates ($k_{\text{HO}\bullet, \text{MTBE}}\langle[\text{HO}\bullet]\rangle + k_{\text{O}_3, \text{MTBE}}[\text{O}_3] = 2.5 \times 10^{-4}\text{s}^{-1}$), suggesting that unknown transient radicals are significantly contributing to CEC decomposition. More importantly, compared to peroxone, the PWR promotes a higher scavenging capacity and a lower oxidant dose while effectively (R_{ct}) and energy efficiently ($\zeta\frac{P}{V}$) producing $\bullet\text{OH}$. In this case, the PWR is roughly an order of magnitude more energy efficient than peroxone at radical production.

In the end, as can be seen in Table 4.6, the PWR can provide different oxidant doses and order of reaction rates that can customize CEC destruction. Future work will include kinetic parametric studies using CEC decomposition trees (Fig. A.1) and their reaction rate coefficients (Tab. A.2) to merge computational and experimental results. Pilot studies will feed data into the global model to better represent custom water matrices. Overall, the variability exhibited by the PWR helps achieve custom treatment objectives over several order of magnitudes.

TABLE 4.5: AOP parameters for MTBE destruction using reaction rate coefficients in Table A.2. Assuming pseudo first-order kinetics (Eqn. 2.2), hydroxyl production rate is expressed as $\zeta \frac{P}{V}$ where ζ is a system-dependent constant, P is power, V is volume, and scavenger S includes dissolved organic carbon, bicarbonate (HCO_3^-), and carbonate (CO_3^{2-}) except for the last three cases; the scavenger capacity for the third- and second-to-last cases were calculated based on byproducts and benzene, respectively (Elovitz and Gunten, 1999; Acero et al., 2001; Bolton et al., 2001; Mitani et al., 2002). The final case is the PWR where the scavenger capacity was approximated using nitrate ($k_{\text{HO}\cdot, \text{NO}_3^-} \langle [\text{NO}_3^-] \rangle$) and $\langle [\cdot\text{OH}] \rangle$ was estimated using 1,4-dioxane as an indicator compound at the same power.

$[\text{H}_2\text{O}_2]$ cm^{-3}	$[\text{O}_3]$ cm^{-3}	$R_{ct} \left(\frac{f[\cdot\text{OH}]dt}{f[\text{O}_3]dt} \right)$	$\langle [\cdot\text{OH}] \rangle$ cm^{-3}	Scavenging Capacity $\sum_j k_{\text{HO}\cdot, S} [S_j] \text{ (s}^{-1}\text{)}$	$\zeta \frac{P}{V}$ $\text{cm}^{-3} \text{ s}^{-1}$	k_{eff} s^{-1}	$\frac{k_{\text{HO}\cdot} \langle [\cdot\text{OH}] \rangle}{k_{\text{O}_3} \langle [\text{O}_3] \rangle}$ $\left(\frac{R_{ct} k_{\cdot\text{OH}}}{R_{ct} k_{\cdot\text{OH}} + k_{\text{O}_3}} \right)$
0	2.5×10^{16}	6.4×10^{-10}	3.1×10^7	5.6×10^4	2×10^{12}	1.1×10^{-4}	8.7 (0.9)
1.2×10^{16}	2.5×10^{16}	4.4×10^{-8}	1.7×10^9	5.6×10^4	9.4×10^{13}	5.3×10^{-3}	600 (0.998)
2.4×10^{16}	5×10^{16}	6.1×10^{-8}	2.2×10^9	5.6×10^4	1.2×10^{14}	6.8×10^{-3}	830 (0.999)
0	2.5×10^{16}	2.8×10^{-9}	1.5×10^8	5.6×10^4	8.3×10^{12}	4.7×10^{-4}	40 (0.97)
1.2×10^{16}	2.5×10^{16}	7.4×10^{-8}	3.8×10^9	5.6×10^4	2.1×10^{14}	1.2×10^{-2}	1000 (0.999)
0	2.5×10^{16}	2.2×10^{-10}	1.6×10^7	6.2×10^4	1.3×10^{12}	6.8×10^{-5}	3 (0.75)
1.2×10^{16}	2.5×10^{16}	1.9×10^{-8}	1.2×10^9	6.2×10^4	7.5×10^{13}	3.8×10^{-3}	260 (0.996)
2.4×10^{16}	5×10^{16}	3.6×10^{-8}	1.7×10^9	6.2×10^4	1×10^{14}	5.3×10^{-3}	490 (0.998)
0	2.5×10^{16}	4×10^{-10}	5.4×10^7	6.2×10^4	3.9×10^{12}	2×10^{-4}	5.4 (0.84)
0	2.5×10^{16}	4×10^{-9}	2.4×10^8	1×10^5	2.4×10^{13}	7.7×10^{-4}	54 (0.98)
1.2×10^{16}	2.5×10^{16}	4.2×10^{-8}	2.6×10^9	1×10^5	2.6×10^{14}	8.3×10^{-3}	570 (0.998)
2.4×10^{16}	5×10^{16}	4.4×10^{-8}	3.2×10^9	1×10^5	3.2×10^{14}	1×10^{-2}	600 (0.998)
0	4.3×10^{16}	1.2×10^{-8}	5×10^8	2.7×10^3	1.4×10^{12}	1.6×10^{-3}	0.52 (0.34)
2.1×10^{16}	4.3×10^{16}	1.2×10^{-8}	5×10^8	2.1×10^5	1.1×10^{14}	1×10^{-3}	0.53 (0.35)
1.4×10^{16}	6.3×10^{14}	1.4×10^{-7}	8.8×10^7	8.8×10^6	7.2×10^{15}	1.6×10^{-3}	6.2 (0.86)

TABLE 4.6: AOP parameters derived from effective CEC reaction rates using the PWR based on reaction rate coefficients in Table A.2. Scavenger capacity was estimated as $k_{\text{HO}\cdot, \text{NO}_3^-} \langle [\cdot\text{OH}] \rangle$. For MTBE and MB, $\langle [\cdot\text{OH}] \rangle$ was estimated using 1,4-dioxane as an indicator compound at the same power. For MB, the hydroxyl production rate is calculated assuming $k_{\cdot\text{OH}, \text{MB}} = 2 \times 10^{-10} \text{ cm}^3 \text{ s}^{-1}$.

$[\text{H}_2\text{O}_2]$ cm^{-3}	$[\text{O}_3]$ cm^{-3}	$R_{ct} \left(\frac{f[\cdot\text{OH}]dt}{f[\text{O}_3]dt} \right)$	$\langle [\cdot\text{OH}] \rangle$ cm^{-3}	Compound C	Scavenging Capacity (s^{-1})	$\zeta \frac{P}{V}$ $\text{cm}^{-3} \text{ s}^{-1}$	k_{eff} s^{-1}	$\frac{k_{\text{HO}\cdot, C} \langle [\cdot\text{OH}] \rangle}{k_{\text{O}_3, C} \langle [\text{O}_3] \rangle}$ $\left(\frac{R_{ct} k_{\cdot\text{OH}, C}}{R_{ct} k_{\cdot\text{OH}, C} + k_{\text{O}_3, C}} \right)$
1.4×10^{16}	6.3×10^{14}	1.4×10^{-7}	8.8×10^7	MB	8.8×10^6	2×10^{13}	4.5×10^{-4}	
1.4×10^{16}	6.3×10^{14}	1.4×10^{-7}	8.8×10^7	MTBE	8.8×10^6	7.2×10^{15}	1.6×10^{-3}	6.2 (0.86)
1.4×10^{16}	6.3×10^{14}	1.4×10^{-7}	8.8×10^7	1,4-dioxane	8.8×10^6	7.8×10^{14}	2.5×10^{-4}	760 (0.999)
1.8×10^{16}	1.3×10^{14}	4.8×10^{-7}	6×10^7	1,4-dioxane	6.3×10^6	3.8×10^{14}	1.7×10^{-4}	2600 (≈ 1)
8.9×10^{15}	1.3×10^{15}	4.5×10^{-8}	5.7×10^7	1,4-dioxane	3.8×10^6	3.5×10^{13}	$0.7 \text{ g kW}^{-1} \text{ h}^{-1}$	250 (0.996)
$0-2.8 \times 10^{16}$	$0-2 \times 10^{15}$	$10^{-8}-10^{-7}$	10^6-10^{12}		$\sim 10^6$	$10^{13}-10^{16}$	$10^{-6}-10^{-1}$	

Chapter 5

Plasma's Forthcoming Role in Resource Recovery

Overall, the Plasma Water Reactor's performance was promising.

5.1 Assessing the PWR's Efficacy

According to 21st century industrial water trends, new water treatment technologies must be effective, efficient, scalable, versatile, and customizable. As technologies evolve, they must be able to: adapt to new contaminants, reduce energy consumption, maintain or improve the proportionality between power and flow, demonstrate various flow capacities, minimize the transformation of existing infrastructure, prepare for imminent regulations, and tailor chemistry to site-specific requirements. Based on the experiments in the previous chapter, the PWR established its potential as a platform water treatment technology.



FIGURE 5.1: Post-treated tap water particulate from induced oxidation and electrocoagulation.

5.1.1 Effectiveness

The PWR was capable of precipitation and mineralization. Particulates formed at the bottom of the contact tank when tap water was treated (Fig. 5.1) whereas concentrations decreased below detectable limits when contaminants were gauged. However, perceived electrocoagulation and complete mineralization still need to be reaffirmed for all water matrices tested, especially when pilots are performed.

Chemical probes must be strategically selected as evident in the disagreement between oxidant concentrations using the chemical probes and the polarographic membraned sensors. Deviations between these measurements can be attributed to interference pathways from the presence of other reactive species, which are typically unknown. Preferred chemical probes are simple and have well known kinetics, particularly byproducts, such as phenol (Banaschik et al., 2015). Therefore, indicator compounds may be used to determine the exclusivity and relative contribution of various AOP pathways.

The PWR used MB, MTBE, and 1,4-dioxane as recalcitrant indicator compounds to

evaluate destruction and its various pathways. These trials confirmed that 1,4-dioxane was the most difficult to treat and was thus utilized as the model contaminant for a full kinetic study. During this study, plasma-based byproducts, particularly nitrate, and 1,4-dioxane transformation products, such as formate and acetate, were formed and exhibited behavior that needs to be better characterized. Ideally, information about the highlighted contaminant and its intermediates can be used to simplify the kinetic model as a function of initial pulser parameters and influent water quality.

5.1.2 Efficiency

Using energy metrics such as E_{EM} (Eqn. 1.1) and E_{EO} (Eqn. 1.2), the PWR fared decently. The PWR exhibited improved energy consumption relative to other plasma-based systems but, its energy consumption was still greater than its AOP counterparts. However, when equivalent low energy densities were used, the PWR was able to provide the optimal ratio for $\frac{[H_2O_2]}{[O_3]}$ similar to traditional peroxone. Depending on pulser parameters, E_{EO} could change over time, implying that the NSP-PWR matching was power-limited, unknown water matrix constituents were affecting the effective flow rate, and the PWR should be able to achieve E_{EO} less than conventional AOPs.

Overall efficiency, defined as deposited power via I-V integration divided by applied power, would stabilize around 25% but, for pulser configurations prone to pseudoarcs, the efficiency would fluctuate between 10–50% at the beginning of the trial. Of the power applied to the circuit, only a small fraction of energy is dissipated in the electrons and this must be evaluated and maximized.

5.1.3 Scalability

Based on E_{EO} 's for various contaminants spiked into DI water, the PWR demonstrated rather low effective flow rates on the order of ~ 0.1 – 0.75 GPM for 90% removal.

E_{EO} behaviors for different contaminants and pulser parameters suggest that these effective flow rates can improve. The power-limited NSP prevented scaling to relevant flow rates (>GPM) but, assuming these flow rates are inert and intrinsic, the modular design of the PWR enables it to be stacked in parallel and achieve the minimum required flow rate of a given application. If certain configurations or greater power density result in upgraded effective flow rates, the PWR must be imaged to verify that the plasma-water interface is enhanced and responsible for improved scale.

5.1.4 Versatility

In addition to allowing it to scale, the modular design enables the PWR to be versatile. Since pilot studies are required to establish credibility, the PWR can be conveniently retrofitted to existing water treatment infrastructure. Also, the PWR's low energy consumption allows it to operate using alternative energy sources. Furthermore, the PWR can address dynamic influent water quality due to its ability to control ROS production. Overall, the PWR enables parametric investigations at different parts of the treatment train that help identify the most suitable application.

5.1.5 Customization

The PWR can vary ROS dose and provide a wide range of $\frac{[H_2O_2]}{[O_3]}$, which can control contaminant destruction and byproduct production, such as bromate. Since several combinations of pulser parameters can deliver the optimal ratio of $\sim 0.5 \frac{\text{mol}}{\text{mol}}$, the PWR can supply the necessary ROS dose then be fine-tuned for a given application. $\frac{[H_2O_2]}{[O_3]}$ was close to the optimal ratio for low energy densities, further promoting the idea that energy efficient configurations can gradually treat water at low power. Moreover, using GlobalKin, changes in treatment volume were used to validate that changes in power density affect kinetics. This confirms the need to perform kinetic computations

when designing the next generation of PWRs to roughly approximate ROS dose prior to extensive pulser parametric studies.

The variability in ROS dose was likely accountable for the different order of reaction rates observed for 1,4-dioxane. Since zeroth- and first-order decomposition were evident, the PWR has the ability to control $\bullet\text{OH}$ production and to tailor dose for a given application. For instance, within the same industry, one company may need a contaminant of concern to be removed as quickly as possible (high flow, lower efficiency) while another may want to deal with the compound cost-effectively over time (low flow, high efficiency).

As a result, kinetic studies and pilots will help determine treatment efficacy for custom water matrices.

5.2 Future Investigations

The upgraded subscale PWR system will be utilized to expand the ROS and 1,4-dioxane kinetic investigations. The same pulser parametric studies will be performed at higher power and other flow configurations including semi-batch and once-through. Higher power should permit higher effective flow rates, which can be justified if ROS dose is sufficient once-through. Based on this inquiry, if once-through is not attainable for a given PWR geometry, PWR modules can be added in series or parallel to fulfill site specifications. Scale remains the goal and a high power, once-through PWR should achieve it. Once better understood, the PWR will be used on different water matrices that are relevant for pilots.

Meanwhile, PFASs and NDMA will be used as indicator compounds to estimate the PWR's reduction and UV capabilities, respectively. UV dose will be assessed, which will improve the PWR's comparison to traditional AOPs. This can also be used to

determine the UV contribution and inactivation potential of the PWR using surrogates, such as MS2.

Scavengers, or any •OH-consuming constituent, will be examined in greater detail, particularly plasma-produced RNS, to determine ROS loss. Since nitrates and nitrites have MCLs for drinking water, their production must be mitigated. If air is used, their production is inherent and denitrification is critical. Other technologies, such as bioreactors, can be coupled to the PWR to denitrify water but, the PWR may assist in nutrient recovery on its own and is the subject of pending work.

Also, the kinetic investigations will be complemented by computational models. GlobalKin can confirm the pulser parametric studies by varying power waveforms and approximating ROS reaction rates. If GlobalKin exhibits ROS behavior similar to the experiments, indicator compounds and their transformation products can be inserted to determine their effective reaction rates. Moreover, if the PWR is represented as circuit components, Simulation Program with Integrated Circuit Emphasis, or SPICE, can verify circuit behavior by sweeping circuit element values and determining which circuit configurations yield waveforms equivalent to the experiment. Therefore, the simulations can include real-time experimental data to approximate power and transient species concentrations. The objective of the hybrid experimental-computational model is to present and predict kinetics as a function of input power parameters.

In addition to GlobalKin or SPICE, a collisional radiative model can be coupled to optical emission spectroscopy to ascertain species concentrations. Using an integration time of 300 ms, an example spectrum of the upgraded PWR is rendered in Figure 5.2. The spectrum indicates peaks similar to those of other non-thermal atm plasmas. The evident low frequency cut-off is from attenuation due to the water jets and acrylic reaction chamber. Nonetheless, the upgraded PWR should be slightly modified to collect real-time optical emission and absorption spectra that can determine UV dose

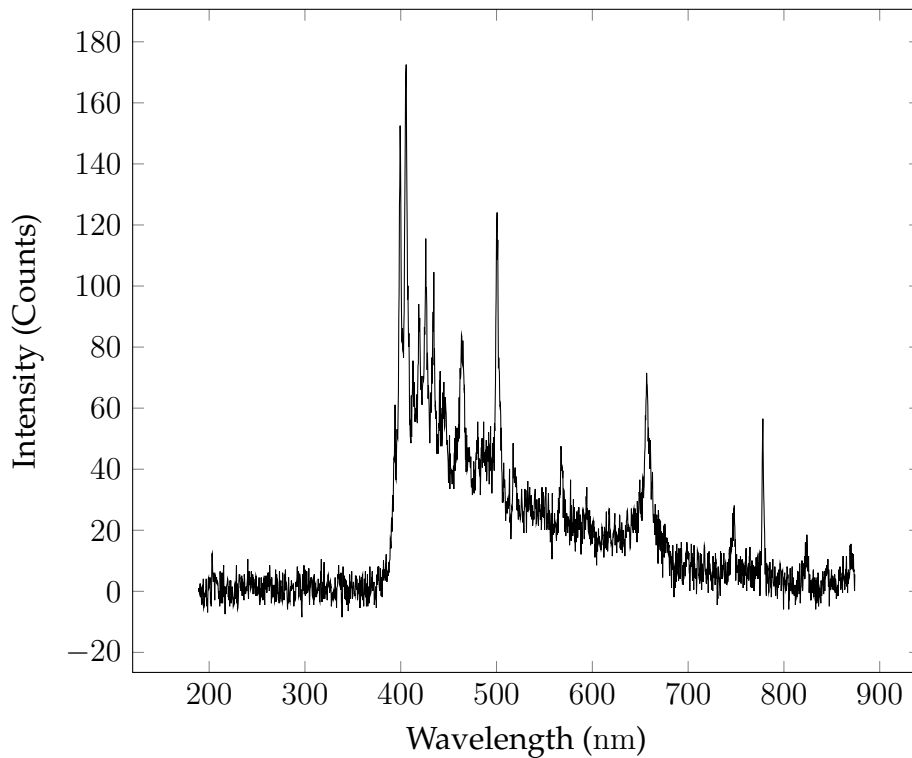


FIGURE 5.2: Optical emission spectrum of upgraded PWR in DI water at (20 kV, 4 kHz, 40 ns).

and supplement existing analytics.

While collecting light to deduce plasma species, imaging can be helpful to prove whether the PWR truly improved plasma-water contact. While simulations indicated streamer formation and propagation throughout most of the reactor, high-speed imaging can verify if the plasma-water interface is enhanced by close-packed water jets. This is a crucial step to validate the PWR's design criteria. However, the PWR electromagnetically interferes with charge-coupled devices due to the fast rise time of pulses. Consequently, EMI must be measured, using a network analyzer, and ultimately mitigated with ferrite cores or an improved Faraday cage.

5.3 Prospects for the Future

Once the laboratory unit has been verified, the next step is to evolve the PWR into the so-called minimum viable product (MVP). The MVP is the simplest embodiment of the PWR that performs its core functions. From a commercialization standpoint, the MVP yields a cost effective starting point for the PWR. The MVP also allows one to quickly manufacture the hardware and get it into the market for early adopters. If the technology is to mature, the target users must also be clearly identified. As scale-up is an ongoing issue with plasma-based systems, it is likely that point-of-use or specialty industries with recalcitrant contaminants and small process volumes will be among the first adopters. Here again, the key is to minimize the cost of treating the burdensome water.

The MVP serves as a basis for field testing. Demonstrations in relevant environments are key for eventual adoption. In general, new technologies in the water treatment sector are field tested via a pilot study. A pilot study refers to testing the MVP in a relevant environment, usually at small-scale. The goal is to characterize performance in a practical setting and to determine whether to proceed to a large-scale project. Piloting also allows for side-by-side comparison with technologies that perhaps it will one day replace. Data from pilot studies help optimize the PWR, determine plasma-based kinetics of various practical water qualities, establish a basis of confidence for the ultimate end users, and directly address public outreach, which is particularly important for acceptance. Finally, the pilot testing is required for regulatory approval, especially in water reuse (eg. Florida FAC 62-610.564; California Title XXII).

Piloting comes in essentially four varieties: (1) bench-scale testing, (2) pilot testing, (3) demonstration testing, and (4) full-scale testing. Determining the appropriate piloting approach is application dependent, often depending on cost. Piloting also addresses issues such as toxicity in a relevant environment. Toxicity considerations for

plasma-based systems include byproducts and nitrification effects, which can be significant if air plasmas are used. The treatment byproducts include residual fragments and unintended reactions and can only be addressed with relevant feed water obtained at an actual treatment facility. The effectiveness of using other treatment methods in tandem, such as activated sludge to denitrify or remove chemical fragments associated with incomplete mineralization, can be assessed via piloting. Indeed, denitrification is a typical step already implemented in treatment plants and thus, existing technologies can be leveraged in terms of integrating a plasma-based system into a commercial water treatment plant.

Finally, to be relevant, the piloting exercise must extract relevant data that can be interpreted and compared to existing treatment methods. In general, the basic characterization of the treated water must include: (1) contaminant concentration, (2) pH, (3) alkalinity (ability of water to resist change in pH), (4) conductivity, (5) turbidity, (6) biological oxygen demand (BOD, oxygen required for aerobic microbes to decompose organics present), (7) chemical oxygen demand (COD, oxidant required to decompose organics present), (8) bacteria, virus, and protozoa, (9) total dissolved solids, and (10) nitrate/nitrite concentration. It should be noted that plasma-activated liquids can interfere with the implementation of some of these tests and thus, care must be taken in applying them to plasma-treated water. For example, excess H_2O_2 in plasma-treated water can actually interfere with conventional COD tests, leading one to conclude that the treatment had minimal effect on the organic load in the water. Instead, H_2O_2 can oxidize the oxidant in the COD kit, leading to a null or little change measured in organic load (Lee et al., 2011). Nevertheless, piloting also allows one to optimize practical implementation of advanced water treatment technologies.

Plasma-based water purifiers are an alternative means of driving advanced oxidation in solution for the purpose of contaminant removal and disinfection. Since plasmas drive a wide range of oxidation pathways at once, it is currently being studied as a means to address recalcitrant contaminants of emerging concern. It does so by efficiently injecting many reactive oxygen species into solution without the need for consumables—the key value proposition. However, the key challenge has been scale-up. As described earlier, the PWR is one of several potential solutions to the scale-up problem. Particularly, the PWR uses close-packed water streams in an attempt to maximize the plasma contact area with the water. The PWR demonstrated the capacity to deliver $\text{H}_2\text{O}_2/\text{O}_3$ dose comparable to conventional methods and degrade contaminants of emerging concern. The next critical step in maturing this water treatment technology is piloting in practical settings, which assesses the PWR's effectiveness in a relevant environment and provides the foundation for acceptance by potential users, particularly early adopters.

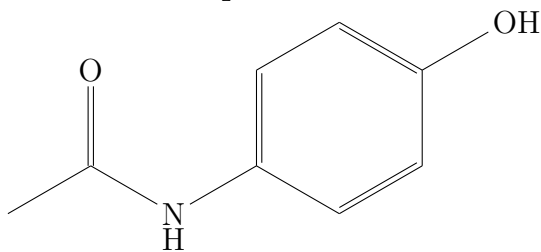
Appendix A

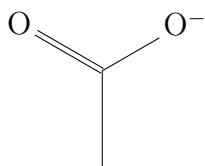
Chemicals and Reactions of Interest

A.1 Mentioned Species

Table A.1 includes legacy and emerging contaminants of concern, reactive molecules, highlighted indicator compounds, and decomposition byproducts.

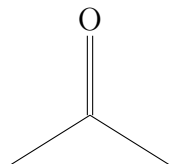
TABLE A.1: Species discussed throughout the thesis.

Chemical Name	Formula
Structure	
Acetaminophen	$C_8H_9NO_2$
	
Acetate	$C_2H_3O_2^-$



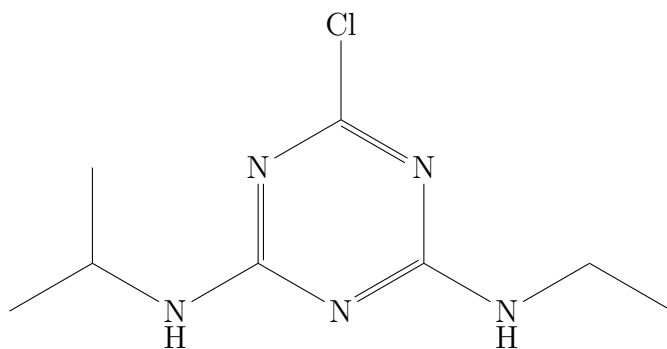
Acetone (or 2-Propanone)

C_3H_6O



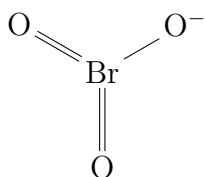
Atrazine

$C_8H_{14}ClN_5$



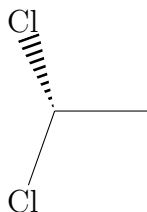
Bromate

BrO_3^-



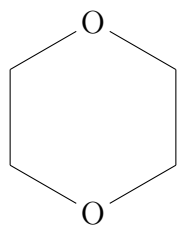
1,1-Dichloroethane

$C_2H_4Cl_2$

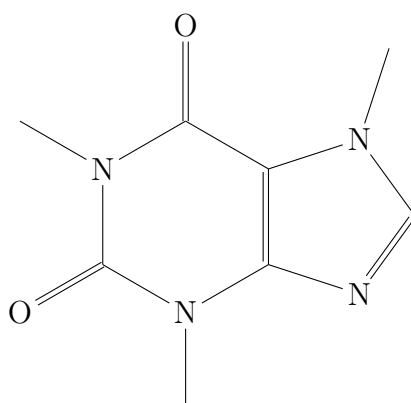
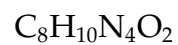


1,4-Dioxane

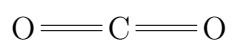
$C_4H_8O_2$



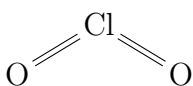
Caffeine



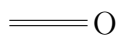
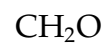
Carbon Dioxide



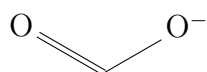
Chlorine Dioxide



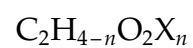
Formaldehyde

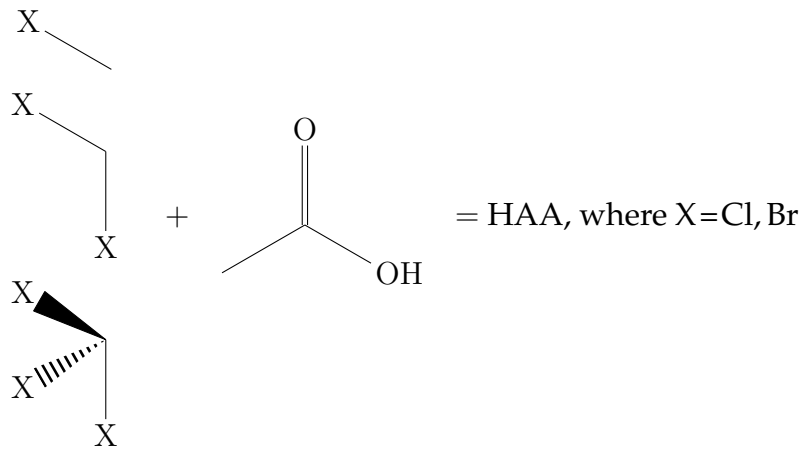


Formate

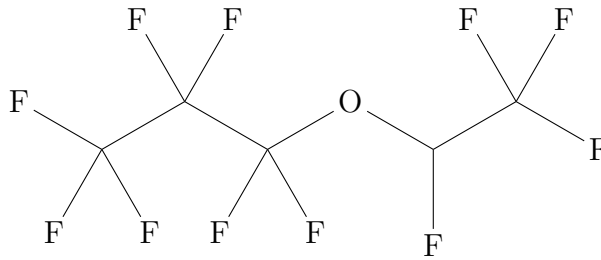


Haloacetic acids (HAAs)



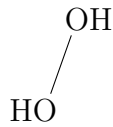


Heptafluoropropyl 1,2,2,2-tetrafluoroethyl ether $\text{C}_5\text{HF}_{11}\text{O}$



Hydrogen Peroxide

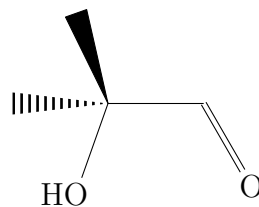
H_2O_2



Hydroxyisobutyraldehyde (HiBA),

$\text{C}_4\text{H}_8\text{O}_2$

or 2-Hydroxy-2-methylpropanal

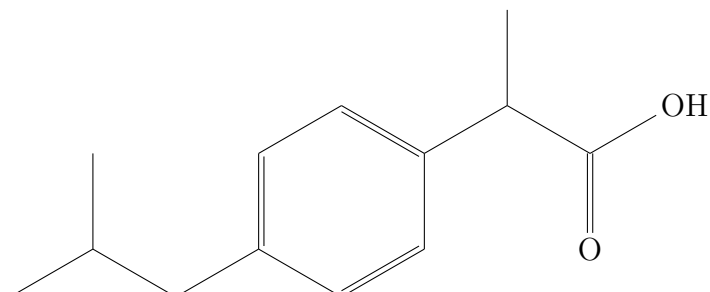
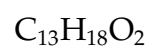


Hypochlorite

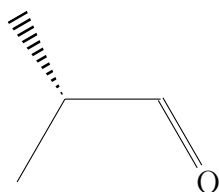
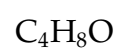
ClO^-



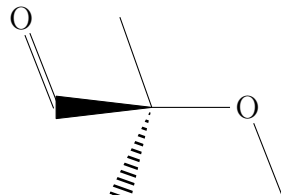
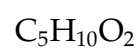
Ibuprofen



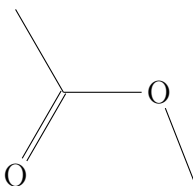
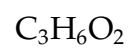
Isobutyraldehyde (iBA)



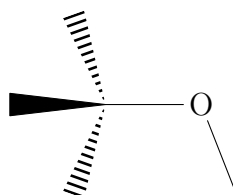
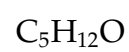
2-Methoxy-2-methyl propionaldehyde (MMP)

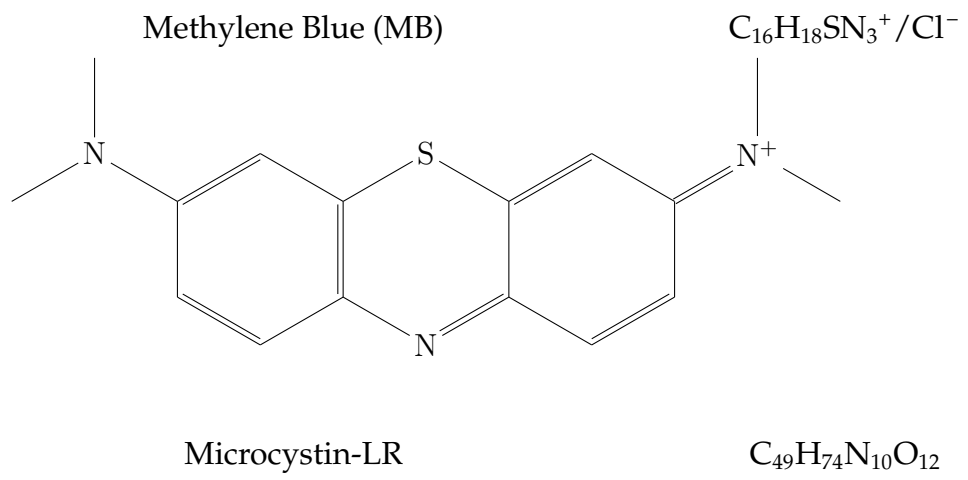


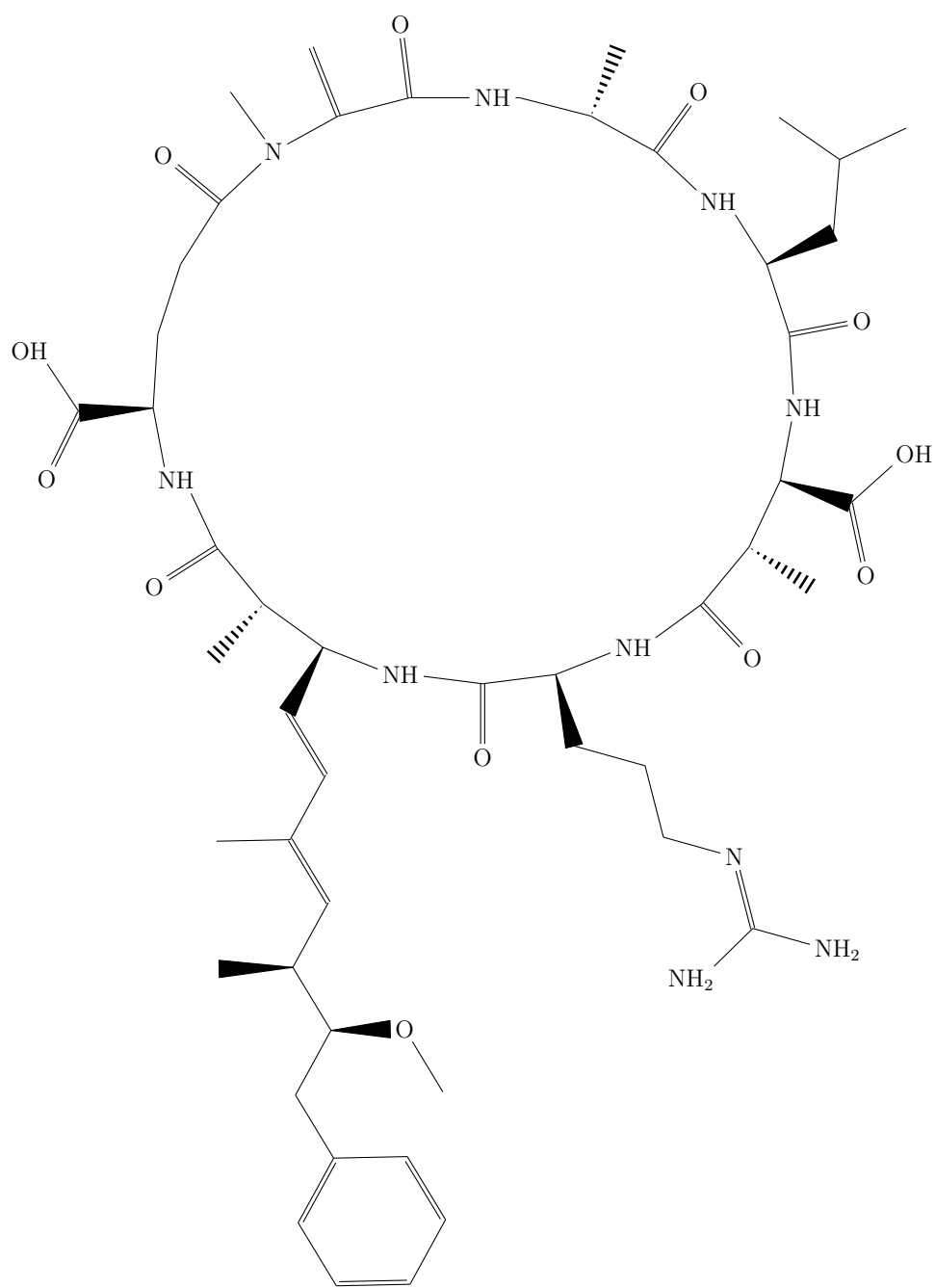
Methyl acetate



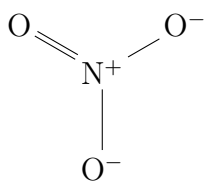
Methyl tertiary-butyl ether (MTBE)





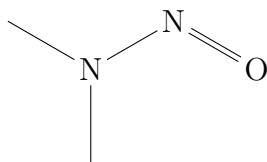
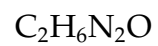


Nitrate

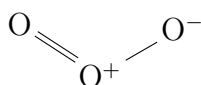


NO₃⁻

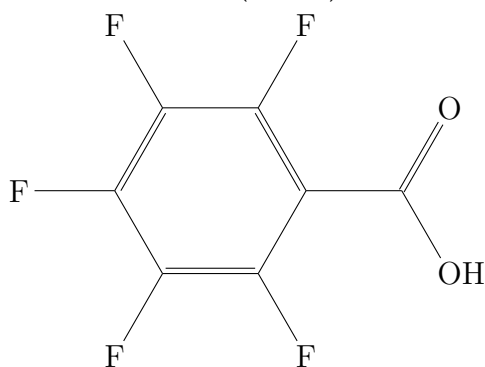
N-Nitrosodimethylamine (NDMA)



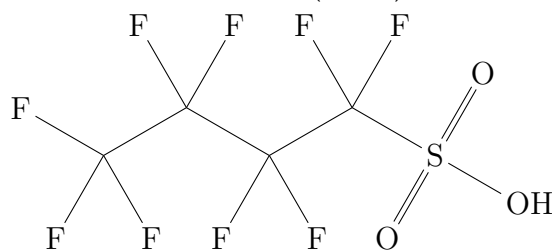
Ozone



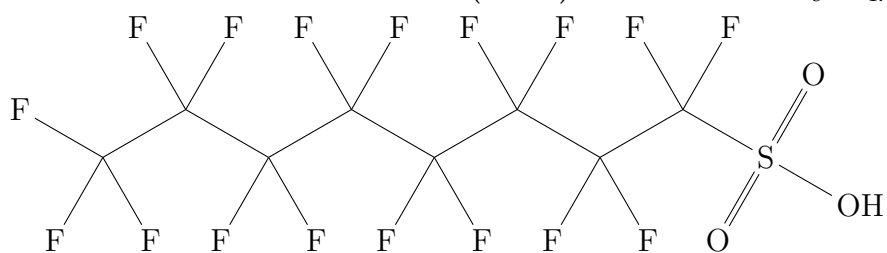
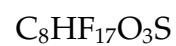
Pentafluorobenzoic acid (PFBA)

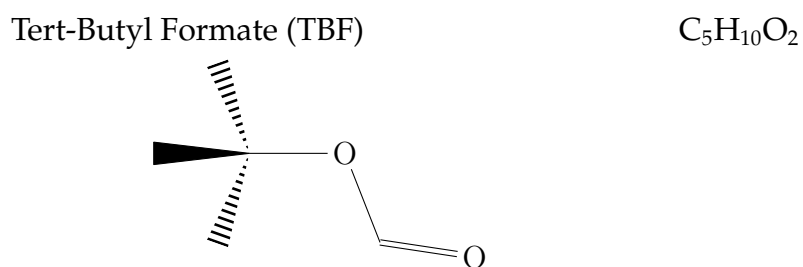
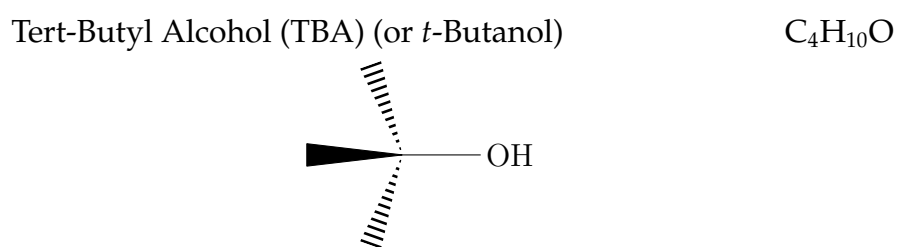
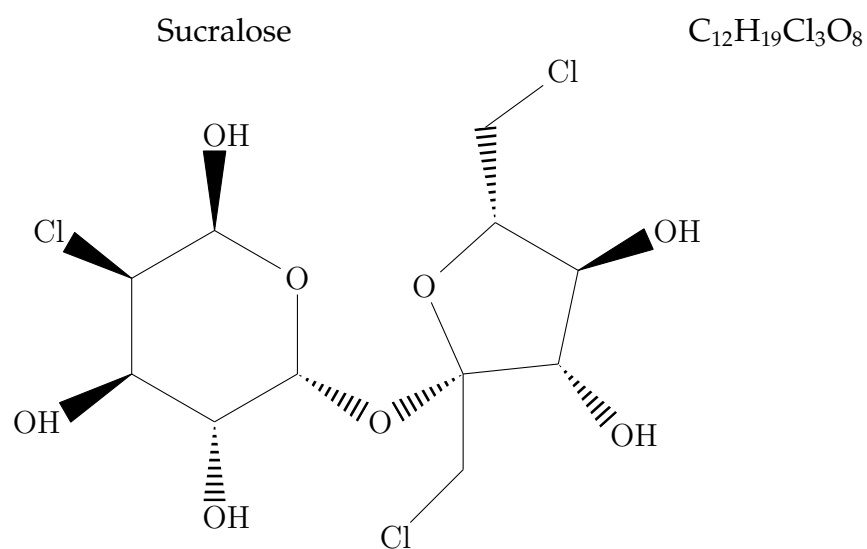
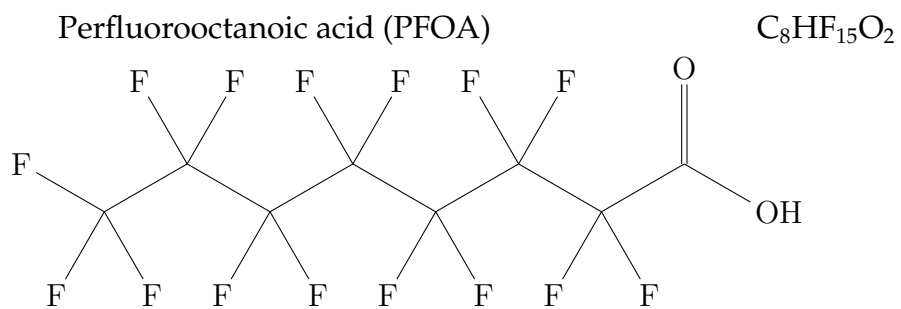


Perfluorobutanesulfonic acid (PFBS)



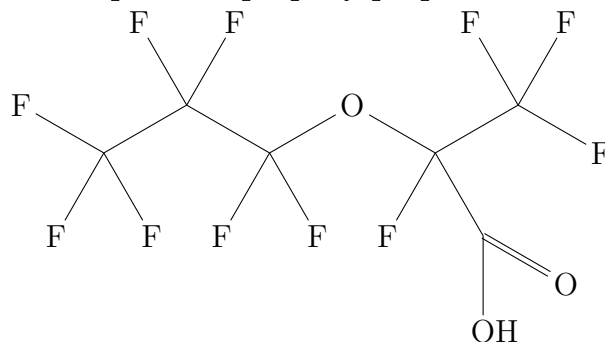
Perfluorooctanesulfonic acid (PFOS)





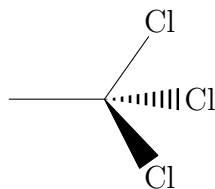
2,3,3,3-Tetrafluoro-2-(heptafluoropropoxy)propanoic acid

$C_6HF_{11}O_3$



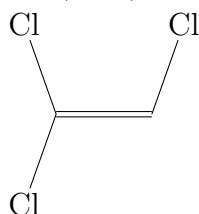
1,1,1-Trichloroethane (1,1,1-TCA)

$C_2H_3Cl_3$



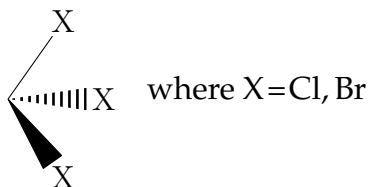
Trichloroethylene (TCE)

C_2HCl_3



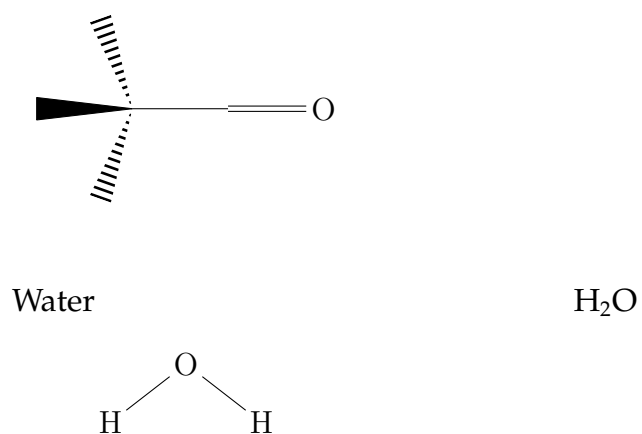
Trihalomethanes (THMs)

CHX_3



Trimethylacetaldehyde (TMA)

$C_5H_{10}O$



A.2 Highlighted Reactions

Tables 2.1 and A.2 lists all reaction rate coefficients considered relevant for ROS production and CEC destruction, respectively. For example, the MTBE decomposition tree in Figure A.1 demonstrates its many transformation products and reaction pathways. AOP metrics for various MTBE contaminated matrices are shown in Table 4.5.

TABLE A.2: List of ozone (O₃) and hydroxyl (•OH) reaction rate coefficients for 1,4-dioxane, MTBE, and their known transformation products at 25 °C calculated using different [H₂O₂] and [O₃]. O₃ and •OH coefficients for MMP and HiBA were estimated based on averaging their respective values obtained for structurally similar TMA and iBA (Buxton et al., 1988; Adams, Scanian, and Secrist, 1994; Acero et al., 2001; Mitani et al., 2002; Butkovskaya et al., 2004; Suh and Mohseni, 2004).

Compound <i>C</i>	$k_{\text{O}_3,C}(\text{cm}^3 \text{s}^{-1})$	$k_{\text{HO}\cdot,C}(\text{cm}^3 \text{s}^{-1})$
MTBE	2.32×10^{-22} – 4.48×10^{-20}	3.2×10^{-12}
TBF	1.30×10^{-21}	1.2×10^{-12}
TBA	4.982×10^{-24}	1.0×10^{-12}
MMP	8×10^{-21}	5.0×10^{-12}
Methyl acetate	1.49×10^{-22}	3.8×10^{-13}
Acetone	5.314×10^{-23}	2.2×10^{-13}
HiBA	8×10^{-21}	5.0×10^{-12}
Formaldehyde	1.7×10^{-22}	1.7×10^{-12}
TMA	9.8×10^{-21}	5.3×10^{-12}
iBA	7.0×10^{-21}	4.6×10^{-12}
Benzene		1.3×10^{-11}
1,4-Dioxane	5.3×10^{-22}	$(1.8\text{--}4.2) \times 10^{-12}$
Acetate		6.6×10^{-13}
Formate		5.3×10^{-12}
Nitrate		2.6×10^{-11}

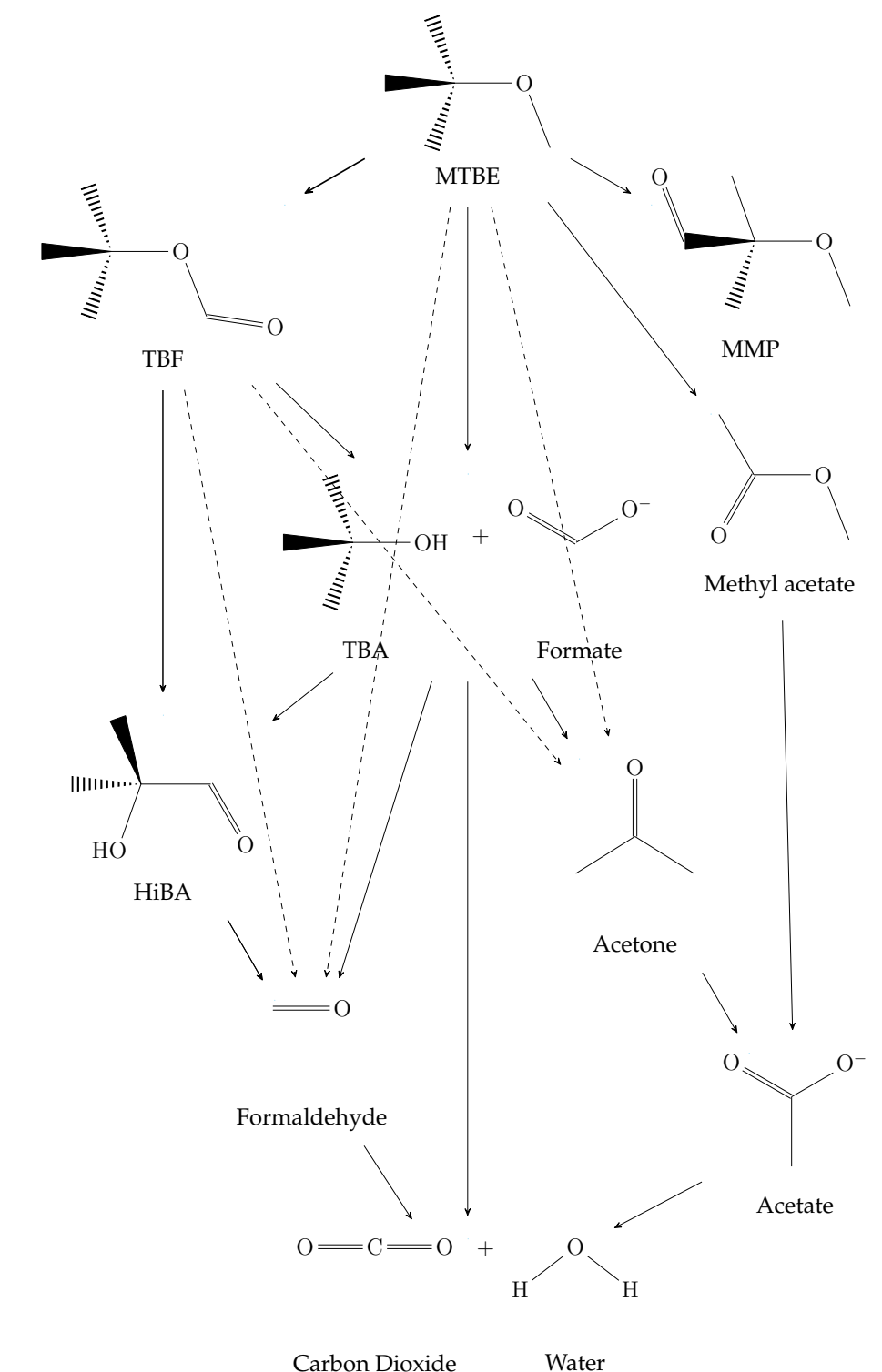


FIGURE A.1: Decomposition pathways of MTBE and its transformation products (Acero et al., 2001; Mitani et al., 2002).

Bibliography

- Aathithan, S. et al. (2001). "Diagnosis of Bacteriuria by Detection of Volatile Organic Compounds in Urine Using an Automated Headspace Analyzer with Multiple Conducting Polymer Sensors". In: *Journal of Clinical Microbiology* 39.7, pp. 2590–2593.
- Acero, Juan L. et al. (2001). "MTBE Oxidation by Conventional Ozonation and the Combination Ozone/Hydrogen Peroxide: Efficiency of the Processes and Bromate Formation". In: *Environmental Science & Technology* 35.21, pp. 4252–4259.
- Adams, Craig D., Patricia A. Scanian, and Neal D. Secrist (1994). "Oxidation and Biodegradability Enhancement of 1,4-Dioxane Using Hydrogen Peroxide and Ozone". In: *Environmental Science and Technology* 28.11, pp. 1812–1818.
- Adamson, David T. et al. (2017). "1,4-Dioxane drinking water occurrence data from the third unregulated contaminant monitoring rule". In: *Science of the Total Environment* 596–597, pp. 236–245.
- Adler, Jonathan H. (2002). "Fables of the Cuyahoga: Reconstructing a History of Environmental Protection". In: *Fordham Environmental Law Journal* 14.
- Al-Jaibachi, Rana, Ross N. Cuthbert, and Amanda Callaghan (2018). "Up and away: ontogenic transference as a pathway for aerial dispersal of microplastics". In: *Biology Letters* 14.
- Allen, Steve et al. (2019). "Atmospheric transport and deposition of microplastics in a remote mountain catchment". In: *Nature Geoscience*.
- Anderson, James L. (1976). "The equations of radiative hydrodynamics". In: *General Relativity and Gravitation* 7.1, pp. 53–67.
- Antonopoulou, M. et al. (2014). "A review on advanced oxidation processes for the removal of taste and odor compounds from aqueous media". In: *Water Research* 53, pp. 215–234.
- APHA, AWWA, and WEF (2017). *Standard Methods For the Examination of Water and Wastewater*. Ed. by E. W. Rice, R. B. Baird, and A. D. Eaton. 23rd. 9780875532875. American Public Health Association, American Water Works Association, and Water Environment Federation.
- Asano, Takashi and Joseph A. Cotruvo (2004). "Groundwater recharge with reclaimed municipal wastewater: health and regulatory considerations". In: *Water Research* 38, pp. 1941–1951.

- Ashley, David L. et al. (1992). "Determining volatile organic compounds in human blood from a large sample population by using purge and trap gas chromatography/mass spectrometry". In: *Analytical Chemistry* 64.9, pp. 1021–1029.
- Attri, Pankaj et al. (2015). "Generation mechanism of hydroxyl radical species and its lifetime prediction during the plasma-initiated ultraviolet (UV) photolysis". In: *Scientific Reports* 5.
- Ausman, E. L. and M. Brook (1967). "Distortion and Disintegration of Water Drops in Strong Electric Fields". In: *Journal of Geophysical Research* 72.24.
- Babaeva, Natalia Yu (2014). "Notes on Streamer discharge". In: *Atmospheric Pressure, Low Temperature Plasma Mini-Course*. ICOPS/Beams Conference.
- Babaeva, Natalia Yu and Mark J Kushner (2008). "Streamer Branching: The Role of Inhomogeneities and Bubbles". In: *IEEE Transactions on Plasma Science* 36.4.
- Babaeva, Natalia Yu et al. (2017). "Streamer breakdown in elongated, compressed and tilted bubbles immersed in water". In: *Journal of Physics D: Applied Physics* 50.364001.
- Bagheri, Mehdi and Madjid Mohseni (2014). "Computational fluid dynamics (CFD) modeling of VUV/UV photoreactors for water treatment". In: *Chemical Engineering Journal* 256.15, pp. 51–60.
- Banaschik, Robert et al. (2015). "Potential of pulsed corona discharges generated in water for the degradation of persistent pharmaceutical residues". In: *Water Research* 84, pp. 127–135.
- Barceló, Damilà (1988). "A review of liquid chromatography in environmental pesticide analysis". In: *Chromatographia* 25.10, pp. 928–936.
- Beck, Sara E. et al. (2016). "Comparison of UV-Induced Inactivation and RNA Damage in MS2 Phage across the Germicidal UV Spectrum". In: *Applied and Environmental Microbiology* 82.5, pp. 1468–1474.
- Berendsen, C W J et al. (2015). "Marangoni flows induced by atmospheric-pressure plasma jets". In: *Journal of Physics D: Applied Physics* 48.2.
- Birkin, Peter R., Yvonne E. Watson, and Timothy G. Leighton (2001). "Efficient mass transfer from an acoustically oscillated gas bubble". In: *Chemical Communications* 24, pp. 2650–2651.
- Blevin, H. A., J. Fletcher, and S. R. Hunter (1985). "Electron-velocity distribution functions in gases: The influence of anisotropic scattering and electron nonconservation by attachment and ionization". In: *Physical Review A* 31.4, pp. 2215–2226.
- Bobkova, Elena S. and Vladimir V. Rybkin (2015). "Peculiarities of Energy Efficiency Comparison of Plasma Chemical Reactors for Water Purification from Organic Substances". In: *Plasma Chemistry and Plasma Processing* 35.1, pp. 133–142.
- Bokare, Alok D. and Wonyong Choi (2014). "Review of iron-free Fenton-like systems for activating H₂O₂ in advanced oxidation processes". In: *Journal of Hazardous Materials* 275, pp. 121–135.
- Bolton, James R. and Mihaela I. Stefan (2002). "Fundamental photochemical approach to the concepts of fluence (UV dose) and electrical energy efficiency in photochemical degradation reactions". In: *Research on Chemical Intermediates* 28.7–9, pp. 857–870.

- Bolton, James R. et al. (2001). *Figures-of-Merit for the Technical Development and Application of Advanced Oxidation Technologies for Both Electric- and Solar-Driven Systems*. Tech. rep. 4. International Union of Pure and Applied Chemistry, pp. 627–637.
- Borchers, James W. et al. (2014). *Land Subsidence from Groundwater Use in California*. Tech. rep. California Water Foundation.
- Brandhuber, Philip J. and Gregory Korshin (2009). *Methods for the Detection of Residual Concentrations of Hydrogen Peroxide in Advanced Oxidation Processes*. Tech. rep. WRF-04-019. WaterReuse Foundation.
- Bruggeman, P J et al. (2016). “Plasma-liquid interactions: a review and roadmap”. In: *Plasma Sources Science and Technology* 25.5.
- Bruggeman, Peter and Ronny Brandenburg (2013). “Atmospheric pressure discharge filaments and microplasmas: physics, chemistry and diagnostics”. In: *Journal of Physics D: Applied Physics* 46.46.
- Bruggeman, Peter and Christophe Leys (2009). “Non-thermal plasmas in and in contact with liquids”. In: *Journal of Physics D: Applied Physics* 42.5.
- Buffle, Marc-Olivier and Urs von Gunten (2006). “Phenols and Amine Induced HO Generation During the Initial Phase of Natural Water Ozonation”. In: *Environmental Science & Technology* 40.9, pp. 3057–3063.
- Butkovskaya, N. I. et al. (2004). “Rate Constant and Mechanism of the Reaction of OH Radicals with Acetic Acid in the Temperature Range of 229–300 K”. In: *Journal of Physical Chemistry A* 108.34, pp. 7021–7026.
- Buxton, George V. et al. (1988). “Critical Review of Rate Constants for Reactions of Hydrated Electrons, Hydrogen Atoms and Hydroxyl Radicals (OH/O⁻) in Aqueous Solution”. In: *Journal of Physical and Chemical Reference Data* 17.2.
- Cabane, Bernard and Rodolphe Vuileumier (2005). “The physics of liquid water”. In: *Comptes Rendus Geoscience* 337, pp. 159–171.
- Calderara, V., Martin Jekel, and C. Zaror (2002). “Ozonation of 1-Naphthalene, 1,5-Naphthalene, and 3-Nitrobenzene Sulphonic Acids in Aqueous Solutions”. In: *Environmental Technology* 23.4, pp. 373–380.
- Campos-Martin, Jose M., Gema Blanco-Brieva, and Jose L. G. Fierro (2006). “Hydrogen Peroxide Synthesis: An Outlook beyond the Anthraquinone Process”. In: *Angewandte Chemie International Edition* 45.42, pp. 6962–6984.
- Carter, Kimberly E. and James Farrell (2008). “Oxidative Destruction of Perfluorooctane Sulfonate Using Boron-Doped Diamond Film Electrodes”. In: *Environmental Science and Technology* 42.16, pp. 6111–6115.
- CDFA (2013). *California Agricultural Statistics Review 2012–2013*. Tech. rep. California Department of Food and Agriculture Office of Public Affairs.
- Chen, Hsin Liang et al. (2008). “Review of Packed-Bed Plasma Reactor for Ozone Generation and Air Pollution Control”. In: *Industrial and Engineering Chemistry Research* 47.7, pp. 2122–2130.
- Chen, Jian, Stephanie Loeb, and Jae-Hong Kim (2017). “LED revolution: fundamentals and prospects for UV disinfection applications”. In: *Environmental Science Water Research and Technology* 3.2, pp. 188–202.

- Coleman, H. M. et al. (2007a). "Degradation of 1,4-dioxane in water using TiO₂ based photocatalytic and H₂O₂/UV processes". In: *Journal of Hazardous Materials* 146.3, pp. 496–501.
- (2007b). "Removal of contaminants of concern in water using advanced oxidation techniques". In: *Water Science and Technology* 55.12, pp. 301–306.
- Creek, Daniel and James Davidson (2008). *Treatment Technologies for Removal of MTBE from Drinking Water: Granular Activated Carbon*. Tech. rep. NWRI-99-06. National Water Research Institute.
- Crittenden, J. C. et al. (2005). *Water Treatment: Principles and Design*. John Wiley & Sons, Inc.
- Crittenden, John C. et al. (2012). *MWH's Water Treatment: Principles and Design*. John Wiley & Sons, Inc.
- Daughton, Christian G. and Thomas A. Ternes (1999). "Pharmaceuticals and Personal Care Products in the Environment: Agents of Subtle Change?" In: *Environmental Health Perspectives* 107.6.
- del Pino, Manuel P. and Bruce Durham (1999). "Wastewater reuse through dual-membrane processes: opportunities for sustainable water resources". In: *Desalination* 124.1–2, pp. 271–277.
- DeMore, William B. (1973). "Rate Constants for the Reactions of Hydroxyl and Hydroperoxyl Radicals with Ozone". In: *Science* 180.4087, pp. 735–737.
- DOE OEERE, U.S. (2017). *Water and Wastewater Annual Price Escalation Rates for Selected Cities across the United States*. Tech. rep. Federal Energy Management Program.
- Dutton, J. (1975). "A survey of electron swarm data". In: *Journal of Physical and Chemical Reference Data* 4.3, pp. 577–856.
- Dutton, J. and J. M. Powell (1971). "The influence of Penning ionization on the experimental determination of ionization coefficients in helium at low values of E/N". In: *Journal of Physics B: Atomic and Molecular Physics* 4.11, pp. 1506–1515.
- Eberle, Dylan, Raymond Ball, and Thomas B. Boving (2016). "Perozone activated persulfate treatment of 1,4-dioxane in the presence of chlorinated solve co-contaminants". In: *Chemosphere* 144, pp. 728–735.
- Eccles, M. J., B. C. O'Neill, and J. D. Craggs (1970). "Electron detachment in oxygen". In: *Journal of Physics B: Atomic and Molecular Physics* 3.12, pp. 1724–1731.
- Eggers, Jens and Emmanuel Villermaux (2008). "Physics of liquid jets". In: *Reports on Progress in Physics* 71.3.
- Elovitz, Michael S. and Urs von Gunten (1999). "Hydroxyl Radical/Ozone Ratios During Ozonation Processes. I. The Rct Concept". In: *Ozone: Science & Engineering* 21.3, pp. 239–260.
- Elovitz, Michael S., Urs von Gunten, and Hans-Peter Kaiser (2000). "Hydroxyl Radical/Ozone Ratios During Ozonation Processes. II. The Effect of Temperature, pH, Alkalinity, and DOM Properties". In: *Ozone: Science & Engineering* 22.2, pp. 123–150.
- Engeling, Kenneth et al. (2018). "Time-resolved evolution of micro-discharges, surface ionization waves and plasma propagation in a two-dimensional packed bed reactor". In: *Plasma Sources Science and Technology* 27.8.

- EPA OW, U.S. (2003). *Wastewater Technology Fact Sheet Disinfection for Small Systems*. Tech. rep. EPA 832-F-03-024. Office of Water.
- (2016). *The Analysis of Regulated Contaminant Occurrence Data from Public Water Systems in Support of the Third Six-Year Review of National Primary Drinking Water Regulations: Chemical Phase Rules and Radionuclides Rules*. Tech. rep. EPA-810-R-16-014. Office of Water.
- Even-Ezra, Itay et al. (2009). “Application of a novel plasma-based advanced oxidation process for efficient and cost-effective destruction of refractory organics in tertiary effluents and contaminated groundwater”. In: *Desalination and Water Treatment* 11, pp. 236–244.
- Fang, Jingyun, Yun Fu, and Chii Shang (2014). “The Roles of Reactive Species in Micropollutant Degradation in the UV/Free Chlorine System”. In: *Environmental Science and Technology*.
- Fick, Adolph (1855). “V. On liquid diffusion”. In: *The London, Edinburgh, and Dublin Philosophical Magazine and Journal of Science* 10.63, pp. 30–39.
- Fischbacher, Alexandra, Holger V. Lutze, and Torsten C. Schmidt (2018). *Ozone/H₂O₂ and ozone/UV processes*. Ed. by Mihaela I. Stefan. IWA Publishing.
- Foster, John E. (2017). “Plasma-based water purification: Challenges and prospects for the future”. In: *Physics of Plasmas* 24.055501.
- Foster, John E. and Janis Lai (2016). “2-D Bubble Test Cell for the Study of Interactions at the Plasma-Liquid Interface”. In: *IEEE Transactions on Plasma Science* 44.7, pp. 1127–1136.
- Foster, John E et al. (2010). “Underwater operation of a DBD plasma jet”. In: *Plasma Sources Science and Technology* 19.
- Foster, John E et al. (2012). “Perspectives on the Interaction of Plasmas With Liquid Water for Water Purification”. In: *IEEE Transactions on Plasma Science* 40.5, pp. 1311–1323.
- Foster, John E. et al. (2013). “A Comparative Study of the Time-Resolved Decomposition of Methylene Blue Dye Under the Action of a Nanosecond Repetitively Pulsed DBD Plasma Jet Using Liquid Chromatography and Spectrophotometry”. In: *IEEE Transactions on Plasma Science* 41.3, pp. 503–512.
- Foster, John E et al. (2018). “Towards high throughput plasma based water purifiers: design considerations and the pathway towards practical application”. In: *Journal of Physics D: Applied Physics* 51.29.
- Freeman, Willard M., Stephen J. Walker, and Kent E. Vrana (1999). “Quantitative RT-PCR: Pitfalls and Potential”. In: *BioTechniques* 26.1, pp. 112–125.
- Gassie, Lucien W. and James D. Englehardt (2017). “Advanced oxidation and disinfection processes for onsite net-zero greywater reuse: A review”. In: *Water Research* 125, pp. 384–399.
- Gebbink, Wouter A., Laura van Asseldonk, and Stefan P.J. van Leeuwen (2017). “Presence of Emerging Per- and Polyfluoroalkyl Substances (PFASs) in River and Drinking Water near a Fluorochemical Production Plant in the Netherlands”. In: *Environmental Science and Technology* 51, pp. 11057–11065.

- Gerrity, Daniel, Fernando L. Rosario-Ortiz, and Eric C. Wert (2018). *Advanced Oxidation Processes for Water Treatment: Fundamentals and Applications*. 3. *Application of ozone in water and wastewater treatment*. Ed. by Mihaela I. Stefan. IWA Publishing.
- Gerrity, Daniel et al. (2013). "Potable reuse treatment trains throughout the world". In: *Journal of Water Supply: Research and Technology-Aqua* 62.6, pp. 321–338.
- Glassmeyer, Susan T. et al. (2016). "Nationwide reconnaissance of contaminants of emerging concern in source and treated drinking waters of the United States". In: *Science of the Total Environment*.
- Gonzalez, Mónica G. et al. (2004). "Vacuum-ultraviolet photolysis of aqueous reaction systems". In: *Journal of Photochemistry and Photobiology, C: Photochemistry Reviews* 5.3, pp. 225–246.
- Gottschalk, Christiane, Judy Ann Libra, and Adrian Saupe (2010). *Ozonation of Water and Waste Water: A Practical Guide to Understanding Ozone and its Applications*. Wiley-VCH Verlag GmbH & Co. KGaA.
- Grady Jr., C.P. Leslie et al. (2011). *Biological Wastewater Treatment*. CRC Press Taylor & Francis Group and IWA Publishing.
- Graves, David B (2012). "The emerging role of reactive oxygen and nitrogen species in redox biology and some implications for plasma applications to medicine and biology". In: *Journal of Physics D: Applied Physics* 45.26.
- Greenlee, Lauren F. et al. (2009). "Reverse osmosis desalination: Water sources, technology, and today's challenges". In: *Water Research* 43.9, pp. 2317–2348.
- Gucker, Sarah M. Nowak (2015). "Plasma Discharges in Gas Bubbles in Liquid Water: Breakdown Mechanisms and Resultant Chemistry". PhD thesis. University of Michigan.
- Gucker, Sarah Nowak, John E Foster, and Maria C Garcia (2015). "An investigation of an underwater steam plasma discharge as alternative to air plasmas for water purification". In: *Plasma Sources Science and Technology* 24.5.
- Guiochon, Georges and Claude L. Guillemin (1990). "Gas chromatography". In: *Review of Scientific Instruments* 61.11, pp. 3317–3339.
- Hardy, C. J. and F. H. Pollard (1960). "Review of Gas-Liquid Chromatography". In: *Chromatographic Reviews* 2, pp. 1–43.
- Harrison, Melvin A. and Ronald Geballe (1953). "Simultaneous Measurement of Ionization and Attachment Coefficients". In: *Physical Review* 91.1.
- Hijnen, W. A. M., E. F. Beerendonk, and G. J. Medema (2006). "Inactivation credit of UV radiation for viruses, bacteria and protozoan (oo)cysts in water: A review". In: *Water Research* 40.1, pp. 3–22.
- Hofman-Caris, Roberta C.H.M. et al. (2012). "Prediction of advanced oxidation performance in various pilot UV/H₂O₂ reactor systems with MP- and LP- and DBD-UV lamps". In: *Chemical Engineering Journal* 210, pp. 520–528.
- Hoigné, Jürg (1997). "Inter-calibration of OH radical sources and water quality parameters". In: *Water Science and Technology* 35.4, pp. 1–8.
- Holgate, J. T., M. Coppins, and J. E. Allen (2018). "Electrohydrodynamic stability of a plasma-liquid interface". In: *Applied Physics Letters* 112.2.

- Hu, Xindi C. et al. (2016). "Detection of Poly- and Perfluoroalkyl Substances (PFASs) in U.S. Drinking Water Linked to Industrial Sites, Military Fire Training Areas, and Wastewater Treatment Plants". In: *Environmental Science and Technology Letters*.
- Hübner, Uwe, I. Zucker, and Martin Jekel (2015). "Options and limitations of hydrogen peroxide addition to enhance radical formation during ozonation of secondary effluents". In: *Journal of Water Reuse and Desalination* 5.1, pp. 8–16.
- Illés, Erzsébet et al. (2014). "Ketoprofen removal by O₃ and O₃/UV processes: Kinetics, transformation products and ecotoxicity". In: *Science of the Total Environment* 472, pp. 178–184.
- Johnson, Derek C. et al. (2016). "An innovative non-thermal plasma reactor to eliminate microorganisms in water". In: *Desalination and Water Treatment* 57, pp. 8097–8108.
- Johnston, Jill E., Emily Werder, and Daniel Sebastian (2016). "Wastewater Disposal Wells, Fracking, and Environmental Justice in Southern Texas". In: *American Journal of Public Health* 106.3, pp. 550–556.
- Joshi, A. A. et al. (1995). "Formation of hydroxyl radicals, hydrogen peroxide and aqueous electrons by pulsed streamer corona discharge in aqueous solution". In: *Journal of Hazardous Materials* 41, pp. 3–30.
- Judd, Simon and Claire Judd, eds. (2006). *The MBR Book Principles and Applications of Membrane Bioreactors in Water and Wastewater Treatment*. Elsevier.
- Justo, Ana et al. (2014). "Application of bioassay panel for assessing the impact of advanced oxidation processes on the treatment of reverse osmosis brine". In: *Journal of Chemical Technology & Biotechnology* 89.8, pp. 1168–1174.
- Katsoyiannis, Ioannis A., Silvio Canonica, and Urs von Gunten (2011). "Efficiency and energy requirements for the transformation of organic micropollutants by ozone, O₃/H₂O₂ and UV/H₂O₂". In: *Water Research* 45.13, pp. 3811–3822.
- Kawasaki, Toshiyuki et al. (2015). "Detection of reactive oxygen species supplied into the water bottom by atmospheric non-thermal plasma jet using iodine-starch reaction". In: *Japanese Journal of Applied Physics* 54.8.
- Kenzie, W. R. et al. (1994). "A massive outbreak in Milwaukee of cryptosporidium infection transmitted through the public water supply". In: *The New England Journal of Medicine* 331, pp. 161–167.
- Kirkpatrick, Michael J. and Bruce R. Locke (2005). "Hydrogen, Oxygen, and Hydrogen Peroxide Formation in Aqueous Phase Pulsed Corona Electrical Discharge". In: *Industrial & Engineering Chemistry Research* 44.12, pp. 4243–4248.
- Klosterhaus, Susan et al. (2013). *Contaminants of Emerging Concern in San Francisco Bay: A Summary of Occurrence Data and Identification of Data Gaps*. Tech. rep. 698. San Francisco Estuary Institute.
- Knobeloch, Lynda et al. (2000). "Blue Babies and Nitrate-Contaminated Well Water". In: *Environmental Health Perspectives* 108.7, pp. 675–678.
- Kobayashi, Kenkichiro, Yasumasa Tomita, and Masahiro Sanmyo (2000). "Electrochemical Generation of Hot Plasma by Pulsed Discharge in an Electrolyte". In: *Journal of Physical Chemistry B* 104.26, pp. 6318–6326.

- Kogelschatz, Ulrich (2003). "Dielectric-barrier Discharges: Their History, Discharge Physics, and Industrial Applications". In: *Plasma Chemistry and Plasma Processing* 23.1.
- Kolb, J F, Joshi S Xiao, and K H Schoenbach (2008). "Streamers in water and other dielectric liquids". In: *Journal of Physics D: Applied Physics* 41.23.
- Kolpin, Dana W. et al. (2002). "Pharmaceuticals, Hormones, and Other Organic Wastewater Contaminants in U.S. Streams, 1999–2000: A National Reconnaissance". In: *Environmental Science and Technology* 36, pp. 1202–1211.
- Kommineni, Sunil et al. (2008a). "Advanced oxidation of methyl-tertiary butyl ether: pilot study findings and full-scale implications". In: *Journal of Water Supply: Research and Technology-Aqua* 57.6, pp. 403–418.
- Kommineni, Sunil et al. (2008b). *Treatment Technologies for Removal of MTBE from Drinking Water: Advanced Oxidation Processes*. Tech. rep. NWRI-99-06. National Water Research Institute.
- Koubek, Edward (1975). "Photochemically Induced Oxidation of Refractory Organics with Hydrogen Peroxide". In: *Industrial and Engineering Chemistry Process Design and Development* 14.3, pp. 348–350.
- Kruithof, A. A. and F. M. Penning (1937). "Determination of the townsend ionization coefficient for mixtures of neon and argon". In: *Physica* 4.6, pp. 430–449.
- Kruszelnicki, Juliusz et al. (2017). "Propagation of negative electrical discharges through 2-dimensional packed bed reactors". In: *Journal of Physics D: Applied Physics* 50.2.
- Kunhardt, E. E. (2000). "Generation of Large-Volume, Atmospheric-Pressure, Nonequilibrium Plasmas". In: *IEEE Transactions on Plasma Science* 28.1, pp. 189–200.
- Kushner, Mark J (2014). *Documentation for GlobalKin*. Tech. rep. University of Michigan.
- Kuster, Marina, Maria López de Alda, and Damilà Barceló (2006). "Analysis of pesticides in water by liquid chromatography-tandem mass spectrometric techniques". In: *Mass Spectrometry Reviews* 25.6, pp. 900–916.
- Kwon, Soon Chul et al. (2012). "Treatment characteristic of 1,4-dioxane by ozone-based advanced oxidation processes". In: *Journal of Industrial and Engineering Chemistry* 18.6, pp. 1951–1955.
- Lai, Janis, Victor Petrov, and John Foster (2018). "Understanding Plasma-Liquid Interface Instabilities Using Particle Image Velocimetry and Shadowgraphy Imaging Methods". In: *IEEE Transactions on Plasma Science* 46.4, pp. 875–881.
- Laroussi, Mounir and Tamer Akan (2007). "Arc-Free Atmospheric Pressure Cold Plasma Jets: A Review". In: *Plasma Processes and Polymers* 4.9, pp. 777–788.
- Le-Clech, Pierre, Vicki Chen, and Tony A. G. Fane (2006). "Fouling in membrane bioreactors used in wastewater treatment". In: *Journal of Membrane Science* 284, pp. 17–53.
- Le Roux, Julien, Hervé Gallard, and Jean-Philippe Croué (2012). "Formation of NDMA and Halogenated DBPs by Chloramination of Tertiary Amines: The Influence of Bromide Ion". In: *Environmental Science & Technology* 46.3, pp. 1581–1589.

- Lee, Changha et al. (2005). "UV Photolytic Mechanism of N-Nitrosodimethylamine in Water: Dual Pathways to Methylamine versus Dimethylamine". In: *Environmental Science & Technology* 39.7, pp. 2101–2106.
- Lee, E. et al. (2011). "Hydrogen peroxide interference in chemical oxygen demand during ozone based advanced oxidation of anaerobically digested livestock wastewater". In: *International Journal of Environmental Science and Technology* 8.2, pp. 381–388.
- Leilei, Wang, Chen Wei, and Lin Tao (2008). "Particle size distribution and property of bacteria attached to carbon fines in drinking water treatment". In: *Water Science and Engineering* 1.2, pp. 102–111.
- Lewis, T. J. (1998). "A New Model for the Primary Process of Electrical Breakdown in Liquids". In: *IEEE Transactions on Dielectrics and Electrical Insulation* 5.3, pp. 306–315.
- Lietz, Amanda M and Mark J Kushner (2016). "Air plasma treatment of liquid covered tissue: long timescale chemistry". In: *Journal of Physics D: Applied Physics* 49.
- (2018). "Electrode configurations in atmospheric pressure plasma jets: production of reactive species". In: *Plasma Sources Science and Technology* 27.10.
- Liu, Wenjun et al. (2003). "Optimal methods for quenching H₂O₂ residuals prior to UFC testing". In: *Water Research* 37.15, pp. 3697–3703.
- Locht, R. and J. Schopman (1974). "The dissociative ionization in oxygen". In: *International Journal of Mass Spectrometry and Ion Physics* 15.4, pp. 361–378.
- Locke, B R et al. (2006). "Electrohydraulic Discharge and Nonthermal Plasma for Water Treatment". In: *Industrial & Engineering Chemistry Research* 45.3, pp. 882–905.
- Loeb, Leonard Benedict (1960). *Basic Processes of Gaseous Electronics*. Berkeley, CA: University of California Press.
- Lu, X, M Laroussi, and V Puech (2012). "On atmospheric-pressure non-equilibrium plasma jets and plasma bullets". In: *Plasma Sources Science and Technology* 21.3.
- Lucas, J., D. A. Price, and J. L. Moruzzi (1973). "The calculation of electron energy distributions and attachment coefficient for electron swarms in oxygen". In: *Journal of Physics D: Applied Physics* 6.12, pp. 1503–1513.
- Malik, Muhammad A. (2010). "Water Purification by Plasmas: Which Reactors are Most Energy Efficient?" In: *Plasma Chemistry Plasma Process* 30, pp. 21–31.
- Manolache, S. et al. (2001). "Dense Medium Plasma Environments: A New Approach for the Disinfection of Water". In: *Environmental Science & Technology* 35.18, pp. 3780–3785.
- Marković, V. Lj., S. N. Stamenković, and S. R. Gocić (2007). "Formative Time Delay in Nitrogen Discharges at Low Pressure". In: *Contributions to Plasma Physics* 47.6, pp. 413–420.
- McCarthy, M. J. and N. A. Molloy (1974). "Review of Stability of Liquid Jets and the Influence of Nozzle Design". In: *The Chemical Engineering Journal* 7.
- McNamara, James D. et al. (2018). "Comparison of Activated Carbons for Removal of Perfluorinated Compounds From Drinking Water". In: *Journal of American Water Works Association* 110.1, E2–E14.

- Mededovic Thagard, Selma et al. (2017). "Plasma-based water treatment: development of a general mechanistic model to estimate the treatability of different types of contaminants". In: *Journal of Physics D: Applied Physics* 50.014003.
- Meek, J. M. (1940). "A Theory of Spark Discharge". In: *Physical Review* 57.8, pp. 722–728.
- Melcher, J. R. (1963). *Field-Coupled Surface Waves: A Comparative Study of Surface-Coupled Electrohydrodynamic and Magnetohydrodynamic Systems*. Cambridge, MA: MIT Press.
- Merényi, Gábor et al. (2010a). "Reaction of Ozone with Hydrogen Peroxide (Perozone Process): A Revision of Current Mechanistic Concepts Based on Thermokinetic and Quantum-Chemical Considerations". In: *Environmental Science and Technology* 44.9, pp. 3505–3507.
- (2010b). "The Reaction of Ozone with the Hydroxide Ion: Mechanistic Considerations Based on Thermokinetic and Quantum Chemical Calculations and the Role of HO₄⁻ in Superoxide Dismutation". In: *Chemistry—A European Journal* 16.4, pp. 1372–1377.
- Miklos, David B. et al. (2018). "Evaluation of advanced oxidation processes for water and wastewater treatment—A critical review". In: *Water Research* 139, pp. 118–131.
- Miller-Schulze, Justin et al. (2014). "Contaminants of Emerging Concern in Puget Sound: A Comparison of Spatial and Temporal Levels and Occurrence". In: *Salish Sea Ecosystem Conference*.
- Mitani, Marie M. et al. (2002). "Kinetics and products of reactions of MTBE with O₃ and O₃/H₂O₂ in water". In: *Journal of Hazardous Materials* B89, pp. 197–212.
- Montijn, Carolynne and Ute Ebert (2006). "Diffusion correction to the Raether-Meek criterion for avalanche-to-streamer transition". In: *Journal of Physics D: Applied Physics*, pp. 2979–2992.
- Mosher, Jeffrey J. and Julie N. Minton (2016). *Potable Reuse Research Compilation: Synthesis of Findings*. Tech. rep. Reuse-15-01. Water Research Foundation.
- Mosher, Jeffrey J. and Gina Vartanian (2018). *Guidance Framework for Direct Potable Reuse in Arizona*. Tech. rep. NWRI-2017-09. National Water Research Institute prepared for WateReuse Arizona.
- Mujovic, Selman, Joseph Groele, and John E. Foster (2015a). "Streamer Formation in Single and Multiple Bubbles in Water". In: *68th Gaseous Electronics Conference*. Vol. 60. 9. Honolulu, Hawaii.
- (2015b). "The Time Evolution and Formation of Streamer Discharges in Single & Multiple Bubbles in Water". In: *6th Annual MIPSE Graduate Student Symposium*. Michigan Institute for Plasma Science and Engineering.
- Mutaf-Yardimci, Ozlem et al. (2000). "Thermal and nonthermal regimes of gliding arc discharge in air flow". In: *Journal of Applied Physics* 87.4, pp. 1632–1641.
- NACWA, WERF, and WEF (2013). *The Water Resources Utility of the Future ... A Blueprint for Action*. Tech. rep. National Association of Clean Water Agencies (NACWA), Water Environment Research Foundation (WERF), and Water Environment Federation (WEF).

- Naidu, M. S., A. N. Prasad, and J. D. Craggs (1972). "Electron transport, attachment and ionization in c-C₄F₈ and iso-C₄F₈". In: *Journal of Physics D: Applied Physics* 5.4, pp. 741–746.
- Neretti, G et al. (2017). "Characterization of a dielectric barrier discharge in contact with liquid and producing a plasma activated water". In: *Plasma Sources Science and Technology* 26.1.
- Newton, Seth et al. (2017). "Novel Polyfluorinated Compounds Identified Using High Resolution Mass Spectrometry Downstream of Manufacturing Facilities near Decatur, Alabama". In: *Environmental Science and Technology* 51.3, pp. 1544–1552.
- Ng, Eddie Yin-Kwee and Du Guannan (2015). "The stability of 30-um-diameter water jet for jet-guided laser machining". In: *The International Journal of Advanced Manufacturing Technology* 78.5–8, pp. 939–946.
- Nonell, Santi and Cristina Flors, eds. (2016). *Singlet Oxygen: Applications in Biosciences and Nanosciences*. Vol. 1. Comprehensive Series in Photochemical and Photobiological Sciences. The Royal Society of Chemistry.
- NWRI (2016). *Final Report of an NWRI Independent Advisory Panel: Recommended DPR General Guidelines and Operational Requirements for New Mexico*. Tech. rep. NWRI-2015-08. National Water Research Institute prepared for New Mexico Environment Department.
- Occiano, Victor and James Strayer (2012). *San Diego Recycled Water Study*. Tech. rep. Project No. 137921. Black & Veatch prepared for City of San Diego, Public Utilities Dept.
- OCWD (2017). *Orange County Water District Budget Report FY 2017–2018*. Tech. rep. Orange County Water District.
- Ødegaard, H., B. Rusten, and T. Westrum (1994). "A New Moving Bed Biofilm Reactor—Applications and Results". In: *Water Science and Technology* 29.10–11, pp. 157–165.
- Ohsawa, A, R Morrow, and A B Murphy (2000). "An Investigation of a DC Dielectric Barrier Discharge Using a Disc of Glass Beads". In: *Journal of Physics D: Applied Physics* 33, pp. 1487–1492.
- Oller, I., S. Malato, and J. A. Sánchez-Pérez (2011). "Combination of Advanced Oxidation Processes and biological treatments for wastewater decontamination—A review". In: *Science of the Total Environment* 409.20, pp. 4141–4166.
- Olmez-Hanci, Tugba, Idil Arslan-Alaton, and Duygu Dursun (2014). "Investigation of the toxicity of common oxidants used in advanced oxidation processes and their quenching agents". In: *Journal of Hazardous Materials* 278, pp. 330–335.
- Olsen, Geary W. et al. (2008). "Decline in Perfluorooctanesulfonate and Other Polyfluoroalkyl Chemicals in American Red Cross Adult Blood Donors, 2000–2006". In: *Environmental Science and Technology* 42.13, pp. 4989–4995.
- Peleg, M. (1976). "The chemistry of ozone in the treatment of water". In: *Water Research* 10.5, pp. 361–365.

- Perez, Erick Roman et al. (2016). "Comparison of LC-MS-MS and GC-MS Analysis of Benzodiazepine Compounds Included in the Drug Demand Reduction Urinalysis Program". In: *Journal of Analytical Toxicology* 40.3, pp. 201–207.
- Petrović, Mira, Susana Gonzalez, and Damilà Barceló (2003). "Analysis and removal of emerging contaminants in wastewater and drinking water". In: *Trends in Analytical Chemistry* 22.10, pp. 685–696.
- Peyton, Gary R. (1990). *Emerging Technologies in Hazardous Waste Management; Chapter 7: Modeling Advanced Oxidation Processes for Water Treatment*. Ed. by D. William Tedder and Frederick G. Pohland. Vol. 422. American Chemical Society, pp. 100–118.
- Peyton, Gary R. and William H. Glaze (1988). "Destruction of pollutants in water with ozone in combination with ultraviolet radiation. 3. Photolysis of aqueous ozone". In: *Environmental Science & Technology* 22.7, pp. 761–767.
- Pines, David S. and David A. Reckhow (2002). "Effect of Dissolved Cobalt (II) on the Ozonation of Oxalic Acid". In: *Environmental Science and Technology* 36.19, pp. 4046–4051.
- Prakash, Ram et al. (2017). "Dielectric Barrier Discharge based Mercury-free plasma UV-lamp for efficient water disinfection". In: *Scientific Reports* 1.
- Prasad, A. N. and J. D. Craggs (1962). "Pure and Applied Physics". In: ed. by D. R. Bates. Vol. 13. Elsevier BV. Chap. 6 - Attachment and Ionization Coefficients, pp. 206–244.
- Price, D. A., J. Lucas, and J. L. Moruzzi (1973). "Current growth in oxygen". In: *Journal of Physics D: Applied Physics* 6.12, pp. 1514–1524.
- Prichard, Emma and Elise F. Granek (2016). "Effects of pharmaceuticals and personal care products on marine organisms: from single-species studies to an ecosystem-based approach". In: *Environmental Science and Pollution Research* 23.22.
- Probstein, Ronald F. (1994). *Physicochemical Hydrodynamics: An Introduction*. John Wiley & Sons, Inc.
- Pröfrock, Daniel and Andreas Prange (2012). "Inductively Coupled Plasma-Mass Spectrometry (ICP-MS) for Quantitative Analysis in Environmental and Life Sciences: A Review of Challenges, Solutions, and Trends". In: *Applied Spectroscopy* 66.8, pp. 843–868.
- Programme, United Nations World Water Assessment (2015). *The United Nations World Water Development Report 2015: Water for a Sustainable World*. Tech. rep. UNESCO.
- (2017). *The United Nations World Water Development Report 2017. Wastewater: The Untapped Resource*. Tech. rep. UNESCO.
- Prosen, Helena and Lucija Zupančič-Kralj (1999). "Solid-phase microextraction". In: *Trends in Analytical Chemistry* 18.4, pp. 272–282.
- Pryor, William A. (1986). "Oxy-Radicals and Related Species: Their formation, Lifetimes, and Reactions". In: *Annual Review of Physiology* 48, pp. 657–667.
- Radjenović, Jelena, Mira Petrović, and Damilà Barceló (2008). "Fate and distribution of pharmaceuticals in wastewater and sewage sludge of the conventional activated sludge (CAS) and advanced membrane bioreactor (MBR) treatment". In: *Water Research* 43.3, pp. 831–841.

- (2009). “Complementary mass spectrometry and bioassays for evaluating pharmaceutical-transformation products in treatment of drinking water and wastewater”. In: *Trends in Analytical Chemistry* 28.5, pp. 562–580.
- Raether, Heinz (1964). *Electron Avalanches and Breakdown in Gases*. London: Butterworths.
- Rahn, Ronald O. (1997). “Potassium Iodide as a Chemical Actinometer for 254 nm Radiation: Use of Iodate as an Electron Scavenger”. In: *Photochemistry and Photobiology* 66.4, pp. 450–455.
- Raina, Renata and Patricia Hall (2008). “Comparison of Gas Chromatography-Mass Spectrometry and Gas Chromatography-Tandem Mass Spectrometry with Electron Ionization and Negative-Ion Chemical Ionization for Analyses of Pesticides at Trace Levels in Atmospheric Samples”. In: *Analytical Chemistry Insights* 3, pp. 111–125.
- Raju, Gorur Govinda (2005). *Gaseous Electronics: Theory and Practice*. 1st. CRC Press Taylor & Francis Group.
- Raucher, Robert and George Tchobanoglous (2014). *The Opportunities and Economics of Direct Potable Reuse*. Tech. rep. WateReuse Research Foundation.
- Reemtsma, Thorsten (2001). “The use of liquid chromatography-atmospheric pressure ionization-mass spectrometry in water analysis—Part II: Obstacles”. In: *Trends in Analytical Chemistry* 20.10, pp. 533–542.
- Rens, Jasper F. M. van et al. (2014). “Induced Liquid Phase Flow by RF Ar Cold Atmospheric Pressure Plasma Jet”. In: *IEEE Transactions on Plasma Science* 42.10, pp. 2622–2623.
- Reuter, Stephan, Thomas von Woedtke, and Klaus-Dieter Weltmann (2018). “The kINPen—a review on physics and chemistry of the atmospheric pressure plasma jet and its applications”. In: *Journal of Physics D: Applied Physics* 51.23.
- Richardson, Susan D. et al. (2003). “Tribromopyrrole, Brominated Acids, and Other Disinfection Byproducts Produced by Disinfection of Drinking Water Rich in Bromide”. In: *Environmental Science & Technology* 37.17, pp. 3782–3793.
- Richardson, Susan D. et al. (2007). “Occurrence, genotoxicity, and carcinogenicity of regulated and emerging disinfection by-products in drinking water: A review and roadmap for research”. In: *Mutation Research* 636.1–3, pp. 178–242.
- Richey, Alexandra S. et al. (2015). “Quantifying renewable groundwater stress with GRACE”. In: *Water Resources Research*.
- Rizzo, Luigi (2011). “Bioassays as a tool for evaluating advanced oxidation processes in water and wastewater treatment”. In: *Water Research* 45.15, pp. 4311–4340.
- Rosenfeldt, Erik J. and Karl G. Linden (2007). “The ROH,UV Concept to Characterize and the Model UV/H₂O₂ Process in Natural Waters”. In: *Environmental Science & Technology* 41.7, pp. 2548–2553.
- Rosenfeldt, Erik J. et al. (2006). “Comparison of the efficiency of OH radical formation during ozonation and the advanced oxidation processes O₃/H₂O₂ and UV/H₂O₂”. In: *Water Research* 40.20, pp. 3695–3704.

- Rosso, Diego, Lory E. Larson, and Michael K. Stenstrom (2008). "Aeration of large-scale municipal wastewater treatment plants: state of the art". In: *Water Science and Technology* 57.7, pp. 973–978.
- Rumbach, Paul, Jean Pierre Clarke, and David B. Go (2017). "Electrostatic Debye layer formed at a plasma-liquid interface". In: *Physical Review E* 95.5.
- Rumbach, Paul et al. (2015). "The solvation of electrons by a atmospheric-pressure plasma". In: *Nature Communications* 6.7248.
- Safarzadeh-Amiri, Ali (2001). "O₃/H₂O₂ treatment of methyl-tert-butyl ether (MTBE) in contaminated waters". In: *Water Research* 35.15, pp. 3706–3714.
- Salveson, Andrew et al. (2009). "Hydro Non-Thermal Plasma for Advanced Oxidation of Water". In: *Annual Conference Proceedings*. Ed. by Jess Brown. American Water Works Association.
- Sander, R. (2015). "Compilation of Henry's law constants (version 4.0) for water as solvent". In: *Atmospheric Chemistry and Physics* 15.8, pp. 4399–4981.
- Scheurer, Marco, Heinz-J. Brauch, and Frank T. Lange (2009). "Analysis and occurrence of seven artificial sweeteners in German waste water and surface water and in soil aquifer treatment (SAT)". In: *Analytical and Bioanalytical Chemistry* 394.6.
- Schimmoller, L. J., M. J. Kealy, and S. K. Foster (2015). "Triple bottom line costs for multiple potable reuse treatment schemes". In: *Environmental Science Water Research and Technology* 1, pp. 644–658.
- Schröder, Horst Fr. and Roland J.W. Meesters (2005). "Stability of fluorinated surfactants in AOPs— A follow up of degradation products using flow injection–MS, LC–MS and LC–multiple stage MS". In: *Journal of Chromatography A* 1082, pp. 110–119.
- Schroeder, Edward et al. (2012). *Direct Potable Reuse: Benefits for Public Water Supplies, Agriculture, the Environment, and Energy Conservation*. Tech. rep. NWRI-2012-01. National Water Research Institute.
- Sedlak, David and Michael Kavanaugh (2006). *Removal and Destruction of NDMA and NDMA Precursors during Wastewater Treatment*. Tech. rep. WRF-01-002. WaterReuse Foundation.
- Setälä, Outi et al. (2018). *Microplastic Contamination in Aquatic Environments: An Emerging Matter of Environmental Urgency*. Ed. by Eddy Y. Zeng. Elsevier.
- Shiklomanov, Igor (1993). *Water in Crisis: A Guide to the World's Fresh Water Resources*. Ed. by Peter H Gleick.
- Shimizu, Tetsuji et al. (2011). "Formation of thermal flow fields and chemical transport in air and water by atmospheric plasma". In: *New Journal of Physics* 13.
- Shneider, M. N., M. Pekker, and A. Fridman (2012). "Theoretical Study of the Initial Stage of Sub-nanosecond Pulsed Breakdown in Liquid Dielectrics". In: *IEEE Transactions on Dielectrics and Electrical Insulation* 19.5.
- Simonaitis, R. and Julian Heicklen (1982). "A kinetic study of the perhydroxyl + perhydroxyl reaction". In: *Journal of Physical Chemistry* 86.17, pp. 3416–3418.
- Skoog, Douglas A., F. James Holler, and Stanley R. Crouch (2018). *Principles of Instrumental Analysis*. 7th. Cengage Learning.

- Smith, Alexander M., Alpha A. Lee, and Susan Perkin (2016). "The Electrostatic Screening Length in Concentrated Electrolytes Increases with Concentration". In: *Journal of Physical Chemistry Letters* 7.12, pp. 2157–2163.
- Soller, Jeffrey et al. (2017). *White Paper on the Feasibility of Establishing a Framework for Public Health Monitoring of Direct Potable Reuse*. Tech. rep. Water Environment & Reuse Foundation.
- Sommers, Bradley S (2013). "Plasma Ignition in Underwater Gas Bubbles". PhD thesis. University of Michigan.
- Sommers, Bradley S et al. (2011). "Observations of electric discharge streamer propagation and capillary oscillations on the surface of air bubbles in water". In: *Journal of Physics D: Applied Physics* 44.082001.
- Sonntag, C. von (2008). "Advanced oxidation processes: mechanistic aspects". In: *Water Science and Technology* 58.5, pp. 1015–1021.
- Stefan, Mihaela I. (2018). *Advanced Oxidation Processes for Water Treatment: Fundamentals and Applications; Chapter 2: UV/Hydrogen peroxide process*. Ed. by Mihaela I. Stefan. IWA Publishing.
- Stefan, Mihaela I. and James R. Bolton (1998). "Mechanism of the Degradation of 1,4-Dioxane in Dilute Aqueous Solution Using UV Hydrogen Peroxide Process". In: *Environmental Science and Technology* 32.11, pp. 1588–1595.
- (2002). "UV Direct Photolysis of N-Nitrosodimethylamine (NMDA): Kinetic and Product Study". In: *Helvetica Chimica Acta* 85.5, pp. 1416–1426.
- Stocking, Andrew et al. (2008). *Treatment Technologies for Removal of MTBE from Drinking Water: Air Stripping*. Tech. rep. NWRI-99-06. National Water Research Institute.
- Stratton, Gunnar R. et al. (2017). "Plasma-Based Water Treatment: Efficient Transformation of Perfluoroalkyl Substances in Prepared Solutions and Contaminated Groundwater". In: *Environmental Science and Technology* 51, pp. 1643–1648.
- Suh, Jung Ho and Madjid Mohseni (2004). "A study on the relationship between biodegradability enhancement and oxidation of 1,4-dioxane using ozone and hydrogen peroxide". In: *Water Research* 38.10, pp. 2596–2604.
- Sutherland, J., C. Adams, and J. Kekobad (2004). "Treatment of MTBE by air stripping, carbon adsorption, and advanced oxidation: technical and economic comparison for five groundwaters". In: *Water Research* 38.1, pp. 193–205.
- Suthersan, Suthan et al. (2016). "Making Strides in the Management of Emerging Contaminants". In: *Groundwater Monitoring and Remediation* 36.1.
- Tchobanoglous, George et al. (2011). *Direct Potable Reuse: A Path Forward*. Tech. rep. Reuse-11-00. WaterReuse Foundation.
- Tendero, Claire et al. (2006). "Atmospheric pressure plasmas: A review". In: *Spectrochimica Acta Part B* 61, pp. 2–30.
- Tian, Wei (2015). "Modelling Interactions of Atmospheric Pressure Plasmas with Liquids". PhD thesis. University of Michigan.
- Tochikubo, Fumiyoshi et al. (2014). "Chemical reactions in liquid induced by atmospheric-pressure dc glow discharge in contact with liquid". In: *Japanese Journal of Applied Physics* 53.12.

- Todd, David K. (1974). "Salt-Water Intrusion and Its Control". In: *Journal of American Water Works Association* 66.3, pp. 180–187.
- Trojanowicz, Marek et al. (2018). "Advanced Oxidation/Reduction Processes treatment for aqueous perfluorooctanoate (PFOA) and perfluorooctanesulfonate (PFOS)—A review of recent advances". In: *Chemical Engineering Journal* 336, pp. 170–199.
- Vaferi, Behzad et al. (2014). "Experimental and theoretical analysis of the UV/H₂O₂ advanced oxidation processes treating aromatic hydrocarbons and MTBE from contaminated synthetic wastewaters". In: *Journal of Environmental Chemical Engineering* 2.3, pp. 1252–1260.
- Van Laer, Koen and Annemie Bogaerts (2016). "Fluid modelling of a packed bed dielectric barrier discharge plasma reactor". In: *Plasma Sources Science and Technology* 25.015002.
- Vescovi, Tania, Heather M. Coleman, and Rose Amal (2010). "The effect of pH on UV-based advanced oxidation technologies—1,4-dioxane degradation". In: *Journal of Hazardous Materials* 182.1–3, pp. 75–79.
- Wang, Ding, James R. Bolton, and Ron Hofmann (2012). "Medium pressure UV combined with chlorine advanced oxidation for trichloroethylene destruction in a model water". In: *Water Research* 46.15, pp. 4677–4686.
- WaterReuse et al. (2015). *Framework for Direct Potable Reuse*. Tech. rep. 14-20. WaterReuse Research Foundation.
- WaterReuse CO (2018). *Development of DPR Regulations in Colorado: Advancing Direct Potable Reuse to Optimize Water Supplies and Meet Future Demands*. Tech. rep. WaterReuse Colorado.
- Weber, Moritz Constantin (1931). "Zum Zerfall eines Flüssigkeitsstrahles". In: *ZAMM—Zeitschrift Für Angewandte Mathematik Und Mechanik* 11.2, pp. 136–153.
- Weber Jr., Walter, Massoud Pirbazari, and Gail Melson (1978). "Biological growth on activated carbon: an investigation by scanning electron microscopy". In: *Environmental Science and Technology* 12.7, pp. 817–819.
- Weinstein, Judith and Benon H. J. Bielski (1979). "Kinetics of the interaction of perhydroxyl and superoxide radicals with hydrogen peroxide. The Haber–Weiss Reaction". In: *Journal of the American Chemical Society* 101.1, pp. 58–62.
- Weiss, Joseph (1935). "Investigations on the radical HO₂ in solution". In: *Transactions of the Faraday Society* 31, pp. 668–681.
- WHO (2003). *Cyanobacterial toxins: Microcystin-LR in Drinking-water*. Tech. rep. WHO/SDE/WSH/03.04/57. World Health Organization.
- Wilf, Mark and Kenneth Klinko (2001). "Optimization of seawater RO systems design". In: *Desalination* 138.1–3, pp. 299–306.
- Winterbourn, Christine C (2008). "Reconciling the chemistry and biology of reactive oxygen species". In: *Nature Chemical Biology* 4.5.
- Wols, Bas A. and Roberta C.H.M. Hofman-Caris (2012). "Review of photochemical reaction constants of organic micropollutants required for UV advanced oxidation processes in water". In: *Water Research* 46.9, pp. 2815–2827.

- Wols, Bas A. et al. (2013). "Degradation of 40 selected pharmaceuticals by UV/H₂O₂". In: *Water Research* 47.15, pp. 5876–5888.
- WRD (2016). *Cost of Service Report*. Tech. rep. Water Replenishment District of Southern California.
- Yusupov, M et al. (2014). "Reactive molecular dynamics simulations of oxygen species in a liquid water layer of interest for plasma medicine". In: *Journal of Physics D: Applied Physics* 47.025205.
- Zhou, Yuan and Richard S. J. Tol (2005). "Evaluating the costs of desalination and water transport". In: *Water Resources Research* 41.3.
- Zhu, Guibing et al. (2008). *Reviews of Environmental Contamination and Toxicology. Chapter: Biological Removal of Nitrogen from Wastewater*. Ed. by David M. Whitacre. Springer New York, pp. 159–195.
- Zwiener, C. and F. H. Frimmel (2000). "Oxidative Treatment of Pharmaceuticals in Water". In: *Water Research* 34.6, pp. 1881–1885.